High Pressure Structural Studies of Organic Molecules

Alice Dawson

A thesis submitted in fulfilment of the requirements for the degree of Doctor of Philosophy to the School of Chemistry, University of Edinburgh

November 2003

Abstract

Procedures for collecting data on a diffractometer equipped with an area detector from samples held within the diamond anvil cell have been developed. The cell construction limits access to reciprocal space and leads to contamination of the diffraction patterns, leading to problems in indexing, data processing and refinement; all of these effects have been investigated and some strategies for overcoming these are described.

Compression studies of the amino acid glycine show the formation of a new polymorph below 8 kbar via a single crystal - single crystal phase transition from the known β-phase of glycine. The formation of this new polymorph can be rationalised on topological grounds by changes in the packing of the molecules to a more favourable body centred cubic based arrangement. γ-glycine was found to undergo a phase transition, characterised using powder diffraction at high pressure. The behaviour is consistent with the formation of δ-glycine. The crystal structure of the amino acid l-alanine is stable to the effects of pressure to at least 70 kbar. The hydrogen-bonding network undergoes significant distortion; this distortion can be explained by the structure adopting a more body centred cubic packing arrangement with increasing pressure.

Crystal growth at high pressure from liquid resulted in the formation of new polymorphs of formamide and pyridine. Growth of crystals of the N-methylated analogues of formamide, N-methyl formamide and N,N-dimethyl formamide, did not. The structure of the high pressure polymorph of formamide formed at 4.4 kbar is closely related to the previously known phase. At 10.8 kbar pyridine crystallises in a much simpler structure than that observed at low temperature, matching the structure observed for the perdeuterated molecule. A novel hemi-hydrate of piperidine is observed when grown from liquid at 3.1 kbar.

Acknowledgements

My supervisor Dr Simon Parsons for all his help and advice, and teaching me all about space groups. And for not being too smug over glycine. Dr. David Allan for all his help with high pressure experimental techniques and "singing".

Dr. Colin Pulham for all his experimental help. Professor Bill David and Dr. Scott Belmonte for help and advice with powder diffraction. Dr Malcolm McMahon and everyone in the High Pressure Condensed Matter Physics group for upkeep of the ruby kit and experimental help. EUCS for rescuing my powder data from DAT tape.

Everyone from the Chemical Crystallography group, past and present, for their help and space group quizzes. Special thanks to Iain Oswald for putting up with me while writing this thesis, and reading it; Dr. Pamela McGregor for providing crystal growing music and slimming companionship; Dr. Andy Parkin for helpful discussions on crystallography and life.

Graeme Dawson and Kai for knowing nothing about crystallography. My parents for all their support.

Contents

Chapter 1

Introduction

1.1 Introduction

Intermolecular interactions are of fundamental importance in controlling the structure and behaviour of materials in the solid state. The response of materials to changes in external conditions can reveal information about the nature of these interactions. Pressure, like temperature, is a thermodynamic variable; the application of pressure can distort the structure of a material, or cause a phase transition. Intermolecular interactions are strongly dependent on intermolecular separations; pressure provides a way of tuning these separations over a wide range in a more direct way than is possible with temperature.

Single crystal X-ray crystallography is the method of choice for obtaining detailed information on matter in the solid state. The combination of X-ray crystallography with high pressure studies allows quantification of the changes induced by pressure in a material.

The work presented in this thesis focuses on the effects of high pressure on the crystal structures of organic compounds. The major intermolecular interaction in these systems is hydrogen bonding. Hydrogen bonds are extremely important in a wide range of systems. Polymorphism in organic molecules can arise through differences in the hydrogen bonding environment of the molecule; by gaining a better understanding of hydrogen bonds through studying their response to pressure it may be possible to better predict and control polymorphism of materials.

Thesis outline

The remainder of this chapter is an introduction to high pressure experimental techniques and methodology. Following a brief discussion of the possible effects of pressure on molecular systems illustrated with examples from the literature an overview of the principles and operation of the diamond anvil cell is given. An outline of the topological analysis of crystal structures is then given.

The second chapter describes in detail procedures for collecting data using a diffractometer equipped with an area detector. Optimal strategies for processing data are discussed. Processing data from samples at high pressure is difficult due to background effects from the diamond anvil cells and poor access to reciprocal space.

Correct choice of absorption correction and data merging is also important. This is examined using acetic acid as a test case.

The remaining chapters describe structural results obtained at high pressure, focussing on the effects of pressure on hydrogen bonding in a range of systems. The third chapter contains details of a new phase of the amino acid glycine, characterised using both single crystal and powder diffraction studies. This new phase is only stable under high pressure. The structural relationship between this new phase and the three previously known phases are described in terms of the hydrogen bonding motifs.

Chapter four continues high pressure studies on amino acids, containing a compression study on the simplest chiral amino acid l-alanine. No phase changes were observed up to a pressure of 70 kbar although the structure undergoes significant distortion. Topological analysis has shown that the structure moves towards a body centred cubic arrangement with increasing pressure.

The fifth chapter considers the behaviour of formamide and its N-methylated analogues under pressure. Crystal growth from liquid at high pressure lead to the formation of a new polymorph of formamide which is closely related to the low temperature, ambient pressure phase. In N-methyl formamide and N,N-dimethyl formamide no new phases are observed.

Chapter six describes a new polymorph of pyridine formed at high pressure. This polymorph has been observed in the perdeuterated molecule at low temperature but is not seen in the non-deuterated case at any temperature. The formation of a novel hemi-hydrate of piperidine formed when crystallised at high pressure is described in the final experimental chapter. The final chapter draws some conclusions from the work presented in this thesis.

1.2 Molecular systems at high pressure

The structures of the elements at high pressure are complex, with extensive pressure induced allotropy observed for many elements. In contrast, only a limited number of studies have been carried out on molecular systems at high pressure. The most recent version of the Cambridge Structural Database (Allan & Kennard, 1993,

CSD version 5.24) has only 114 entries containing the word "pressure" (omitting "blood pressure"). The effects of pressure on molecular crystals have been reviewed by Hemley & Dera (2000) and Boldyreva (2003); some recent examples are discussed here to illustrate the effects of pressure on molecular systems and the type of changes observed.

High pressure studies of molecules have focussed on two areas: compression of crystalline samples to observe the effects of pressure on intra- and intermolecular interactions within one phase, and the generation of new polymorphs through the application of pressure. In the former area, studies of hydrogen bonded systems have shown the importance of the supramolecular structure in determining the anisotropy of the compression.

A problem in the compression studies is that phase transitions in solid samples often lead to deterioration of the sample, from a single crystal to a polycrystalline mass. Powder - powder transitions often result in poor quality, poorly averaged samples. A powerful tool for forming new phases is direct crystal growth from liquid at high pressure, thus avoiding the problems caused by solid-solid transitions for samples with sufficiently low melting points to allow direct crystal growth at high pressure. This technique has been recently extended to crystal growth from solution at high pressure (Fabbiani *et al.*, 2003), which can be used for compounds with melting points too high to allow direct growth.

1.2.1 Compression studies

The behaviour of paracetamol (acetaminophen, Figure 1.1) with increasing pressure has been characterised by Boldyreva *et al.* Under ambient conditions three polymorphs of paracetamol have been observed, only two of which have been structurally characterised; phase I is more stable monoclinic, and phase II is orthorhombic and metastable. A single crystal compression study of the monoclinic form (Boldyreva *et al.*, 2000) showed no evidence of any phase transition up to 40 kbar. The volume of the unit cell decreased with increasing pressure although the compression was highly anisotropic, with the *c* unit cell dimension increasing with applied pressure following an initial decrease. This anisotropy can be linked to the hydrogen bonded structure; the molecules are arranged in layers, with maximum compression occurring normal to these layers. The expansion of *c* is due to flattening out of these layers to give more dense packing. The intramolecular bonds did not

change with increasing pressure, with the exception of the C=O bond, which acts as a hydrogen bond acceptor. This increased by 0.023 Å at 40 kbar; this is due to the shortening of the C=O...H-O hydrogen bond. The intramolecular torsion and the dihedral angle between the planes described by the benzene ring and the amide group decreased - the molecules become flatter with increasing pressure.

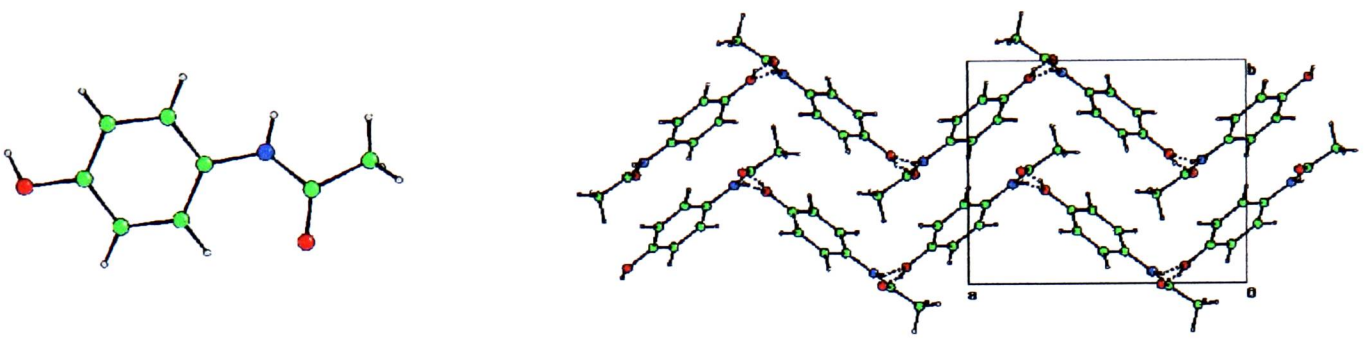

Figure 1.1. Left: the paracetamol molecule. Right: packing in monoclinic paracetamol. Maximum compression occurs normal to the layers.

Further experiments using powder diffraction experiments showed evidence of an irreversible transition from phase I to the orthorhombic form at increased pressure (Boldyreva *et al.*, 2002). The transition was found to be highly dependent on the precise conditions of pressure increase and decrease. No transition was observed on rapidly increasing pressure to 40 kbar or on slow pressure release, only when the pressure was slowly increased to 42 kbar and then slowly released to 13 kbar. Grinding during sample preparation of phase II caused partial transformation to the monoclinic phase.

Compression of phase II in powder diffraction experiments showed similar behaviour to the monoclinic polymorph (Boldyreva *et al.*, 2002). The largest compression was again normal to the hydrogen bonded layers. Isotropic compression of the layers was observed, in contrast to the expansion seen in the monoclinic phase. Detailed structural information on the compression of the hydrogen bonds themselves was not obtained.

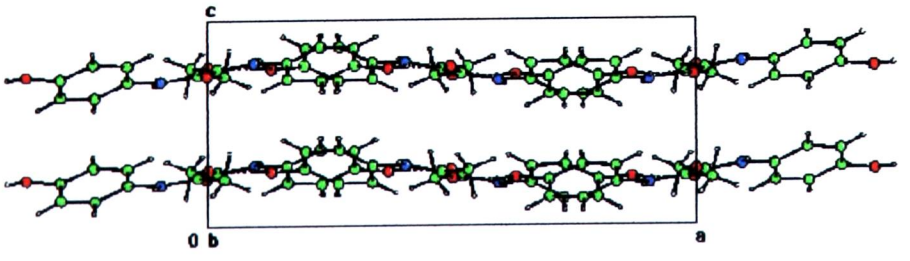

Figure 1.2. Packing in orthorhombic paracetamol

Phase transitions can be observed using single crystal compression studies. Studies of diones showed that while 1,3-cyclopentanedione (CPD) undergoes a phase transition that results in collapse of the single crystal (Katrusiak, 1990a), 1,3-cyclohexadione (CHD, Figure 1.3) survived a pressure induced transition (Katrusiak, 1990b).

The phase transition in CHD occurs between ambient pressure and 3 kbar. The unit cell undergoes a large change in this region, with *a* decreasing by 7% and *c* increasing by 6%. Two changes occurred in the molecule with increasing pressure. Atom C(5) is disordered over two positions under ambient conditions; with increasing pressure the disorder reduces. At 5 kbar C(5) still undergoes large vibrational motion, which is greatly reduced over 11 kbar. The second change in the molecule arises from the donor hydrogen atom transferring site, reversing the sequence of the conjugated O=C-C=C-OH bond system. These structural changes are accompanied by a change in the appearance of the crystal due to the anisotropic compression of the unit cell dimensions. Similar changes were observed on cooling CHD below 287 K (Katrusiak, 1991).

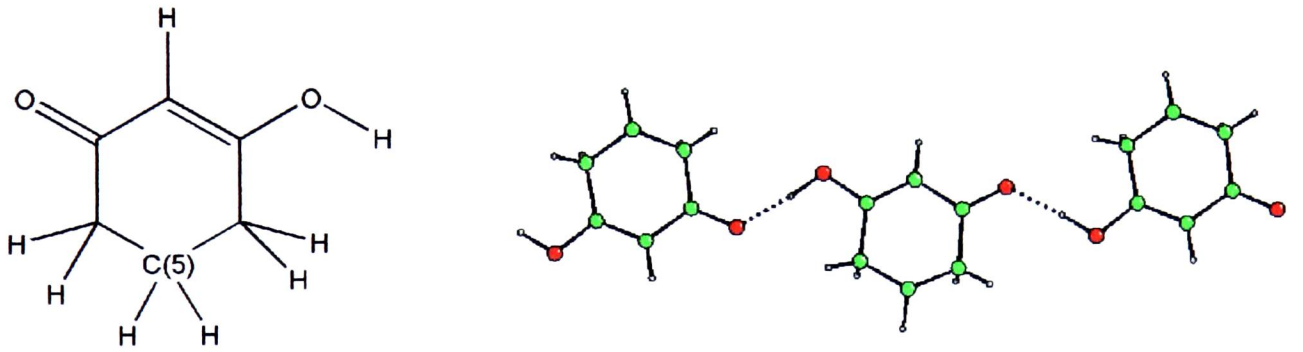

Figure 1.3. Left: the CHD molecule. Right: Hydrogen bonded chains in the structure of 1,3-cyclohexadione

In addition to the changes in the molecular structure the packing of the molecules changed. The hydrogen bonded chains did not compress significantly; the direction undergoing most compression was normal to the sheets of hydrogen bonded chains, similar to the behaviour of both polymorphs of paracetamol. There are only weak van der Waals interactions in this direction. The length of the molecule along the chain and the chain separation were not significantly affected by the phase transition. The parameters most altered were the position of the molecule within the chain and the relative displacements of the molecules in neighbouring chains.

1.2.2 Polymorphism from crystal growth at high pressure

The study of a related series of compounds will eventually allow overall conclusions on the behaviour of a particular type of hydrogen bond with increasing pressure to be drawn. The Edinburgh group has investigated the behaviour of the alkyl monoalcohols with this aim. These compounds tend to have melting points close to or below room temperature, allowing crystal growth at high pressure avoiding problems due to sample deterioration following a phase transition.

Common packing motifs have been identified in the crystal structures of the monoalcohols at low temperature, due to the differing packing requirements of the alkyl (R) groups and the hydroxyl groups, which must be close together for hydrogen bonding to occur (Brock & Duncan, 1994). For small, or "thin", R groups the molecules tend to form chains where the molecules are related by a 2_1 screw axis or a glide plane. Steric hindrance prevents this for bulkier R -groups; these molecules tend to form threefold or higher helical chains. The (pseudo)-symmetry of the helix can be higher than the symmetry of the structure by the inclusion of more than one molecule in the asymmetric unit. This is reflected in the increased occurrence among the monoalcohols of $Z' > 1$ structures. The monoalcohols present a useful series of compounds containing the same primary functional group; the effect of pressure on the O...H-O hydrogen bond can be studied in a range of chemically similar molecules.

Methanol has two low temperature polymorphs; β-methanol (*Cmcm*, $Z'=1$, Tauer & Lipscomb, 1952) is formed just below the melting point at 175 K and transforms to α-methanol ($P2_12_12_1$, $Z'=1$, Torrie *et al.*, 1989) on cooling to 157 K. The hydrogen bonded chains have different conformations in the two polymorphs (Figure 1.4). Methanol crystallises at 35 kbar although it is easy to superpress the liquid through rapid compression. The structure formed at high pressure (γ-methanol) also consists of hydrogen bonded chains (Allan *et al.*, 1998); these chains are significantly different to those in the low temperature polymorphs. γ-methanol is triclinic, $P\bar{1}$, with $Z'=3$. The chains have an unusual 2-1-2-1 alternation in the orientation of the molecules (Figure1.4). The vitrification at high pressure could be due to the strained geometry of the hydrogen bonds. There is no symmetry relationship (beyond translation) between the molecules in one chain; the inversion centre relates the chains, not the molecules within the chains.

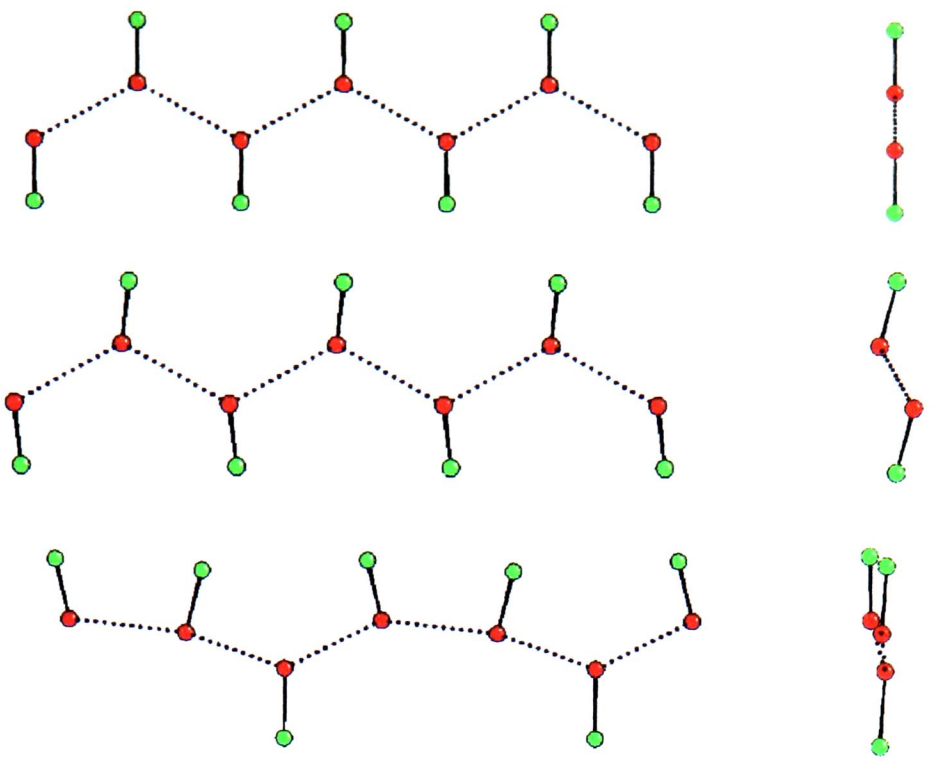

Figure 1.4. Hydrogen bonded chains in the polymorphs of methanol. Top: β-methanol. Middle: α-methanol. The difference in conformation is clear from the side views of the chains (right). Bottom: γ-methanol. In the α- and β-polymorphs the molecules alternate on each side of the chain (leading to the 1-1-1-1 designation); in γ-methanol the molecules form a 2-1-2-1 arrangement where two molecules sit on one side of the chain.

The high pressure polymorph of methanol is more strained than the low temperature polymorphs. The reverse is true for ethanol. At low temperature ethanol crystallises in the space group *Pc* (Jonsson, 1976). There are two independent molecules in the structure, with different conformations with respect to the OH group, with one molecule *gauche* and the second *trans*. The hydrogen bonded chains adopt a 2-2-2-2 conformation (Figure 1.5). Each chain contains both independent molecules; pairs of molecules are related by the *c* glide. The methyl groups are approximately perpendicular to the plane of the hydrogen bonds. At 3 kbar ethanol crystallises in $P2_1/c$, with $Z'=1$ (Allan & Clark, 1999). In this polymorph the chains have a 1-1-1-1 conformation (Figure 1.5) with the angle of the hydrogen bond close to linear at 178.8°, whilst at low temperature the angles range from 172° to 176° indicating slightly higher strain. Synchrotron experiments (Allan *et al.*, 2001) found the hydroxyl hydrogen atom to be disordered, with 0.7(1) occupancy for the *trans* conformer. The molecules within one chain are related by the 2_1 screw axis.

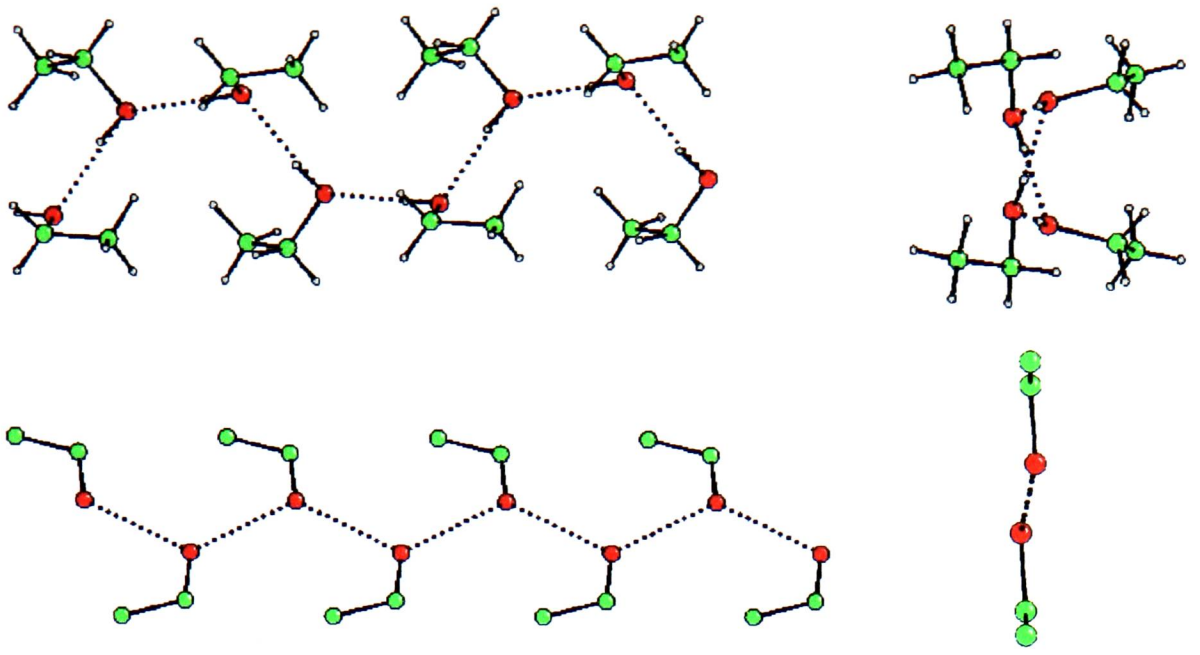

Figure 1.5. Hydrogen bonded chains in the polymorphs of ethanol. Top: *Pc* phase, showing 2-2-2 arrangement of molecules in one chain.. Bottom: $P2_1/c$ high pressure phase, with 1-1-1 configuration of molecules. The change in conformation of the CH_3 group is clear when the chains are viewed from the side (right).

Under ambient pressure phenol forms hydrogen bonded chains of molecules which have pseudo threefold symmetry (Figure 1.6). The structure is monoclinic, $P2_1$, with three independent molecules in the asymmetric unit (Zavodnik *et al.*, 1987). The benzene ring in this structure is acting as a bulky R group, with the molecules within the turn of the helix unrelated by symmetry; the 2_1 axis relates the chains of molecules.

The high pressure polymorph is also monoclinic $P2_1$ with $Z' = 3$; however the structure now has packing motifs similar to the small R structures (Allan *et al.*, 2002). The chains now form "ribbons" rather than helical strands (Figure 1.6); the situation is slightly complicated by the non equivalence of the molecules. One chain consists of molecules of one type related by the 2_1 screw axis; the second chain has pairs of other two molecules, also related by the screw axis. The effect of pressure has been to overcome the steric hindrance of the phenyl group, forcing the phenyl ring to act as a "thin" alkyl group. The hydrogen bonds in the high pressure polymorph are slightly weaker than in the ambient pressure phase - the reduction in enthalpy for this structure comes from the increased packing efficiency of the planar chains.

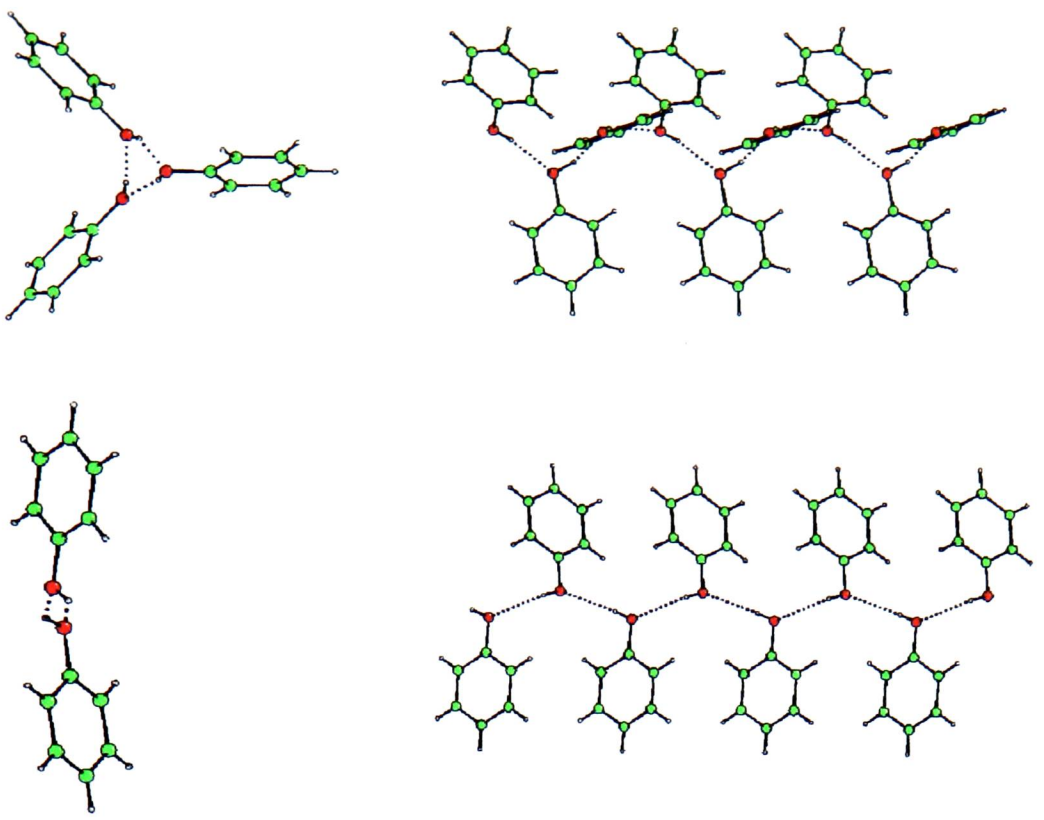

Figure 1.6. Hydrogen bonded chains in phenol, showing the change from helical chains at low temperature to ribbon-like chains at high pressure, viewed parallel and perpendicular to chains
Top: low temperature phase. Bottom: high pressure phase.

Tertiary-butyl-alcohol (t-butanol) behaves differently to phenol. Calorimetric studies (Oetting, 1963) indicate the existence of four phases at low temperature. Two of these have been fully structurally characterised; phase IV (Steininger *et al.*, 1989) forms at room temperature and has the characteristic monoalcohol hydrogen bonded chains, with three independent molecules forming a pseudo-threefold helix. Phase II (McGregor *et al.*, 2003) has a different motif; three independent molecules form two independent hydrogen bonded hexamers (Figure 1.7). This phase is stable at 281 K and 3.5 kbar; the tertiary-butyl group is too bulky to allow the formation of the coplanar chains seen in the high pressure phase of phenol, with the hydrophobic interactions of the butyl groups dominating the structure. The hydrogen bond lengths of the two phases are comparable.

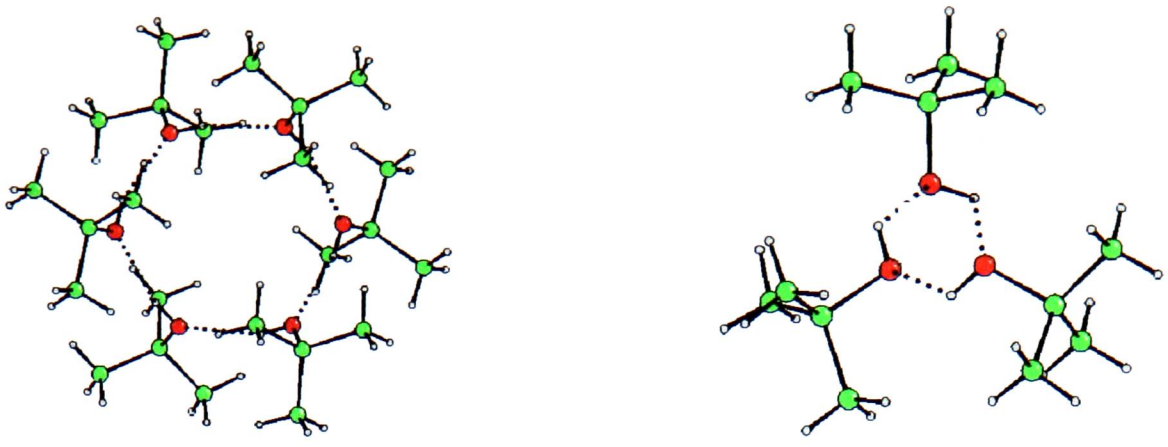

Figure 1.7. Hydrogen bonding motifs in t-butanol. Phase II (left) contains hexameric rings, while phase IV (right) forms pseudo threefold helices

The monoalcohols illustrate the formation of polymorphs at high pressure. Although each molecule described above contains the same type of O...H-O hydrogen bond, each high pressure polymorph has a different hydrogen bonding motif. The alkyl group had a significant effect on the structure of the polymorph. In the case of phenol, the effect of pressure is to overcome the steric effect of the bulky phenyl group forcing it to act as a thin R group. This is not true for t-butanol in the small pressure region studied to this point: higher pressures may result in a "thin" polymorph.

1.3 High pressure experimental techniques

1.3.1 Cell construction

The gasketed diamond anvil cell is the standard tool used for high pressure experimental studies, suitable for a range of techniques including Raman spectroscopy and single crystal X-ray diffraction. The basic principle of the diamond anvil cell is illustrated in Figure 1.8. The sample is held between two gem quality diamonds, with a metal gasket providing the walls of the sample container. A load is applied to the large outer face of the diamonds, which is multiplied many times at the small inner face (culet). As the diamonds are pushed together the gasket extrudes outwards around the culets sealing the sample chamber.

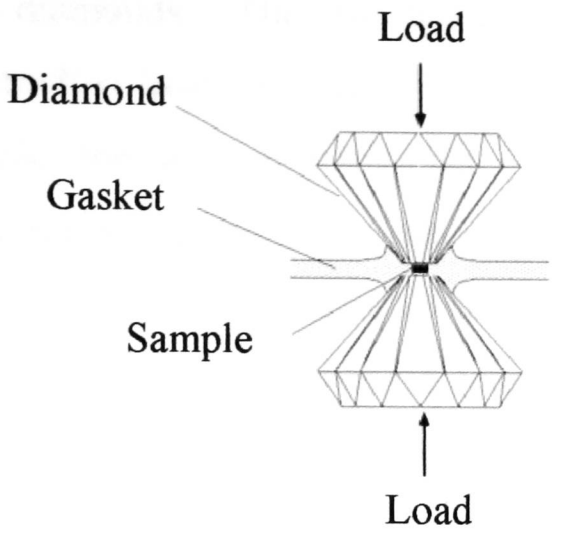

Figure 1.8. Principle of the diamond anvil cell

There are various cell designs, which have been extensively reviewed (Jayaraman, 1986; Dunstan & Spain, 1989; Miletich *et al.*, 2000). The experimental work in this thesis was carried out using a cell based on the Merrill-Bassett design (Merrill & Bassett, 1974). Figure 1.9 shows a schematic of this type of cell.

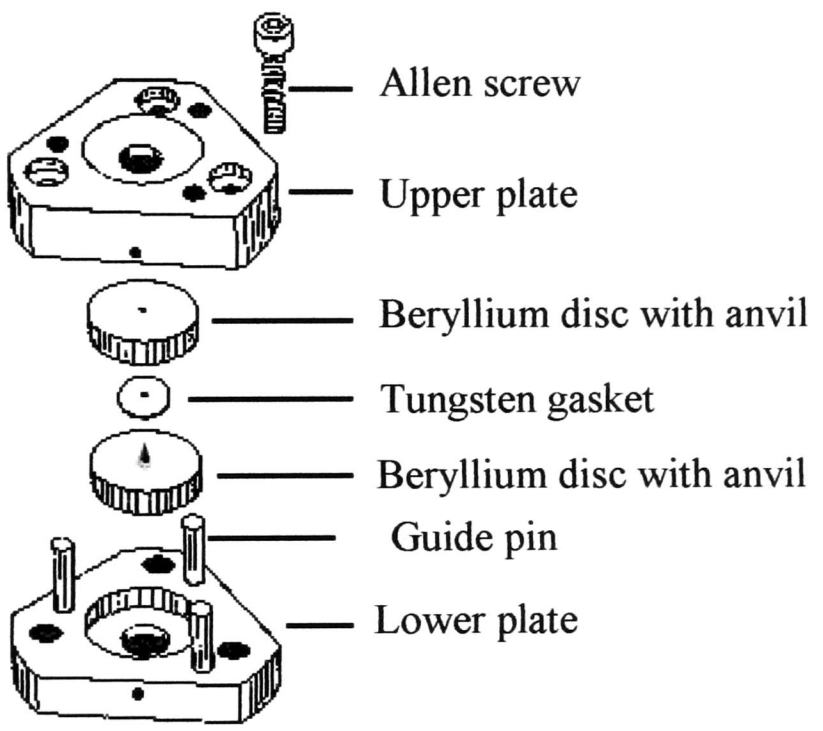

Figure 1.9. Schematic of the Merrill - Bassett diamond anvil cell (taken from Miletich *et al.*, 2000)

The diamond anvils are attached to two beryllium plates (discs). A small conical or cylindrical hole is drilled into the centre of the beryllium discs to allow optical observation of the sample. The beryllium discs are held within two stainless steel supports (the cell body); small adjustments to the positions of the discs can be made through the grub screws holding the disc in place to allow lateral alignment of

the diamonds. The two halves can be accurately combined via three guide pins protruding from one side. Load is applied to the diamonds by tightening three bolts, forcing the two halves together. This type of cell is small enough to be mounted on a conventional goniometer head and fit into a standard diffractometer.

The pressure limit of these cells is about 120 kbar. This is modest compared to the pressures required for other areas such as modelling planetary interiors which require pressures in excess of 1 Mbar, but sufficient for the chemical systems under study in this work. The cell bodies are fabricated in house, reducing the cost, and the cells are relatively simple to use.

1.3.2 The components of the cell

Each component of the cell is important. The maximum pressure attainable is limited by a number of factors including the culet size of the diamonds, the size of the gasket hole, the pressure transmitting fluid used, the mechanical properties of the gasket material and the depth of the indent made in the gasket.

Diamonds

Diamond is the hardest material known, and is transparent to electromagnetic radiation over a wide wavelength range. Diamonds are divided into two classes, I and II, depending on the amount of dissolved nitrogen. Both types are suitable for use in high pressure work. Type I diamonds have high fluorescence making them unsuitable for use in spectroscopic studies; type II can be used in a wider range of techniques but are considerably more expensive. Both types are used in the cells in Edinburgh.

The culet size of the diamond anvils is important in determining the pressure limit of the cell. Smaller culets (to the same table diameter) allow higher pressures to be reached; however this is at the expense of the sample volume. The most common diameter used in this work is 600 μm, with 400 and 800 μm also used. In order to reach very high pressures the culet face can be bevelled. This prevents penetration of the culet edge into the gasket material which causes failure of the culets.

In the pressure region used in this work the most common cause of diamond failure is poor alignment. The original Merrill - Bassett design had no mechanism for altering the diamond alignment. The backing discs fitted exactly into the steel body. In the modified version used here lateral alignment is possible as there is space around

the disc, which is held in place by three grub screws. No adjustment of the parallelism of the culets is incorporated into the cell design. The diamonds are attached to the beryllium with epoxy glue. The diamonds "settle" slightly when initially compressed together, improving the parallel alignment; however this lack of adjustment does limit the maximum pressures obtainable.

Backing discs

Beryllium is commonly used for the backing plates, and has been used in these studies. Due to its low atomic number Be is relatively transparent to X-rays, allowing wide angle X-ray access to the sample. It can be used to reach pressures in excess of 200 kbar. However (as shown in Chapter 2) beryllium leads to a high background in the diffraction pattern in a single crystal experiment. A further disadvantage is the high cost - a pair of discs is comparable in price to one type II diamond anvil. Other materials can be used in place of beryllium, such as tungsten carbide (Brister, 1997). This highly absorbing material reduces reciprocal space access. This can be overcome by use of a conical access hole, but in practice this reduces the mechanical strength of the disc, limiting the pressure range.

Gasket

The gasket plays an important role in the high pressure experiment. In addition to providing the "walls" of the sample chamber, the gasket provides mechanical support for the diamond anvils, reducing the shear stress at the culet tips. A number of metals can be used for the gasket, such as rhenium, tungsten, steel and inconel (an alloy of Ni, Cr and Fe). Different metals have different mechanical properties; the choice will depend on the pressures to be reached and the materials under study. Deformation of the gasket is necessary for increasing pressure as the gasket should intrude into the hole. Tungsten is suitable for large sample volumes; it has high mechanical strength, maintaining the sample volume although this limits the pressures attainable.

For the pressure to increase the sample volume must decrease. The force pushing outwards from the sample must be equalled by the inwards force from the shear strength of the gasket and the friction between the diamond culets and the walls of the gasket hole. The thickness of the gasket is of key importance; if the gasket is too thick the outwards force from the sample will exceed the friction, the hole will

expand and no pressure will be applied. The thinness of the gasket limits the size of the sample: in single crystal compression studies the crystal should not bridge the culet faces.

Gasket preparation prior to sample loading is very important. Before drilling the hole the gasket is indented between the diamonds to the required thickness (typically in the range 125 - 175 μm). Massive support from the increased thickness of gasket outside the anvils allows considerably higher pressure to be reached than calculated from the anvil size, gasket hole and gasket thickness alone (Dunstan, 1989). The thick flank supports the culets, reducing the shear stress of the diamonds. The indenting work hardens the gasket improving its mechanical stability.

The hole diameter also limits the pressure reached; the smaller the hole diameter, the higher the pressure that can be reached, again at the expense of the sample volume. The maximum hole diameter that can be used is approximately one half of the culet diameter. The hole should be accurately positioned in the centre of the culet face, as there is a pressure gradient from the culet edge to the centre.

Pressure medium

In order to ensure the pressure environment at the sample is hydrostatic a pressure transmitting medium is needed. The choice of medium is restricted by the pressure required and the sample; clearly the sample should not dissolve in the medium. A 4:1 methanol : ethanol mixture remains quasi-hydrostatic to pressures of approximately 100 kbar. Isopentane : n-pentane can be used for samples soluble in methanol or ethanol to reach approximately 70 kbar. Water and paraffin can be used if lower pressures are required. Gases such as helium have a larger hydrostatic range but are more difficult to load into the cell.

1.3.3 Sample preparation

Following an initial check on the diamond alignment the gasket is indented. A polarising microscope is used to gauge the depth of the indent. The gasket is then marked to allow later accurate replacement relative to the culets. The indent depth is measured using a micrometer.

The hole is then drilled. Accurate alignment of the drill is crucial to allow centring of the hole in the indent. Tungsten wire of the required hole diameter acts as

the anode and a spark is produced between the tip of the wire and the gasket, both of which are immersed in a dielectric fluid (typically paraffin). An initial mark is made to the side of the indent to align the drill and the mounted microscope every time a hole is drilled.

The gasket is then replaced over one diamond culet, held in position by Blu-tak. The sample can then be loaded. In the case of a crystalline solid, the crystal is placed on the opposite diamond face, secured with silicone grease or a similar material. A small chip of ruby for pressure measurement (below) is placed next to the sample. The crystal should be no larger than two-thirds of the diameter of the hole to allow for intrusion of the gasket. The pressure transmitting medium (typically a methanol: ethanol mixture or paraffin) is dripped in to the sample hole and the cell is closed. Small air bubbles may be "squeezed out" by tightening the bolts; if a larger bubble is present in the sample chamber the cell must be opened and the sample reloaded. In the case of a liquid sample, no pressure transmitting medium is required - the liquid is simply dripped into the sample hole.

Procedures for collecting diffraction data for a single crystal in a diamond anvil cell are described in detail in Chapter 2.

1.3.4 Pressure measurement

Direct pressure measurement from the applied load is inaccurate as the distortion of the applied over the anvils is variable and cannot be measured. In the experiments described in this thesis ruby fluorescence (Piermarini *et al.*, 1975) was used to determine pressure. In this technique a laser is used to excite the spectral lines of a small chip of ruby placed inside the sample chamber; the ruby is sufficiently small and has a high mosaic spread so that no diffraction from the ruby is observed. The fluorescence peak at 694.2 nm (the R_2 peak) shifts linearly with increasing pressure at a rate of 0.364 nm GPa^{-1} (Chen & Silvera, 1996). This technique can be used to measure pressures up to 500 GPa (5000 kbar), far in excess of the pressures used in this study. Above this pressure the changes in the optical properties of the diamond anvils due to distortion are so high that it is no longer possible to excite the ruby fluorescence lines. The ruby fluorescence was recorded using a Jobin-Yvon LabRam 300 instrument with excitation by a HeCd laser operating at 441.34 nm.

1.4 Topology

In Section 1.2.1 the role of the hydrogen bonded network in controlling response to pressure was illustrated for paracetamol. For more complex three dimensional hydrogen bonded networks it can be more difficult to rationalise the structural distortions caused by pressure. Topological analysis of the structures can be useful in these situations, and is used extensively in this thesis.

The most familiar topological classifications are those used to describe the packing of hard sphere structures. The most efficient packings are hexagonal and cubic close packing (HCP and CCP) in which each sphere has a coordination number of 12; these two arrangements differ in the repetition of the layers. In the slightly less efficient body centred cubic (BCC) each sphere is 14 coordinate, with eight neighbours closer to the central atom than the other six; the closer eight neighbours form the corners of the cube, and the six longer contacts to the body centres of adjacent cubes form an octahedron around the central atom. These three arrangements account for the majority of elemental metallic crystal structures.

The coordination environment can be visualised using a Voronoi-Dirichlet polyhedron (or VDP). Voronoi-Dirichlet analysis is a method for partitioning space amongst points occupying that space. It can be illustrated in two dimensions using the random set of points in Figure 1.10. A point is separated from a neighbouring point by a line bisecting the vector between them. This construction is then repeated for every pair of points in the diagram to yield a subdivision of the space into cells which each contain one point. Long line segments appear between closely-situated points. This is a versatile geometric structure and is used in numerous fields, including geography, where the cells might be used to define the trading areas of towns, biology, robotics and astronomy. The construction can be extended to three dimensions, where the cells become polyhedra. The number of faces of the polyhedron corresponds to the coordination number; the area of the face gives the strength of the contact formed across that face.

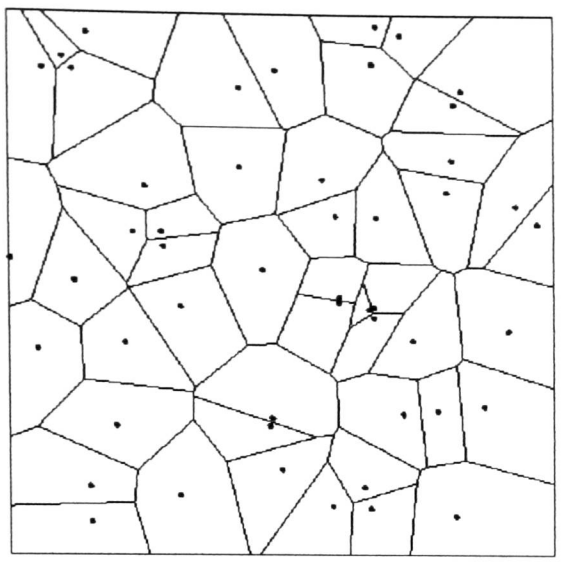

Figure 1.10. Partition of two dimensional space into Voronoi-Dirichlet cells (Byers, 1992)

In addition to the coordination number certain other parameters can be defined to characterise packing. The coordination sequence is the number of neighbours in the first, second, third... coordination spheres. HCP, CCP and BCC have the coordination sequences 12-44-96, 12-42-92 and 14-50-110 respectively. The packing coefficient, k, is the volume of all the spheres in the unit cell divided by the cell volume. HCP and CCP have the highest value of this parameter (0.740); the value for BCC is 0.680.

Kitaigorodski (1973) sought to apply the principles of packing topology to molecular crystals. He showed that packing coefficients tended to fall into the range 0.65 - 0.77, and that the most common molecular coordination number was 12. Though these findings bore parallels with metallic crystal structures and the packing of hard spheres described above, they were based on only 150 crystal structures. A more extensive survey revealed that the most common coordination number is in fact 14, though other coordination numbers are far from uncommon.

Blatov (2000) has extended the VDP analysis of hard sphere structures to molecular crystal structures. Two types of VDP can be constructed. A *lattice* VDP can be constructed from the geometrical centroids of the molecules; nearest neighbour interactions of these centroids give rise to the lattice VDPs. These provide a simpler method of analysis than the *molecular* VDPs. These are defined by constructing VDPs around each atom taking into account both intra and intermolecular contacts.

Whilst the lattice VDP characterises the distribution of the molecules in a crystal structure, it may only approximately represent the arrangement of molecules around a central one - the approximation becoming progressively worse as the

molecules deviate from spherical symmetry. A *smoothed* VDP is generated by connecting molecular centroids only if a real intermolecular interaction (contact) exists between the molecules in question. The number of faces of a smoothed VDP forms the most rigorous definition of a molecular coordination number. The lattice VDP and the smoothed VDP for a structure may suggest different coordination numbers. It is the size of a face of the VDP, not the length of the contact that matters.

1.5 References

Allan, D.R., Clark, S.J., Brugmans, M.J.P., Vos, W.L. (1998). *Phys Rev. B.*, **58**, r11809- r11812

Allan, D.R., Clark, S.J. (1999). *Phys. Rev. B*, **60**, 6328 - 6334

Allan, D.R., Parsons, S., Teat, S.J. (2001). *J. Synchrotron Rad.*, **8**, 10 -17

Allan, D.R., Clark, S.J., Dawson, A., MacGregor, P.A., Parsons, S. (2002). *Acta Cryst.* B**58**, 1018 -1024

Allen, F.H. & Kennard, O. (1993). *Chem Design Autom. News*, **8**, 31-37

Blatov, V.A., Peresypkina, E.V. (2000). *Acta Cryst.*, **B56**, 510 -511

Boldyreva, E.V., Shakhtshneider, T.P., Vasilchenko, M.A., Ahsbahs, H, Uchtmann, H. (2000). *Acta Cryst.*, **B56**, 299 - 309

Boldyreva, E.V., Shakhtshneider, T.P., Ahsbahs, H, Sowa, H., Uchtmann, H. (2002). *J. Therm. Anal. Calor.*, **68**, 437 - 452

Boldyreva, E.V. (2003). *J.Mol.Struct.*, **647**, 159 - 179

Brister K, *Rev. Sci. Instr.*, **68**, 1629 - 1647 (1997)

Brock, C.P., Duncan, L.L. (1994). *Chem. Mater.*, 1307 - 1312

Byers, , J.A. (1992). *J. Anim. Ecol.*, **61**, 759 - 768,

http://www.wcrl.ars.usda.gov/cec/java2/dirichle.htm

Chen, N., Silvera, I. (1996). *Rev. Sci. Instrum.* **67**, 4275 - 4278

Dunstan, D.J. (1989). *Rev. Sci. Instrum.*, **60**, 3789 - 3795

Dunstan, D.J., Spain, I.L. (1989). *J. Phys. E. Sci. Instrum.*, **22**, 913 - 923

Fabbiani, F., David, W.I.F., Parsons, S., Pulham, C.R., Allan, D.R., Dawson, A., McGregor, P.A., Oswald, I.D.H. (2003). *Chem. Commun.* in press

Hemley, R.J. & Dera, P. (2000). *Reviews in Mineralogy and Geochemistry*, **41**, 335-419

Katrusiak, A. (1990a). *Acta Cryst.* **C46**, 1289 - 1293

Katrusiak, A. (1990b). *Acta Cryst.* **B46**, 246 - 256

Katrusiak, A. (1991). *Acta Cryst.* **B47**, 398 - 404

Kitaigorodskii, A.I. (1973). *Molecular Crystals and Molecules*. New York: Academic Press

Jayaraman, A. (1986). *Rev. Sci. Instrum.*, **57**, 1013 - 1031

Jonsson, P.G. (1976). *Acta Cryst.* **B32,** 232 - 235

McGregor, P.A., Allan, D.R., Clark, S.J., Dawson, A. (2003). in preparation

Merrill, L., Bassett, W.A. (1974). *Rev. Sci. Instrum,* **45**, 290 - 294

Miletich, R., Allan, D.R., Kuhs, W.F. (2000). *Reviews in Mineralogy and Geochemistry*, **41**, 445 - 519

Oetting, F.L. (1963). *J. Phys. Chem.*, **67**, 2757 - 2761

Piermarini, G.J., Block, S., Barnett, , J.D., Forman, R.A. (1975). *J. Appl. Phys.*, **46**, 2774 - 2780

Steininger, R,. Bilgram, J.H., Gramlich, V., Potter, W. (1989). *Z. Kristallogr.*, **187**, 1

Tauer, K.J., Lipscomb, W.N. (1952). *Acta Cryst.*, **5**, 606 - 612

Torrie, B.H., Weng, S.-X., Powell, B.M. (1989). *Mol. Phys.*, **67**, 575

Zavodnik, V.E., Bel'skii, V.K., Zorkii, P.M. (1987). *Zh. Strukt. Khim.* **28**. 175

Chapter 2

The Use of CCD Detectors in Crystal Structure Determinations at High Pressure

2.1 Introduction

Although the majority of single crystal diffraction studies at high pressure have been performed using four circle diffractometers with point detectors, data collection times may run into weeks. This is especially so for relatively weakly diffracting organic samples with low symmetry crystal systems and unit cell volumes in excess of 1000 $Å^3$. This area has recently been the subject of a series of important reviews in *Reviews in Mineralogy and Geochemistry*, including Miletich *et al.* (2000), Hemley & Dera (2000) and Angel *et al.* (2000). There are clear potential advantages in the use of area detectors for this work. CCD diffractometers are now used ubiquitously in chemical crystallography; this chapter describes the application of the Bruker-Nonius Smart Apex in high-pressure diffraction.

The Smart consists of an X-ray source, a CCD detector and a three-circle goniometer. The detector can move around 2θ, and the sample can be oriented about ω and ϕ, but χ is fixed at 54.76°. The advantage of this very open arrangement is that it can accommodate bulky sample environments, such as various designs of high-pressure cell. The Merrill-Bassett diamond-anvil cell (Merrill & Bassett, 1974) is one of the most widely used high-pressure devices. It is suitable for obtaining pressures up to about 120 kbar. Its compact size means that it can be mounted on a standard goniometer head.

Centring the sample may be difficult because of the restrictions on viewing by the body of the pressure cell; procedures such as eight-point centring (Angel *et al.*, 2000) can not be used on fixed-χ instruments. Diffraction images contain not only sample spots, but also powder lines from the gasket and backing disc materials and very intense spots from the diamond anvils (Figure 2.1). This results in a high and variable background which can present problems during indexing and unit cell determination. Shading of the detector by the body of the pressure cell means that only a restricted volume of reciprocal space can be sampled, and this results in very low data completeness for samples in the triclinic and monoclinic crystal systems. The lack of a χ-circle on the Smart potentially exacerbates this problem. The high background and shading also introduce problems during integration. After integration the absorption correction needs to take into account not only sample anisotropy, but

also absorption by the diamonds and backing discs. The aim of this chapter is to describe some procedures by which these difficulties can be addressed.

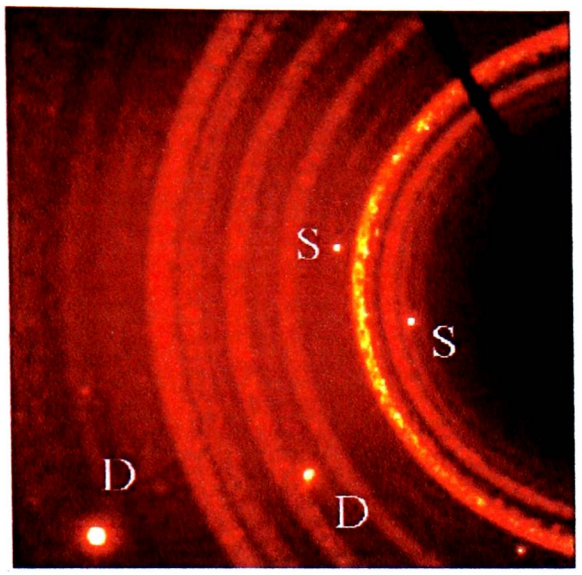

Figure 2.1. A typical data collection frame taken with a Merrill-Bassett diamond-anvil cell. Reflections from the sample are labelled 'S', those from the diamonds, 'D'. The powder rings are derived from the Be backing discs (see Figure 2.2).

2.2 Experimental

2.2.1 General details and procedures

Acetic acid was chosen as a test system for this study. Glacial acetic acid was obtained from Aldrich and used as received. After being loaded as a liquid into the pressure cell it was crystallised by the procedure described by Allan and Clark (1999). The pressure was found to be 4.6 kbar using the ruby fluorescence method.

With the exception of ψ-scan measurements, which were carried out using the procedure based on that described by Angel *et al.* (2000) on a CAD-4 diffractometer, all data collections were performed at room temperature on a Bruker Smart Apex diffractometer with graphite-monochromated Mo-Kα radiation from a conventional sealed-tube source operating at 2 kW. A few modifications to the diffractometer were necessary to allow high-pressure data to be collected. To generate more space for movement of the diamond-anvil cell the standard collimator (17.3 cm) was replaced by a locally fabricated short collimator (12.3 cm). Also for reasons of maximising space around the sample, and for the purposes of centring the sample (see below) a

beam stop was not used, and during data collection the detector positioned so that the direct beam did not impinge on it.

Merrill-Bassett diamond-anvil cells were manufactured locally with 400 μm culet diamonds, 1.3cm diameter beryllium backing discs (Diacell Products) and 250 mm tungsten foil (Aldrich) as a gasket (Figure 2.2). The cell was super-glued to a small metal platform designed to fit into a standard goniometer head.

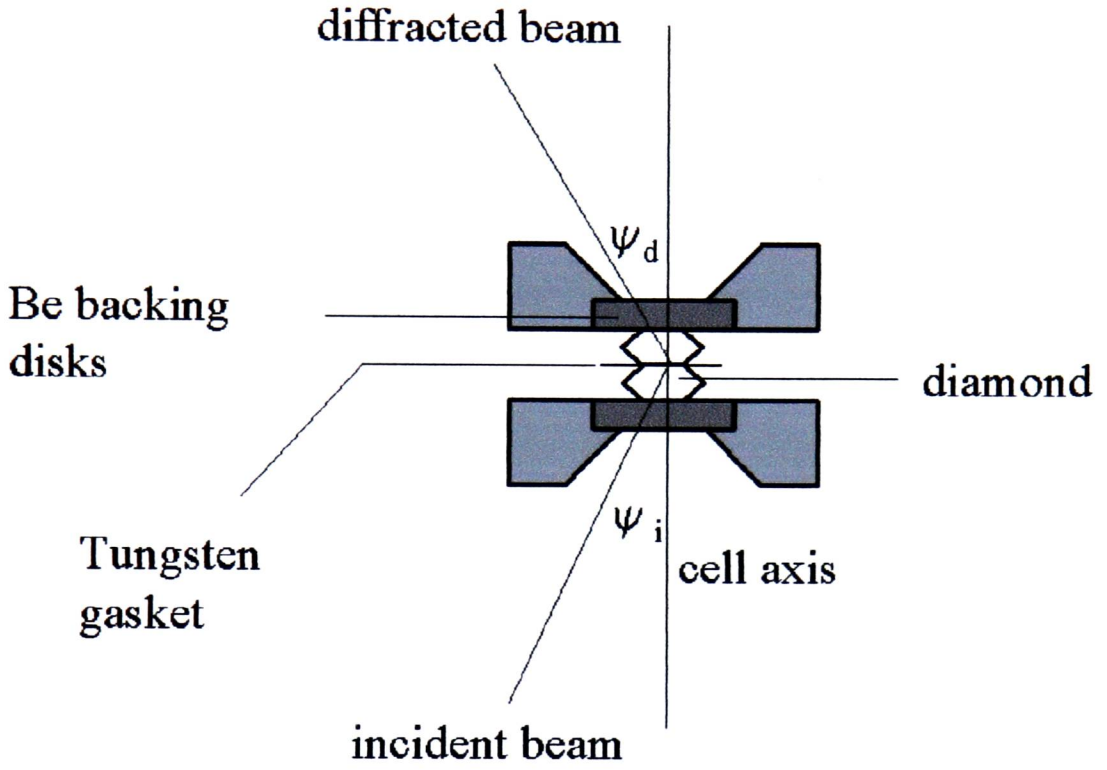

Figure 2.2. Schematic representation of a section through a Merrill-Bassett diamond-anvil cell showing the definition of the cell axis.

2.2.2 Sample Centring

When a sample is contained in a Merrill-Bassett cell it can only be viewed along the direction parallel to the cell axis through the diamond anvils. Optical centring of the sample in the two orthogonal directions perpendicular to this is relatively straightforward, although it is important to ensure that the cell axis is aligned coaxially with the line of view. Let ϕ_0 be the value of ϕ for which the cell axis is parallel to the direct beam at $\omega = 0°$.

Accurate optical centring along the cell axis is not possible because the sample is obscured by the gasket, and centring in this direction is achieved by a three stage procedure. Initially, centring the edge of gasket acts to centre the sample

approximately. The cell is then rotated so that the line of view is through the diamond anvils. The video camera, used for viewing the sample, is mounted on an adjustable platform fitted with a micrometer; the camera is first focussed on the sample with $\phi = \phi_0$, and the micrometer reading noted. The cell is then rotated to $\phi = (\phi_0 + 180)°$, the camera refocused on the sample and the new micrometer reading noted. The video camera is then moved to the midpoint of the two micrometer readings and the position of the cell adjusted so as to re-establish a focussed image of the sample. This procedure is then repeated until the sample is in focus with the cell in both settings of ϕ.

A final check on the centring of the sample in the direction of the cell axis was first suggested to us by Meyer (2002). An image of the direct beam is acquired on the CCD detector with the X-ray generator set at low power (30 kV and 10 mA), the detector at $2\theta = 0°$ and the sample at some non-zero value of ω (typically 25°) and $\phi = \phi_0$. A second image with the sample at $-\omega$ (-25°) is then acquired, and the images subtracted. If the cell is correctly centred the pixel values in the subtracted image at the position of the direct beam should be zero. Miscentring along the axis of the pressure cell is therefore readily detected, and small adjustments to the centring can be made to remedy it. Miscentring of the gasket hole in the other translation axes of the goniometer head can be checked with direct beam images taken at $\omega = 0°$ and $\phi = \phi_0$ and $(\phi_0 + 180)°$ and at $\omega = 0°$, $\phi = \phi_0$ and $\omega = 180°$, $\phi = (\phi_0 + 180)°$.

Another procedure for centring, based on diffractometric measurements has been described by Dera & Katrusiak (1999).

2.2.3 Data collection strategy

Diffraction data can only be acquired at limited values of ω and ϕ because the pressure cell body completely obscures the sample from the X-ray beam or the detector in certain orientations. Data were collected in steps of ω in a series of eight settings of 2θ and ϕ in which the detector was set to $2\theta = \pm 28°$ with two settings of ϕ (ϕ_0 and $\phi_0 + 180°$). A typical data collection sequence is shown in Table 2.1. Data completeness can be enhanced if the sequence shown in Table 2.1 is carried out at several different settings of χ. Since the Smart Apex has χ fixed at 54.75°, this can be

simulated by recollecting data with the pressure cell attached to the goniometer head on another of its three sides.

Run	2θ/°	ϕ/°	range of ω/°
1	-28	90	-10 to -40
2	28	90	40 to -25
3	-28	90	-155 to -220
4	28	90	-140 to -170
5	-28	270	-155 to -220
6	28	270	-140 to -170
7	-28	270	-10 to -40
8	28	270	40 to -25

Table 2.1. Summary of a high-pressure data collection strategy assuming a Merrill-Bassett cell with an opening angle of 40°. ϕ_0 (see Experimental section 2.2.2) is assumed to be 90°. Exact ranges of ω will vary with cell design. Limiting values of ω-2θ are 20.5 and -200.5°, though we usually avoid approaching these within 2° or so. The ω range is defined by (*i*) the need for the incident beam to illuminate the sample, so that the angle between the incident beam and the cell axis should be no more than 40°, and (*ii*) no more than 80% of the detector should be shaded.

2.2.4 Indexing

The diffraction pattern obtained from a sample in a high-pressure cell contains not only sample peaks, but also λ and λ/2 reflections from the diamonds and the powder rings from the beryllium backing discs. 'Default' indexing procedures often fail to index the diffraction pattern and use of a program designed for twinned samples is usually necessary. In other high-pressure diffraction studies automatic peak-finding has yielded a set of reflections that can be indexed, but this was not the case for the sample of acetic acid used in this work. Where automatic procedures fail, manual harvesting of reflections frequently results in a list of reflections that can be indexed. Out of 49 reflections selected from runs 1 and 2 of the data collection images (see Table 2.1), 31 were indexed (GEMINI, Sparks, 2000) on the basis of the acetic acid unit cell. The orientation matrix was then refined, but the limited range of data used to index the sample meant that the matrix was inaccurate and imprecise. It was improved by integrating all the runs using the program SAINT (Bruker-AXS,

2003), and using the positions of all intense reflections in the data set in a constrained cell refinement.

2.2.5 Integration

The data set was integrated (SAINT) using box-size parameters derived from the observed profile of the peaks in the diffraction pattern. These were not allowed to optimise during integration. The orientation matrix which had been refined in a previous integration run (see above) was not allowed to refine further.

A mask was generated for each diffraction image so that pixels shaded by the pressure cell were not integrated. A shaded pixel was identified by evaluating the angle subtended by a vector, **D**, drawn from the crystal to the pixel in question and the vector, **C**, passing through the sample perpendicular to the diamond culets and backing discs (the cell axis). It is convenient to carry out this calculation in the laboratory axis system with basis vectors ($\mathbf{X}_L$, $\mathbf{Y}_L$, $\mathbf{Z}_L$). On the Smart diffractometer $\mathbf{X}_L$ points along the forward direction of the X-ray beam, $\mathbf{Z}_L$ is vertical, pointing up, and $\mathbf{Y}_L$ completes a right-handed set (Figure 2.3). Images on the Smart are read in 'frames' of 512 by 512 pixels, with pixel [0,0] at the bottom left of the detector and the pixel with coordinates [511,511] at the top right. When $2\theta = 0°$ the detector **x**-axis is parallel to $-\mathbf{Y}_L$, and the detector **y**-axis is parallel to $+\mathbf{Z}_L$.

Consider a pixel with coordinates [x, y] on the detector, which is positioned at $2\theta = 0°$; the crystal-detector distance is d (mm). The coordinates of this point in mm, referred to an origin at the centre of the detector face are $[x_{mm}, y_{mm}] = [p(x-x_{centre}), p(y-y_{centre})]$ where p is the pixel size in mm, and (x_{centre}, y_{centre}) are the pixel coordinates of the point at which the direct X-ray beam hits the detector when $2\theta = 0°$. In the laboratory frame the vector, **D**, describing the position of the pixel is therefore:

$$\mathbf{D} = \begin{pmatrix} d \\ -p(x - x_{centre}) \\ p(y - y_{centre}) \end{pmatrix}.$$

If the detector is at some swing-angle 2θ **D** becomes:

$$\mathbf{D} = \begin{pmatrix} Cos2\theta & -Sin2\theta & 0 \\ Sin2\theta & Cos2\theta & 0 \\ 0 & 0 & 1 \end{pmatrix} \begin{pmatrix} d \\ -p(x - x_{centre}) \\ p(y - y_{centre}) \end{pmatrix}.$$

Consider a unit vector, **C**, lying along the pressure cell axis. If the cell is mounted on the goniometer so that the cell axis points along $+\mathbf{X}_L$ when $\omega = 0$,

$$\mathbf{C} = \begin{pmatrix} 1 \\ 0 \\ 0 \end{pmatrix}.$$

As the cell is rotated about ω, **C** becomes:

$$\mathbf{C} = \begin{pmatrix} Cos\omega & -Sin\omega & 0 \\ Sin\omega & Cos\omega & 0 \\ 0 & 0 & 1 \end{pmatrix} \begin{pmatrix} 1 \\ 0 \\ 0 \end{pmatrix}.$$

The angle between **C** and **D** is calculated from the dot-product **C•D**. If the angle is greater than the half opening angle of the cell (40° in our case) the pixel was considered to be shaded, and the pixel mask given a value of 0. Unshaded pixels have a mask value of 64. Since the Smart Apex detector does not use a magnification glass taper no spatial correction was required and no further calculation was necessary to generate the mask files.

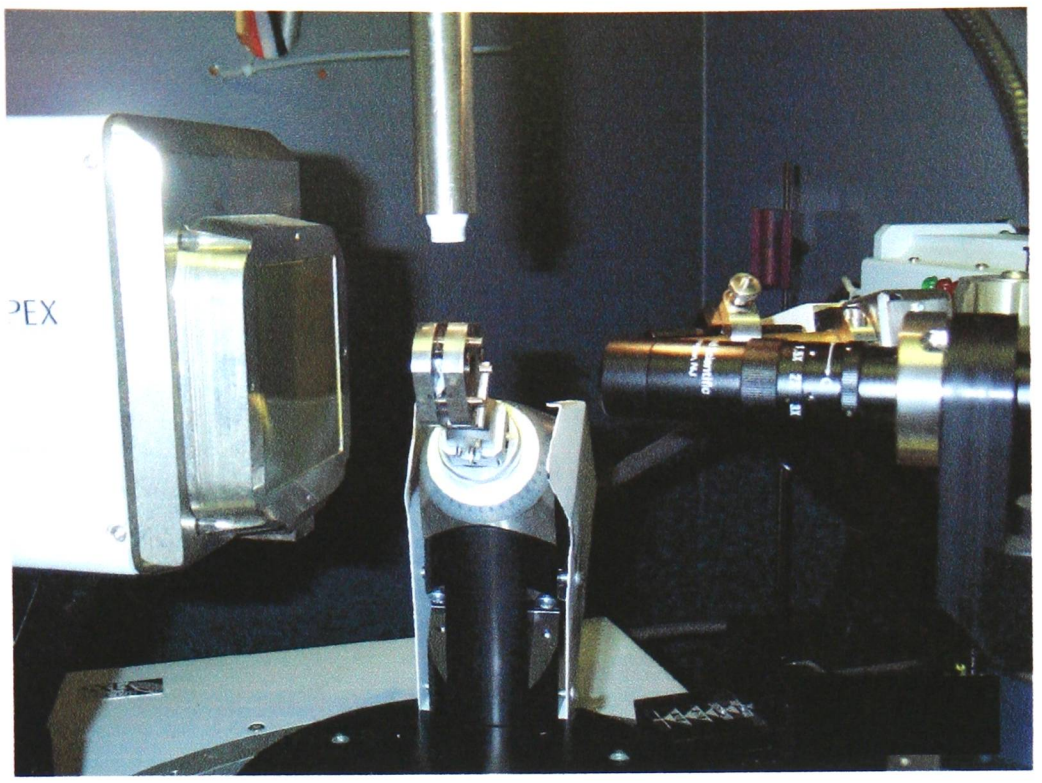

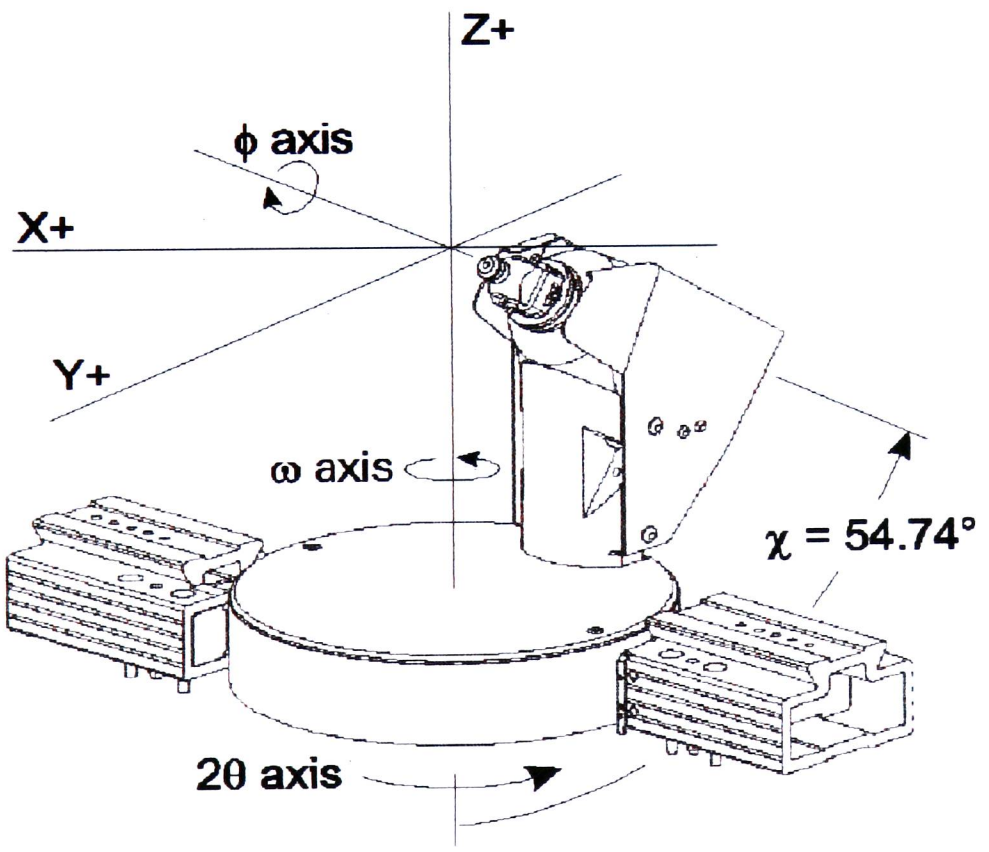

Figure 2.3: View of instrument and axis system.

2.2.6 Absorption Correction and Merging

Absorption by the pressure cell was treated either analytically, empirically or using the multiscan method. In the analytical correction the path length of the incident and diffracted beams through the beryllium and diamonds of the cell were used to calculate the absorption correction factor for each reflection. In the empirical correction an absorption curve was measured by performing a ψ-scan on one half of the same pressure cell used for data collection. In the multiscan method variation in the intensities of equivalent reflections was used to model the absorption surface. The analytical and empirical corrections were both accomplished using the program ABSORB (Angel, 2003); the multiscan correction was carried out with SADABS (Sheldrick, 2002). The results of these three procedures, and some combinations of them, are compared in Table 2.2. The influence of different weighting strategies during merging [SORTAV (Blessing, 1997), as incorporated into WINGX (Farrugia, 1999)] are also compared in Table 2.2 (Section 2.3).

2.2.7 Refinement

Refinement was carried out using the previously determined structure for the high-pressure phase of acetic acid (Allan & Clark, 1999). Refinements were against $|F|^2$, using all data (CRYSTALS, Watkin *et al.*, 2003). The weighting scheme applied was

$$w = \frac{1}{\sigma^2(F^2) + (aP)^2 + bP}$$

where

$$P = \frac{1}{3}MAX(F_o^2, 0) + \frac{2}{3}F_c^2$$

and a and b are adjustable parameters (Sheldrick, 1993; Wilson, 1976). The program enables a robust-resistant modifier (Prince & Nicholson, 1983) to be applied to weights, though the results of the procedure were, in this case, almost indistinguishable from those obtained with unmodified weights. H-atom positions were refined subject to restraints such that the methyl group had local three-fold symmetry, the O-H bond distance was 0.81(1) Å and the COH angle was 109(1)°. All other parameters, including anisotropic displacement parameters of the carbon and oxygen atoms, were refined freely. The total number of parameters was 50.

2.3 Discussion

This chapter describes a case study in which the crystal structure of acetic acid at high pressure was determined using data collected using a CCD area detector. The advantage of using a liquid crystallised *in situ* under pressure is that this avoids pressure-induced peak broadening that may occur when pressure is applied to a crystal obtained under ambient conditions.

2.3.1 Data collection strategy

Diffraction data can only be acquired at limited values of ω and ϕ because the pressure cell body completely obscures the sample from the X-ray beam or the detector in certain orientations. A typical data collection sequence is shown in Table 2.1. Data completeness could be increased if the sequence shown in Table 2.1 were to be carried out at several different settings of χ. Since the Smart Apex has χ fixed at 54.75°, this can be simulated by repeating the data collection with the pressure cell attached to the goniometer head on another of its three sides. The completeness (to 0.9 Å) of each single run was 46%, but this could be increased to 56% if data from the two collections were combined. Each data set was integrated, treated for absorption separately, and the two data sets then scaled and merged (see below).

2.3.2 Indexing and orientation matrix optimisation

Determination of the orientation matrix was not attempted until data collection had completed. For strongly diffracting samples automatic peak harvesting works well, provided the beryllium powder rings are excluded, for example by means of a minimum count threshold. Reflections from the diamond anvils are naturally included in the array of data used for indexing, but many of these can be excluded on the basis of their high intensities. For more weakly diffracting samples, peaks may be harvested manually. In this case sample reflections are identified by eye, and only these reflections used for indexing. However even this method leads to the inclusion of spurious peaks in the reflection array in the form of $\lambda/2$ reflections from the diamond anvils.

Both methods for harvesting reflections led to a reflection array which contains not only sample peaks but also peaks from the diamonds, and it is usually necessary to use a twin-indexing routine, such as DIRAX (Duisenberg, 1992) or GEMINI, for determination of the orientation matrix.

The orientation matrix obtained in this way is not very accurate. Generally it will fit the runs from which the most reflections have been harvested better than the remainder. In order to obtain a more accurate orientation matrix the orientation refinement in the integration program SAINT was used. The initial matrix is used as a starting value for the integration, during which the orientation is allowed to refine with the cell parameters constrained according to symmetry restrictions.

2.3.3 Integration

Contamination of the diffraction pattern by scattering from the beryllium backing discs and the diamonds, combined with shading of the detector by the body of the pressure cell, present certain difficulties during integration. The two principal issues to be addressed are (i) rejection of data from regions of the detector shaded by the pressure cell and (ii) choice of parameters for integration. Of course, a well-determined orientation matrix is essential for successful integration (see above under indexing, Section 2.2.4).

As the data collection proceeds different areas of the detector become shaded by the body of the cell, and the integration should avoid these regions (Figure 2.4, left). The need to optimise both redundancy and data set completeness means that it is still necessary to harvest sample diffraction peaks even from images where the majority of the detector area was obscured by the cell. If a data-set is integrated normally - that is, without regard to shading - the output contains reflections harvested from shaded regions of the detector. A procedure has previously been described (Allan *et al.*, 2000) by which such reflections can be identified and omitted from a data set, which may then be corrected for absorption, merged and used for refinement. Although this procedure yields data sets suitable for structure analysis, the diagnostic output of the integration listing is next to worthless because 'data' harvested from shaded regions contribute to profile and merging statistics.

Masking of detector regions during integration is a well-established means for avoiding areas of the detector shaded by hardware items, such as the beam stop, during integration. In general, such masks are *static* - that is the same mask can be

used during processing of a whole series of diffraction images. This would not be appropriate for a data collection with a high-pressure cell because the shaded region is different for each image. Instead a series of masks were calculated which modelled the changing orientation of the cell with respect to the detector. This means that each image had its own mask file; this is known as *dynamic masking*.

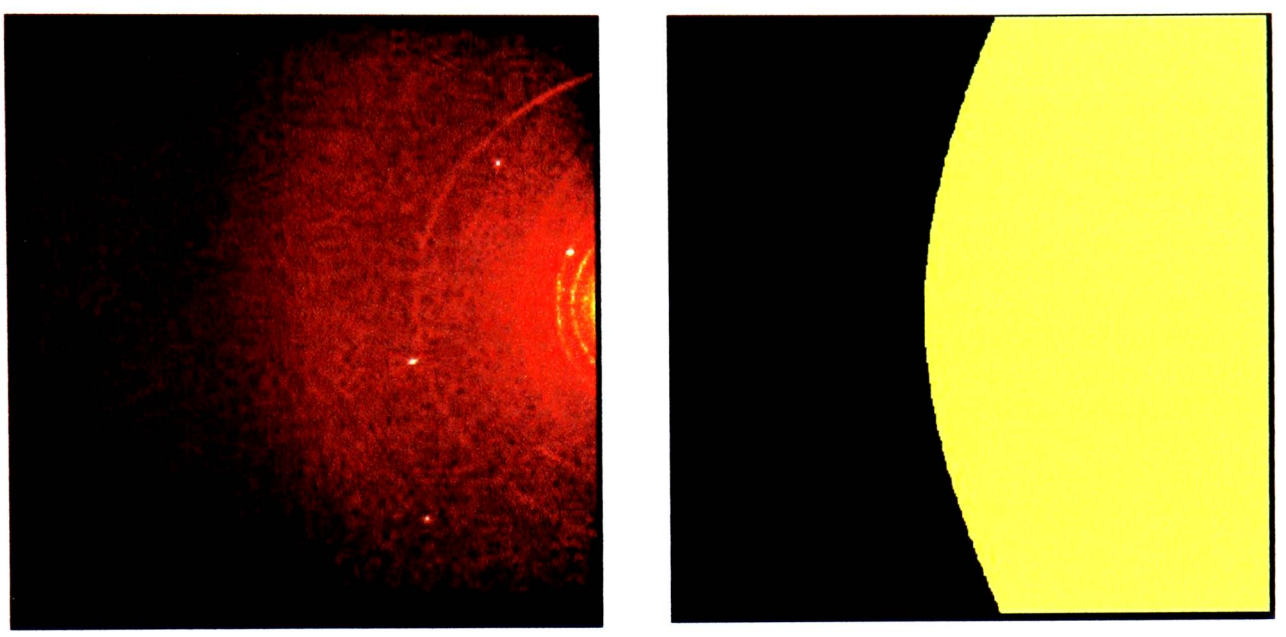

Figure 2.4. Most data collection frames are shaded by the steel support components of the pressure cell. These regions are excluded from the integration by means of dynamic masks. This figure shows a partially-shaded frame (left) and its corresponding mask (right). The masked region is black. Note that, by contrast to the frame shown in Figure 2.1, the cell was at such an angle that the incident beam did not pass through a Be backing disc; therefore no Be powder lines are observed. The narrow powder lines on this image derive from the tungsten gasket.

In the procedure currently implemented the angle subtended by the cell axis and a vector from the centre of the cell to a pixel on the detector is calculated. If this angle is greater than half the opening angle of the cell (typically 40°) the pixel is shaded. This calculation is performed for every pixel on the detector in every diffraction image. This is a time-consuming calculation, and mask generation may take between 1 and 2 hours on a 1 GHz pc; a computationally more efficient procedure would be to perform this calculation 'on the fly' during integration. However, what is lost in computational efficiency is gained in flexibility: it is a simple matter to adapt the computer code used for these calculations to mask any feature, for example particularly intense beryllium powder rings.

The quality of a structure refinement can be influenced by choice of integration parameters, particularly box-size. We typically carry out at least one integration in order to optimise the orientation matrix for the whole data collection; this matrix is then used in a subsequent cycle of integration. Automatic procedures for optimising integration parameters which work well for ambient pressure data collections are less successful in high-pressure work. Automatic box-size optimisation can fail because of the presence in the diffraction pattern of a high background and beryllium rings. The optimisation may also be imprecise when only a few reflections are available because the material being studied has a small unit cell. In most cases it is preferable to obtain an estimate of the box-size directly from the data collection images and hold it constant during integration. It may be increased or decreased manually after inspection of the integration statistics, such as plots of the average peak profile.

2.3.4 Absorption Corrections and Merging

Several methods for calculating an absorption correction and merging the data were tested, and the results are summarised in Table 2.2. Although refinements were carried out versus $|F|^2$ we have chosen to compare refinements of the unweighted R factor calculated on $|F|$ using all data. In contrast to the weighted residual wR_2, this parameter is not sensitive to the numerical values used for the weights. With a small data set the conventional R-factor calculated on $|F|$ using data with $|F| > 4\sigma(|F|)$ can vary as a result of the differing σ's output by different programs.

Systematic absorption errors in data sets collected at high pressure arise not only from the sample, but also because of variation of the beam path through the beryllium backing discs and the diamonds. Shading by the gasket constitutes another systematic error. We have previously described a method (Allan *et al.*. 2000) by which the lengths of the beam paths through the diamonds and backing discs can be calculated from the direction cosines of the incident and diffracted beams and the orientation matrix, and this procedure has been incorporated into the program ABSORB (Angel, 2003). This problem has also been discussed by Katrusiak (2001). Among the numerous other options available in ABSORB is a procedure for a gasket correction (this procedure is described in the program manual). Reference to Table 2.2 (lines 1 and 2) shows that this analytical procedure leads to an improvement in R

of 1.9%. A normal probability plot (Abrahams & Keve, 1971) obtained from this refinement is shown in Figure 2.5. The linearity of this plot and its intersection near the origin confirm that systematic errors have been effectively removed by this absorption correction.

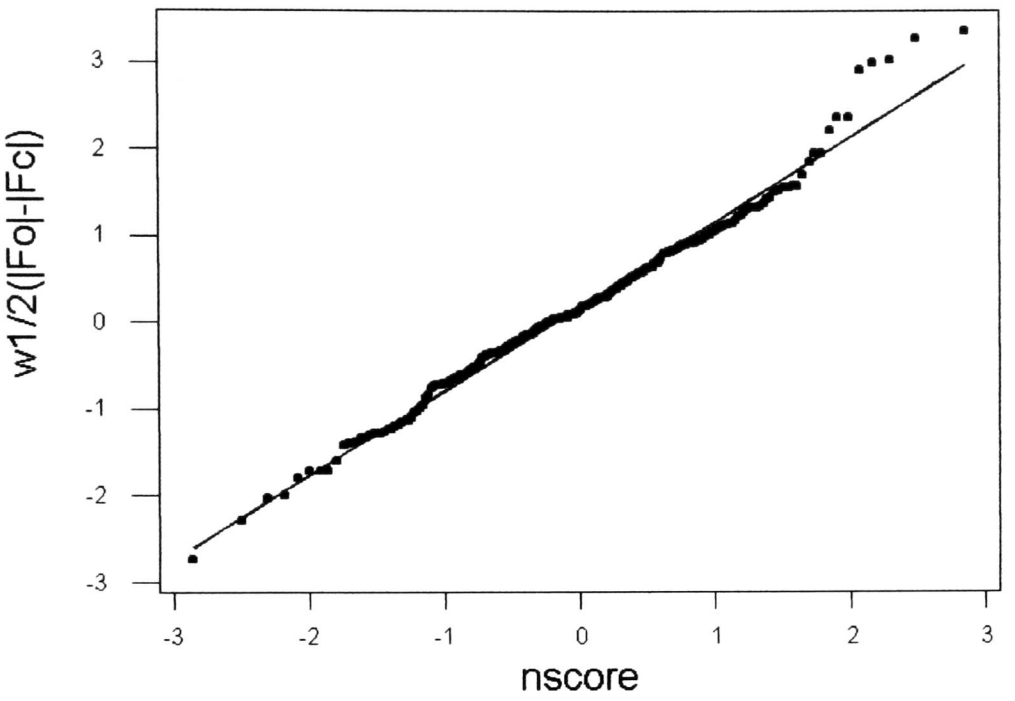

Figure 2.5. Normal probability plot showing 239 values of observed values of $w^{1/2}(|F_o|-|F_c|)$ for the refinement of the crystal structure of acetic acid at 4.6 kbar against their normal scores (nscore). These data derive from refinement 2 in Table 2.2 The equation of the line is $w^{1/2}(|F_o|-|F_c|) =$ 0.18 + 0.97*nscore.

The analytical correction assumed that the crystal filled the gasket hole, and for a crystal grown *in situ* by pressurising a liquid this is a fair approximation. Nevertheless an incomplete crystal habit description can form an important source of residual errors after an analytical absorption correction has been carried out on a data set. Other residual errors can arise from slight misalignment of the pressure cell, and deviations from assumptions made in the gasket correction.

Multi-scan absorption corrections, which exploit the high redundancy of data sets collected with area detectors, are now well-established and provide a means of correcting for any systematic error that leads to variations in the intensities of symmetry of ψ-equivalent reflections. The programs SADABS (Sheldrick, 2002) and SORTAV (Blessing, 1995) use spherical harmonic functions to model absorption anisotropy, and other systematic errors. Although the completeness of data sets collected using high-pressure cells is low, redundancy is generally adequate for multi-scan methods. An effective absorption correction was obtained by multi-scan

procedures alone, (Table 2.2, line 4). In this case the *R*-factor obtained was somewhat higher than that obtained with the analytical procedure, though in other cases we have observed it to yield lower residuals.

In general, we have found the most effective corrections are obtained using a two-stage procedure, in which residual errors present after an analytical correction are treated using a subsequent multi-scan correction. The results for acetic acid are shown in Table 2.2, row 6, and are quite similar to those in row 2, except that there are more data with $|F| > 4\sigma(|F|)$.

Absorption correction 1 (ψ cut-off/°)	Absorption correction 2	Merging weights	R($\|F\|$, all data)	R[$\|F\|$, $F>4\sigma(\|F\|)$]	Number of obs. data/all data
1. None	None	$1/\sigma^2$, RR	8.52	6.23	165/234
2. Analytical, 40	None	$1/\sigma^2$, RR	6.65	4.33	176/239
3. Analytical, 40	None	$1/\sigma^2$	6.84	4.23	175/239
4. None	Sadabs	$1/\sigma^2$, RR	7.14	4.76	178/234
5. None	Sadabs	$1/\sigma^2$	7.30	4.73	175/234
6. Analytical, 40	Sadabs	$1/\sigma^2$, RR	6.72	4.89	191/239
7. ψ-scans, 40	None	$1/\sigma^2$, RR	12.49	5.87	178/239
8. ψ-scans, 35	None	$1/\sigma^2$, RR	6.90	4.88	167/222

Table 2.2. Comparison of absorption correction and merging strategies for refinement of the crystal structure of acetic acid at 4.6 kbar. For the analytical correction reflections may be excluded on the basis of an upper limit placed on the angle (ψ) between the cell axis and the diffracted or incident beams (see also Figure 2.2). Usually this is set to the half opening-angle of the cell. The maximum even and odd-order spherical harmonics for absorption correction 2 were 4 and 1, respectively. Merging was carried out using the program SORTAV; $1/\sigma^2$ indicates that what Blessing (1997) describes as *experimental weights* were used. This scheme was used in preference to unit weighting because data from two different data collections were being merged. 'RR' designates the use of robust-resistant outlier down-weighting, also described by Blessing (1997). Blessing's z_{max} parameter was set to 6.

The change in the absorption profile of a diamond-anvil cell as a function of ω can be measured in a ψ-scan using one half of the cell (Angel *et al.*, 2000). A typical absorption profile is shown in Figure 2.6; transmission is highest at ω values

close to 0° because in this orientation the incident beam passes through the hole in the beryllium backing disc. The data in Figure 2.6 may be used to carry out a ψ-scan absorption correction, and the results are shown in Table 2.2, rows 7 and 8. This correction performs poorly near the limit of the opening angle of the cell because the sharp rise in absorption by the cell at 35° makes empirically obtained transmission factors between 35 and 40° sensitive to small errors in ω calculated for particular reflections. It is for this reason we prefer the analytical correction described above, which performs well even at extreme values of ψ.

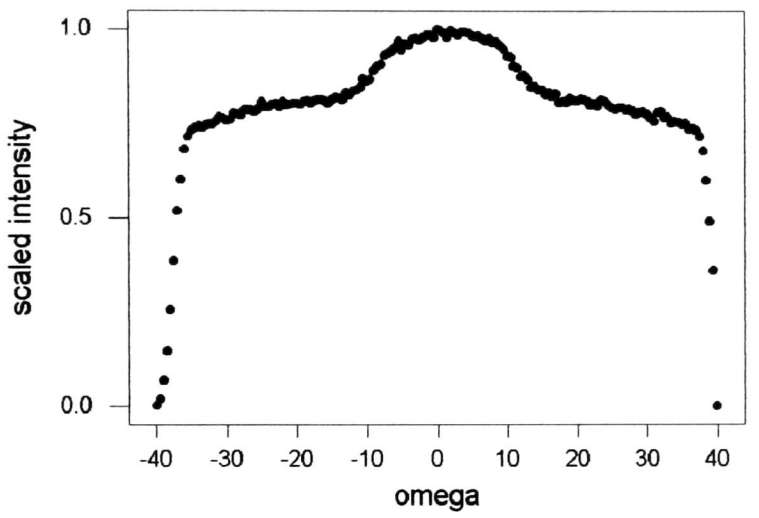

Figure 2.6: ψ-scan profile obtained by measuring the intensity of the direct beam as a function of ω = angle between direct beam and the pressure cell axis.

In spite of the corrections described above, data collected using pressure cells still suffer from substantial systematic errors. These arise, for example, from overlap of reflections with beryllium powder rings, but a few reflections may be wildly in error if they overlap with reflections from the diamonds. Blessing (1997) has described how the effect of outlying data can be treated in a controlled way using a robust-resistant weighting scheme, and this procedure is available in the program SORTAV. Our experience, which is illustrated in Table 2.2 rows 2-5, is that use of robust-resistant weights in merging yields superior results to simple unit or reciprocal variance weights. Use of robust-resistant weight modifiers during refinement is also an important tool in high-pressure crystallography if the data are still subject to errors, and this has been discussed in some detail by Prince and Nicholson (1983) and more recently by Angel *et al.* (2000).

2.4 References

Abrahams, S.C. & Keve, E.T. (1971). *Acta Cryst. A***37**, 157-165.

Allan, D.R. & Clark, S.J. (1999). *Phys. Rev. B.* **60**, 6328-6334

Allan, D.R., Clark, S.J., Parsons, S. & Ruf, M. (2000). *J. Phys. Condens. Matter*, **12**, L613 – L618

Angel, R.J. (2003). ABSORB version 5.3. Crystallography Laboratory, Department of Geological Sciences, Virginia Tech., Blacksburg, VA, USA

Angel, R.J., Downs, R.T. & Finger, L.W. (2000). *Reviews in Mineralogy and Geochemistry*, **41**, 559-596.

Blessing, R. H. (1995). *Acta Cryst. A***51**, 33-38.

Blessing, R.H. (1997). *J. Appl. Cryst.* **30**, 421-426.

Bruker-AXS (2003). SAINT version 7.01A, Bruker-AXS, Madison, Wisconsin. USA.

Dera, P. & Katrusiak, A. (1999). *J. Appl. Cryst.* **32**, 510-515.

Duisenberg, A.J.M. (1992). *J Appl. Cryst.* **25**, 92-96.

Farrugia, L. J. (1999). *J. Appl. Cryst.* **32**, 837-838.

Hemley, R.J. & Dera, P. (2000). *Reviews in Mineralogy and Geochemistry*, **41**, 335-419.

Katrusiak, A. (2001). *Z. Krist.* **216**, 646-647.

Miletich, R., Allan, D.R. & Kuhs, W.F. (2000). *Reviews in Mineralogy and Geochemistry*, **41**, 445-519.

Merrill, L. & Bassett, W.A., (1974). *Rev. Sci. Instrum.* **45**, 290-294.

Meyer, M. (2002). *Private Communication.*

Prince, E. & Nicholson, W.L. (1983). *Acta Cryst. A***39**, 407-410.

Sheldrick, G.M. (1993). SHELXL-93, University of Göttingen, Germany.

Sheldrick, G.M. (2002) SADABS, version 2.04, University of Göttingen, Germany.

Sparks, R.A. (2000). GEMINI version 1.05, Bruker-AXS, Madison, Wisconsin. USA.

Watkin, D.J., Prout, C.K., Carruthers, J.R., Betteridge, P.W. & Cooper, R.I. (2003). CRYSTALS. Issue 12. Chemical Crystallography Laboratory, OXFORD, UK.

Wilson, A.J.C. (1976). *Acta Cryst. A***32**, 994-996.

Chapter 3

The formation of a new polymorph of glycine at high pressure

3.1 Introduction

3.1.1 The glycine molecule

Glycine (Figure 3.1) is the simplest amino acid, and the second most commonly occurring in proteins and enzymes after l-alanine. It has a number of biologically important roles - in the human body it is associated with the manufacture of hormones and in the biosynthesis of bile acids, porphyrins and nucleic acids. It has been found to inhibit neurotransmitter signals in the central nervous system. Glycine molecules have recently been detected in interstellar space (Kuan *et al.*, 2003).

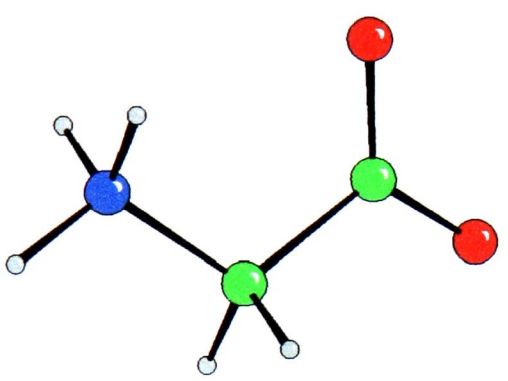

Figure 3.1 The glycine molecule

In the solid state glycine exists as a zwitterion, while in the gas phase the molecule is neutral. In solution glycine can be cationic, zwitterionic or anionic depending on the pH.

3.1.2 Crystal structure at ambient pressure

The structural behaviour of glycine has been the subject of extensive study over a number of years, with twenty-seven entries in the Cambridge Structural Database (Allan & Kennard, 1993, CSD v5.42). To date, three polymorphs have been identified, the structure of each being dominated by hydrogen bonding. The structural features of these are summarised below, with a more detailed examination of the hydrogen bonding made in Section 3.4.

α-glycine

α-glycine is a centrosymmetric structure, crystallising in the monoclinic space group $P2_1/n$. The structure consists of hydrogen bonded double layers (Figure 3.2); due to the orientation of the ammonium groups (discussed in more detail in Section

3.4) there are no hydrogen bonds between these double layers. α-glycine can be prepared by recrystallisation of glycine from water in the absence of any additives. This polymorph was first reported by Albrecht and Corey (1939) and redetermined by Marsh (1958) using single crystal X-ray diffraction. The structure determined by neutron diffraction was reported by Jőnsson and Kvick (1972).

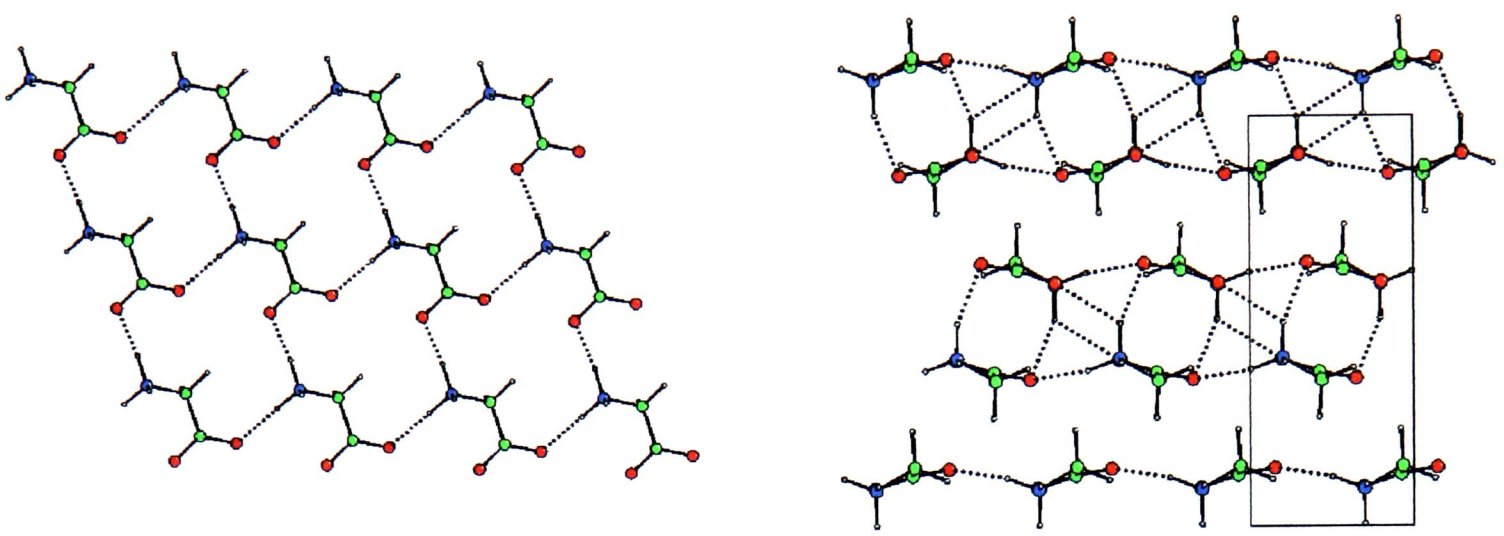

Figure 3.2. Double layer formation in the crystal structure of α-glycine. Left: one layer is formed through a network of N-H...O hydrogen bonds. These layers are linked into double layers (right); there are no hydrogen bonds between the layers.

β-glycine

β-glycine is the least stable of the three polymorphs (Perlovich *et al.*, 2001) and is closely related to the α form. The structure consists of layers (identical to those in α-glycine) but in this case the layers are single rather than double, with bifurcated hydrogen bonds linking the layers (Figure 3.3). The structure is non-centrosymmetric, crystallising in $P2_1$. The polarity arises from the orientations of the NH_3^+ groups relative to the (0 1 0) family of planes. β-glycine was originally isolated from aqueous solution with a small amount of added ethanol (Itaka, 1960). β-glycine transforms to the α polymorph over time, especially if left in humid conditions, and is also unstable with respect to mechanical disturbance. The structure of β-glycine was first reported by Itaka (1960) and more recently by Boldyreva *et al.* (2002), both studies using single crystal X-ray diffraction.

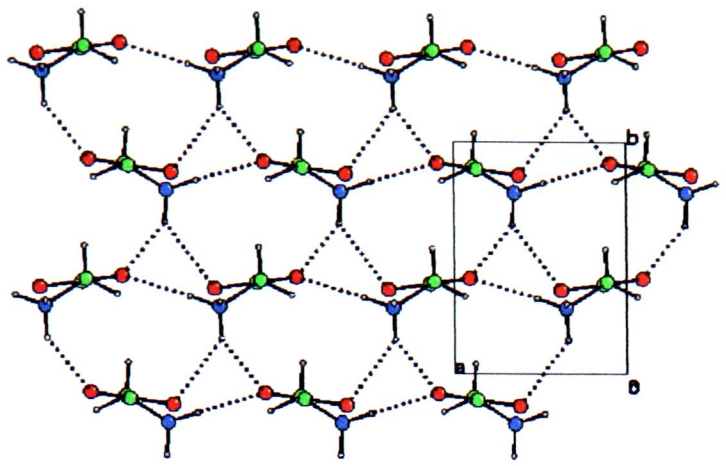

Figure 3.3. The structure of β-glycine (viewed along the (0 0 1) direction). The layers are linked by bifurcated hydrogen bonds; the ammonium groups all have the same orientation giving rise to the polarity of the structure.

γ-glycine

γ-glycine has a very different structure to the other ambient pressure phases. As in the β polymorph, the structure is non-centrosymmetric, crystallising in the trigonal space group $P3_1$. Here the molecules form helices parallel to the *c* axis, which are then further linked by weaker hydrogen bonds (Figure 3.4). γ-glycine crystals can be grown from aqueous solution made acidic with acetic acid. γ-glycine can also be prepared by laser induced nucleation of a supersaturated aqueous solution (Zaccaro *et al.*, 2001). This polymorph was first reported by Itaka (1961) from single crystal X-ray diffraction data, and by neutron diffraction by Kvick *et al.* (1980). The absolute structure was determined by Shimon *et al.* (1986).

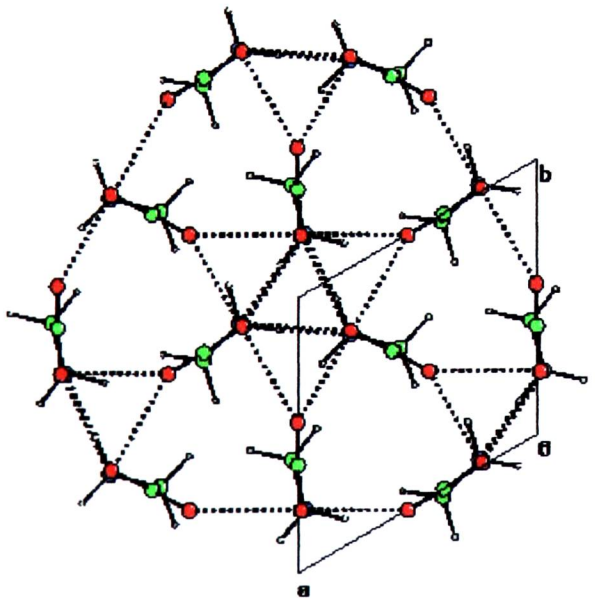

Figure 3.4. The structure of γ-glycine viewed along [0 0 1].

The unit cell parameters at room temperature are summarised in Table 3.1, from the most recent reports available on the CSD.

Polymorph	*a* / Å	*b* / Å	*c* / Å	β / °	Space group	Density (exp) / g cm^{-3}
α[1]	5.1047(3)	11.9720(14)	5.4631(3)	111.740(5)	$P2_1/n$	1.615
β[2]	5.0932(16)	6.272(3)	5.3852(18)	113.19(3)	$P2_1$	1.576
γ[1]	7.0383(7)	7.046(3)	5.4813(8)	-	$P3_1$*	1.584

1.Boldyreva *et al.* (2003a)
2. Boldyreva *et al.* (2002), X-ray diffraction * Absolute structure was determined by Shimon *et al.* (1986)
Table 3.1. Summary of the unit cell parameters of the polymorphs of glycine

The isolation of the various polymorphs can be difficult as polymorph formation is extremely sensitive to the crystallisation conditions. For example, in the most recent report of β-glycine (Boldyreva *et al.*, 2002) the crystal was prepared from a saturated aqueous solution which also contained acetic acid, which is also reported to give the γ-polymorph. The three polymorphs are concomitant, and undergo phase transitions depending on the crystal environment (Section 3.1.3) It is thought that in solution the glycine molecules form dimers, favouring the formation of the α-polymorph which contains cyclic dimer units (Gidalevitz *et al.*, 1997). Addition of acetic acid protonates the COO^- group making the formation of these cyclic dimer units less favourable, giving rise to the β and γ forms.

The bond lengths and angles do not vary between the polymorphs. There is one important difference - the torsion angle between the carboxyl group and the ammonium group. This has values of 19°, 25° and 15.6° respectively in the α, β and γ phases.

3.1.3 Known transitions between polymorphs

γ→α

The γ and α polymorphs of glycine are related enantiotropically; the relative stabilities of the two phases inverts below the melting point. Heating of γ-glycine results in the formation of the α phase. This transition was first reported by Itaka (1961), who noted that the transition temperature was difficult to determine precisely. More recent work by Perlovich *et al.* (2001) using Differential Scanning Calorimetry (DSC) showed that the transition temperature has a strong dependence on the

preparation, treatment and habit of the γ-glycine crystal. Heating of the crystal prior to the DSC measurement raised the transition temperature from 462.3 K to 473.7 K. The enthalpy of the transition was also affected by heat treatment. Crystals of differing habit had transition temperatures ranging from 441.4 K to 454.7 K.

The γ→α transition proceeds via a single crystal – single crystal phase transition, demonstrated by Perlovich. Diffraction data were collected on the same sample before and after the phase transition. Refinement against these data showed the formation of the α-glycine polymorph. No mechanism has been proposed for this phase transition. Given the large differences in structure (Section 3.4) it is surprising that the transition proceeds in a single crystal - single crystal mechanism.

α→γ transition

The reverse transition α→γ has also been observed, in a solvent mediated mechanism. Glycine has some industrial uses as described in Section 3.1.1. Industrial glycine typically consists of a mixture of the α and γ polymorphs, but on storage caking occurs, caused by the transformation of the α phase to the γ phase. It has been shown (Sakai *et al.*, 1992) that the presence of water is required for the transition to occur; the mechanism is thought to be the dissolution of α crystals followed by growth of crystals of γ-glycine. Solubility studies (Park *et al.*, 2003) show that the solubility of the α phase is slightly higher than that of γ-glycine at room temperature.

β→α transition

β-glycine is the least stable of the three phases, transforming to the α-polymorph following mechanical shock or if left in humid conditions (Itaka, 1960). DSC measurements (Perlovich *et al.*, 2001) have shown that β-glycine does not transform with changing temperature, that is β-glycine is monotypic with respect to the α and γ phases. The β→α transition is solvent mediated, as in the α→γ case. β-glycine is more soluble than the α form. Detailed study of this transition (Ferrari *et al.*, 2003) showed that the rate-limiting step was the dissolution of the β-glycine crystals. The rate of this transition was dependent on temperature and scale, amongst other experimental factors.

3.1.4 Effects of temperature on the structures of the polymorphs

A recent study by Boldyreva *et al.* (2003a) examined effects of cooling on each of the polymorphs using single crystal X-ray diffraction studies on non-deuterated samples. No phase changes were observed on cooling of α and γ-glycine to 150 K or in β-glycine on cooling to 105 K. Each phase contracted highly anisotropically; details of the changes are given later where they are discussed in the context of hydrogen bonding.

The structural effects of heating on α-glycine up to 427 K were reported by Langan *et al.* (2002). No phase transition was observed, nor did the geometrical parameters of the molecule change significantly. The increase in volume with increasing temperature was directly proportional to the increase in the *b* lattice parameter, corresponding to increased separation of the layers of molecules caused by a large anisotropic libration motion.

3.1.5 Glycine at high pressure

Concurrently with the experimental work described in this thesis, the results of other high pressure experiments on glycine have been reported (Boldyreva *et al.*, 2003b). Pressure studies on a mixed powder sample of α and γ-glycine were interpreted by the authors as showing no evidence of phase transition up to 4.0 GPa (40 kbar). As in the temperature case, the contraction with pressure was found to be anisotropic. Temperature and pressure were observed to have slightly differing effects on the structures of both polymorphs. The details of these experiments are discussed more fully in Section 3.4 in context with our own results.

3.2 Experimental work

3.2.1 Single crystal experiments

α-glycine

Crystals of α-glycine were grown from aqueous solution of glycine (Aldrich). No transition was observed up to 55 kbar (McGregor, 2000). The cell dimensions at this pressure are shown in Table 3.2.

β-glycine

Crystals of β-glycine were grown by slow diffusion of ethanol into a concentrated aqueous solution of glycine, and could be identified by the crystal habit. The crystals were found to transform quickly to α-glycine when removed from solution. A crystal was cut to the required size and quickly loaded into a cell equipped with diamonds with 600 μm culets, a tungsten gasket with a 300 μm hole and a chip of ruby for pressure measurement. A 4:1 mixture of methanol : ethanol was used as the pressure transmitting medium. Data were then collected at ambient pressure, 8 kbar and 19 kbar. The pressure was then released, and the sample recovered from the diamond anvil cell. The crystal was mounted on a standard fibre and data collected at room temperature. A reversible phase transition to a new polymorph occurred between ambient pressure and 8 kbar via a single crystal - single crystal phase transition.

γ-glycine

Crystals of γ-glycine were grown from aqueous solution of glycine made acidic with a small amount of acetic acid. Crystals were identified from the unit cell prior to loading in the diamond anvil cell. The crystals were found to undergo a phase transition to a polycrystalline material at 17 kbar (Figure 3.5). It was not possible to characterise this phase transition using single crystal techniques; high pressure powder diffraction was used to gain more information (section 3.2.2).

Phase	Pressure	*a* / Å	*b* / Å	*c* / Å	β / °
α	55kbar	4.898(3)	11.088(9)	5.382(9)	116.72(7)
γ	13kbar	6.890(4)	-	5.426(3)	-

Table 3.2. Cell measurements for α and γ-glycine at elevated pressure

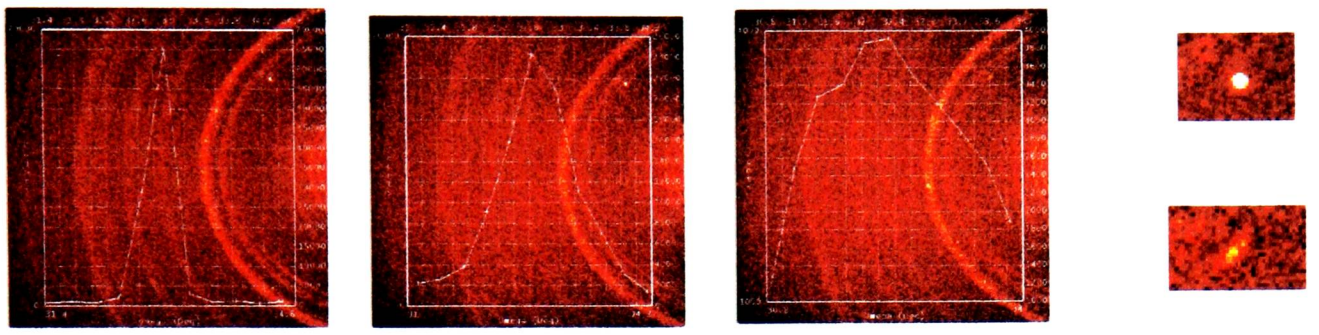

Figure 3.5. Changes in peak profile for the -2 3 0 reflection. Left - ambient pressure. Centre - 13 kbar. Right - 19 kbar. Far right - close up on the spot shape at ambient pressure and 19 kbar.

3.2.2. High pressure powder diffraction on γ-glycine

A powder sample of the γ polymorph was obtained by crushing a single crystal of γ-glycine (previously identified by unit cell determination). To minimise mechanical strain in preparation of the powder sample, the crystal was not ground but simply crushed into the sample hole of a Merrill - Bassett diamond anvil cell. Paraffin was used as the pressure transmitting medium.

The powder experiments were carried out at Station 9.1 at the SRS, Daresbury, using the experimental procedures described by Nelmes and McMahon (1994). The wavelength used was 0.4654 Å; using a short wavelength reduces the resolution of the powder patterns but means that the whole pattern can be observed within the angular range of the cell. An image plate was used to record the powder patterns; collecting complete Debye - Scherrer rings can overcome some of the problems in preferred orientation and poor powder averaging common in high pressure powder diffraction. Accurate sample centring prevents contamination of the pattern with lines from the beryllium rings or the gasket material. Use of synchrotron radiation allows the collection of a pattern in one hour. The data from the image plate were integrated using Edipus (Piltz *et al.*, 1992).

Data were collected on a sample of γ-glycine powder at ambient pressure, 29 kbar and 43 kbar. The pressure was then released and two further data collections

performed, one immediately following pressure release and the second after eight hours.

3.3 Results

3.3.1 Solution and refinement of the new phase of glycine

Each high pressure data set was indexed using Gemini (Sparks, 2000), and integrated using Saint (Bruker-AXS, 2003) using dynamic masks, as discussed in Chapter 2. An analytical correction for the absorption by the diamond anvil cell components was applied using Shade (Parsons, 2003). An absorption correction for the crystal was applied using Sadabs (Sheldrick 2002). The data were merged in point group 2/*m* using Sortav.

The structure of the new polymorph formed between ambient pressure and 8 kbar was solved in $P2_1/n$ using direct methods (Shelxs, Sheldrick, 1997). Given the poor data completeness and quality, the solution of structures from data collected on samples loaded in diamond anvil cells is difficult, with a lack of data in specific directions (Figure 3.6). In this case a solution was obtained, albeit with some difficulty, from conventional direct methods; later work has shown that the structure can be solved more easily using the direct space powder solution program DASH (David, 2003).

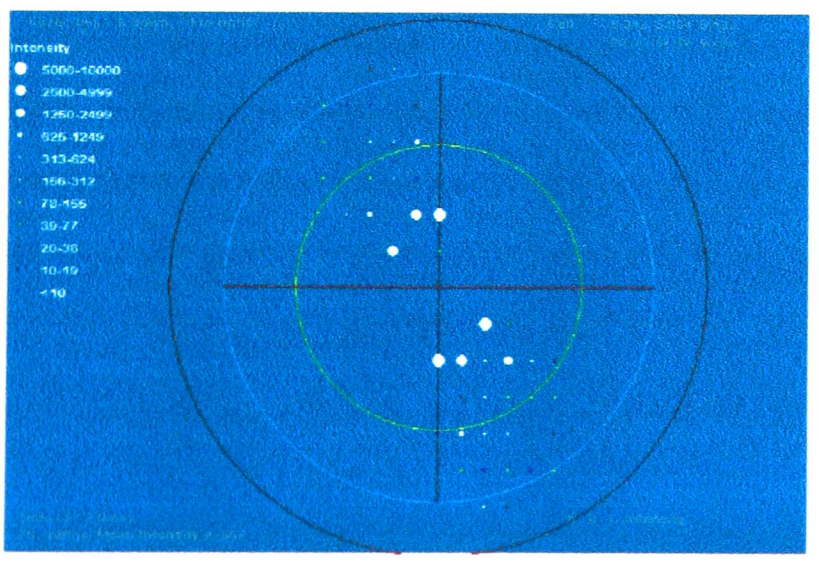

Figure 3.6. Reciprocal space plot of the 0 k l layer in the diffraction pattern of δ-glycine at 19 kbar

The structure was refined against $|F|^2$ using Crystals (Watkin *et al*, 2003). Distance restraints based on the bond lengths of the molecule under ambient conditions (based on Boldyreva *et al.*, 2003a) were applied. Difference Fourier synthesis showed the position of one of the hydrogen atoms of the ammonium group, allowing the entire group to be placed in the staggered position relative to the α-C. This orientation places the hydrogen atoms in positions where short contacts between the nitrogen and oxygen atoms are made – in the correct positions for hydrogen bonding. Full refinement details are shown in Table 3.3.

The data collected for the recovered crystal at ambient pressure and temperature were integrated using routine procedures. An absorption correction was applied using Sadabs, and the structure was refined against $|F|^2$ using Crystals. Full refinement details are shown in Table 3.3.

3.3.2 Powder analysis of γ-glycine

Rietveld refinement for each powder pattern was carried out using Topas 2.0 (Bruker, 2000). In each case the background was modelled using a six term Chebychev polynomial. The peak shapes were modelled using a pseudo-Voigt function where six parameters - three to describe the peak half widths and three to describe the Lorentzian fraction of the peak - were used and refined. In each figure (unless otherwise noted) the top trace is the actual pattern collected, overlaid in red with the calculated pattern from the current model. The lower line is the difference between the two patterns.

The diffraction data obtained were of relatively poor quality, with spotty areas indicative of poor powder averaging (Figure 3.7). This is to be expected from the sample preparation stage - the samples were not ground to form a smooth powder to minimise mechanical strain caused during the sample preparation stage. Due to the small sample volume, powder averaging is a problem in high pressure powder diffraction experiments.

Crystal Data				
Space group	$P2_1$	$P2_1/n$	$P2_1/n$	$P2_1$
a / Å	5.088(4)	9.219(16)	9.122(4)	5.083(8)
b / Å	6.266(3)	6.024 (6)	5.8644(11)	6.270(10)
c / Å	5.340(3)	5.361(4)	5.3417(17)	5.380(9)
β / °	113.11(6)	97.67(13)	97.49(4)	113.09(2)
V / Å^3	158.0(2)	295.1(7)	283.32(16)	157.7(4)
Z	2	4	4	2
ρ_{calc} / Mg m^{-3}	1.577	1.685	1.760	1.581
Number of reflections for cell (θ range, °)	235 (5.2 < θ < 26.3)	104 (4.6 < θ < 25)	133 (6 < θ < 23)	303 (4 < θ < 26)
Crystal description, size / mm	Colourless block, 0.15 x 0.1 x 0.1			
Pressure / kbar	Ambient, loaded into DAC	8	19	Ambient pressure, recovered from cell
Data Collection				
Reflections collected	481	615	701	994
Independent reflections	125	164	194	411
R_{int}	0.1337	0.1693	0.1315	0.04
h	-4 to +4	-6 to +6	-7 to +7	-6 to +6
k	-7 to +7	-6 to +6	-6 to +6	-8 to +7
l	-6 to +6	-4 to +4	-4 to +4	-7 to +5
Solution and Refinement				
Solution (Program)	Known	Direct	Direct	Direct
Hydrogen atom placement	Geometric	See text	See text	Geometric
H refinement	No refinement			
R [F_o>4σ(F_o)]	0.0955 (88)	0.0674 (84)	0.0831 (145)	0.0647
wR_2 (all data)	0.1776	0.1478	0.1918	0.1896
Goodness of fit on F^2	1.075	0.973	0.950	1.0052
Restraints	4	9	9	0
Parameters	21	21	21	46
Maximum Δ/σ	0.001	0.000	0.000	0.000
Weighting scheme x, y*	0, 0.840	0, 1.330	0.088, 1.595	0.075, 0
Largest difference map residuals [e Å^{-3}]	0.48, -0.58	0.51, -0.37	0.71, -0.47	0.49, -0.65

* where $w = 1/ [\sigma^2(F_o^2) + xP^2 + yP$, $P=(F_o^2 + 2F_c^2)/3$

Table 3.3. Crystal data and refinement details for δ-glycine

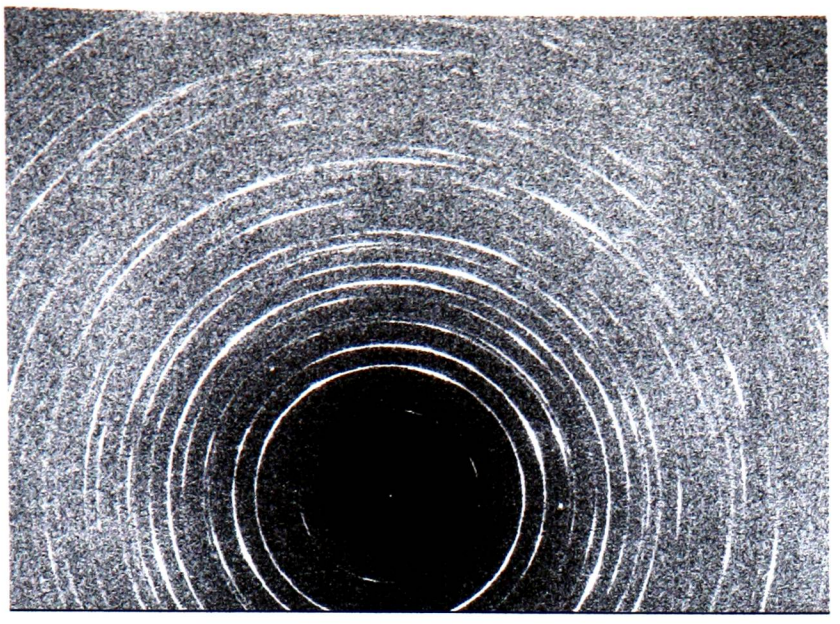

Figure 3.7. Raw image plate data for γ-glycine at ambient pressure prior to pressure application. The poor powder averaging can be seen in the lack of smoothness in the powder rings.

γ-glycine at ambient pressure

Rietveld refinement indicated that there was a significant amount of preferred orientation in the powder before the application of pressure (Figures 3.8 and 3.9). This is consistent with other reported powder diffraction studies on glycine (Boldyreva *et al.*, 2003b). Preferred orientation causes systematic distortions of the reflection intensities, and arises when there is some physical property of the crystallites which leads to a preference for some particular orientations. This was modelled using a spherical harmonic expansion, based on the method of Jarvinen (1993). Expansion to fourth order terms with three refinable parameters was sufficient to model the preferred orientation. Increasing the order to six introduced a further three parameters with no appreciable effect on the refinement.

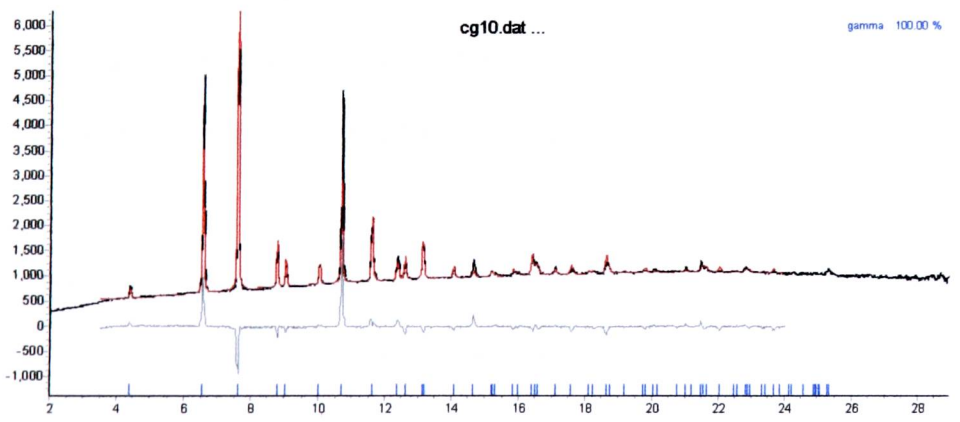

Figure 3.8. Refinement without preferred orientation correction. The peak positions match well but the intensities of several reflections are particularly poorly modelled, with the 1 0 -1 (equivalent to the 1 0 1 reflection) and the 1 0 2 (1 0 -2) significantly underestimated and the 2 -1 0 reflection overestimated.

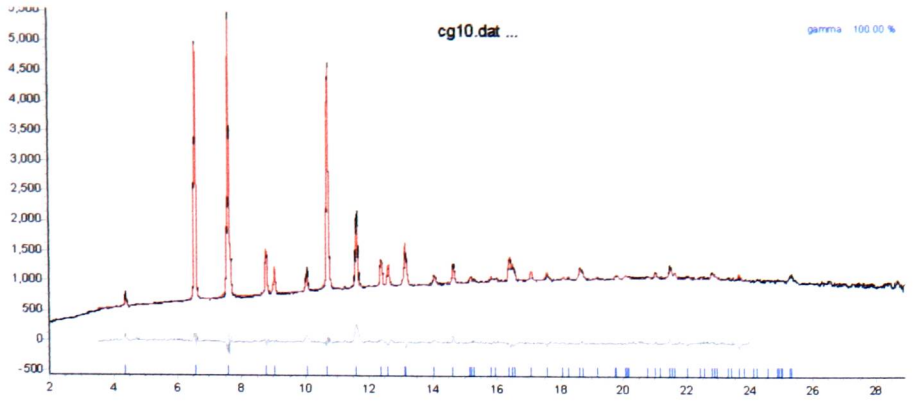

Figure 3.9. Incorporation of a spherical harmonic correction to model the preferred orientation has improved the fit considerably (c.f. Figure 3.8).

a / Å	*c* / Å
7.0345(5)	5.4789(3)

Table 3.4. Cell dimensions of γ-glycine from ambient pressure powder

The largest peak in the difference curve is now due to the (3 -2 0) reflection, which is now underestimated: however the difference peak is much smaller than without the spherical harmonic correction. This difference could be caused by poor powder averaging, since the sample was not finely ground. Incomplete powder averaging differs from preferred orientation in that there is no special physical property of the solid leading to poor averaging, rather due to the graininess of the sample (or small sample volume) there are insufficient crystallites to adequately fulfil the criterion that every possible orientation is adopted. This cannot be corrected for in the same way as preferred orientation (Young, 1993).

The refined cell dimensions (Table 3.4) are reasonable compared to published structures (Table 3.1). Given the problems of preferred orientation and incomplete powder averaging identified in this initial powder sample only limited information is available from the higher pressure data.

γ-glycine at 29 kbar

There is clear evidence of a phase transition at this pressure, with the appearance of two high intensity peaks in the 5° - 10° range (Figure 3.10). The quality of the pattern is much poorer, with a significant amount of peak broadening. This is a common feature in high pressure powder experiments and arises from pressure inhomogeneity in the sample. The reduction in intensity of the peaks relative

to the ambient pressure pattern (Figure 3.8) is due to the decay of the synchrotron beam.

Fitting the data with only the γ-glycine structure (Figure 3.10) the difference from the initial powder pattern is clear.

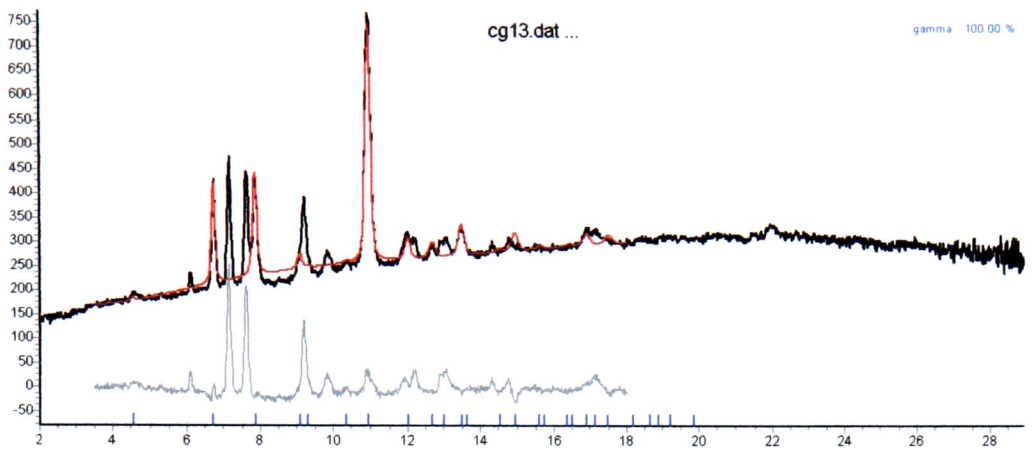

Figure 3.10. Powder pattern at 29 kbar fitted with only the γ-glycine structure. There are three large peaks in the difference curve (lower pattern).

The unit cell dimensions for α and δ glycine are similar (the relationship is discussed in more detail in section 3.4). The powder patterns are closely related (Figure 3.12): distinguishing these two phases may be difficult.

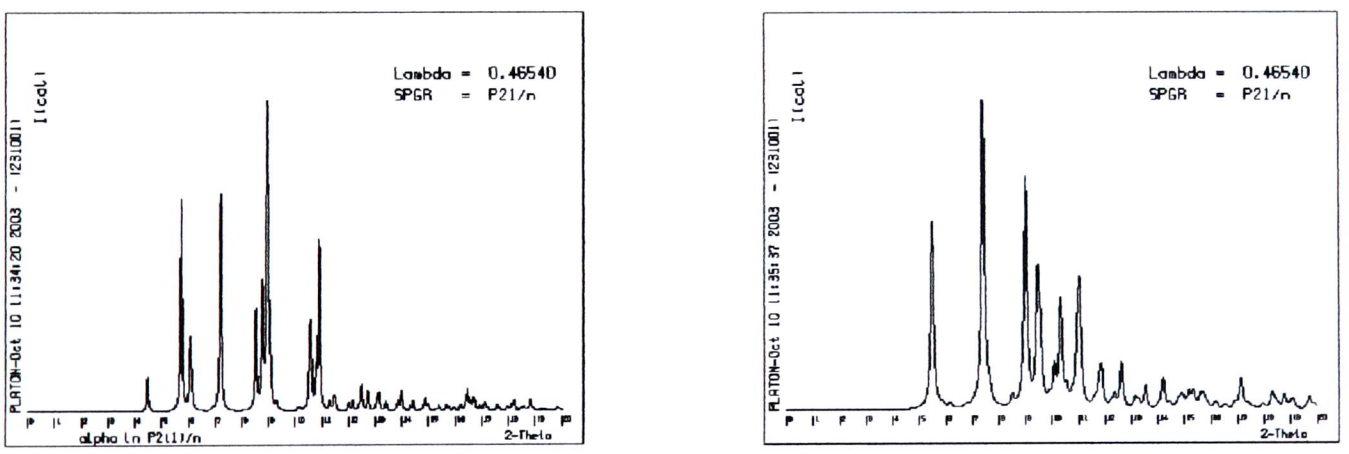

Figure 3.12. Simulated powder patterns for α, ambient pressure (left) and δ, 17kbar (right) glycine. (Patterns were simulated using Platon (Spek, 1990) .

Whole pattern decomposition using the Pawley method (Pawley, 1981) for a mixture of γ and δ, and then γ and α was performed. This allows refinement of the unit cell parameters but does not include any other structural information. The results are shown in Figure 3.11, and the refined unit cell parameters are listed in Table 3.5.

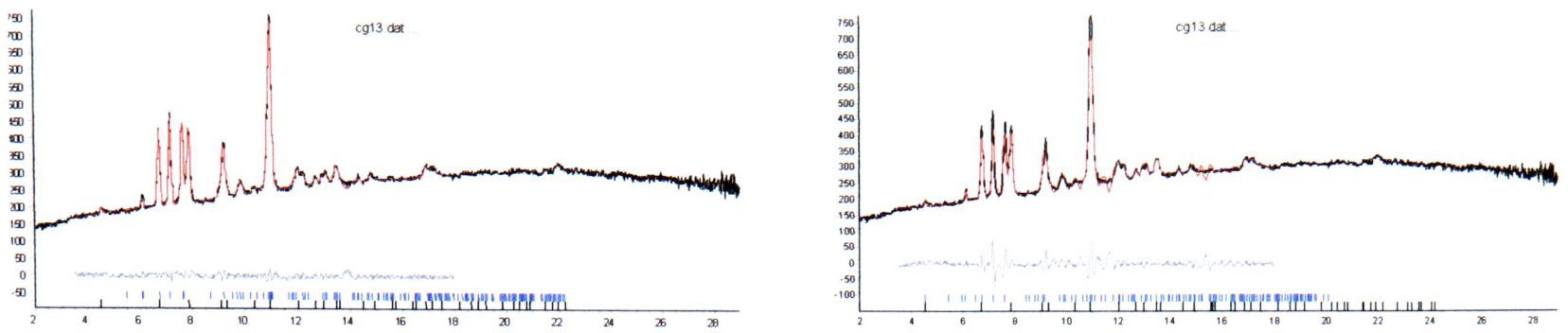

Figure 3.11. Pawley refinement using γ and δ (left) and γ and α (right). The black tick marks in each case correspond to the γ peak positions. The difference curve is lower for the γ/δ mixture.

Phase	*a* / Å	*b* / Å	*c* / Å	β[°]
γ	6.803	-	5.377	-
δ	8.854	5.822	5.430	97.2
γ	6.813	-	5.581	-
α	5.113	11.775	5.710	109.4

Table 3.5. Results of the Pawley unit cell refinements.

The refined unit cell parameters for α-glycine are unrealistic from the Pawley refinement- the unit cell appears to have increased in volume on the application of pressure. The *c* length has increased by 0.25 Å relative to the room temperature, ambient pressure determination. The *c* dimension has also increased for γ-glycine in this γ/α mixture. By contrast the unit cell dimensions obtained for both phases in the γ/δ mixture are more reasonable, although there has been a slight increase in *a* for δ-glycine. The difference curve is much smoother for the γ / δ model.

Inclusion of the crystal structure co-ordinates in the refinement model in a Rietveld refinement gives a worse fit to the measured pattern (Figure 3.13). It is not possible to refine these co-ordinates because of the low quality of the data. The structures will have distorted from those observed in the single crystal studies, explaining in part the poor fits.

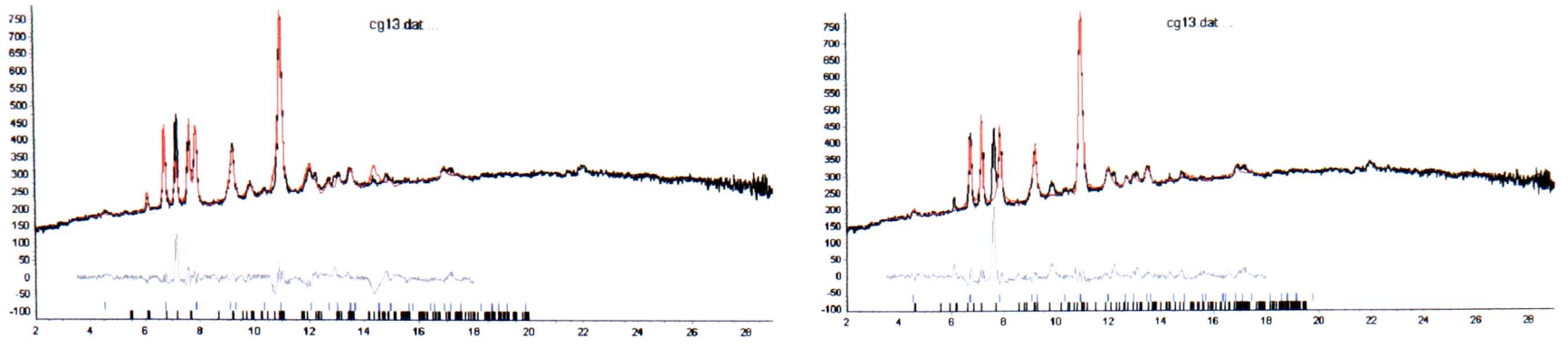

Figure 3.13. Rietveld refinement of the data using γ/δ (left) and γ/α (right) obtained at 29 kbar

The refinement using a γ/δ mixture results in better fit to the data than a γ/α mixture (Figure 3.13). The unit cell dimensions for α-glycine refine to unrealistic values, inconsistent with the measurements made by Boldyreva (2003b) and the results of Density Functional Theory (DFT) calculations (Clarke, 2003), which both show an increase β with pressure rather than the decrease derived from this powder refinement. The refined unit cell of α-glycine has increased in volume, which is unlikely.

Mixture	Phase	*a* / Å	*b* / Å	*c* / Å	β [°]	R_{wp}	R_p	S
γ/δ	γ	6.792(4)	-	5.375(4)	-	4.835	3.187	0.81
	δ	8.823(7)	5.812(4)	5.424(3)	97.36(7)			
γ/α	γ	6.816(8)	-	5.390(6)	-	6.241	3.384	1.05
	α	5.222(9)	11.644(13)	5.463(7)	108.81(13)			
γ/α/δ	γ	6.810(4)	-	5.390(5)	-	1.998	2.555	0.43
	δ	8.850(5)	5.839(5)	5.453(8)	97.26(6)			
	α	5.150(5)	11.640(5)	5.521(3)	108.40(7)			

Table 3.6. Cell dimensions and refinement statistics at 29 kbar.

Refining using all three phases improves the fit (Figure 3.14); however the cell dimensions of the α phase again refine to unreasonably large values (Table 3.6). The improvement in fit is probably due to overfitting of the data rather than any real improvement in the refinement, seen by the very low goodness-of-fit for the three

phase refinement. The α lattice parameters are highly correlated with the background parameters. Close examination of the peaks shows that inclusion of the α phase does not lead to more peaks being indexed - the improved fit is largely due to the increased contribution to the peak at 7.15° (-1 1 1 peak in δ-glycine).

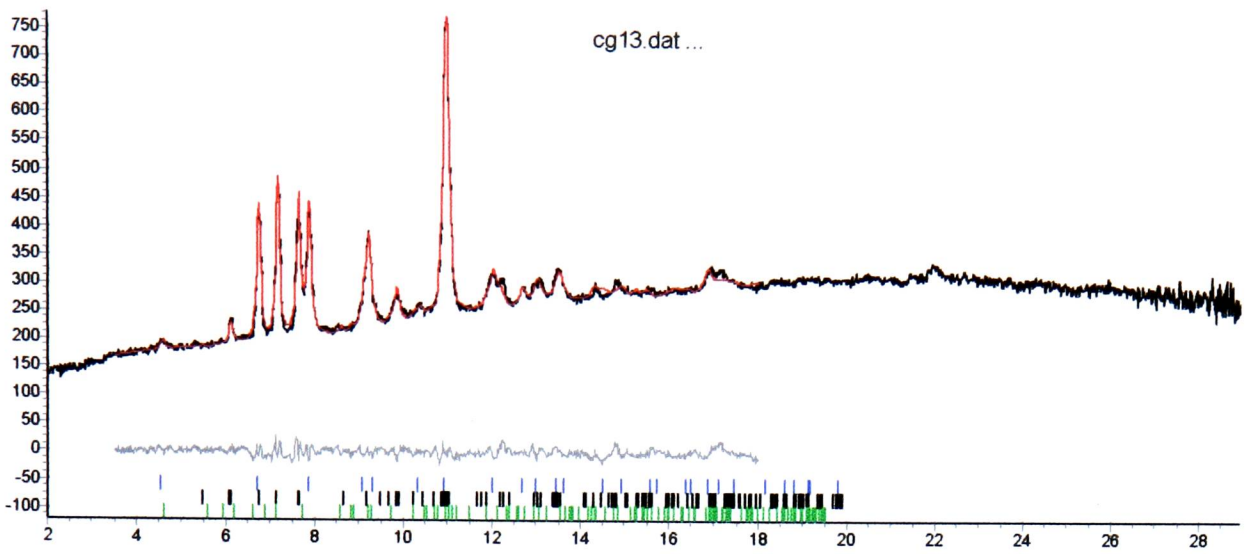

Figure 3.14 Refinement using three phase fractions

The refinement does yield some information about the structures of the two polymorphs at this pressure. The γ phase has contracted in the *a* (and therefore *b*) unit cell directions with little change in *c*. Similarly there has been little change in the *c* length of the δ phase. Along these directions there are hydrogen bonded chains of molecules (section 3.4).

γ-glycine at 43 kbar

The pattern has simplified at 43 kbar (Figure 3.15). The γ-glycine peaks between at 6.7° and 7.9° at 29 kbar have reduced in intensity, although the strong peak at 11° is still present. As at 29 kbar, the -1 1 1 reflection from δ-glycine is poorly fitted when a mixture of γ and δ-glycine is used in the refinement model.

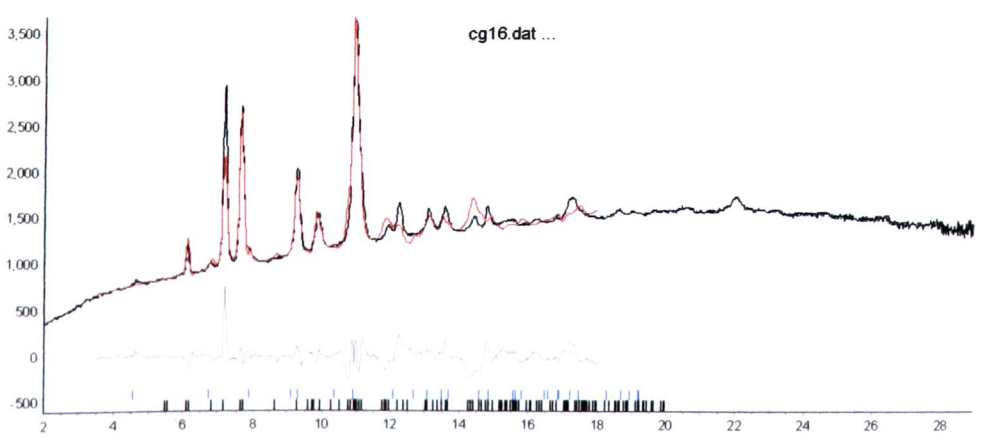

Figure 3.15. Refinement of the pattern at 43 kbar

Phase	*a* / Å	*b* / Å	*c* / Å	β / °
γ	6.770(10)	-	5.402(5)	-
δ	8.85(10)	5.772(5)	5.423(5)	97.98(7)

Table 3.7 Cell dimensions at 43 kbar.

Inclusion of α-glycine improves the fit; again the correlation between parameters increases and the main contribution of the α phase is to increase the intensity of the peak at 7°. There has been little change in the unit cell parameters relative to 29 kbar.

Pressure release

The pattern obtained on release of pressure shows the reverse transition has occurred, with restoration of the γ-glycine peaks. Figure 3.16 shows the overlay of this pattern with that obtained prior to the application of pressure.

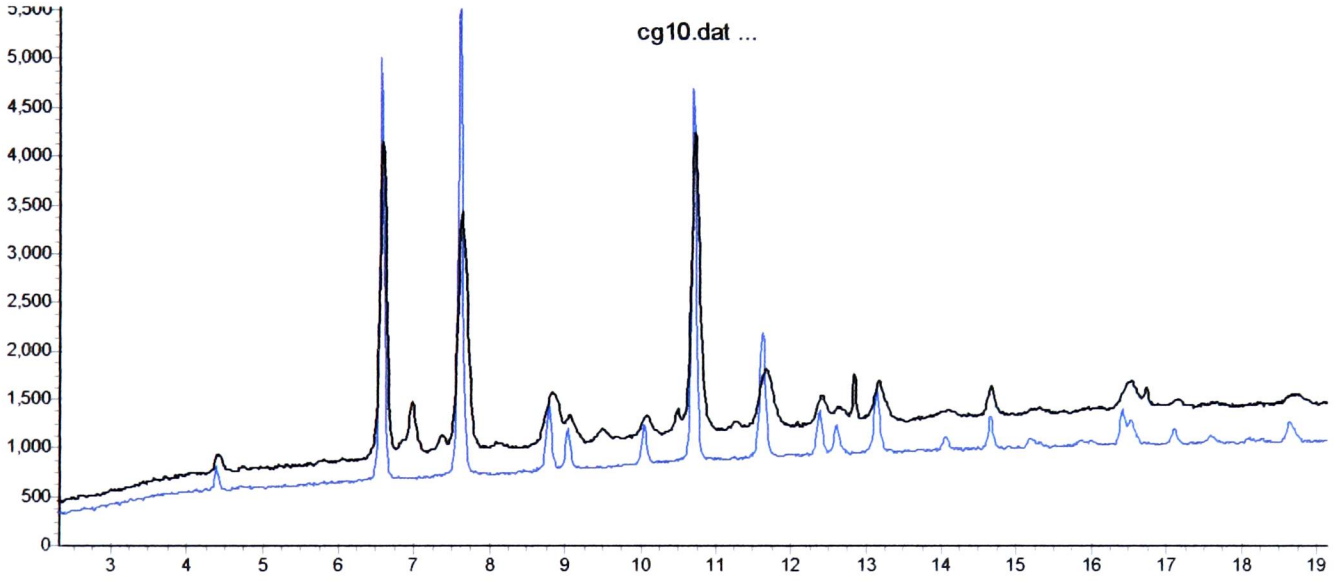

Figure 3.16 Overlay of initial (blue) powder pattern and after pressure release (black)

There are some peaks that do not correspond to γ-glycine. There is some residual intensity at 6.96° and 7.36°, indicating that not all of the high pressure phase has transformed back to γ-glycine. Given the low intensity of these peaks it is not possible to perform any meaningful two phase refinement.

The intensity of the strongest γ-glycine peaks has changed; prior to the phase transition the $1\ 0\ \bar{1}$ reflection (at 6.56°) was less intense than the $2\ \bar{1}0$ reflection (7.6°). This relationship is now reversed. This is consistent with an increase in the

preferred orientation of the powder sample, an effect noted by Boldyreva *et al* (2003b).

Eight hours after pressure release

Eight hours after the pressure was released the small peak at 6.96° is still present, with reduced intensity. The ratio of this peak to the γ-glycine reflection at 6.56° was 2.833:1; the ratio is now close to 4:1, indicating that the reverse phase transition has not yet reached completion.

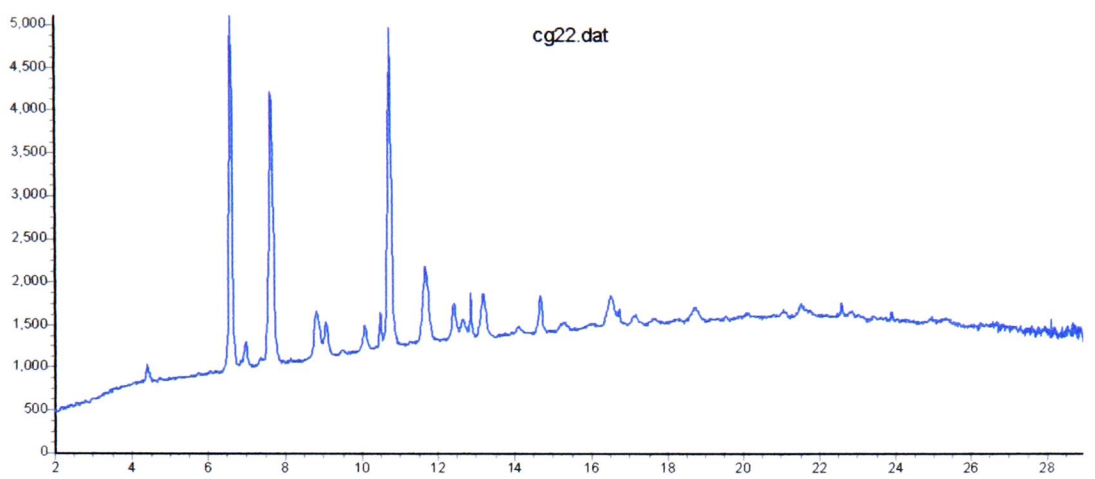

Figure 3.19 Powder pattern eight hours after pressure release

Conclusions from powder experiments

The powder diffraction experiments show clear evidence of a phase transition in γ-glycine. At 29 kbar there are new peaks in the diffraction pattern, and at 43 kbar the γ-glycine peaks have almost disappeared. The changes in the pattern have been shown by the refinements above to be consistent with the formation of δ-glycine. Refinement using the α phase lead to unrealistic increases in the unit cell volume, which is inconsistent with both the measurements made by Boldyreva *et al* and DFT calculations by Clarke.

The reversibility of the phase transition shown by the recovery of the γ pattern is a further indication that the δ-phase (known from the original single crystal work to be unstable at ambient pressure) rather than the α phase was formed. Due to the graininess of the powder, clear from the initial refinement of the γ powder and the image plate images, it is not possible to obtain more detailed structural information from the powder data regarding changes in both phases with pressure.

High pressure neutron powder diffraction experiments by Nelmes *et al.* (2003) on deuterated γ-glycine have confirmed there is a phase transition with increasing pressure. As in the powder experiments described here, the diffraction patterns obtained were consistent with the formation of δ-glycine but proved difficult to refine.

3.4 Discussion

3.4.1 Structural comparison of the polymorphs

The crystal structure of δ-glycine is apparently more complex than that of the other phases. In place of the layer structure of α and β-glycine and the helical structure of γ-glycine, δ-glycine has a three dimensional hydrogen bonded network. The density of the δ phase is 7% greater than that of the α polymorph, and 10% greater than the β and γ forms. In order to understand fully the formation of this new phase and the relationship with the known polymorphs, a full comparison of the hydrogen bonding in each polymorph is required, and is given in the following discussion. The lengths of the hydrogen bonds are given, with a brief outline of how the hydrogen bonds combine to give the crystal structure of each polymorph. Similarities in the networks are then considered.

The graph set analysis of Etter *et al.* (1990) is used to describe the hydrogen bonding patterns. In this system of characterising hydrogen bonding, motifs are identified on the basis of donor and acceptor atoms. There are four descriptors of patterns: chains (C), rings (R), discrete complexes (D), and intra molecular rings (S). This letter symbol is combined with the number of atoms in the pattern (n), the number of donor atoms (d) and the number of acceptor atoms (a) to give the symbol for the pattern, written as $X_d^a(n)$.

α-glycine

Based on the N...O separations alone each molecule has four possible hydrogen bonding contacts, requiring one hydrogen atom to be bifurcated over two oxygen atoms. The first use of the term "bifurcated hydrogen bond" appeared in the first determination of α-glycine (Albrecht & Corey, 1939; Jeffrey, 1997). However single crystal neutron diffraction shows that the O...H distance for the minor

component of this bifurcated interaction is long for a hydrogen bond; this contact could be classified as a short van der Waals contact rather than a weak hydrogen bond. Each molecule forms six hydrogen bonds which link to five separate molecules, with two interactions formed to the same molecule (Table 3.8 and Figure 3.18).

Interaction	H....O / Å	N...O separation / Å	O..H-N angle / °
1	1.7293(17)	2.7713(9)	169.23(17)
2	1.820(2)	2.8474(10)	168.8(2)
3	2.101(2)	3.0650(12)	154.26(17)
(4	2.362(2)	2.9504(10)	114.92(17))

Table 3.8. Hydrogen bond lengths in α-glycine (values from Langan *et al.*, 2002, neutron diffraction, T=288 K). Contact 4 is included for information. The numbers refer to the interaction labels in Figures 3.18 and 3.19.

One hydrogen bond per oxygen atom is used to form the layer structure of α-glycine. These are the shorter interactions in the structure. One hydrogen bond (1 in Table 3.8) links glycine molecules to form chains parallel to the c axis (Figure 3.20). These chains are linked by the second hydrogen bond to form layers in the structure, forming $R_4^4(16)$ interactions.

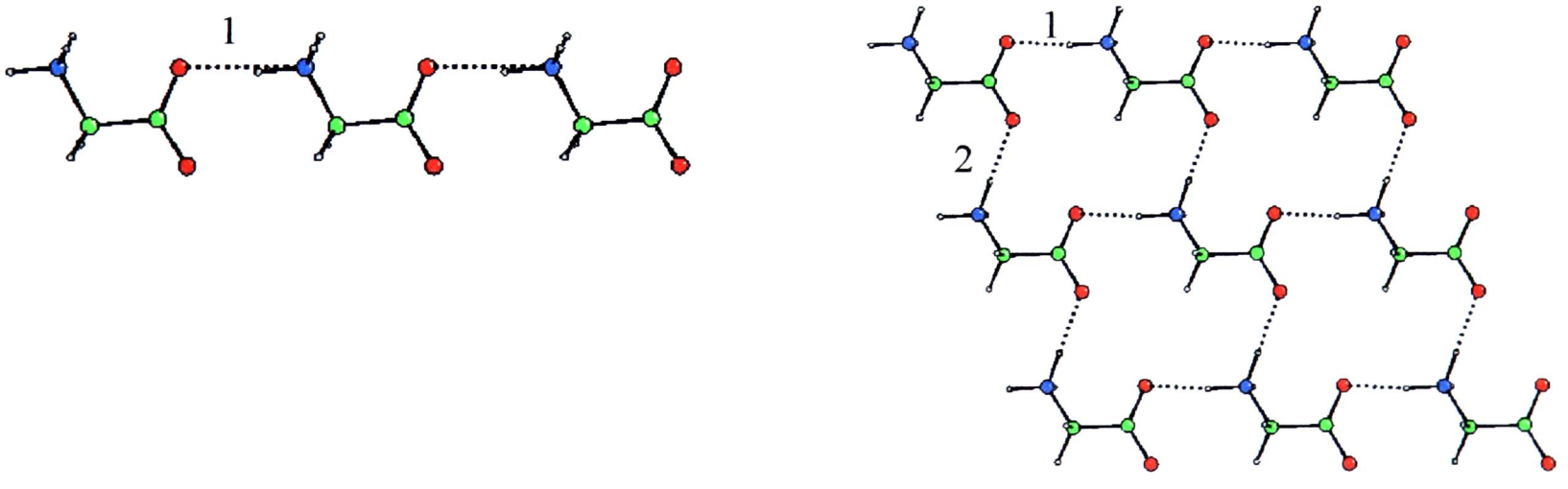

Figure 3.18. Interactions within one layer of α-glycine. The numbers refer to the interactions listed in Table 3.8.

The remaining unique hydrogen bond links the single layers to form the double layer arrangement. Each molecule is linked to another in the next layer

through a cyclic dimer, or in graph set notation an $R_2^2(10)$ motif (Figure 3.19).

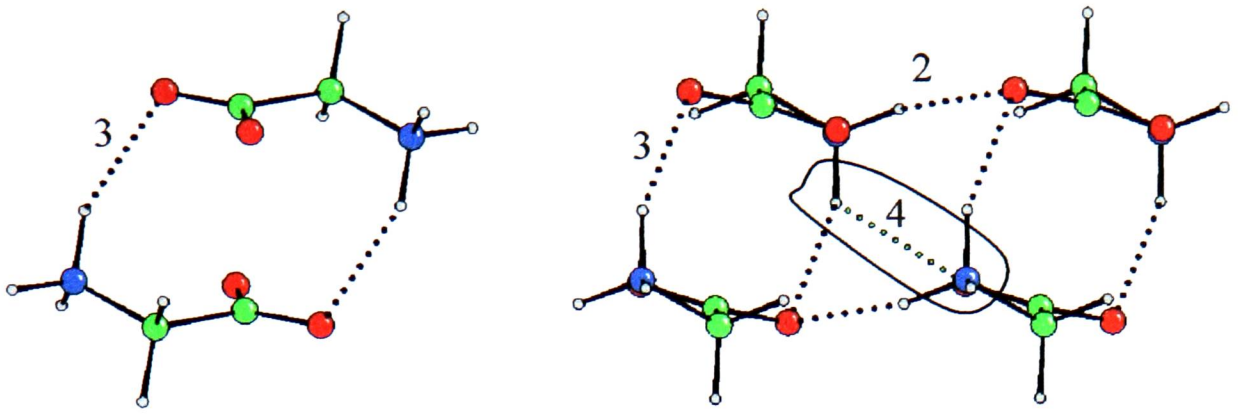

Figure 3.19. Cyclic dimer formation in α-glycine. Shown in green (ringed) in the right diagram is the fourth contact of the ammonium group.

Within one single layer the molecules point in the same direction with respect to the *c* axis; within one double layer the molecules are antiparallel to give the overall centrosymmetric structure. The closest contacts between the double layers are C-H...O contacts of 2.446 Å and 2.535 Å - there are no N-H..O hydrogen bonds linking the layers.

β-glycine

In β-glycine there are four unique hydrogen bonds (Table 3.9); one hydrogen atom is bifurcated over two interactions. In contrast to the α phase, the "bifurcated" hydrogen atom is symmetrically positioned between the two acceptor atoms to form a three centre interaction.

Interaction	H...O / Å	N...O / Å	O...H-N angle / °
1	1.866(16)	2.7626(11)	174.4(17)
2	1.97(2)	2.8509(13)	176.6(17)
3	2.23(2)	2.9785(13)	140.7(16)
4	2.30(2)	2.9795(15)	132.6(14)

Table 3.9. Hydrogen bonds in β-glycine (values from Boldyreva *et al.*, 2002, X-ray diffraction, T=294 K). The O...H distances are taken from Boldyreva; the N-H bond lengths were not normalised to neutron values.

As in α-glycine, one interaction per oxygen atom links the molecules into layers with the first interaction forming chains of molecules, which are then linked

into layers through $R_4^4(16)$ rings. The layer forming interactions are the shorter in the structure. The difference in between the α and β forms lies in the interaction between layers. The bifurcated hydrogen bond links the layers; the molecules are linked in a series of three and four membered rings, with the hydrogen atom bifurcated over the two types (Figure 3.20).

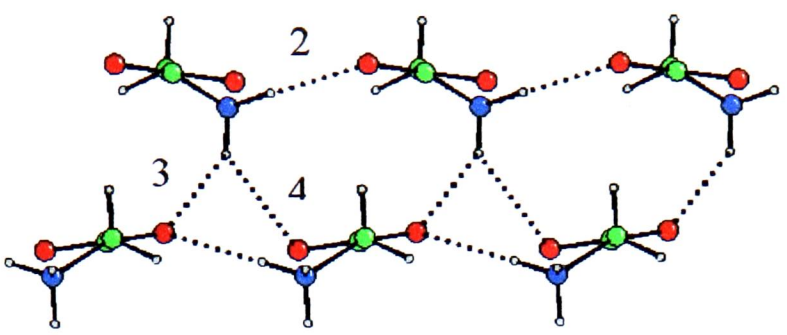

Figure 3.20. Links between layers in β-glycine, viewed along the (0 0 1) direction. The numbers refer to Table 3.9. Interaction 1 forms chains as in α-glycine, parallel to the line of view.

The chains in adjacent layers are antiparallel (this must be the case as they are related by the screw axis); the polarity in the structure comes from the orientation of the ammonium groups.

γ-glycine

γ-glycine has a different hydrogen bonding pattern to α and β-glycine. From the structure determined by neutron diffraction each hydrogen atom makes one long and one short contact to an oxygen atom (Kvick *et al.*, 1980). As in α-glycine, the N...O separations imply there are six hydrogen bonds; using the O...H separations only three of these contacts can be classified as hydrogen bonds (Table 3.10).

Interaction	H...O / Å	N...O / Å	O...H-N angle / °
1	1.763(3)	2.809(2)	171.3(1)
2	1.828(3)	2.809(2)	155.8(1)
3	1.960(3)	2.987(2)	171.9(1)

Table 3.10. Hydrogen bonds in γ-glycine (values from Kvick *et al.*, 1980, neutron diffraction, T=298 K))

One hydrogen bond links the molecules into chains parallel to the *c* axis. This is the shortest hydrogen bond. The next shortest links the chains into three fold helices (Figure 3.21). The interactions between the chains form an $R_4^4(16)$ graph set.

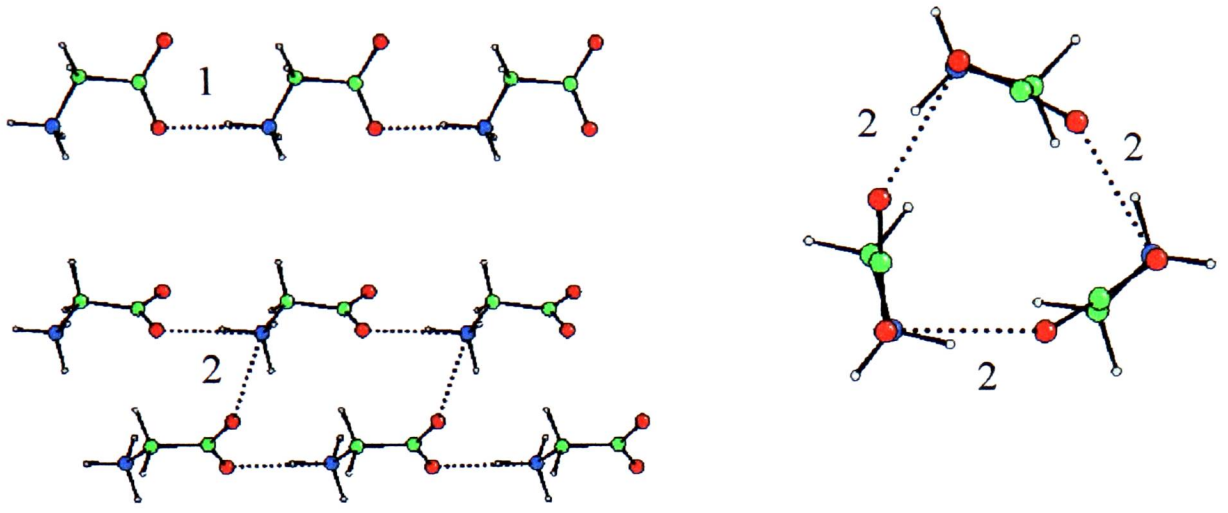

Figure 3.21. Helix formation in γ-glycine. Top left - hydrogen bonded chain. Bottom left - interactions of two chains via $R_4^4(16)$ graph set. Right - one helix (viewed along the [0 0 1] direction)

The third (and longest) hydrogen bond links the helices via a $R_4^3(14)$ graph set (Figure 3.22). Each chain is linked to two separate helices through this interaction (one as a donor, one as an acceptor) forming a three dimensional hydrogen bonded network. The C-C bond in each molecule is perpendicular to the *c* axis; the carboxyl group of each molecule must point in the same direction from the polar space group symmetry. Two of the remaining short N...O van der Waals contacts form additional contacts between the helices.

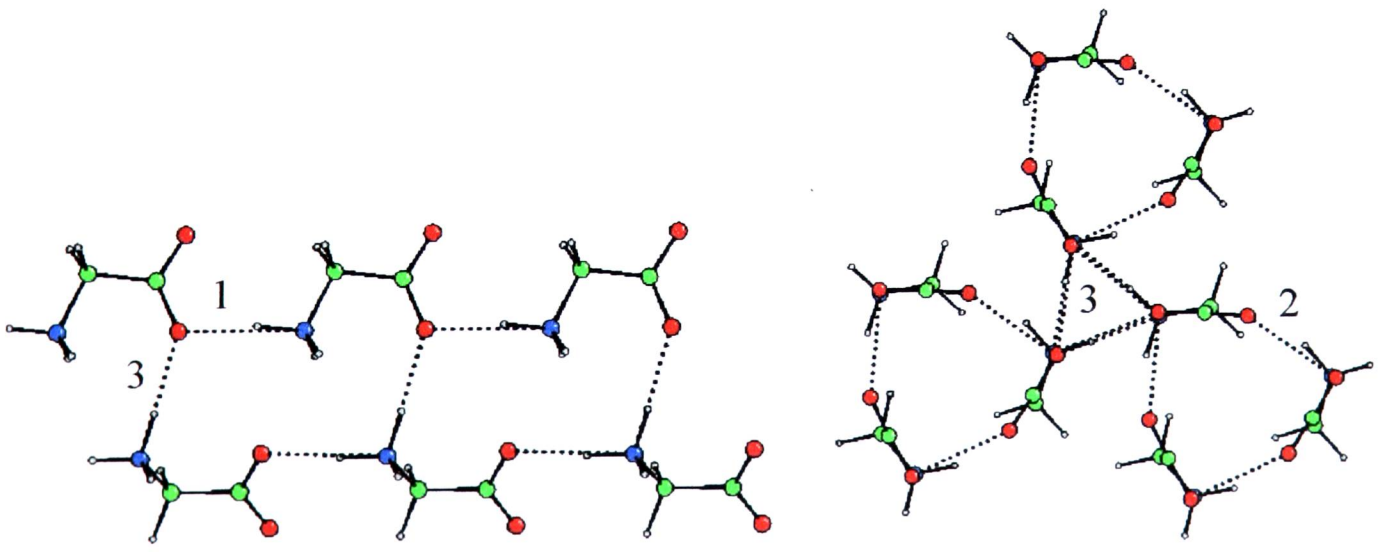

Figure 3.22. Interhelix hydrogen bonds in γ-glycine.

δ-glycine

In this new polymorph there are four N...O close contacts (Table 3.11). Although the ammonium hydrogen atoms positions were not refined, the positions were deduced from difference Fourier synthesis, showing the hydrogen atoms were staggered with respect to the CH_2 group (in common with the other three polymorphs). This allows classification of the hydrogen bonds on O...H grounds as well as from N...O separations, which may be misleading as in α and γ-glycine. There are four unique hydrogen bonds in δ-glycine; each molecule forms eight hydrogen bonds to seven adjacent molecules. The bifurcated hydrogen atom makes two similar contacts to adjacent oxygen atoms.

Interaction	O...H / Å	N...O / Å
1	1.828	2.762(12)
2	1.945	2.788(13)
3	2.100	2.883(8)
4	2.137	2.917(7)

Table 3.11. Hydrogen bonds in δ-glycine at 19 kbar. The N-H bond lengths have been normalised to typical neutron values.

One hydrogen bond (interaction 1 in Table 3.11) links the molecules into chains, as seen in the other polymorphs. These run parallel to the *c* axis. The second non-bifurcated interaction links these chains into layers via $R_4^4(16)$ graph sets, similar to α and β-glycine (Figure 3.23).

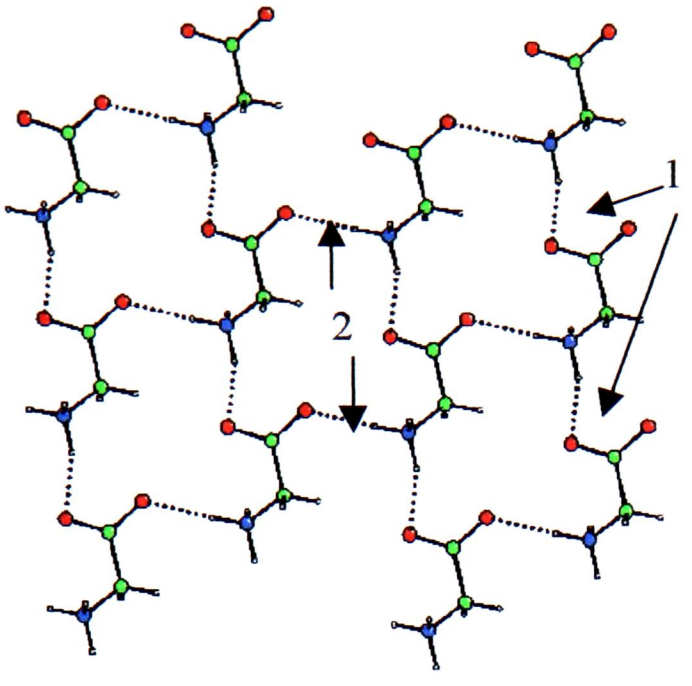

Figure 3.23. One layer in the structure of δ-glycine. The number indicate the interactions listed in Table 3.11.

The bifurcated hydrogen bonds link the layers within the crystal structure. One chain linking interaction forms a series of $R_2^2(10)$ and $R_4^2(8)$ groups. A similar pattern is seen in α-glycine, formed by the long hydrogen bond / short van der Waals contact. The other hydrogen bond is part of a second $R_4^4(16)$ ring (Figure 3.24). One hydrogen atom is bifurcated over both of these interactions.

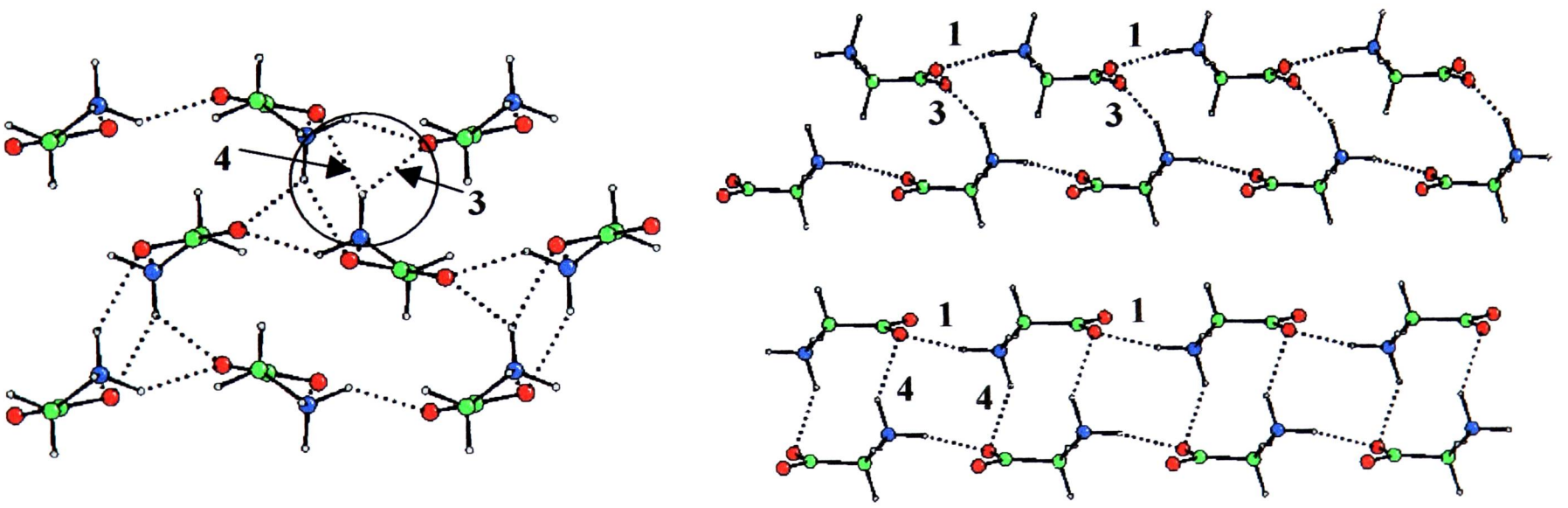

Figure 3.24. Interlayer interactions in δ-glycine. Left: The ringed section highlights the bifurcated interactions. Right (top): $R_4^4(16)$ graph set formed between two chains, using hydrogen bond **3**. Right (bottom): Series of rings formed by hydrogen bond **4**.

3.4.2 Common features in the polymorphs

There are two important shared features of the polymorphs of glycine. Each of the four phases contains hydrogen bonded chains of molecules. Secondly, the α, β and δ polymorphs have layered structures.

Hydrogen bonded chains

The oxygen atom *cis* to the nitrogen atom forms a *syn* hydrogen bond to an adjacent molecule in each polymorph (as shown for α-glycine in Figure 3.18), forming hydrogen bonded chains in the structures parallel to the *c* axis. This type of hydrogen bonded chain is common in the structures of amino acids, with a similar interaction in l-alanine and l-serine.

Polymorph	N...O / Å	O...H / Å	Angle with respect to *c* / °
α	2.7713(9)	1.7923(17)	1.2
β	2.7626(11)	1.866(16)	10.36
γ	2.809(2)	1.763(3)	2.09
δ (19 kbar)	2.762 (12)	1.828	12.3

Table 3.12. Chain forming hydrogen bonds in the polymorphs of glycine

The length of the hydrogen bond (N...O) connecting the molecules within the chain varies by 0.038(2)Å between the four polymorphs, in each case being the shortest hydrogen bond in the structure (Table 3.12). In each of the polymorphs the chains are parallel to one lattice direction although the hydrogen bond is not parallel to the axis in the β and δ polymorphs. This is caused by the difference in torsion of the glycine molecule in these two structures.

The *c* unit cell length delimits the minimum repeating unit in the chain. The *c* unit cell length is 0.1186(17) Å shorter in δ-glycine than in α-glycine; the molecules in one chain are 0.11186(17) Å closer together despite the similarity of the hydrogen bond length (2.7713(9) in α, 2.764(14) in δ). *c* changes only a small amount (0.043(2)Å) in the phase transition from β to δ. The length of this hydrogen bond is not significantly different in β-glycine at ambient pressure and δ-glycine at 19 kbar.

A further difference in the δ form is the decreased distance to the second oxygen atom - the δ phase has the most bifurcated interaction of the four polymorphs.

Cooling studies of the three polymorphs (Boldyreva *et al.*, 2003a) and compression of α and γ-glycine (Boldyreva *et al.*, 2003b) have shown the *c* unit cell length is the least sensitive to external conditions. This can be related to the strong hydrogen bonds within the chains, although identification of structural changes based solely on changes in the unit cell can be misleading, as shown for l-alanine in Chapter 4.

Hydrogen bonded layers

The structure of δ-glycine is closely related to the layer based structures of α and β-glycine. The relationship between these three polymorphs is clear from consideration of the cell dimensions in each case. The relationship in *c* is discussed in the previous section. Relative to α, *b* is halved in the β and δ phases. The change in *a* is complicated by the reduction in the β angle, however considering rather the change in d_{100} it is clear that there has been doubling in this direction relative to the α and β phases (Table 3.13).

Polymorph	*a* / Å	*b* / Å	*c* / Å	β / °	d_{100} / Å	d_{layer} / Å
α	5.1047(3)	11.9720(14)	5.4631(3)	111.740(5)	4.742	2.993
β	5.0932(16)	6.272(3)	5.3852(18)	113.19(3)	4.682	3.136
δ (19 kbar)	9.122(4)	5.864(11)	5.3417(17)	97.49(4)	9.044	2.932

Table 3.13. Comparison of cell dimensions of α, β and δ-glycine

The doubling in *a* indicates a difference in the layers between the β and δ phases. The halving of *b* in δ and β relative to α indicates that the orientation of each layer is equivalent as opposed to the double layer structure in the α polymorph.

The layers of molecules in α and β glycine consist of molecules related by translational symmetry; all the molecules are parallel so that all the ammonium groups point in the same direction, towards only one adjacent layer. In α-glycine one of the ammonium group hydrogen atoms points towards the other layer within the double

layer, and in β-glycine one hydrogen atom is oriented towards the next layer throughout the structure (Figure 3.25).

In the δ polymorph the molecules in one layer are related by the operation of the glide plane; the molecules are not parallel and the orientation of the ammonium group alternates. Hydrogen bonds are made to two adjacent layers, through both donor and acceptor interactions, with alternate molecules interacting with alternating layers (Figure 3.25).

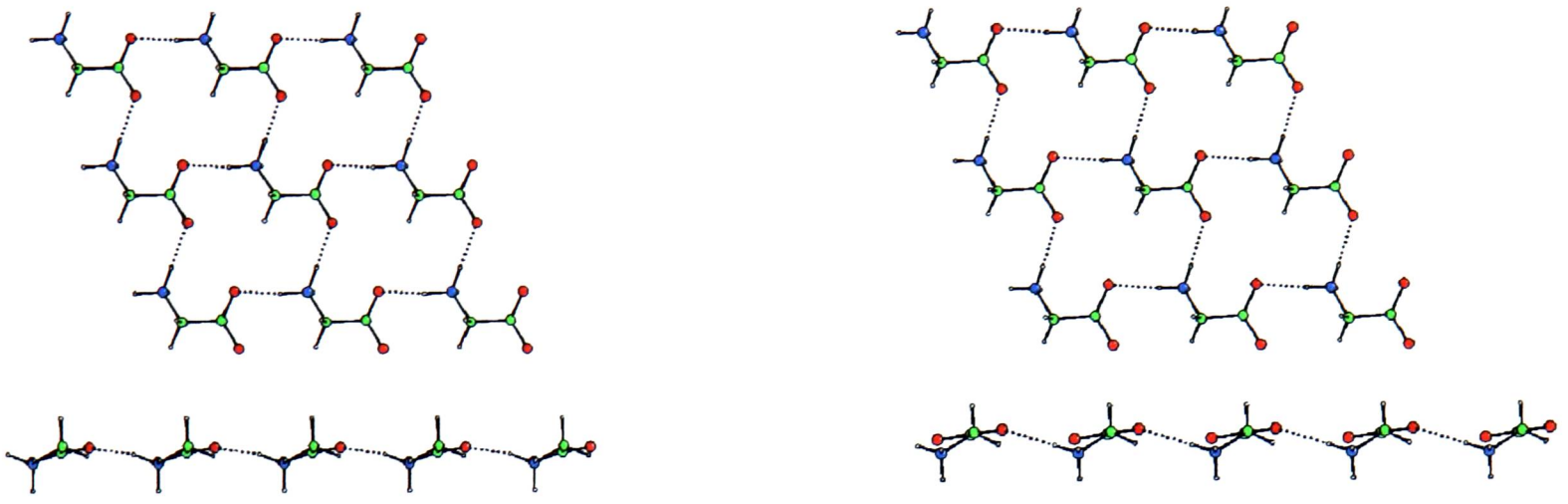

Figure 3.25.
a) above left. One layer in α-glycine, viewed from above and from the side
b) above right. One layer in β-glycine, viewed from above and from the side
c) left. One layer in δ-glycine, viewed from above and from the side. The alternation in orientation of the ammonium groups is clear.

The average distance between the hydrogen bonded layers in the α and δ forms is almost the same, with the α-layers slightly closer (Table 3.13). The distance separating the mean plane of the molecular centroids in each layer within a double layer is 2.79 Å; the distance between non interacting layers is 3.18 Å. One hydrogen atom is involved in the interlayer interactions; in α-glycine all the interlayer links from one layer are formed to the same adjacent layer forming the double layer

structure. In δ-glycine each alternate molecule links to the layer above or below to give the three dimensional hydrogen bonded network. The net effect is that there are half as many hydrogen bonds linking the layers in δ-glycine, but every layer is linked, giving a value for the layer separation the average of the α-glycine interactions.

Every second layer in β and δ-glycine is equivalent by lattice repeat; this is true for every fourth layer in α-glycine. The layers are antiparallel in β and δ-glycine (with respect to the direction of the carboxylate groups). Pairs of layers have the same orientation in α-glycine; these pairs of layers are two halves of adjacent double layers (Figure 3.26).

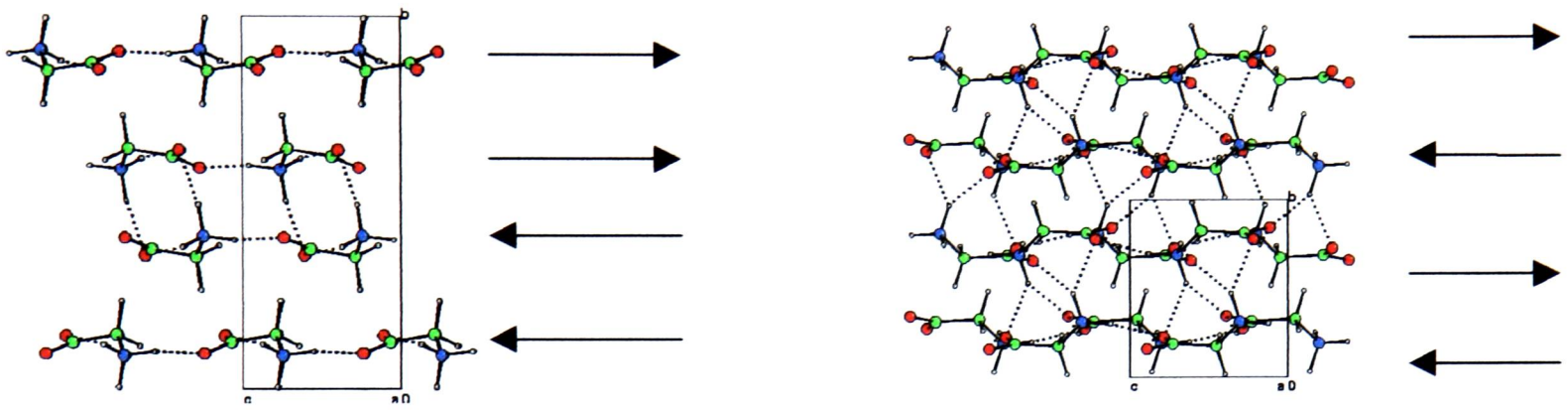

Figure 3.26. Relative direction of carboxyl groups. Left: α-glycine. Right: δ-glycine. The arrows indicate the direction of the carboxyl groups.

The phase transition from β-glycine to δ-glycine has been caused by the movement of every second molecule in the structure. This must be accompanied by the breaking and formation of a large number of hydrogen bonds in the structure. The resulting hydrogen bonds are shorter (Tables 3.9 and 3.11), but not sufficiently short to explain the increased density of δ-glycine or the driving force for the phase transition.

3.5 Topological Analysis

The relationships that exist between the four polymorphs of glycine are difficult to discern by examination of their hydrogen bonded networks alone. Blatov (2000) has described a topological approach to the problem of drawing such comparisons in which molecules are replaced by their geometric centroids. The shortest contacts between the centroids are used to partition the structures into Voronoi-Dirichlet domains (*lattice Voronoi-Dirichlet Polyhedra* or VDPs in Blatov's notation). In many cases the topological parameters of these domains and the numbers of centroids in successive coordination spheres can be used to relate molecular crystal structures to the well-known sphere packings (cubic close packing, hexagonal close packing and body-centred cubic packing). Body centred cubic packing is illustrated in Figure 3.27 using the structure of tungsten.

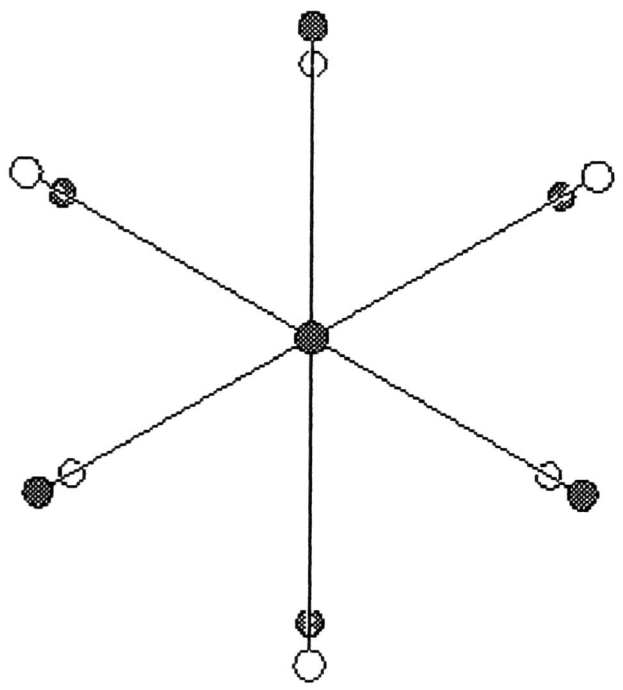

Figure 3.27. Body centred cubic packing in tungsten, viewed along the [1 1 1] direction. The distances from the central atom to the shaded and unshaded atoms is 2.74Å and 3.17Å respectively. The eight shorter contacts describe the vertices of the body centred cube; the six longer contacts form an octahedron linking the body centres of six adjacent cubes.

When reduced to an array of centroids γ-glycine resembles a distorted body-centred cubic (BCC) structure. This view of the structure is presented in Figure 3.28. The coordination sequence is 14-50-110 (the molecular coordination number is 14,

and there are 50 and 110 atoms in the second and third coordination spheres, respectively), which makes the structure topologically similar to BCC. There are six centroid-centroid distances falling in the range 4.42 - 4.46 Å which form an octahedral array about the central molecule, and eight at 5.43-5.48 Å which form a cube like array: that is the cube forming distances are *longer* than the octahedron-forming distances, which is the opposite to what is observed in perfect BCC packing (Figure 3.27).

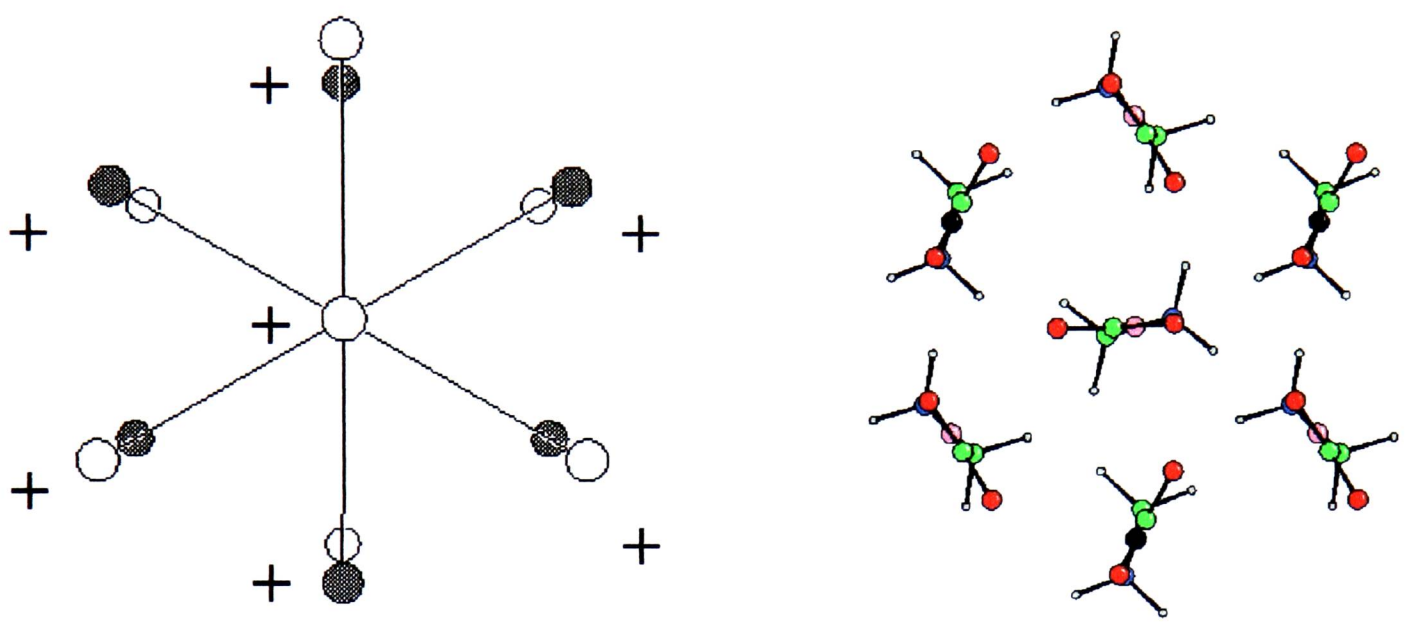

Figure 3.28. Distorted body centred cubic packing in γ-glycine, viewed along the [0 0 1] direction, along the direction of the hydrogen bonded chains. The diagram on the left shows the molecular centroids of the molecules on the right. The shaded circles indicate the centroids separated from the central molecule by 4.42 - 4.46 Å; the open circles represent the centroids separated by 5.43 - 5.48 Å. The + symbols show the sense of the chain direction. In γ-glycine all the chains have the same sense: the carboxyl groups all point in the same direction.

The coordination sequences of α and β glycine are also 14-50-110, and both of these polymorphs are also based on BCC topology. These are more distorted (Figure 3.29), however, and neglect of long contacts yields coordination sequences of 13-27-104 (α) and 12-44-96 (β), respectively, the latter being characteristic of hexagonal closest packing. (Long contacts are defined by Blatov as those which correspond to VDP faces which subtend solid angles of less than 0.01*4π steradian. In this study this corresponds to centroid-centroid contacts of more than 6 Å).

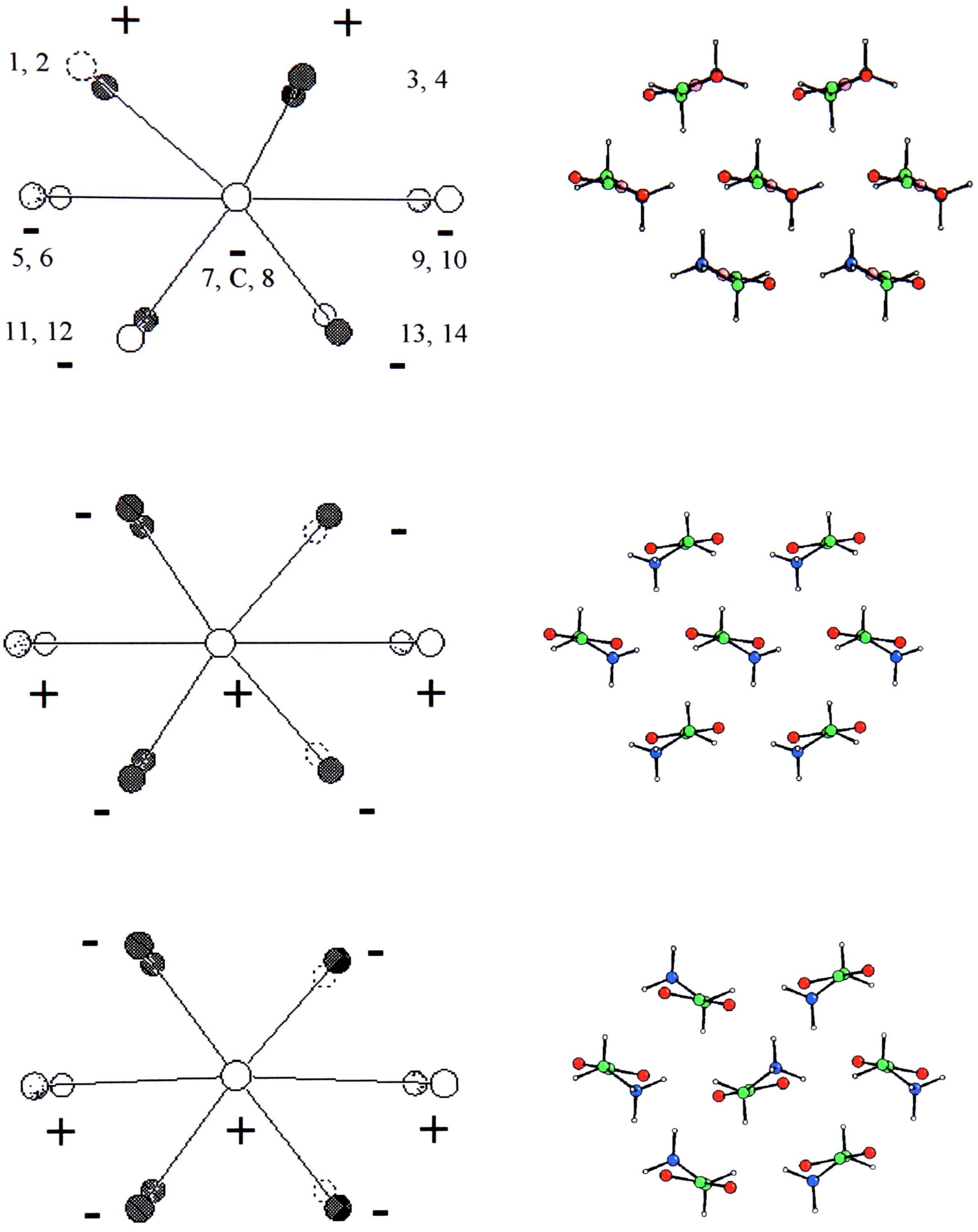

Figure 3.29. Distorted body centred cubic packing in α (top), β (middle) and δ-glycine (bottom). The circles represent the molecular centroids viewed along the [0 0 1] direction; the molecules thus represented are shown on the right. The hydrogen bonded layers are horizontal with respect to the page. The + and - signs represent the sense of the chains in terms of the direction of the carboxyl group (see Figure 3.26). The centroid separations are given in Table 3.14. The same numbering scheme as shown for α-glycine applies to the three polymorphs.

	Separation / Å				Separation / Å		
Molecule	α	β	δ	Molecule	α	β	δ
1	6.693*	4.484	4.47	8	5.093	5.387	5.342
2	4.531	4.665	4.538	9	5.917	5.751	5.581
3	4.261	4.094	3.669	10	5.463	5.076	4.980
4	3.812	6.336*	6.021*	11	5.398	4.484	4.470
5	5.463	5.076	4.980	12	4.33	4.665	4.538
6	5.917	5.751	5.581	13	4.33	4.094	3.976
7	5.093	5.387	5.342	14	5.398	6.336*	6.213*

Table 3.14. Centroid separation in α, β and δ-glycine. The distortion from body centre cubic packing is clear from the long contacts (*)

The topology of the molecular centroids is illustrated in Figure 3.29, and its close resemblance to the topology of β-glycine is immediately obvious. Application of pressure to β-glycine can be considered to cause a concerted compression of the centroid-centroid distances and loss of polarity in the [010] direction. The latter is expressed in the angle made by the mean plane of the non-H atoms in the glycine molecules with the crystallographic (010) planes; in β-glycine this is 14.3°, and in δ-glycine, ±16.1° at 19 kbar. Since this is only a modest change, the ability of this transition to occur from one single crystal to another is readily understandable. A transition from the γ phase to δ-glycine involves a substantial rearrangement in the relative polarities of neighbouring chains, and this transition has only been observed by powder diffraction.

Boldyreva *et al.* (2003b) observed no transition in γ-glycine by powder diffraction. The temperature of the transition from γ --> α varies depending on the prior treatment of the sample. The liquid used as a pressure medium can have a dramatic effect on the behaviour of a sample at high pressure; $[Co(NH_3)_5NO_2]I_2$ undergoes a phase transition only when a MeOH:EtOH:H_2O mixture is used (Boldyreva, 2003c). Paraffin was used in the experimental work described in this chapter but ethanol/methanol used in the published experiments. A second possibility is that there was in fact a transition - at 40 kbar the authors report the lines due to γ-

glycine "fell down", being restored on returning the sample to ambient pressure with a significant change in the preferred orientation of the γ component. This mirrors the results of the powder experiments carried out in this work. Finally, the use of a mixed phase sample complicates the analysis, especially as γ-glycine was the minor component of the mixture.

3.6 Conclusions

A new polymorph of glycine has been identified, formed by the reversible transformation of β-glycine on the application of pressure via a single crystal - single crystal phase transition between ambient pressure and 8 kbar. Powdered γ-glycine was found to undergo a partial phase transition at 29 kbar, which gave a powder pattern consistent with the new δ polymorph.

Analysis of the hydrogen bonding in the crystal structure of the new polymorph indicates that the structure is similar to the previously characterised α and β polymorphs of glycine, having a layered structure with comparable hydrogen bonding to these phases. Topological analysis shows that the transition from β→δ can be explained by distortion towards a more body centred cubic packing arrangement. It is possible that α-glycine will undergo a transition at higher pressures than have so far been reached.

3.7 References

Albrecht, G., Corey, R.B. (1939). *J. Amer. Chem.Soc.*, **61**, 1087-1103

Allen, F.H. & Kennard, O. (1993). *Chem Design Autom. News*, **8**, 31-37

Allen, K., Davey, R.J., Ferrari, E., Towler, C., Jones, M.O., Pritchard, R.G., *Cryst. Growth. Des.*, **2**, 523 – 527

Blatov, V.A., Peresypkina, E.V. (2000). *Acta Cryst.*, **B56**, 510 -511

Boldyreva, E.V., Drebushchak, T.N., Shutova, E.S. (2003a). *Z. Kristallogr.* **218**, 366 - 376

Boldyreva, E.V., Ahsbahs, H., Weber, H.P. (2003b). *Z. Kristallogr.* **218**, 231 - 236

Boldyreva, E.V., Drebushchak, T.N., Shutova, E.S. (2002). *Acta Cryst.* **E58**, o634 – o636

Boldyreva, E.V. (2003c). *J. Mole. Struct.*, **647**, 159 - 179

Bruker-AXS (2003). SAINT version 7.01A, Bruker-AXS, Madison, Wisconsin. USA.

Bruker-AXS (2000). TOPAS version 2.0, Bruker-AXS, Madison, Wisconsin. USA

Clarke, S.J. Private communication

David, W.I.F. (2003). Private communication

Etter, M.C., MacDonald, J.C., Bernstein, J. (1990). *Acta Cryst.* **B46**, 256 262

Ferrari, E.S,. Davey, R.J., Cross, W.I., Gillon, A.L., Towler, C.S. (2003). *Cryst. Growth. Des.*, **3**, 53-60

Gidalevitz, D., Feidenhansl, R., Matlis, S., Smilgies, D-M., Christensen, M.J., Leiserowitz, L. (1997. *Angew. Chem. Int. Ed. Engl.*, **36**, 955-959

Itaka, Y. (1960) *Acta Cryst.* **13**, 35 – 45

Itaka, Y. (1961) *Acta Cryst.* **14**, 1 - 10

Jarvinen M. (1993). *J. Appl. Cryst.*, **26**, 525 - 531

Jeffrey, G.A. (1997). *An Introduction to Hydrogen Bonding.* New York, Oxfor University Press

Jőnsson, P.G., Kvick, A. (1972). *Acta Cryst.* **B28**, 1827 - 1833

Kvick, A., Canning, W.M., Koetzle, T.F., Williams, G.J.B. (1980). *Acta Cryst.* **B36**, 115 - 120

Kuan, Y-J., Charnley, S.B., Huang , H-C., Tseng ,W-L., Kisiel, Z. (2003). *Astrophys. J.*, **593**, 848 - 867

Langan, P., Mason, S.A., Myles, D., Schoenborn, B.P. (2002). *Acta Cryst.* **B58**, 728-733

McGregor, P.A. (2000). unpublished results

Marsh, R.E. (1959). *Acta Cryst.* **11**, 654 - 663

Nelmes, R.J., McMahon, M.I. (1994). *J. Synch. Rad.* **1**, 69 - 73

Nelmes, R.J,. Loveday, J … (2003). Private communication

Park, K., Evans, J.M.B., Myerson, A.S. (2003). *Cryst. Growth. Des,* **3**, 991 - 995

Parsons, S. (2003) , SHADE: Program for elimination of obscured reflections from high pressure data sets, The University of Edinburgh

Pawley, G.S. (1981). *J. Appl. Cryst.*, **14**, 357 - 361

Perlovich, G.L., Hansen, L.K., Bauer-Brandl, A. (2001). *J. Therm. Anal. Cal.*, **66**, 699 – 715

Piltz, R.O., McMahon, M.I., Crain, J., Hatton, P.D., Melmes, R., Cernik, R.J., Bushnell-wye, G. (1992). *Rev. Sci. Instrum.*, **63**, 700 - 703

Sakai, H., Hosogai, H., Kawakita, T. (1992). *J. Cryst. Growth*, **116**, 421 - 426

Sheldrick, G.M. (1997) SHELXS97, University of Göttingen, Germany

Sheldrick, G.M. (2002) SADABS, version 2.04, University of Göttingen, Germany

Shimon. L.J.W., Lahav, M., Leiserowitz, L. (1986). *New J. Chem.* **10**. 723 - 737

Sparks, R.A. (2000). GEMINI version 1.05, Bruker-AXS, Madison, Wisconsin. USA.

Spek, A.L. (1990). *Acta Cryst.* **A46**, C34

Watkin, D. J., Prout, C. K., Carruthers, J. R., Betteridge, P. W. & Cooper R. I. (2003) CRYSTALS. Issue 12. Chemical Crystallography Laboratory, University of Oxford, England.

Young, R.A. (1993). *The Rietveld Method*, IUCr Monographs on Crystallography Volume 5, edited by R.A. Young, pp 1- 38, Oxford University Press

Zaccaro, J., Matic, J., Myerson, A.S., Garetz, B.A. (2001). *Cryst. Growth. Des.*, **1**, 5-8

Chapter 4

Anisotropic compression of l-alanine

4.1 Introduction

4.1.1 The l-alanine molecule

L-alanine (Figure 4.1) is the simplest of the chiral amino acids, having only a methyl group attached to the α-carbon atom. It is a non-essential amino acid - it can be synthesised by the body rather than being required in the diet. Alanine was first discovered in 1850, as the unexpected product of a chemical reaction rather than from protein hydrolysis. It was later isolated from the hydrolysis of egg albumen (Vickery & Schmidt, 1931). L-alanine is predominately produced by chemical methods, as production by fermentation is hampered by racemisation - the d-form of alanine is used by bacteria to build cell walls. The l-form is in the *S*-configuration. Alanine is a very common residue in proteins, and is a strong α-helix former (Goliaei & Minuchehr, 2003). Uses for alanine include dosimeters for high energy γ-radiation, where free radicals are produced from alanine by the radiation which are then detected using electron paramagnetic resonance spectroscopy (Yordanov & Gancheva, 1999). It can also be used as a flavour enhancer in food (Yamamoto, 1980).

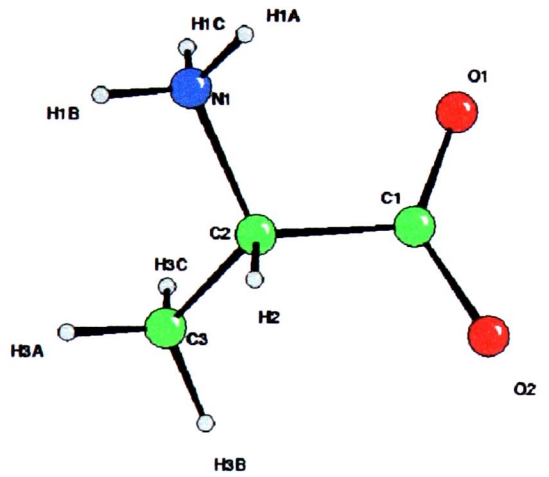

Figure 4.1. The l-alanine molecule

4.1.2 Crystal structure of l-alanine at ambient pressure

There is only one known crystalline phase of alanine, which is orthorhombic with space group $P2_12_12_1$. In the solid state l-alanine exists in the zwitterionic form, as do many other amino acids. The crystal structure of l-alanine was first investigated by Bernal (1931). The full structure by X-ray diffraction was reported by Simpson and Marsh (1966) and Dunitz (1966), and by neutron diffraction by Lehmann, Koetzle and

Hamilton (1972). The structure at 23 K was determined by Destro, Marsh and Bianchi (1988) using single crystal X-ray diffraction.

In common with other amino acids, the structure of l-alanine in the solid state is dominated by hydrogen bonding. Each molecule is hydrogen bonded to six other molecules via three unique N-H...O interactions, with the ammonium group making three hydrogen bonds to the carboxyl groups of three separate molecules. One oxygen of the carboxyl group makes two hydrogen bonds, with the other only making one such contact at ambient pressure. The carbon – oxygen bond lengths in the carboxyl group differ by 0.019(1) Å at 23 K; this has been ascribed to the difference in hydrogen bonding environment of the two atoms. There are two *anti* hydrogen bonds and one in the *syn* configuration (Figure 4.2). The hydrogen bond lengths are summarised in Table 4.1, and the hydrogen bonds formed by one carboxyl group are shown in Figure 4.2.

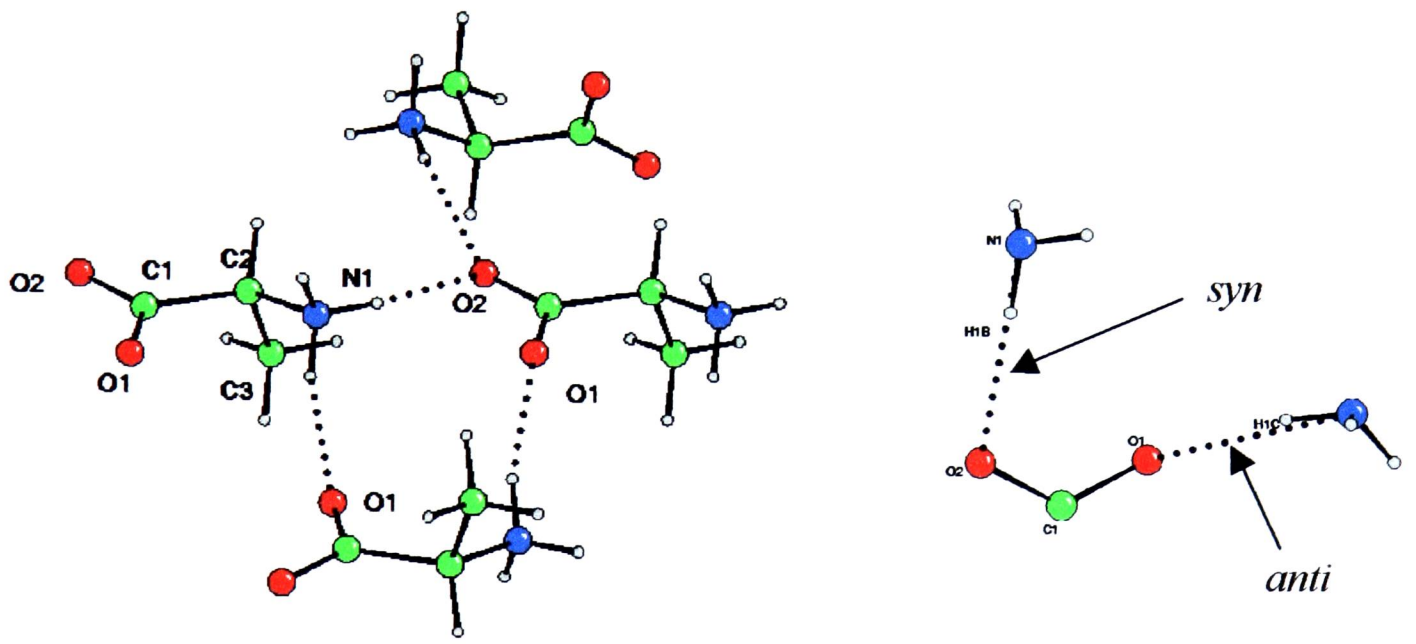

Figure 4.2. The hydrogen bonding environment of one molecule shown for the carboxyl group. The schematic to the right illustrates the *syn* and *anti* configurations for a hydrogen bond to a carboxyl group.

The *syn* N(1)-H(1B)...O(2) hydrogen bond in Table 4.1 links the molecules into chains parallel to the *a* axis (Figure 4.3). A similar chain structure is seen in the four polymorphs of glycine (Chapter 3); the hydrogen bond in the glycine structures is formed from the nitrogen to the oxygen *cis* to the nitrogen atom on the adjacent molecule.

Interaction	Neutron (298 K)	X-ray (23 K)
N-H(1C)...O(1) angle	160.9(2)°	161.0(8)°
N...O(1)	2.853(1) Å	2.835(1) Å
N-H(1A)...O(2) angle	163.7(2)°	161.2(7)°
N...O(2)	2.832(2) Å	2.814(1) Å
N-H(1B)...O(2) angle	168.1(2)°	169.5(7)°
N...O(2)	2.813(1) Å	2.792(1) Å

Table 4.1. The hydrogen bond interactions in l-alanine (from Marsh *et al.*, 1988). Typical values for these interactions are discussed in more detail in Section 4.4.1.

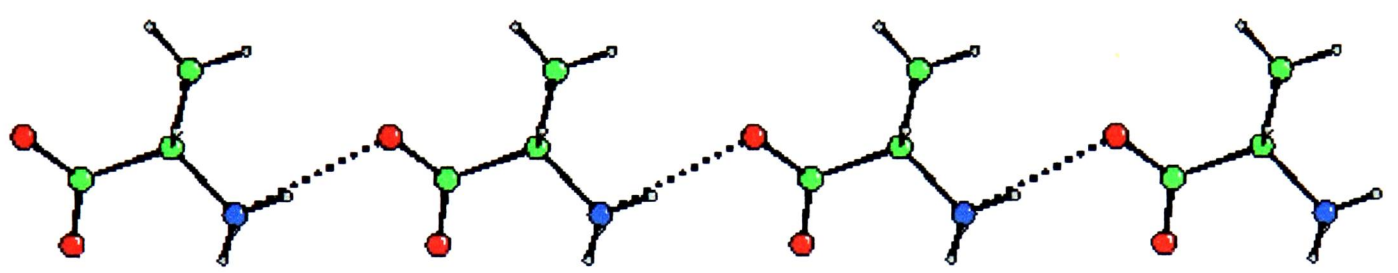

Figure 4.3. Hydrogen bonded chains within the structure of l-alanine

The two *anti* hydrogen bonds link these chains to give a three dimensional hydrogen bonded network. The N(1)-H(1C)...O(1) hydrogen bond links two chains, forming $R_3^3(11)$ rings (Figure 4.4a), while the N(1)-H(1A)...O(2) interaction links chains through $R_4^3(14)$ units (Figure 4.4b).

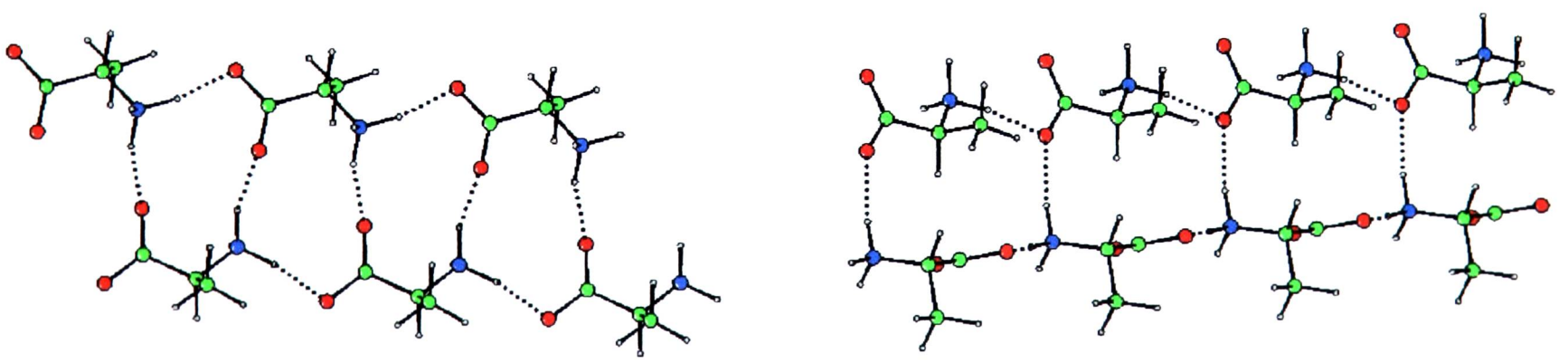

Figure 4.4. The hydrogen bonded chains in l-alanine are linked by $R_3^3(11)$ (left) and $R_4^3(14)$ (right) interactions

Each chain is hydrogen-bonded to two other chains using both of these motifs, giving rise to the overall structure which can be described as consisting of channels running parallel to the *a*-axis. The methyl groups point into the centre of these channels, as shown in Figure 4.5. The crystal structure is very similar to that of the orthorhombic polymorph of l-cysteine (Kerr & Ashmore, 1973).

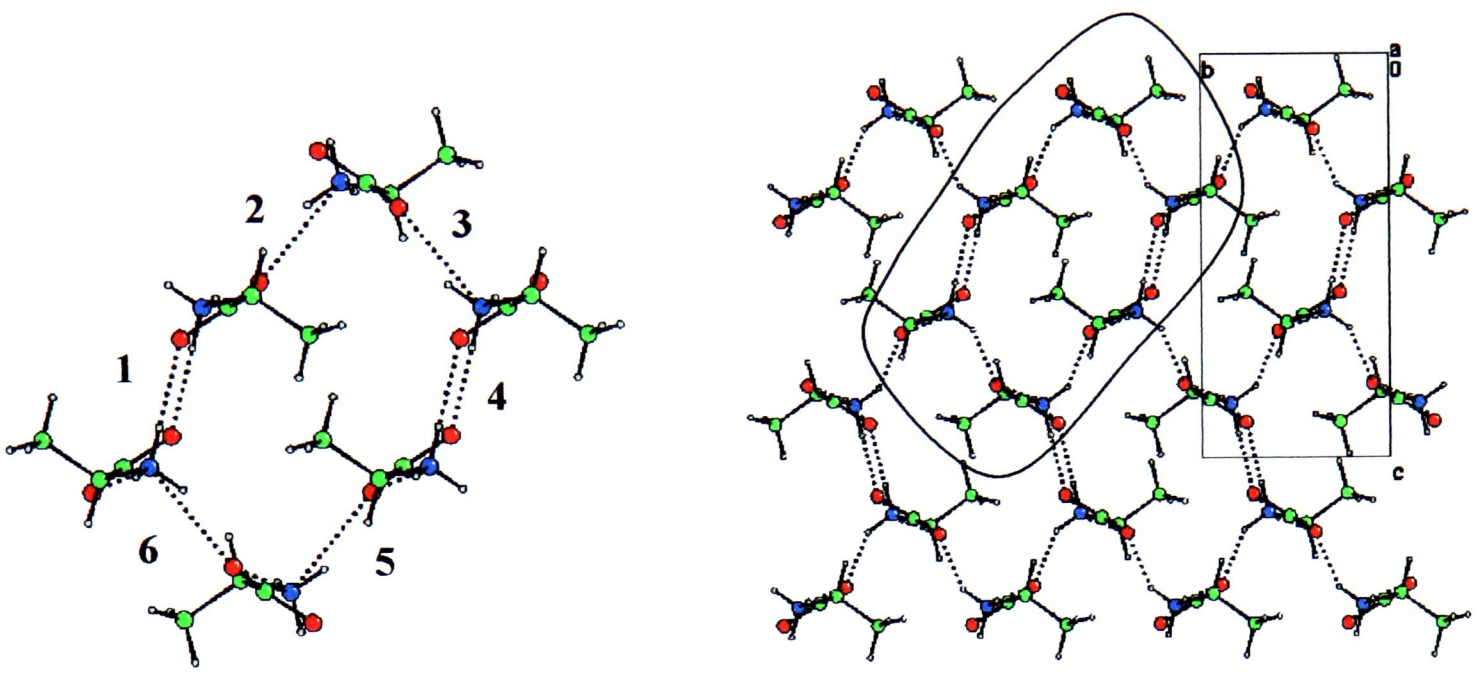

Figure 4.5. Channel formation in the crystal structure of l-alanine. The structure is viewed along the *a* unit cell axis.
Left: One channel formed by the interaction of six chains (the structure is viewed along the chains). The numbers indicate the six interactions; interactions **1** and **4** are through $R_3^3(11)$ groups. Interactions **2,3,5** and **6** are $R_4^3(14)$.
Right: The complete crystal structure. The ringed area represents one channel.

There is a fourth tentative hydrogen bonding contact in the structure of l-alanine. From the crystal structure it is clear that the N(1)-H(1B)...O(2) hydrogen bond is in the *syn* configuration. The neutron study (Lehmann *et al.*, 1972) shows that the hydrogen atom is asymmetrically positioned between the two carboxylate oxygen atoms. The O(1)...N-H(1B)...O(2) interaction could be described as a three centre or bifurcated hydrogen bond (Jeffrey & Mitra, 1984). This type of structural arrangement is quite common in amino acid structures. However, the number of structures with this arrangement in which there is a significant interaction between the second oxygen atom and the hydrogen is small (Gorbitz & Etter, 1992).

Parameter	Value (neutron)
φ_1	168.1(2)°
φ_2	69°
r_1	1.780(2) Å
r_2	2.532 Å

Table 4.2. Parameters for the "bifurcated" hydrogen bond in l-alanine

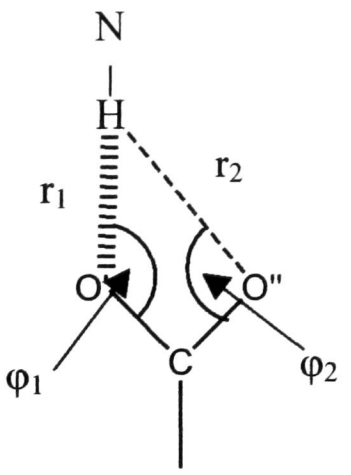

Figure 4. 6. Schematic of the configuration of a bifurcated hydrogen bond

In both the neutron determination and the 23 K X-ray structure the relevant hydrogen atom points almost directly at O(2), with an N-H...O angle of 168.1°. The N-H...O(1) angle is correspondingly large at 130°. Gorbitz and Etter conclude that the key parameter in classifying this kind of interaction as three centre or two centre is the C-O''...H angle (φ_2 in Figure 4.6 above), with the lower limit being 90°. At ~70° in l-alanine, the O...H-N angle is too small for this interaction to be classed as a three centre hydrogen bond. In addition, the N-H(1C)...O(2) hydrogen bond is also the most linear of the three – a secondary interaction with O(1) would be expected to reduce the linearity of the primary interaction (Gorbitz & Etter, 1992).

The electron density distribution of the lone pairs on the oxygen atoms obtained at 23 K (Destro *et al.*, 1988) confirms that the N-H(1C)...O(2) hydrogen bond is the strongest in the structure. From the N...O separation listed in Table 4.1 this is the shortest hydrogen bond in the structure. The lone pair distribution of O(2) is polarized into this hydrogen bond, unlike the two *anti* hydrogen bonds. There is no interaction of H(1C) with O(1). The 23 K multipole analysis also suggests that there is slightly more negative charge on O(2) than O(1), indicating that O(2) is a better hydrogen bond acceptor than O(1).

4.1.3 Effect of temperature on the crystal structure of l-alanine

The structure of l-alanine at low temperature (23 K) was investigated by Destro, Marsh and Bianchi (1988) using single crystal X-ray diffraction. No phase transition was observed on cooling to this temperature, even after repeated temperature cycling. As expected, *b* and *c* contracted with decreasing temperature, however *a* was observed to increase slightly (Table 4.3).

Temperature / K	*a* / Å	*b* / Å	*c* / Å
293	5.784(1)	6.032(1)	12.343(1)
23	5.794(1)	5.928(1)	12.260(2)

Table 4.3. The effect of temperature on unit cell parameters.
Note: In this study the cell dimensions are quoted in the standard setting for orthorhombic $P2_12_12_1$, not in the setting used by the original authors

At this low temperature there is a uniform contraction of the hydrogen bonds of 0.019(1)Å (Table 4.1). However, as shown by the lengthening of the *a* axis , there has been some slight rearrangement of the molecules in addition to the reduction of thermal motion. The structural changes are very slight and are reflected in the changes to the hydrogen bond lengths (Table 4.1). The thermal motion of the atoms is least in the direction of the *a* axis.

4.1.4 High pressure studies on l-alanine

The high pressure behaviour of l-alanine has been investigated using Raman spectroscopy by Teixeira *et al.* (2000). From the change in intensities of the lattice modes the authors concluded there was a phase change at about 23 kbar, although they offered no conclusions as to the changes in the structure giving rise to this phase change. There were two main regions of interest in the spectra. Firstly, there are changes in the intensities of very low frequency bands (in the 40 cm^{-1} region), and the authors suggest that these changes could be due to changes in the molecular configuration. There is also a change in the spectrum at ~120 cm^{-1}, where a new band is observed at pressures above 23 kbar. The band due to torsion of the NH_3^+ group was too weak to allow changes in the hydrogen bonds to be analysed.

4.2 Experimental

4.2.1 Single crystal studies

Crystals of l-alanine (Aldrich, used as received) were grown by evaporation from a saturated aqueous solution. The crystals obtained in this way were of good quality, but were too large for use in the diamond anvil cell and so were cut before use. A suitable crystal was loaded into a diamond anvil cell, equipped with 600 μm diamonds, a gasket with a 300 μm hole and a chip of ruby for pressure measurement. A 4:1 mixture of methanol: ethanol was used to ensure a hydrostatic pressure environment. Due to impurities in the mixture used, the pressure medium crystallised at about 60 kbar. A new crystal was then loaded, using a freshly prepared sample of methanol : ethanol. Attempts to increase the pressure above 70 kbar were unsuccessful.

All data were collected using a Bruker SMART Apex using Mo-K_α radiation, using the procedures detailed in Chapter 2. The first data collection was performed on the sample loaded in the cell at ambient pressure, with no pressure medium added. Only half of the full data collection was collected, as the aim of this first collection was to establish the starting phase of the sample. The first three datasets were collected using thirty second exposures, with the rest being collected using fifty second exposures.

Each dataset was indexed using Gemini (Sparks, 2000) and integrated using Saint (Bruker - AXS, 1993), with dynamic masks enabled. Data were integrated to 0.9Å resolution. Corrections for the pressure cell and absorption were made using Absorb5.3 (Angel, 2003) and Sortav (Blessing, 1995), as detailed in Chapter 2. All data were merged using Sortav (Blessing, 1997). Since the anomalous scattering for l-alanine is too small to be measurable using Mo radiation, the data were merged in *mmm* rather than *222*. The cell dimensions at each pressure are summarised in Table 4.5.

4.2.2 Structure refinement

The co-ordinates from the low temperature (23 K) determination (Destro *et al.*, 1988) were used as a starting point for refinement. Each structure was refined

against $|F|^2$ using Shelxl (Sheldrick, 1997). Anisotropic refinement was not carried out, as the data to parameter ratio was unacceptably low (3:1 with anisotropic refinement in place of 7:1 with isotropic thermal parameters). Distance restraints based on the ambient pressure structure refinements were applied – without these restraints bond lengths refined to unreasonable values. Although the low temperature structure shows a slight variation in the C-O bond lengths, these were restrained to be the same at high pressure as unrestrained the bond lengths measurements are not sufficiently precise. Details of the refinements are summarised in Table 4.5.

4.3 Results

4.3.1 Changes in the unit cell dimensions of l-alanine with pressure

The cell dimensions determined for each pressure measurement are listed in Table 4.5, and summarised graphically in Figure 4.7. Compared to the effects of low temperature, even relatively modest pressure has a significant effect on the structure, with a 3.2% reduction in unit cell volume at 4.8 kbar. At the maximum pressure reached of 72 kbar, the total reduction in cell volume was 20%.

From the cell dimensions alone, it is obvious that the main contraction is perpendicular to the network of channels in the structure (Figure 4.5 above). The *a* lattice direction contracts by only a small amount over the entire pressure range studied with an overall reduction of 0.248(3) Å at 72 kbar, or 4.3%. The reduction in *a* is relatively uniform as the pressure is increased, in contrast to the behaviour of *b* and *c*. As the unit cell is orthorhombic, the principal axes of the strain tensor must lie along the unit cell axes.

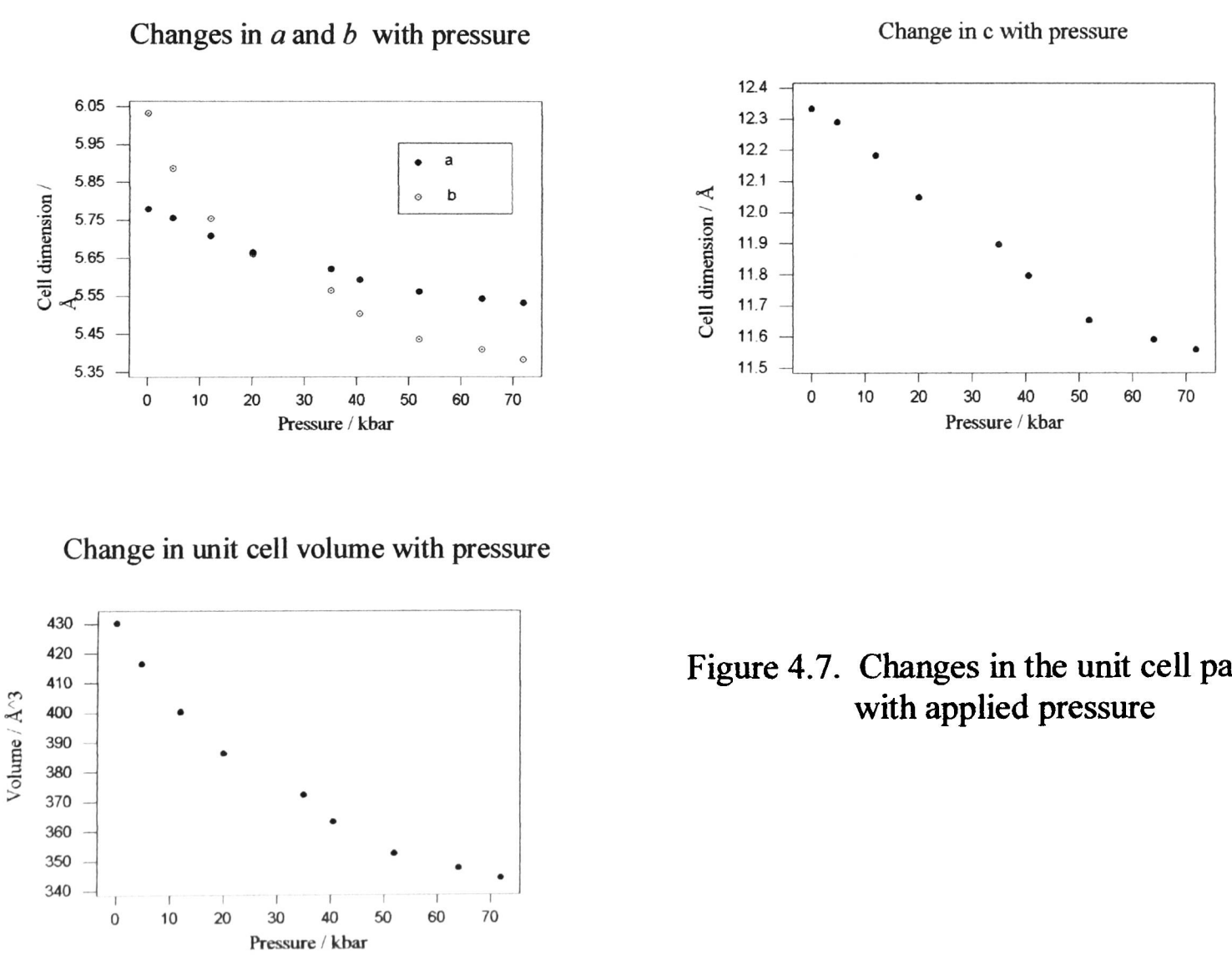

Figure 4.7. Changes in the unit cell parameters with applied pressure

Crystal Data				
Crystal system	Orthorhombic			
Space group	$P2_12_12_1$			
a / Å	5.7796(19)	5.7560(7)	5.7092(9)	5.665(3)
b / Å	6.0323(19)	5.8871(16)	5.7555(18)	5.6604(19)
c / Å	12.333(3)	12.289(3)	12.183(3)	12.047(3)
V / Å^3	430.0(2)	416.42(16)	400.32(16)	386.3(3)
Z	4	4	4	4
ρ_{calc} / Mg m^{-3}	1.376	1.421	1.478	1.532
Number of reflections for cell (θ range, °)	112 (3.3 < θ < 18.9)	200 (3.3 < θ < 23.1)	232 (3.4 < 20.7)	130 (3.4 < 15.7)
Crystal description, size [mm]	Colourless block, 0.2 x 0.2 x 0.1			
Pressure [kbar]	ambient	4.8	12	20
Data Collection				
Reflections collected	591	1130	912	1167
Independent reflections	166	199	159	209
R_{int}	0.1427	0.1441	0.2014	0.115
h	-4 to 4	-6 to 6	-5 to 5	-6 to 6
k	-4 to 4	-4 to 4	-3 to 3	-4 to 4
l	-12 to 12	-12 to 12	-12 to 12	-13 to 13
Solution and Refinement				
Solution (Program)	Known (CSD refcode LALNIN03)			
Hydrogen atom placement	Geometric			
H refinement	Riding			
R [F_o>4σ(F_o)]	0.0809 (124)	0.0721 (152)	0.0846 (123)	0.0614 (151)
wR_2	0.1583 (166)	0.1549 (199)	0.1575 (159)	0.1585 (190)
Goodness of fit on F^2	1.094	1.105	1.190	1.147
Restraints	5	5	5	5
Parameters	25	25	25	25
Maximum Δ/σ	0.000	0.000	0.000	0.000
Weighting scheme x,y*	0, 2.0	0.0533, 0.4042	0.061, 0.227	0.0828, 0.00
Largest difference map residuals [e Å^{-3}]	+0.22, -0.172	+0.233, -0.202	+0.248, -0.213	+0.211, -0.201

* where $w = 1/ [\sigma^2(F_o^2) + xP^2 + yP$, $P=(F_o^2 + 2F_c^2)/3$

Table 4.5. Crystal data and refinement details for l-alanine.

Crystal Data				
Crystal system	Orthorhombic			
Space group	$P2_12_12_1$			
a / Å	5.6217(6)	5.5941(9)	5.5620(11)	5.5429(13)
b / Å	5.5645(12)	5.5039(19)	5.437(2)	5.410(3)
c / Å	11.897(2)	11.795(3)	11.652(4)	11.590(4)
V / Å^3	372.16(11)	363.16(17)	352.3(2	347.5(2)
Z	4	4	4	4
ρ_{calc} [Mg m^{-3}]	1.590	1.630	1.680	1.703
Number of reflections for cell (θ range, °)	260 (3.4 < θ < 18.9)	237 (3.5 < θ < 16)	227 (3.5 < θ < 16.2)	130 (3.5 < θ < 15.3)
Crystal description, size [mm]	Colourless block, 0.2 x. 0.2 x. 0.1			
Pressure [kbar]	35	40.5	52	64
Data Collection				
Reflections collected	1068	1027	1005	996
Independent reflections	189	178	175	175
R_{int}	0.1148	0.1095	0.1647	0.2606
h	-6 to 6	-6 to 6	-6 to 6	-6 to 6
k	-4 to 4	-4 to 4	-4 to 4	-4 to 4
l	-12 to 12	-12 to 12	-12 to 12	-12 to 12
Solution and Refinement				
Solution (Program)	Known (CSD refcode LALNIN03)			
Hydrogen atom placement	Geometric			
H refinement	Riding			
R [F_o>4σ(F_o)]	0.0604 (149)	0.0691 (156)	0.0602 (143)	0.1013 (117)
wR_2 (all data)	0.1339 (189)	0.1377 (178)	0.1251 (174)	0.2111 (175)
Goodness of fit on F^2	1.081	1.166	1.078	1.161
Restraints	5	5	5	5
Parameters	25	25	25	25
Maximum Δ/σ	0.000	0.000	0.000	0.000
Weighting scheme x, y*	0.0703, 0	0.0692, 0	0.0525, 0	0.074, 0
Largest difference map residuals [e Å^{-3}]	+0.253, -0.241	+0.223, -0.195	+0.22, -0.25	+0.252, -0.331

* where $w = 1/ [\sigma^2(F_o^2) + xP^2 + yP$, $P=(F_o^2 + 2F_c^2)/3$

Table 4.5. Crystal data and refinement details (cont.)

Initially as pressure is applied, *b* contracts more rapidly than the *c* lattice direction. Once the applied pressure exceeds 40 kbar the situation reverses, with *c* contracting by a larger amount than *b*. The rate of reduction in both the *b* and *c* lattice parameters decreases as the pressure exceeds 50 kbar. At the highest pressure reached the contraction in *b* is 0.649(4) Å, which is 10.8% of the ambient pressure value. The change in *c* is slightly greater at 0.775(6) Å, although as a fraction of the initial value this is a smaller contraction than *b* at 6.3%.

At about 20 kbar *b* has contracted sufficiently that it is smaller than *a*. This is the approximate pressure at which the Raman study (Teixara *et al.*, 2000) appeared to show a phase transition. It is also above this pressure that the *c* unit cell axis starts to decrease more rapidly.

4.3.2 Effect of pressure on torsion angle of l-alanine

Although the modest pressures in this study are not sufficient to cause any major changes in the intramolecular bond lengths and primary angles there is the possibility of change in the torsion angle between the carboxyl and ammonium groups. The O(1)-C(1)-C(2)-N(1) torsion angle at each pressure is listed in Table 4.6.

Pressure / kbar	Torsion / °
0	-17.7 (17)
4.8	-20.9(15)
12	-16.2(14)
20	-14.3(12)
35	-15.1(13)
40.5	-15.1(13)
52	-14.7 (13)
64	-13(2)
72	-14.7 (10)

Table 4.6. Change in the O(1)-C(1)-C(2)-N(1) torsion angle with pressure

4.4 Discussion

The effect of pressure on the structure of l-alanine was studied up to 72 kbar. Single crystal experiments become more difficult relative to powder experiments with increasing pressure due to the mechanical properties of the gasket material. In order for the pressure to increase, the gasket must extrude into the hole to reduce the volume; the fluid is more compressible than the sample and as the pressure increased the hole will become more deformed in shape. In powder experiments the sample occupies a much larger volume of the gasket hole so the compression of the fluid is less important. In this case the gasket became very badly deformed and cracks formed around the hole above 70 kbar in repeated attempts.

Although no phase transition was observed up to 72 kbar, the structure has changed significantly with the application of pressure. Figure 4.8 below shows the structure viewed down the *c* axis at ambient and 52 kbar. Looking at the circled area, for example, there has been a large shift in the positions of the l-alanine molecules.

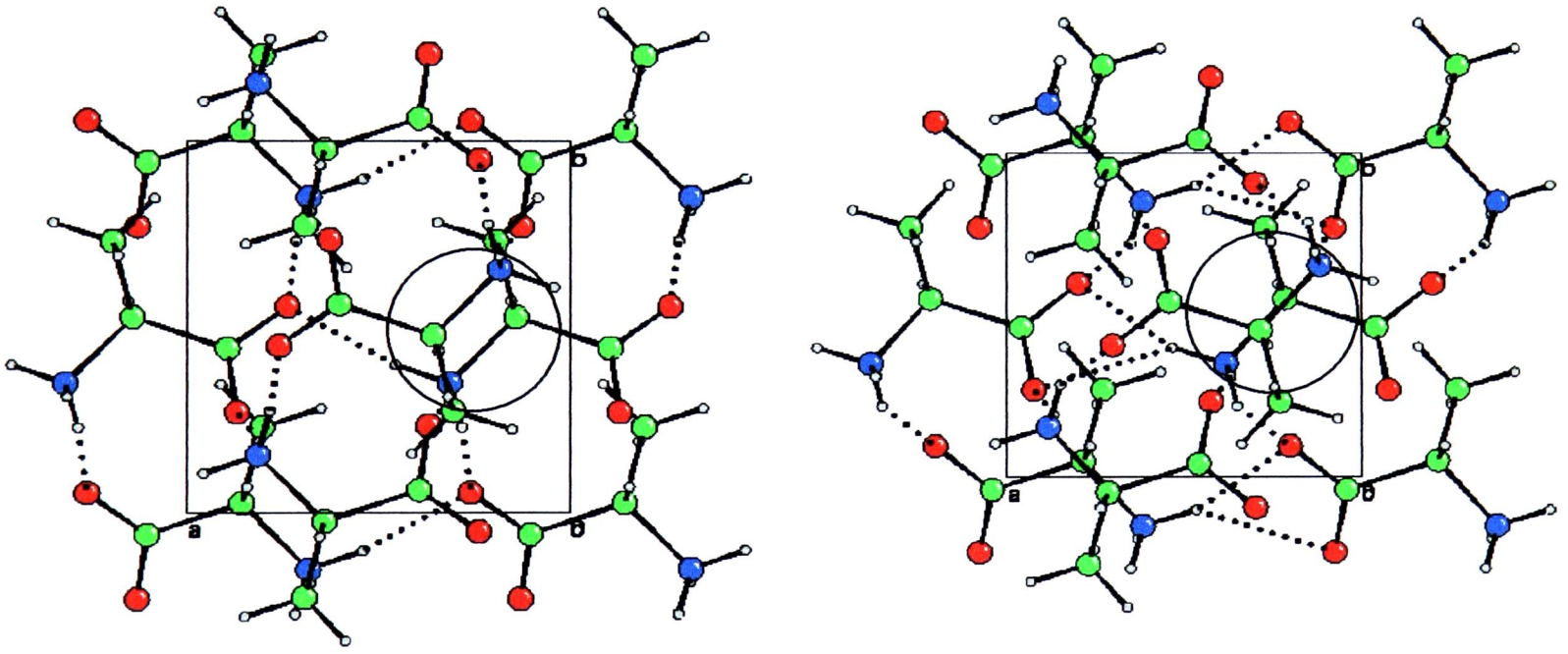

Figure 4.8. Structure of l-alanine viewed down the *c* axis at ambient pressure (left) and 52 kbar (right). The circled areas indicate an area of significant change in the crystal structure with increasing pressure.

In order to make clearer the effects of pressure on the crystal structure of l-alanine, various structural aspects will be considered. The hydrogen bonds, the chains, both types of interactions between two chains and finally the overall structure will be discussed. Changes up to 52 kbar will be discussed; the same crystal was used

for measurements to this pressure. The refinement at 64 kbar was poor due to the deterioration of the crystal due to poor pressure hydrostaticity. As the effects of pressure will vary slightly from sample to sample the crystal at 72 kbar will not be included in the following discussion.

4.4.1 Changes in hydrogen bond lengths with increasing pressure

Given the relatively poor data completeness it is often impossible to locate the hydrogen atoms from high pressure data collected on a laboratory source. Instead in this case the effects on hydrogen bonding are quantified by the changes in the N...O separation. The effects of pressure on the hydrogen bonds are summarised in Table 4.7.

Pressure (kbar)	N...O / Å		
	N(1)-H(1C)...O(1)	N(1)-H(1A)...O(2)	N(1)-H(1B)...O(2)
0	2.877(13)	2.820(15)	2.795(15)
4.8	2.843(11)	2.794(12)	2.800(11)
12	2.811(13)	2.776(15)	2.764(15)
20	2.780(9)	2.753(10)	2.760(9)
35	2.744(9)	2.743(10)	2.749(9
40.5	2.725(9)	2.720(10)	2.737(9)
52	2.703(8)	2.707(9)	2.734(8)
64	2.680(16)	2.699(18)	2.731(16)
72	2.684(7)	2.687(8)	2.727(8)

Table 4.7. Changes in the lengths of hydrogen bonds with pressure

N(1)-H(1B)...O(2)

This interaction links molecules into chains along the channels in the structure, parallel to the *a* axis. At 52 kbar the reduction in *a* is 0.219(19) Å, however the reduction in this hydrogen bond is only just statistically significant at 0.061(17) Å. Shrinkage in this direction has not come from compression of this hydrogen bond, but rather from some other rearrangement of the molecules, which has left the length of this hydrogen bond unchanged. This is discussed in more detail in Section 4.4.2.

N(1)-H(1C)...O(1) and N(1)-H(1A)...O(2)

As described in Section 4.1.2, these hydrogen bonds link the chains in the structure into a three dimensional hydrogen bonded network. These bonds are perpendicular to the [1 0 0] direction. These two hydrogen bonds have significantly compressed, by 0.174(15) Å and 0.113(17) Å respectively at 52 kbar – however, as in the N-H...O(2) hydrogen bond, the overall compression in the *b* and *c* direction far exceeds this change.

In order to put the values for the compression of the hydrogen bonds in context, a search of the Cambridge Structural Database (Allen & Kennard, 1993) was performed. The values for the N...O distance for $CNH_3^+...O_2C$ containing structures were measured, and are shown in Figure 4.9.a. There were 1076 structures giving a total of 4614 N...O contacts between 2.6Å and 3.8Å. Reducing the search further to only $O_2CH(C/H)N$ acceptors gave 339 structures with 1527 contacts between 2.6 and 3.8Å (Figure 4.9b).

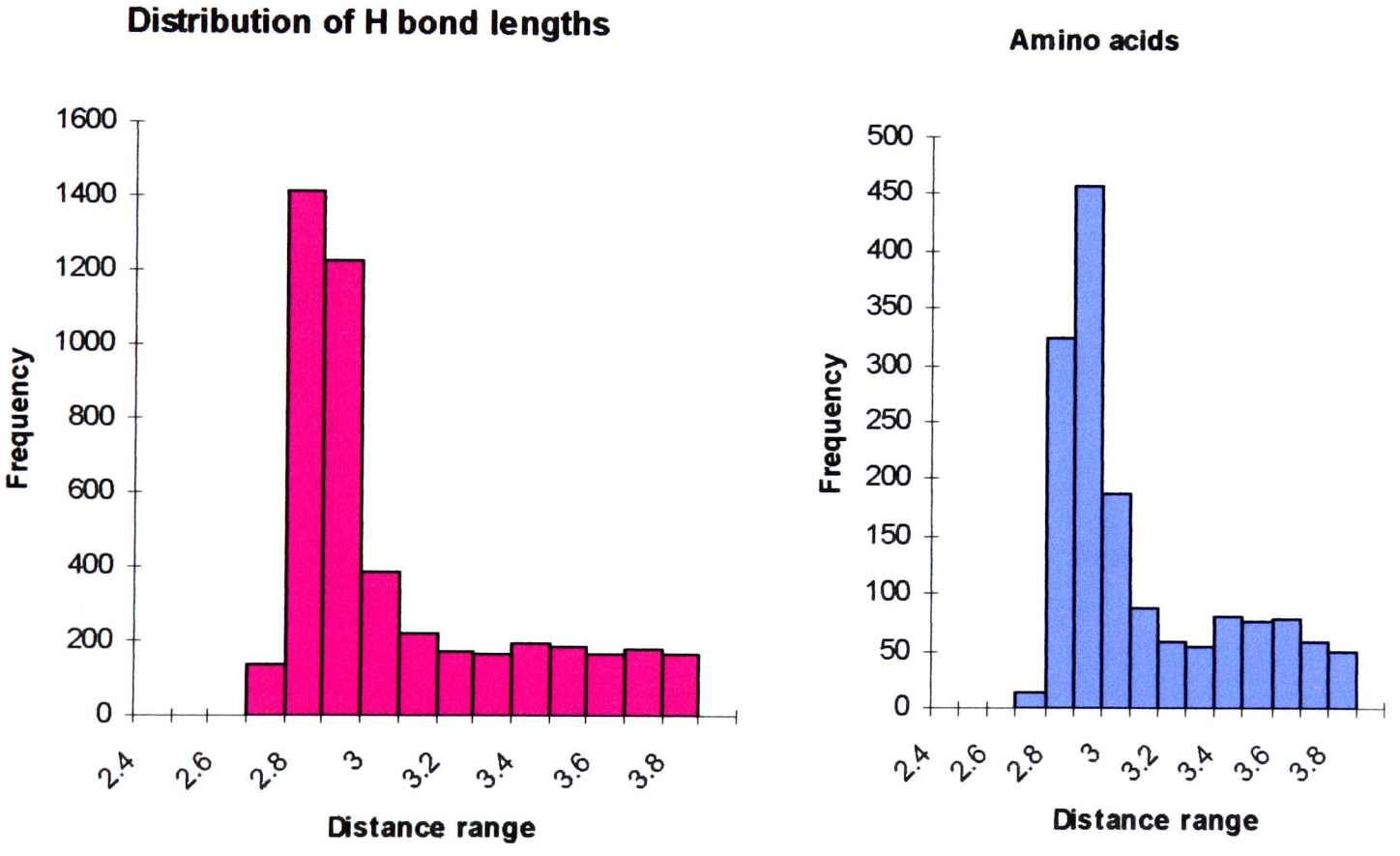

Figure 4.9. Hydrogen bond lengths in the CSD.
a. Left - all $CNH_3^+...O_2C$ fragments b. Right- $CNH_3^+...O_2CH(C/H)N$ fragments

For all $CNH_3^+...O_2C$ hydrogen bonds there are 142 entries in the database with an N...O distance in the range 2.4 - 2.7Å, of which only four are less than 2.6Å.

For those fragments with an amino acid acceptor there are 13 entries with N...O separations in the range 2.6 - 2.7Å with none shorter than 2.63Å. The hydrogen bonds in l-alanine at ambient pressure are in the range 2.795 - 2.877 Å; these values are towards the lower end of the range for hydrogen bonds. At 52 kbar the hydrogen bonds lengths have reached the lower limit for these interactions.

4.4.2 Changes in the hydrogen bonded chains

The length of the N(1)-H(1B)...O(2) hydrogen bond decreases from 2.795(15) Å at ambient pressure to 2.734(8) Å at 52 kbar. This small change in the length of the hydrogen bond masks alterations within the chains of molecules linked by this interaction. Figure 4.10 shows two molecules linked via this hydrogen bond. The O(2)...N(1)-C(2) angle decreases with increasing pressure. As the molecules move closer in *a* there is also movement in the *b* direction, shown by the change in the angles made between the oxygen and nitrogen atoms. Table 4.8 shows the values of some of the intermolecular separations illustrated in Figure 4.10 at 52 kbar and ambient pressure.

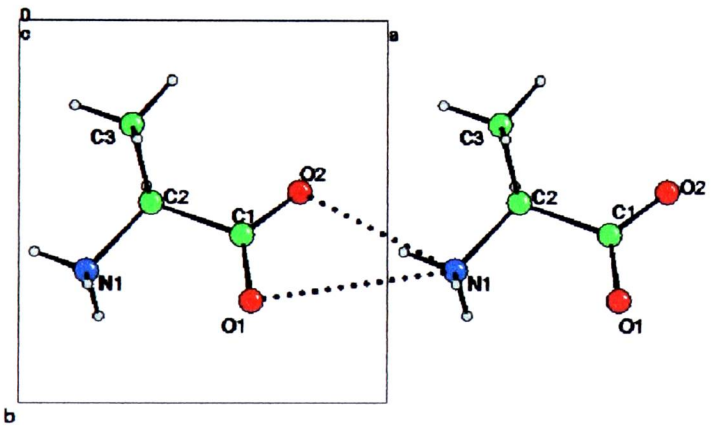

Figure 4.10. N...O interactions within one hydrogen bonded chain viewed perpendicular to the *c* axis

Pressure	N1...O1 / Å	N1...C1 / Å	C1-O2...N1 angle / °	C1-O1...N1 angle / °
ambient	2.795(15)	3.394(14)	107.9(8)	83.2(8)
52 kbar	2.734(8)	3.261(8)	103.7(6)	86.9(4)

Table 4.8. Changes in the interactions within one hydrogen-bonded chain

The N(1)...C(1) separation has decreased by more than the O(2)...N(1) hydrogen bond at 52 kbar, demonstrating that the separation of the molecules has decreased by more than the reduction in the hydrogen bond suggests.

The effects of this movement on the chain are illustrated in Figure 4.11. The dotted molecules show the position of three molecules at ambient pressure. Superimposed in full are the positions of the same molecules at 52 kbar (viewed perpendicular to the *c* axis). The chain contraction in *a* and the movement relative to *b* can be clearly seen.

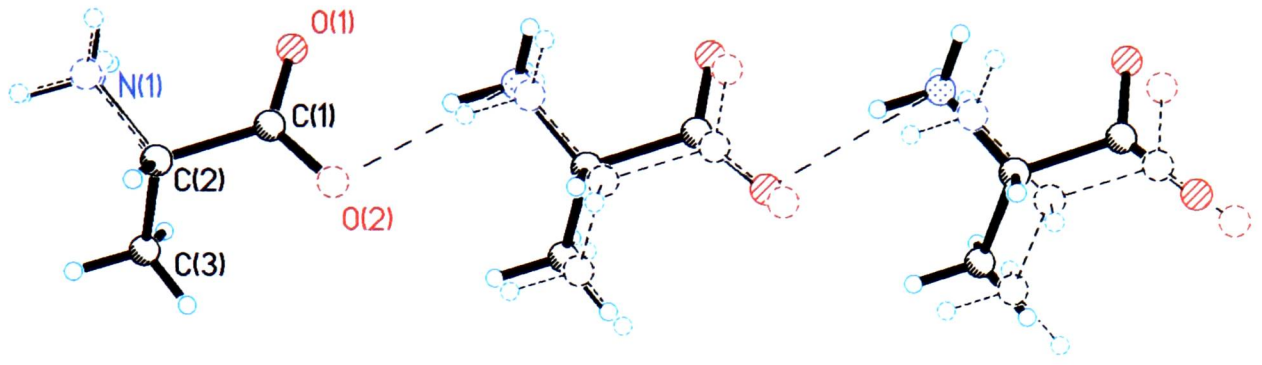

Figure 4.11 Overlay of ambient pressure (dashed lines) and 52 kbar (full) hydrogen bonded chains. The leftmost molecules are exactly overlaid; the shift in position of the rest of the molecules is clear.

This pushing together of the molecules also shortens the contact between O(1) and N(1). As discussed in the introductory section, at ambient pressure this contact is rather too long to be considered as a hydrogen bonding interaction and the O...H-N angle is unfavourable. With increasing pressure, this N...O distance decreases relatively smoothly (Table 4.9 and Figure 4.12).

Pressure / kbar	N(1)-H...O(1) / Å
0	3.306(14)
4.8	3.317(9)
12	3.248(13)
20	3.192(8)
35	3.155(6)
40.5	3.117(7)
52	3.083(7)
64	3.072(13)
72	3.055(7)

Table 4.9 Change in N(1)...O(1) interaction

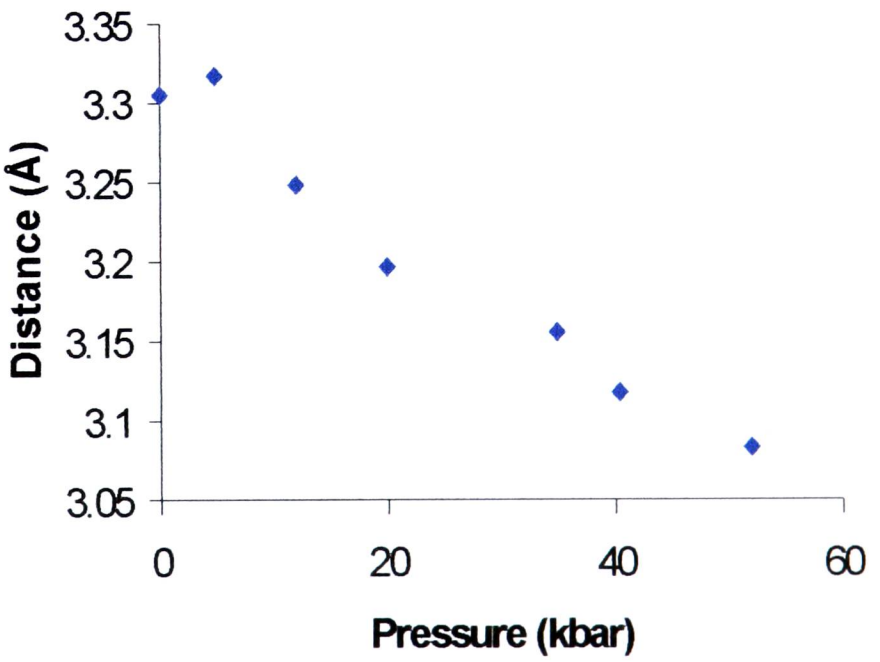

Figure 4.12 Change in N(1)...O(1) interaction

The change in the nitrogen – oxygen separation could result from the nitrogen interaction becoming bifurcated between the two carboxyl oxygen atoms. The displacement of the nitrogen atom with respect to the carboxylate oxygen atoms has become more symmetric. At ambient pressure, the vertical displacement of N(1) along the oxygen – oxygen vector is 0.42 Å from O(2) (**x** in Figure 4.13 below), with the total length of the vector 2.240(12) Å. At 52 kbar this has increased to 0.655 Å, with the total length 2.206(10) Å. The horizontal distance (**y** in Figure 4.13) has decreased by a smaller amount from 2.76 Å to 2.65 Å. This is a consequence of the compression in the structure along the *b* direction.

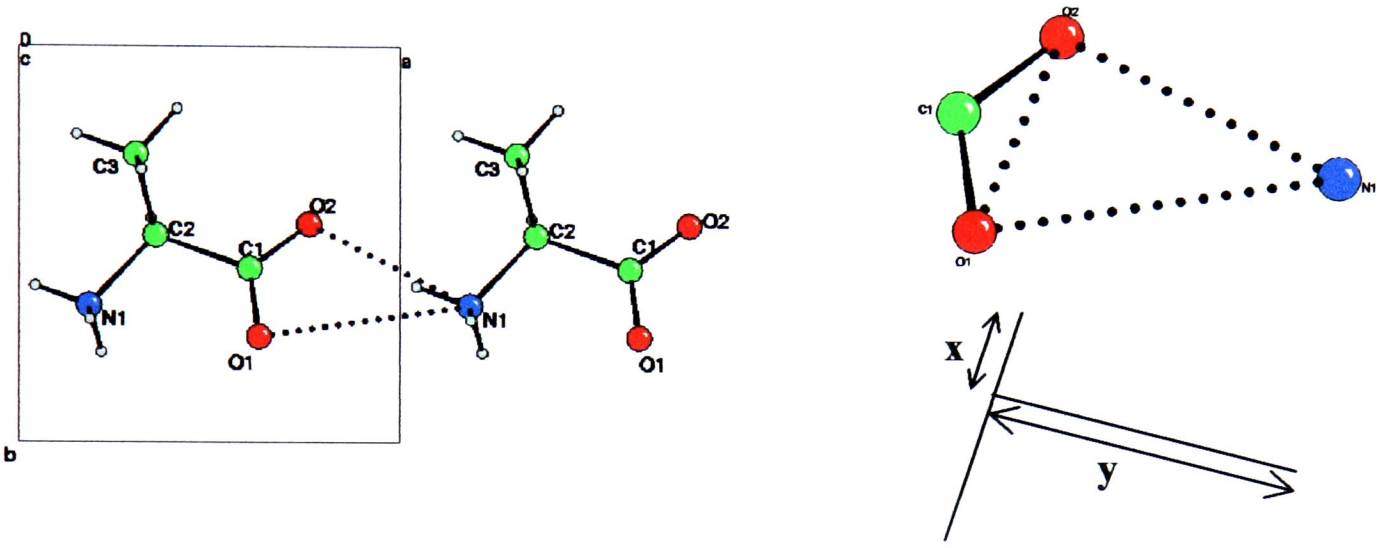

Figure 4.13 Displacement of the nitrogen with respect to carboxylate groups in the "bifurcated" hydrogen bond

It is impossible to tell if the hydrogen atoms have rotated to a more favourable position (this would affect the other hydrogen bonds in the structure), and without detailed hydrogen atom position information, drawing any firm conclusions is difficult. However the C(1)-O(1)...N(1) angle has opened up slightly (Table 4.8) – the angle of interaction to the hydrogen could have become more favourable. Pressure appears to have promoted bifurcation of this hydrogen bond. A similar effect is seen in glycine, where δ-glycine has the most bifurcated example of a *syn* hydrogen bond.

4.4.3 Changes in the interactions between chains

The hydrogen-bonded chains interact via the two *anti* N-H...O hydrogen bonds. N-H(1A)... O(2) links the chains into $R_4^3(14)$ rings, and the N-H(1C)...O(1) bond links chains into $R_3^3(11)$ rings, as shown in Figure 4.5 above. Pressure has affected these interactions in different ways. The effects on the lengths of these interactions have been summarised in Table 4.7 above - the following analysis concentrates on the effects on the relative positions of two chains.

Changes in $R_4^3(14)$ *rings*

The application of pressure has altered the interactions between the chains. This can clearly be seen when the changes in both hydrogen bonds made by O(2) are considered together. The angle made by these interactions at the oxygen atom (N1...O2...N1 in Figure 4.14) has decreased from 109.4(4)° at ambient pressure to 95.62(19)° at 52 kbar, a reduction of 13.8(4)°. To better quantify the separations of the molecules the centroids of the four molecules shown in Figure 4.14 were calculated and their separations determined (Table 4.10 and Figure 4.15).

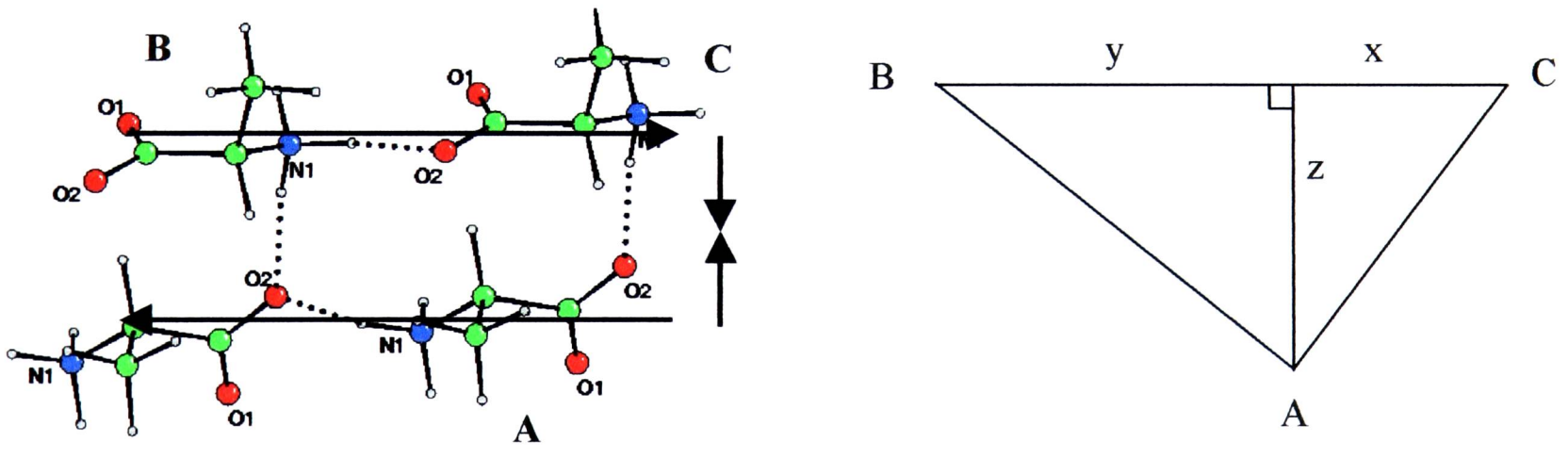

Figure 4.14. a. (left) Interactions of the O(2) atom. The arrows indicate the movement of the chains with increasing pressure.
b. (right) schematic of the molecular centroids. Distance BC is the *a* unit cell length. A, B and C mark the molecular centroids. Changes in the positions of these centroids are given in more detail in Figure 4.15.

Pressure / kbar	N-O-N angle / °	A...B separation / Å	x / Å	x / *a*	y / Å	z / Å
ambient	109.4(4)	5.84	1.76	0.305	4.020	4.236
52	95.62(19)	5.009	2.471	0.444	3.091	3.942

Table 4.10. Interactions in the $R_4^3(14)$ units

It is clear from the values in Table 4.10 that there have been two changes in this chain interaction. The vertical distance between chains, as quantified by ***z*** in Figure 4.14, has reduced by 0.3 Å at 52 kbar. There has also been a considerable alteration in the relative horizontal positions of the chains, measured by parameters ***x*** and ***y***.

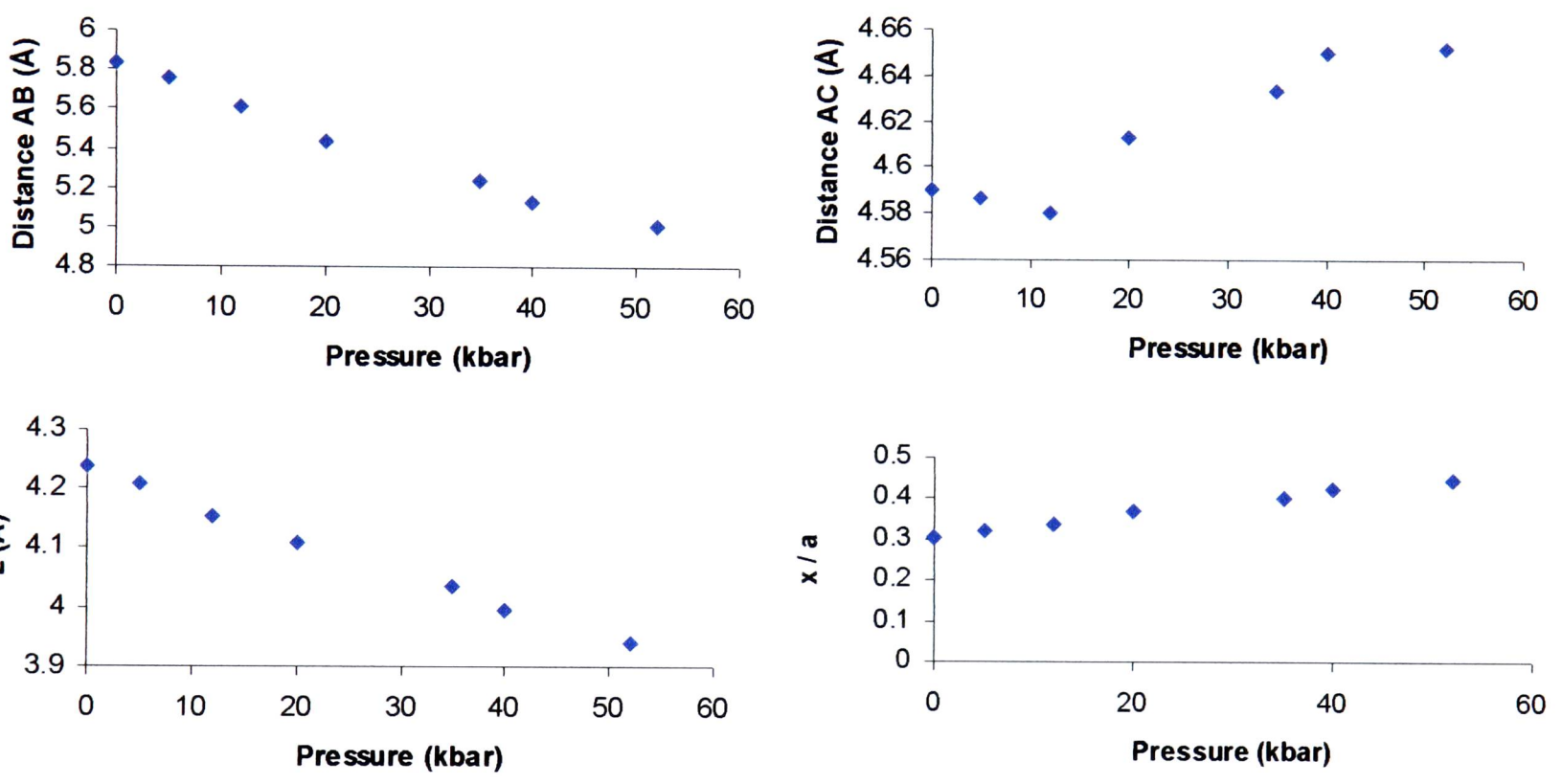

Figure 4.15. Change in separation of centroids with pressure. Distance labels refer to parameters shown in Figure 4.14.
i. Top left. Decrease of centroid separation of molecules A and B with increasing pressure. The overall change in this parameter is 0.8 Å.
ii. Top right. Change of centroid separation of molecules A and C with increasing pressure. The distance between these molecules is almost unchanged.
iii. Bottom left. Variation of perpendicular separation of chains with increasing pressure. The decrease is smaller than the decrease is AB centroid separation.
iv. Bottom right. Change in displacement of molecule A with respect to molecules B and C, as a fraction of the *a* unit cell length.

Within any chain the centroids of adjacent molecules are separated by one unit cell length (*a*). The molecular centroids in the next chain are not evenly spaced between these nitrogen atoms. It is clear from the values in Table 4.10 that at ambient pressure the molecular centroids (A, B and C) are less evenly distributed than at 52 kbar. A is just under a third along the B...C vector at ambient pressure, moving to almost half-way at 52 kbar (parameter x/*a*, Figure 4.15.iv). These parameters vary smoothly with increasing pressure (Figure 4.15 i-iv) - there is no abrupt change indicating a phase transition. There is some variation in the AC distance with pressure, with a minimum occurring at about 10 kbar. This could be related to the "phase transition" observed in the Raman spectrum by Teixeira *et al.*. The overall change in this parameter is small at 0.08 Å.

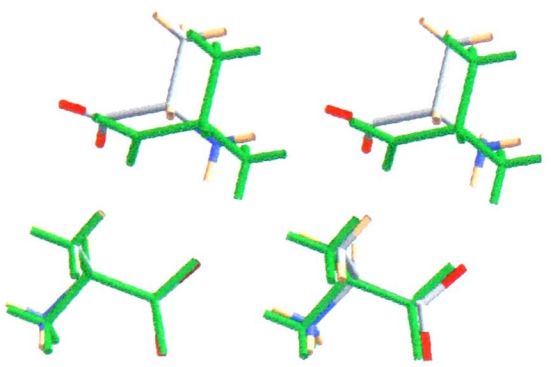

Figure 4.16. (left) The effect of the movement of the chains. The structure at 52 kbar (in green) is overlaid on the ambient pressure structure. The difference in relative positions of the chains is much more marked than the contraction of the individual chains.

This movement of chains causes an important change in the overall structure of l-alanine which will be discussed in more detail in Section 4.4.4.

Changes in $R_3^3(11)$ *rings*

The molecules in the chains forming either side of these rings are related by a 2_1 screw axis in the low temperature structure – the molecules must be evenly distributed. As the space group symmetry has been conserved, the chains cannot slip in the same way as in the $R_3^3(14)$ rings above. There are more hydrogen bonds connecting the chains in this case compared to the $R_3^3(14)$ units, which will impede the movement of the chains.

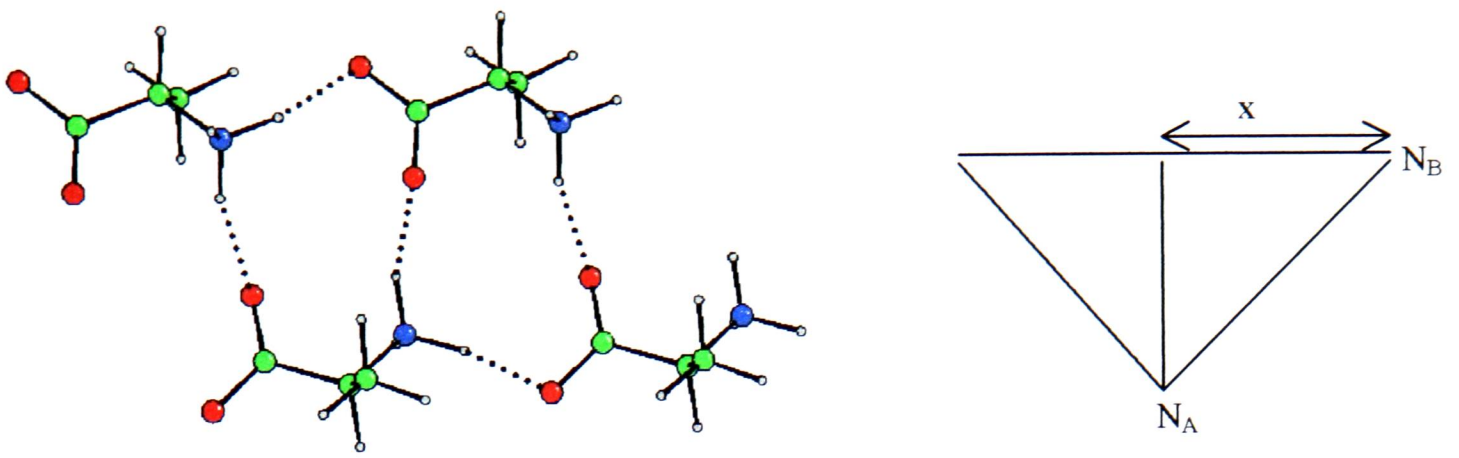

Figure 4.17. Left: Two $R_3^3(11)$ rings in the structure of l-alanine. Right: schematic showing the N…N separation (Table 4.11)

Pressure / kbar	N_A…N_B / Å	C-O-N angle / °	N…midpoint / Å	N…O / Å
0	4.645(16)	137.7(11)	3.639	2.877(13)
52	4.335(9)	135.5(8)	3.455	2.703(8)

Table 4.11. Interactions in $R_3^3(11)$ units

Here the chains are closer together initially than in the $R_4^3(14)$ case. The compression between the chains, measured as in the previous case by the distance between the midpoint of the N…N vector in one chain and a nitrogen atom in the next chain, is comparable at 0.2 Å (0.3 Å in the $R_3^3(14)$ pattern). Information regarding the hydrogen atom position would be very useful here – it is possible that the NH_3^+ group has rotated as the chains have been forced together, to reduce the O…H repulsion. This would also move H(1B) into a better position to make a hydrogen bond to O(1). The N(1)-O(1)-C(1) angle has not significantly reduced.

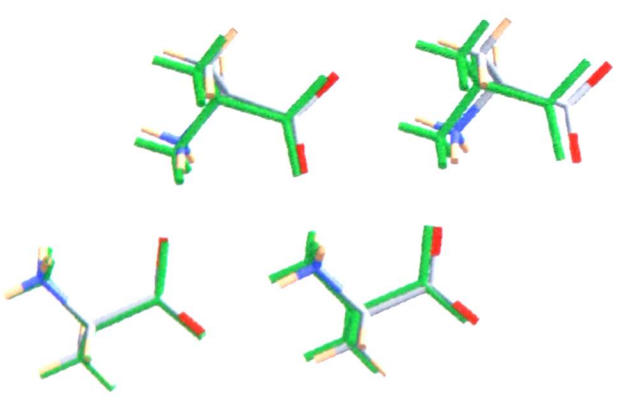

Figure 4.18. Overlay of the structure at ambient pressure and 52 kbar (green)

4.4.4 Overall effect of pressure on l-alanine

Up to this point only the changes in the local environment of a molecule have been discussed. The structure of l-alanine is a three dimensional hydrogen bonded network of crystallographically equivalent molecules - the changes described above must be propagated through the entire crystal structure. There must be co-operative movement of the molecules as the single crystal morphology is conserved to pressures of (at least) 70 kbar.

Quantifying the total effect of application of pressure from the perspective of the hydrogen bonding interactions above is complex. Figure 4.19 below shows the interaction of four chains in the structure (Section 4.4.3). The net movement of the chains must be as shown, from the changes described in Section 4.4.3. The two central chains (linked via $R_3^3(11)$ interactions) are essentially unmoved, while the two outer chains have slipped relative to the central pair.

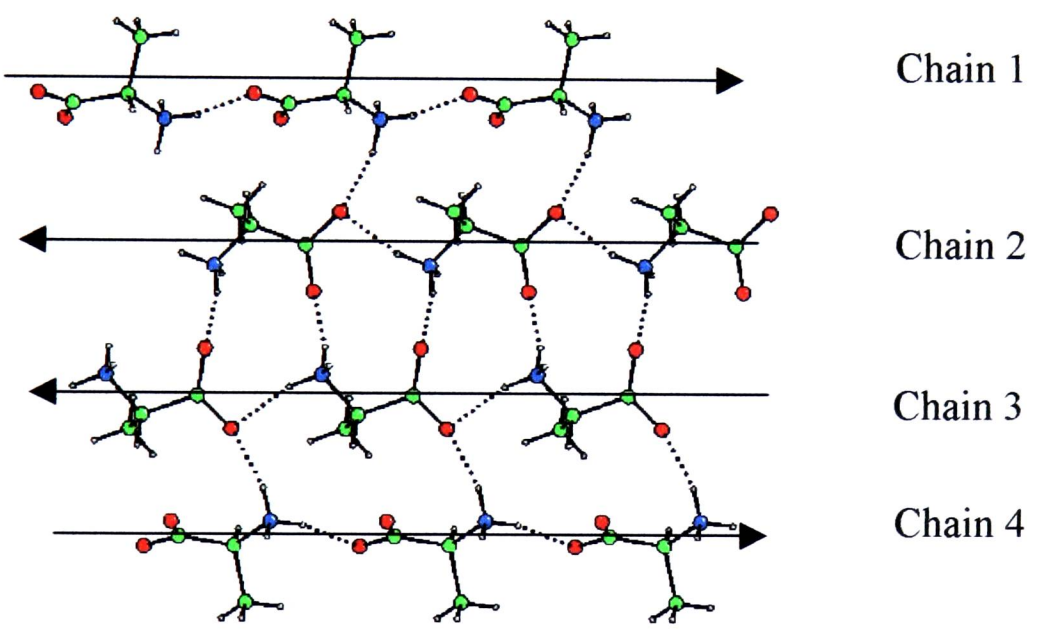

Figure 4.19. Relative displacement of four chains with increasing pressure. The arrows indicate the direction of displacement.

The propagation of the chain movement throughout the structure is complicated by the fact that each chain is hydrogen bonded to three other chains, via both $R_3^3(11)$ and $R_3^3(14)$ interactions. (Chain 2 in Figure 4.19 forms a third hydrogen bond above the plane of the diagram, and so on.) Nevertheless it is possible to identify which groups have moved and which have remained unchanged. This information is summarised in Figure 4.20.

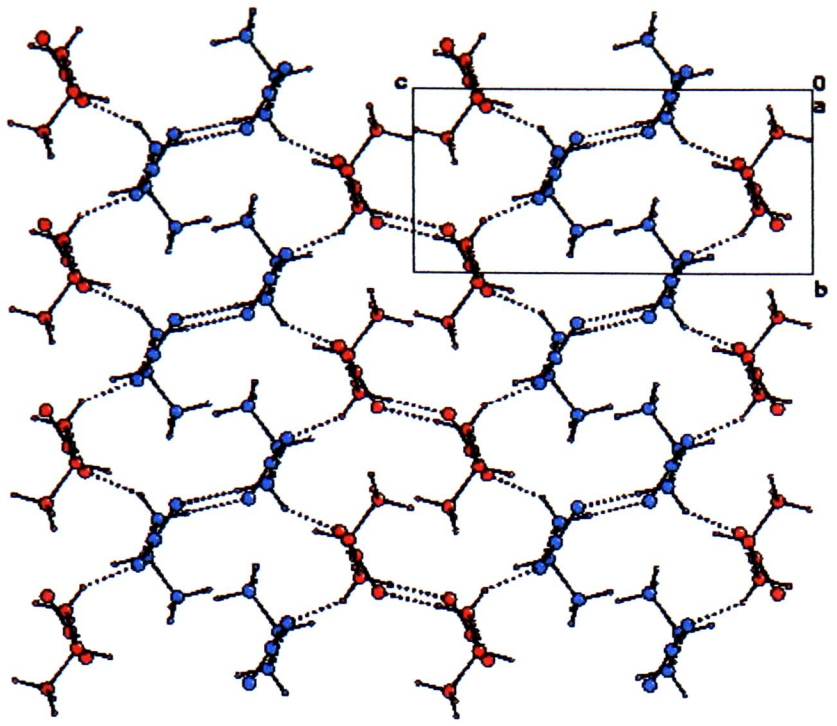

Figure 4.20. Net displacement in the crystal structure of l-alanine viewed along the *a* axis. In blue are molecules that are stationary with respect to chain slippage. In red are molecules that are displaced forwards, out of the plane of the diagram.

4.5 Topological analysis

The complicated hydrogen bonding network in l-alanine makes analysis of the structural changes complex. There are no obviously unfavourable contacts relieved by the chains moving over one another in the way described in Section 4.4.3. Instead a topological analysis of the structure is necessary to understand the changes in l-alanine, analysing the structure in terms of packing of the molecular centroids. Analysis of the topology of l-alanine using TOPOS 3.2 (Blatov *et al.*, 2000) showed that the crystal structure is based on a body centred cubic arrangement of centroids.

The fourteen closest neighbours of one alanine molecule are shown in Figure 4.21, with the distance between the centroids of the molecules listed in Table 4.12.

Molecule	ambient	52 kbar		Molecule	ambient	52 kbar
A	5.780	5.562		H	5.840	5.009
B	6.032	5.437		I	4.590	4.652
C	6.032	5.437		J	4.590	4.652
D	5.780	5.562		K	5.165	4.694
E	6.271	5.847		L	5.350	5.115
F	6.271	5.847		M	5.165	4.694
G	5.840	5.009		N	5.350	5.115

Table 4.12. Separation (Å) of the centroids of a central molecule (C1) and its fourteen nearest neighbours. The molecules involved are shown in Figure 4.21.

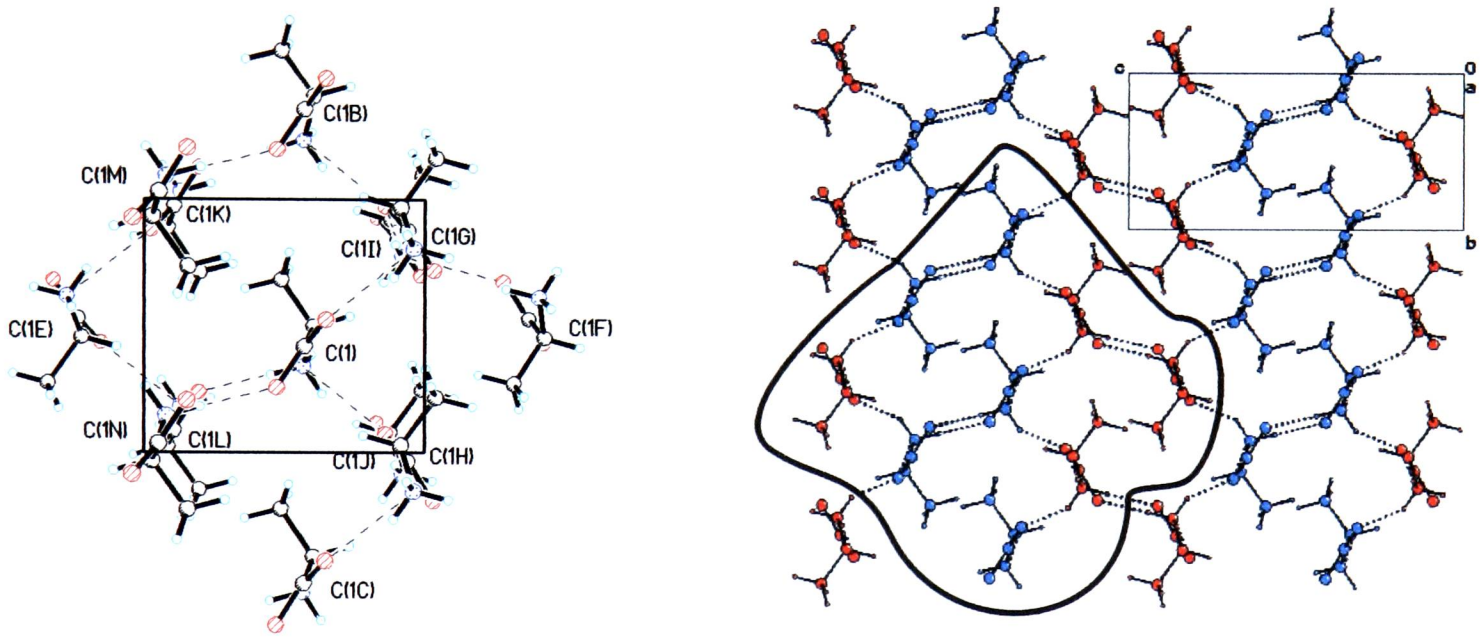

Figure 4.21. Closest contacts in the structure of l-alanine.
Left. Two molecules related to the central molecule by lattice repeat along *a* (immediately above and below the plane of the diagram, around the central molecule, A and D) have been removed for clarity. The lines on the diagram show the approximate body centred cube.
Right. A copy of Figure 4.20 with the ringed area indicating the molecules shown in Figure 4.21. The box in this diagram is the unit cell.

There are two ranges of contacts, corresponding to the pseudo-body centred cubic packing arrangement; molecules G to N are the eight closest, forming the corners of the cube and molecules A to F are the body centres of the adjacent cubes. This division is more obvious at 52 kbar, with the shorter contacts ranging from 4.652 Å to 5.009 Å and the longer contacts 5.437 Å to 5.487 Å. The changes in these two groups will be considered separately.

The six longer contacts do not compress equally. The pair of molecules A and D are related to the centre molecule by unit cell translation along *a* - each of the three molecules occupies a different unit cell. The compression in these contacts is therefore simply the compression in the *a* unit cell length, with the angle made at the central molecule 180°. Similarly B and C are related to the central molecule by translation along *b*, with the compression of this contact the much larger compression in *b*.

The compression of the separation to molecules E and F is different. Here the three molecules are not related by simple unit cell translation - molecules E and F are separated by *c*, related to the central molecule by the screw axis parallel to *c*. The three molecules are therefore not necessarily arranged in a linear fashion. At ambient pressure the angle made at the central molecule is 159°. At 52 kbar the angle increases to 170.4° - the interaction is becoming more linear (Figure 4.22), as would be the case in a truly body centred cubic structure. Figure 4.21 shows that molecules E and F are in part of the structure that has slipped relative to the central molecule. The chain slippage has made the structure closer to a body centred cubic arrangement.

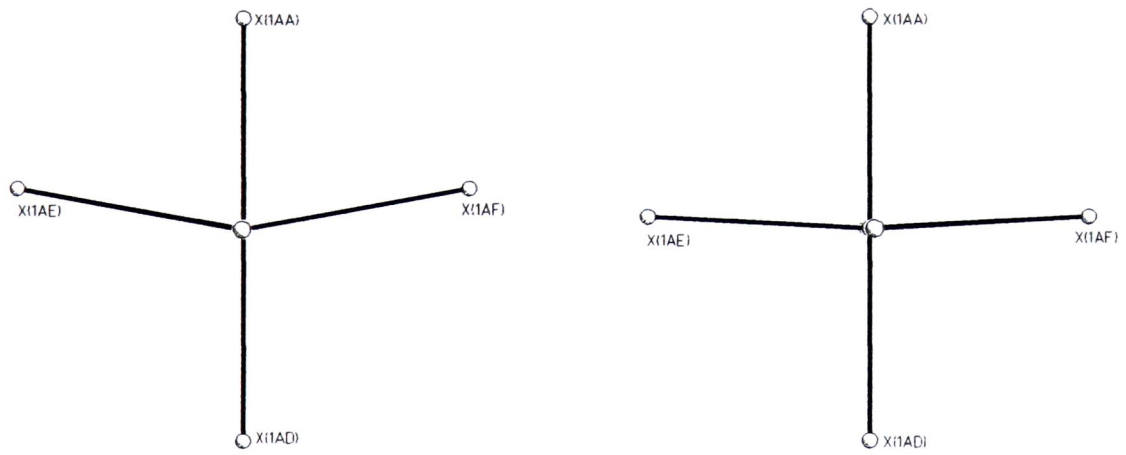

Figure 4.22 Interactions of the centroids of the body centres of the cubes, viewed parallel to the A-D direction. Left - ambient pressure. Right - 52 kbar.

The changes in the shorter interactions are complicated by the symmetry relationships between the molecules. The central molecule must be related by symmetry to each of the eight surrounding molecules, but not by the same symmetry operators. There are four pairs of interactions to the central molecule, formed by the molecule pairs GH, IJ, KM and LN (Figure 4.21 shows the construction of the cube). Molecules L and N are separated by *a*. This pair is related to the central molecule by the screw axis about *a* - the central molecule must be evenly spaced between these

two. The situation is the same with respect to K and M. Molecules G and H separated by *b* and are related to the central molecule by the screw axis about *b*. Again, the central molecule must be symmetrically placed between molecules G and H (and similarly I and J). There are no such constraints on the distribution of the central molecule between other possible "pairs" of molecules, for example molecules N and I (pairs between adjacent corners of the cube). A larger division of the contacts is into two groups of four - molecules G, H, I and J form one face of the cube and are all related by the screw axis about *b* with K, L, M and N forming the second face and related by the screw axis about *a*.

It is clear from Table 4.12 above that the largest change in the central molecule is relative to molecules G and H. The distance for these molecules to the central atom has decreased by 0.83 Å. This is due to the large compression in *b*. However the most interesting change with respect to the topological analysis is to molecules G and I (or equally H and J). The position the arrangement has become more symmetric (Figure 4.23).

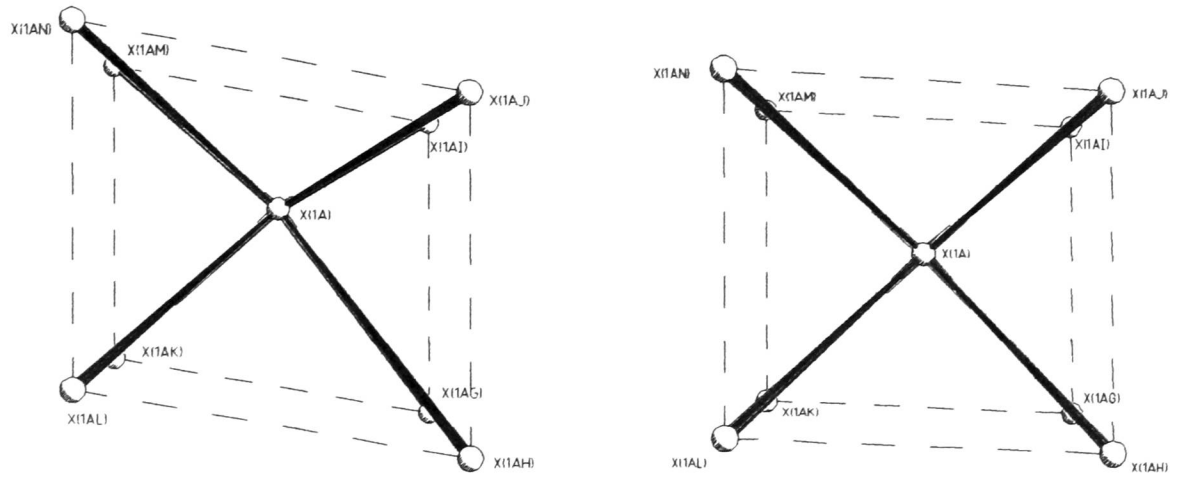

Figure 4.23. The approximate body centred cube in l-alanine. Left - ambient pressure. Right - 52 kbar. The distortion towards bcc packing with increasing pressure is clear.

Molecules I and J have slipped relative to G and H by the movement of the hydrogen bonded chains described in Section 4.3.3. This is a second illustration of how the movement of the chains has made the packing of the structure closer to body centred cubic.

Use of the Continuous Symmetry Measure (Pinsky & Avnir, 1994) allows quantitative analysis of the closeness of the packing to the ideal body centred cubic packing. The CSM of alanine at ambient pressure is 1.00 (where 0 is ideal); at 52

kbar this has reduced to 0.28 (Table 4.13). The lattice Voronoi-Dirichlet Polyhedra for the structure at ambient pressure and 52 kbar illustrate the distortion towards body centred cubic packing very well (Figure 4.24).

Pressure / kbar	CSM
0	1.00
4.7	0.93
12	0.81
20	0.60
35	0.44
40	0.34
52	0.28

Table 4.13. Changes in the Continuous Symmetry Measure of l-alanine as a function of pressure with respect to body centred cubic packing.

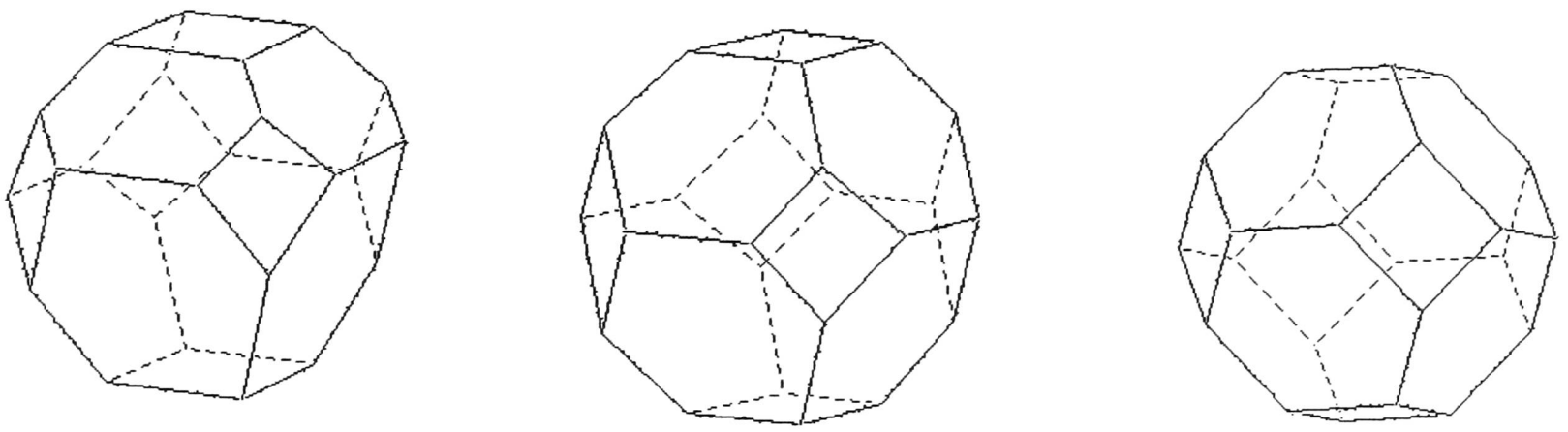

Figure 4.24. Lattice Voronoi-Dirichlet Polyhedra for l-alanine at ambient pressure (left) and 52 kbar (centre), and for perfect body centred cubic packing (right). The distortion towards body centred cubic packing is clear.

4.6 Conclusions

The structure of L-alanine is stable with respect to a phase transition to the effects of externally applied pressure up to at least 70 kbar. The structure does undergo significant distortion as the applied pressure is increased. Of the three hydrogen bonding interactions at ambient pressure, one does not shorten as the pressure is increased although pressure does appear to promote bifurcation of this

hydrogen bond over the second oxygen atom. The remaining two hydrogen bonds shorten to the lower length limit of this type of interaction.

In addition to changes in the lengths of the hydrogen bonds, the angles between them have changed significantly. This has resulted in a large distortion of the structure with increasing pressure, in particular movement of molecules relative to the *a* unit cell direction. From the reduction in pressure of the cell dimensions, it appears that there is least change along *a*; fuller analysis shows that the largest change in the structure is along this direction. Topological analysis shows that the changes in the structure can be explained by the packing of the molecules moving closer to a body centred cubic arrangement at higher pressures.

4.7 References

Allen, F.H. & Kennard, O. (1993). *Chem Design Autom. News*, **8**, 31-37

Angel, R.J. (2003). ABSORB version 5.3. Crystallography Laboratory, Department of Geological Sciences, Virginia Tech., Blacksburg, VA, USA

Bernal, J.D. (1931). *Z. Kristallogr.* **78**, 363

Blatov, V.A., Shevchenko, A.P., Serezhkin, V.N. (2000). *J. Appl. Cryst.*, **33**, 1193

Blessing, R. H. (1995). *Acta Cryst. A***51**, 33-38.

Blessing, R.H. (1997). *J. Appl. Cryst.* **30**, 421-426.

Bruker-AXS (2003). SAINT version 6.41A, Bruker-AXS, Madison, Wisconsin. USA

Destro, R,. Marsh, R.E., Bianchi, R. (1988). *J.Phys. Chem.* **92**, 966-973. CSD refcode LALNIN03

Dunitz, J.D., Ryan, R.R. (1966). *Acta Cryst.* **21**, 617-618

Goliaei, B., Minuchehr, Z. (2003). *FEBS Lett.* **537**, 121-127

Gőrbitz, C.H., Etter, M.C. (1992). *J. Chem. Soc. Perkin Trans. 2*. 131-135

Jeffrey, G.A., Mitra, J. (1984). *J. Am. Chem. Soc.* **106**, 5546-5553

Kerr, K.A., Ashmore, J.P. (1973). *Acta Cryst.* **B29**, 2124 - 2127

Lehmann, M.S, Koetzle, T.F., Hamilton, W.C. (1972). *J. Am. Chem. Soc.* **94**, 2657 - 2660

Pinsky, M., Avnir, D. (1994). *Inorg. Chem.*, **37**, 5575 - 5582

Sheldrick, G.M. (1997). SHELXL97. University of Göttingen, Germany.

Simpson, H.J. & Marsh, R.E. (1966). *Acta Cryst.* **20**, 550 – 555

Sparks, R.A. (2000). GEMINI version 1.05, Bruker-AXS, Madison, Wisconsin. USA

Teixara, A.M.R., Freire, P.T.C., Moreno, A.J.D., Sasaki, J.M., Ayala, A.P., Mendes Filho, J., Melo, F.E.A. (2000). *Solid State Commun.* **116**, 405-409

Vickery, H.B., Schmidt, C.L. (1931). *Chem. Rev.* **9**, 169 - 318

Yamamoto, A. (1980). *Amino acids survey,* Encyclopaedia of Chemical Technology, Vol. 2, edited by M. Grayson, Wiley (3rd edition)

Yordanov, N.D., Gancheva, V. (1999) *J. Radioanalytical and Nuclear Chemistry,* **240**, 215-217

Chapter 5

The effect of pressure on the crystal structures of formamide, N-methyl formamide and N,N-dimethyl formamide

5.1 Introduction

Formamide (Figure 5.1) is the simplest molecule with the CONH moiety of the peptide bond, and as such has been the subject of a number of structural and theoretical studies. Formamide was the first molecule containing four elements to be observed in interstellar space (Eberling, 1980). It has a number of industrial uses, including as a solvent, as a paper fastener and as an intermediate in the synthesis of formic acid. Under ambient conditions of pressure and temperature, formamide is a colourless liquid with a freezing point of 2.55°C.

N-methyl formamide (NMF, Figure 5.1) has also been used as a model of the peptide bond. NMF does not have any major chemical uses and is highly toxic and teratogenic, although it has potential use as an anti-cancer drug (Ramp *et al.*, 1992). It is liquid under ambient conditions, with a freezing point of -3.8°C.

N,N-dimethyl formamide (DMF, Figure 5.1) is used as a solvent in many chemical reactions, being a useful solvent for both inorganic and organic species. It is used industrially as a solvent in many processes, for example in the production of polymers and as a crystallisation medium for pharmaceuticals (Eberling, 1980). DMF has a much lower freezing point than formamide and NMF at -60°C, reflecting the lack of N...O intermolecular hydrogen bonding interactions.

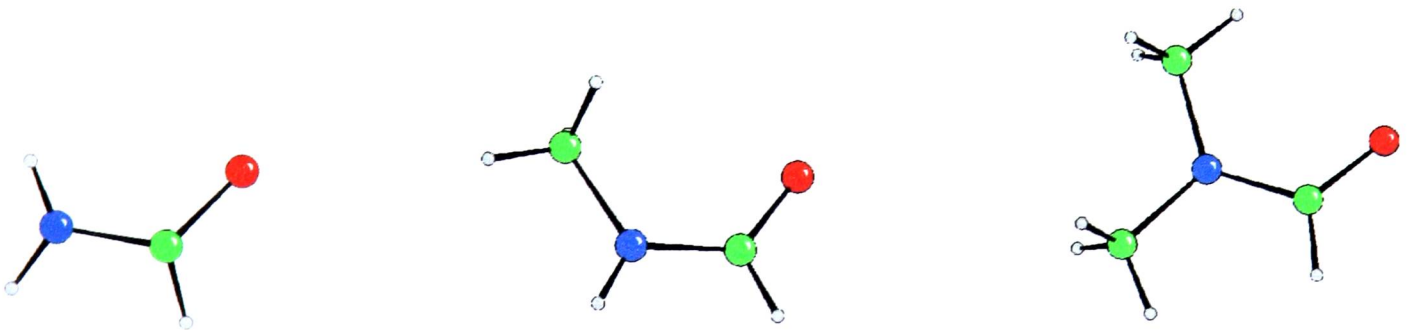

Figure 5.1. Formamide, N-methyl formamide and N,N-dimethyl formamide molecules

Formamide and its N-methylated analogues provide a group of molecules which are chemically closely related but have quite different crystal structures. The group of molecules described in this chapter allow the change in structure type with replacement of one functional group to be studied.

5.1.1 Low temperature crystal structures

Formamide

The crystal structure of formamide at 223 K was first determined by Ladell and Post (1954) using single crystal X-ray diffraction. A low temperature (90 K) electron density distribution study was performed by Stevens (1978). Formamide crystallises in the monoclinic space group $P2_1/n$ when crystallised at low temperature. The structure consists of hydrogen bonded layers parallel to the (1 0 1) plane, with no N-H...O hydrogen bonding interactions between the layers (Figure 5.2). The closest contact between layers is a C-H...O contact of 2.634 Å. The structure is discussed in more detail in Section 5.3.

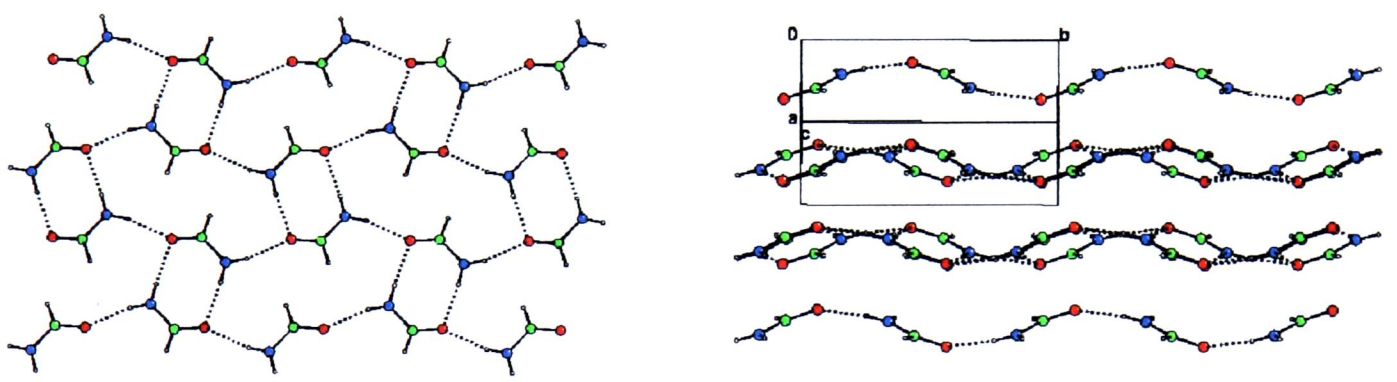

Figure 5.2. Crystal structure of formamide at 90 K. Left: The molecules are linked into layers by N-H...O hydrogen bonds. Right: There are no N-H...O hydrogen bonds linking the layers, which have a sinusoidal topology.

The behaviour of formamide at high pressure up to 100 kbar has been studied using Raman spectroscopy (Shimizu *et al.*, 1988). An apparent phase transition occurred at 50 kbar, identified by a change in the pressure dependence of the intra- and intermolecular vibrational modes. However, although using a single crystal grown at 5 kbar for the Raman measurements, the starting phase was not identified but assumed to be the known phase by extrapolation of the peak positions to ambient pressure. The authors speculate that this transition is due to breaking of some hydrogen bonds within the layers of the structure accompanied by shortening of the interlayer separations, possibly with formation of some interaction between the layers.

The formamide structure has been studied by Raman spectroscopy to 20 K (Torrie & Brown, 1994). The structure was determined at this temperature by neutron powder diffraction, and found to be the same as that determined by Ladell and Post.

The authors do note that there are more bands in the spectrum than expected at 20 K, which could be evidence of a different phase formed at very low temperature, although they conclude these extra bands are second order features associated with the hydrogen bonds.

Liquid formamide has a high dielectric constant (ε = 111) which has been interpreted as evidence of association in the liquid. There have been a number of studies on the structure of liquid formamide, the results of which are inconclusive and contradictory. The debate has centred on whether the molecules are associated into chains or rings in the liquid phase, with different experiments showing different types of association; for example one X-ray scattering study was interpreted to show chains (Ohtaki *et al.*, 1983) while another showed the presence of rings in the liquid (Miyake *et al.*, 1985). An X-ray scattering study (Nasr & Bosio, 1998) on amorphous formamide showed it to be more structured than the liquid and was interpreted as showing structure similar to the known crystal structure.

The effects of pressure on liquid formamide have been investigated. Again, the results are contradictory with one NMR study reporting the formation of more ring units with increasing pressure to 0.4 kbar (Ohtaki *et al.*, 2000) while a separate study using X-ray and neutron diffraction showed more chains to be formed at high pressure up to 4 kbar (Nasr & Bosio, 1997). This latter study determined the change in melting point with pressure of formamide, as the temperature had to be increased to keep the sample liquid.

Ab initio calculations on formamide have shown that the lowest energy configuration for two formamide molecules is a cyclic dimer similar to that seen in the crystal structure (Cabaleiro-Lago & Otero, 2002), as shown in Figure 5.2.

N-methyl formamide

The crystal structure of N-methyl formamide is described by Neuefeind *et al.* (1996) in the context of structure in the liquid. However the crystal structure has not been published; full structural parameters are not available, neither are the co-ordinates nor indeed the unit cell. The structure described by Neuefeind consists of helical chains of hydrogen bonded molecules in the *trans* conformation with respect to the oxygen and the amide hydrogen atoms. The solid-state structure has also been studied using inelastic neutron scattering (Bour *et al.*, 1998).

Studies on liquid N-methyl formamide (Neuefeind *et al.*, 1996; Hammai *et al.*, 2002) have shown that the molecules are hydrogen bonded and are in the *trans* conformation. Microwave experiments on NMF in the gas phase have shown the molecule to be in the *trans* configuration (Fantoni & Caminati, 1996).

c) N,N-dimethyl formamide

The structure of DMF was reported recently by Borrmann *et al.* (2000). At 90 K DMF crystallises in the triclinic space group $P\bar{1}$, with two crystallographically independent molecules in the structure (Figure 5.3). In this case the only hydrogen bonding interactions are weak C-H...O hydrogen bonds via the formyl C-H group and one methyl group per molecule. The structure is described in more detail in Section 5.3.

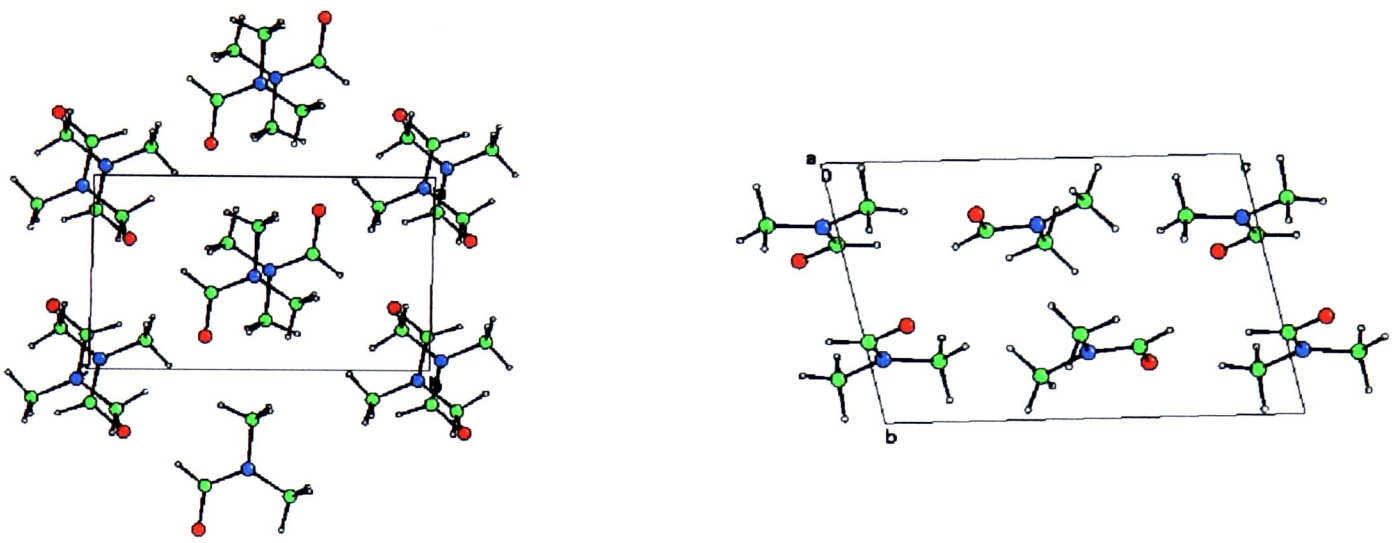

Figure 5.3. Crystal structure of DMF at 90 K. Left: viewed along (0 1 0). Right: viewed along (1 0 0)

5.2 Experimental

5.2.1 Crystal growth, data collection and refinement

Formamide

A sample of formamide (Aldrich, used as received) was loaded into a Merrill - Bassett diamond anvil cell equipped with 600 μm diamonds, a tungsten gasket with a 300 μm hole, and a chip of ruby for pressure measurement. Application of pressure caused the sample to crystallise into a polycrystalline mass, which was then carefully

heated until the crystallites began to melt. Heating was stopped when one crystallite remained. As the cell cooled the crystal grew to fill the gasket hole.

Several crystals were grown using this procedure. The first experiment showed that a new phase of formamide was formed when crystallised at high pressure. Unfortunately the ruby chip was washed out when the sample was loaded so that the pressure could not be measured. Further experiments showed that the low temperature phase (phase I) could be grown at 2 kbar, while the new phase (phase II) was formed at 4.4 kbar.

Data were collected using a Bruker SMART Apex diffractometer equipped with Mo-K_α radiation using the procedures described in Chapter 2. For one sample of phase II data were collected with the diamond anvil cell in three orientations (glued to the goniometer head on the three different sides of the cell) to simulate three different values of χ.

Data in each case were integrated using dynamic masks using Saint (Bruker-AXS, 2003). For the sample grown at 4.4 kbar, each of the three data-sets collected were separately corrected for the effects of absorption by the diamond anvil cell using Absorb5.3 (Angel, 2003). A further absorption correction was applied using Sortav (Blessing, 1995). The three (unmerged) reflection files were then scaled and merged using Sortav to yield one reflection file. For the sample at 2 kbar only one set of diffraction data were collected; these were corrected for absorption effects due to the diamond anvil cell using Shade (Parsons, 2003) and crystal absorption effects using Sortav. The data were merged using Sortav.

At 4.4 kbar formamide crystallises in the monoclinic system, space group $P2_1/n$, with two independent molecules in the asymmetric unit. The new high pressure structure was solved using direct methods (Shelxs; Sheldrick, 1997), and refined against $|F|^2$ using Shelxl (Sheldrick, 1997). Full refinement details are shown in Table 5.2.

Refinement of phase I of formamide at 2 kbar used the previously determined structure co-ordinates (Stevens, 1978, CSD refcode FORMAM02) as a starting point. The structure was refined against $|F|^2$ using Shelxl. Full refinement details are shown in Table 5.2.

N-methyl formamide

Low temperature

A sample of N-methyl formamide (Aldrich, used as received) was loaded into a capillary and a crystal was grown *in situ* on the diffractometer, using the method of Boese and Nussbaumer (1994) at a temperature of 250 K. A hemisphere of data were collected at 250 K. The crystal was then slowly cooled to 150 K and a further hemisphere collected. Further data collections were performed at 100 K and following heating to 200 K. The data were integrated using routine procedures and an absorption correction applied using Sadabs (Sheldrick, 2002).

At low temperature N-methyl formamide crystallises in the monoclinic space group $P2_1/c$, with two independent molecules in the asymmetric unit. The unit cell has high pseudo symmetry with all angles close to 90° and three similar unit cell lengths (Table 5.1). The merging statistics show the true symmetry to be monoclinic, with R_{int} for tetragonal 0.67 and orthorhombic 0.45 compared to 0.05 for the correct monoclinic setting. The structure was solved using direct methods (Shelxs) and refined against $|F|^2$ using Shelxl. Full refinement details for the 250 K structure are shown in Table 5.3. Details of the other low temperature refinements are given in the Appendix, with the cell dimensions shown in Table 5.1. A check for missed symmetry made using Platon (Spek, 1990) confirmed the monoclinic structure setting was correct.

Temperature /K	*a* / Å	*b* / Å	*c* / Å	β / °
100	8.7329(13)	8.4148(13)	8.5959(13)	90.351(2)
150	8.7754(11)	8.4720(11)	8.6045(11)	90.243(2)
200	8.774(5)	8.486(6)	8.601(5)	90.081(9)
250	8.817(9)	8.661(9)	8.591(9)	89.691(19)
20 kbar	8.460(10)	7.653(5)	8.360(6)	90.75(10)

Table 5.1. Unit cell dimensions of N-methyl formamide under different conditions

High pressure crystal growth

Crystals were grown at high pressure using the method described for formamide. Several crystals were grown, each of which had the same unit cell as the crystal grown at low temperature. The crystals grew at high pressure with an obvious

square shape before growing to fill the gasket hole. Attempts were made to grow a crystal at higher pressure, but as melting point increases with increasing pressure these experiments were unsuccessful.

Data were collected using the procedures described in Chapter 2. For a crystal grown at 3 kbar two data sets were collected with the cell in different orientations. The pressure on this sample was then increased to 20 kbar and a further dataset collected. Data were also collected for a sample grown at 5 kbar. Due to the high pseudo symmetry of the unit cell it was difficult to determine the correct setting for use in data processing. Initial integration in each case was unconstrained, as was the unit cell refinement. The transformation matrix was identified using XPREP on this unconstrained refined cell and data, and a transformed cell used for further integrations. Dynamic masks were used in integration. Absorption corrections and data merging were carried out using similar procedures as those described for formamide. The program Shade was used in place of Absorb5.3 for the cell correction.

The structure at 3 kbar was solved using direct methods (Shelxs), and refined against $|F|^2$ using Shelxl. Similarity restraints were applied to the independent molecules. Details for the refinement of both the high pressure and low temperature crystals of N-methyl formamide are shown in Table 5.3. The data collected on the sample at 20 kbar were of too poor quality to allow structure refinement; due to the non-hydrostatic pressure environment of the crystal the peaks became very broad. The crystal bridged the culet faces - when pressure was applied the crystal itself rather than a surrounding medium was directly compressed. The unit cell parameters are included in Table 5.1 for comparison. Anisotropic refinement was not possible for the sample at 5 kbar.

c) N,N-dimethyl formamide (DMF)

Crystals of dimethyl formamide (Aldrich, used as received) at high pressure were grown using the procedure described above. No new phase was identified. The pressure of one sample was increased to determine the effect of pressure on the structure. Data were collected at 11 kbar, 14 kbar, 26 kbar and 43 kbar. Two datasets were collected at 11 kbar with the cell in differing orientations. The data were

integrated, an absorption correction applied and merged as described for formamide. The absorption correction for the diamond anvil cell was applied using Shade.

The structure of DMF was refined using the previously determined co-ordinates at low temperature (Borrmann *et al.*, 2000, CSD refcode KAQPUN). Refinement was against $|F|^2$ using Crystals (Watkin *et al.*, 2003), with isotropic treatment of thermal motion. Similarity and distance restraints were applied based on the geometry of the molecule at low temperature. Refinement details are shown in Table 5.4. Only a limited amount of data was collected at 43 kbar as it was obvious the peaks were very broad; the unit cell dimensions are included for comparison. The data collected at 26 kbar were also too poor to allow structure refinement. As in NMF, the poor quality of the higher pressure data can be ascribed to the pressure environment which was far from hydrostatic.

In the original structure determination for DMF (Bormann *et al.*, 2000) the authors describe the formation of a metastable phase. Attempts were made to grow this phase at low temperature but proved unsuccessful.

	Phase I	Phase II
Crystal Data		
Crystal system	Monoclinic	Monoclinic
Space group	$P2_1/n$	$P2_1/n$
a / Å	3.6812(4)	3.6006(6)
b / Å	9.2666(9)	18.828(3)
c / Å	6.7968(16)	6.3072(9)
β / °	99.448(6)	93.556(11)
V / Å^3	228.71(6)	426.76(11)
Z	4	8
ρ_{calc} [Mg m^{-3}]	1.308	1.402
Number of reflections for cell (θ range, °)	253 (4.4 < θ < 25.8)	779 (3.4 < θ < 23.1)
Crystal description, size / mm	colourless cylinder 0.3 x 0.3 x 0.15	colourless cylinder 0.3 x 0.3 x 0.15
Pressure / kbar	2	4.4
Data Collection		
Reflections collected	672	3585
Independent reflections	140	424
R_{int}	0.0779	0.1088
h	-4 to +4	-3 to +3
k	-10 to +10	-20 to +20
l	-3 to +3	-6 to +6
Absorption correction (T_{min}, T_{max})	0.784, 1.358	0.860, 1.504
Solution and Refinement		
Solution (Program)	Known (CSD refcode FORMAM03)	Direct (Shelxs)
Refinement program	Shelxl	Shelxl
Hydrogen atom placement	Geometric	Geometric
H refinement	Riding	Riding
R [F_o>4σ(F_o)]	0.0614 (118 data)	0.0726 (312 data)
wR_2	0.1753	0.1557
Goodness of fit on F^2	1.295	1.212
Restraints	0	0
Parameters	28	56
Maximum Δ/σ	0.000	0.000
Weighting scheme x,y*	0.0982, 0.0083	0.0553, 0.1999
Largest residuals [e Å^{-3}]	+ 0.101, -0.129	+ 0.136, - 0.169

* where $w = 1/ [\sigma^2(F_o^2) + xP^2 + yP$, $P=(F_o^2 + 2F_c^2)/3$

Table 5.2. Crystal data and refinement details for formamide

Crystal Data			
Crystal system	Monoclinic	Monoclinic	Monoclinic
Space group	$P2_1/n$	$P2_1/n$	$P2_1/n$
a / Å	8.817(9)	8.794(2)	8.776(3)
b / Å	8.661(9)	8.5234(12)	8.3748(14)
c / Å	8.591(19)	8.5860(16)	8.5629(17)
β / °	89.961(19)	90.12(2)	90.2(3)
V / Å^3	656.0(12)	643.6(2)	629.3(3)
Z	8	8	8
ρ_{calc} / Mg m^{-3}	1.196	1.219	1.247
Number of reflections for cell (θ range, °)	867, (2.3 < θ < 23.4)	581, (3.35 < θ < 26.1)	489, (3.4 < θ < 23.1)
Crystal description, size / mm	Colourless cylinder, 0.35 x 0.35 x 1.00	Colourless cylinder, 0.30 x 0.30 . 0.2	Colourless cylinder, 0.30 x 0.30 . 0.2
Temperature / K	250	293	293
Pressure / kbar	Ambient	3	5
Data Collection			
Reflections collected	3820	3527	1499
Independent reflections	1557	470	320
R_{int}	0.0469	0.0995	0.1606
h	-11 to 11	-3 to 4	-3 to 4
k	-4 to 11	-10 to 10	-9 to 9
l	-11 to 10	-10 to 10	-9 to 9
Absorption correction (T_{min}, T_{max})	0.626, 1.0	0.788, 1.289	0.851, 1.367
Solution and Refinement			
Solution (Program)	Direct (Shelxs)	Direct (Shelxs)	Known
Refinement program	Shelxl	Shelxl	Shelxl
Hydrogen atom placement	Geometric	Geometric	Geometric
H refinement	Riding / Rotating	Riding	Riding
R [F_o>4σ(F_o)]	0.0549 (1002 data)	0.0516 (286 data)	0.0618 (199 data)
wR_2	0.1602	0.1328	0.1798
Goodness of fit on F^2	1.037	1.054	1.053
Restraints	0	12	5
Parameters	75	74	43
Extinction coefficient	-	0.069(19)	-
Maximum Δ/σ	0.001	0.000	0.000
Weighting scheme x,y*	0.0630, 0.0771	0.0691, 0.0071	0.0702, 0.5177
Largest residuals [e Å^{-3}]	+0.179, -0.211	+0.086, -0.086	+0.116, -0.121

* where $w = 1/ [\sigma^2(F_o^2) + xP^2 + yP$, $P=(F_o^2 + 2F_c^2)/3$

Table 5.3. Crystal data and refinement details for N-methyl formamide

Crystal Data				
Space group	$P\bar{1}$	$P\bar{1}$	$P\bar{1}$	$P\bar{1}$
a / Å	5.8483(14)	5.8022(15)	5.721(4)	5.65(4)
b / Å	6.7991(9)	6.7021(9)	6.490(3)	6.493(17)
c / Å	10.173(2)	10.113(3)	10.002(7)	9.97(4)
α / °	77.546(16)	77.468(17)	77.18(5)	77.2(3)
β / °	88.408(16)	88.302(16)	88.15(5)	88.4(4)
γ / °	75.369(19)	75.673(19)	76.14(6)	76.5(4)
V / Å^3	382.02(14)	371.85(15)	351.5(3)	346(2)
Z	4	4	4	4
ρ_{calc} [Mg m^{-3}]	1.271	1.306	1.38	-
Number of reflections for cell (θ range / °)	342 (3 < θ < 21)	339 (3 < θ < 21)	133 (3 < θ < 23)	-
Crystal description, size / mm	Colourless cylinder, 0.3 x 0.3 x 0.2	Colourless cylinder, 0.3 x 0.3 x 0.2	Colourless cylinder, 0.3 x 0.3 x 0.2	Colourless cylinder, 0.3 x 0.3 x 0.2
Pressure / kbar	11	14	26	43
Data Collection				
	11kbar		14kbar	
Reflections collected	1864		948	
Independent reflections	371		305	
R_{int}	0.0843		0.0858	
h	-4 to 3		-4 to 3	
k	-7 to 7		-7 to 7	
l	-10 to 10		-10 to 10	
Absorption correction (T_{min}, T_{max})	0.832, 1.450		0.942, 1.150	
Solution and Refinement				
Solution (Program)	Known (CSD refcode KAQPUN)		Known (CSD refcode KAQPUN)	
Refinement program	Crystals		Crystals	
Hydrogen atom placement	Geometric		Geometric	
H refinement	no refinement		no refinement	
R [F_o>4σ(F_o)]	0.0804 (241 data)		0.0846 (303 data)	
wR_2	0.1729		0.2398	
Goodness of fit on F^2	1.0251		0.946	
Restraints	20		32	
Parameters	41		41	
Maximum Δ/σ	0.04		0.021	
Weighting scheme	0, 1.17		0.146, 0.85	
Largest residuals [e Å^{-3}]	+0.23, -0.28		+0.28, -0.34	

* where $w = 1/ [\sigma^2(F_o^2) + xP^2 + yP$, $P=(F_o^2 + 2F_c^2)/3$

Table 5.4. Crystal data and refinement details for N,N-dimethyl formamide.

5.2.2 Differential Scanning Calorimetry

In order to determine whether any of the three compounds had different phases accessible through changes in temperature, differential scanning calorimetry (DSC) measurements were made for each compound. Traces were recorded using a Perkin Elmer Pyris DSC 1 instrument, with the samples contained in closed aluminium pans. The temperature ranges used are shown in Table 5.5. Formamide and NMF samples were initially cooled and then heated; the sample of DMF was quenched to 103 K and then heated and cooled to mimic the experiment of Borrmann *et al.* (2000).

Sample	Cooled to	Heated to
Formamide	229 K	308 K
N-methyl formamide	104 K	290 K
N,N-dimethyl formamide	103 K	295.5 K

Table 5.5. Temperature ranges used for differential scanning calorimetry measurements

5.3 Discussion

5.3.1 Formamide

At 4.4 kbar formamide crystallises in a layered structure closely related to that formed at low temperature. The high pressure structure is shown in Figure 5.4 below, with the low temperature structure for comparison. In each phase each molecule forms four hydrogen bonds, forming layers parallel to the (1 0 1) plane.

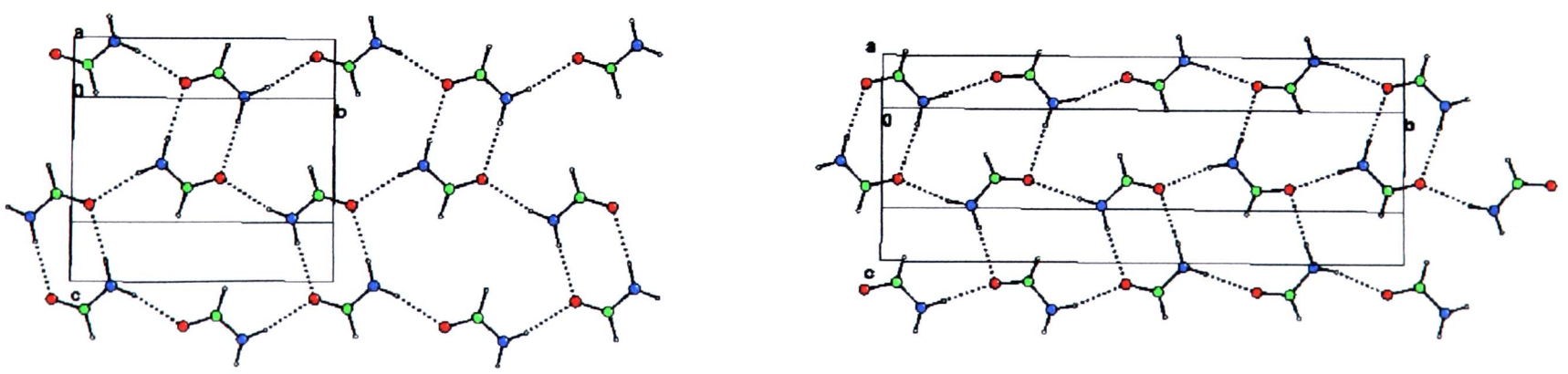

Figure 5.4. Layer formation in phase I (left) and phase II (right) of formamide. The layers in the two phases are closely related.

It is clear from Figure 5.4 that the two structures are closely related. This can also be seen from the unit cell dimensions (Table 5.6). *a* is very similar in both structures, while *b* is approximately doubled in the higher pressure phase and *c* is close. In phase I at 2 kbar, *a* and *b* are slightly larger than at 90 K by 2.1% and 2.5% respectively, while *c* is larger by 2.8%. The density is slightly lower at 2 kbar.

Conditions (phase)	*a* / Å	*b* / Å	*c* / Å	β / °	density / Mg cm^{-1}
90K (I)	3.604(2)	9.041(3)	6.994(2)	100.50(5)	1.331
2kbar (I)	3.6812(4)	9.2666(9)	6.7968(16)	99.448(17)	1.308
4.4kbar (II)	3.6006(6)	18.828(3)	6.3072(9)	93.556(11)	1.402

Table 5.6. Comparison of cell dimensions of phase I and II of formamide

The difference between the two phases lies in the change in orientation of one molecule. Both structures can be considered to consist of hydrogen bonded chains parallel to the *b* axis, interlinked by further hydrogen bonds forming layers. In phase I, the repeating unit of the chain consists of two molecules, a $C_2^2(8)$ graph set. The molecules within one chains alternate in orientation, and are related by the screw axis. In phase II the repeating unit is twice as long, consisting of four molecules, or $C_4^4(16)$, with the orientation alternating in groups of two molecules. The independent molecules alternate along one chain, with the pairs of molecules related by the screw axis. This explains the doubling of *b* in phase II relative to phase I.

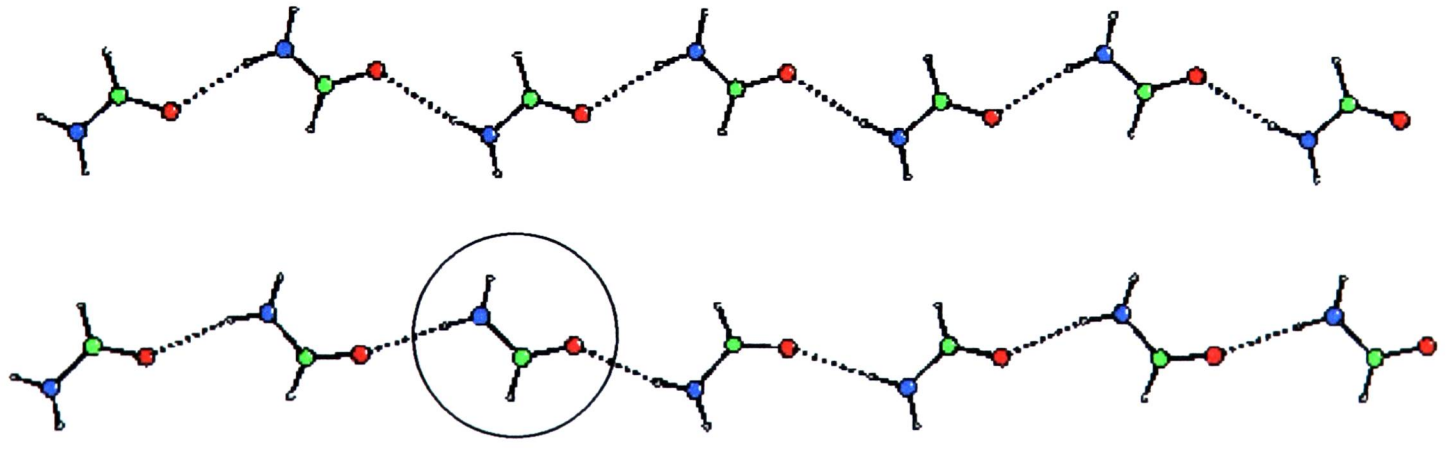

Figure 5.5. Hydrogen bonded chains in phase I (top) and phase II (bottom) of formamide. The third molecule (ringed) in phase II has rotated by 180° relative to phase I.

The first two molecules of the $C_4^4(16)$ unit in phase II have similar orientations to the $C_2^2(8)$ group in phase I. The third molecule and fourth molecules have rotated by 180° around *b* relative to the chain in phase I. Moving further along, the fifth and sixth molecule have the same orientation in each chain. This explains the approximate doubling of the *b* unit cell length in phase II. In the low temperature structure the first two molecules are related by the 2_1 axis - in the structure at 4.4 kbar there is no such relationship.

The change in orientation of the molecule has changed the overall hydrogen bonding pattern within one layer. The phase I crystal structure has two distinct hydrogen motifs (Figure 5.6). The first links two molecules into a dimer unit, denoted $R_2^2(8)$ in graph set notation. Description of this interaction as a dimer is not strictly correct as the hydrogen bonds linking the molecules are longer then those between the "dimers". The second motif in the structure consists of larger $R_6^4(16)$ rings, formed by the interaction of four of the smaller $R_2^2(8)$ units (Figure 5.6, shown in blue).

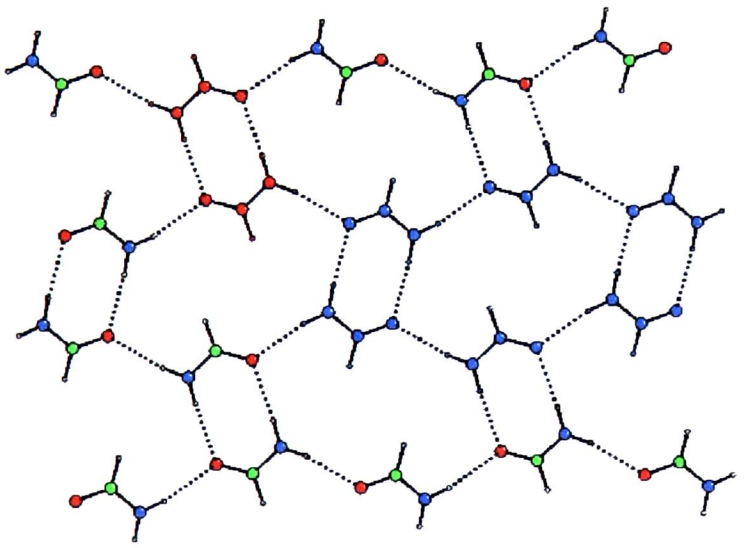

Figure 5.6. Hydrogen-bond motifs in the low temperature structure of formamide. The $R_2^2(8)$ interaction is shown in red and the $R_6^4(16)$ interaction in blue.

The lengths of the hydrogen bonds in this structure at 90 K and 2 kbar are shown in Table 5.7. These hydrogen bond lengths are not significantly different under these two conditions; the angles made along the chain are different, explaining the increase in the *b* axis at 2 kbar.

Conditions	N...O $R_2^2(8)$ / Å	N...O-C / °	N...O $R_6^4(16)$ / Å	N...O-C / °
90 K	2.948	117.92	2.883	127.5
2 kbar	2.949(13)	119.15	2.901(7)	134.37

Table 5.7. Hydrogen bond lengths in phase I of formamide at 90 K and 2 kbar

In the new phase of formamide formed at 4.4 kbar, there are three hydrogen bonding motifs. As in phase I there are $R_4^3(12)$ and $R_6^4(16)$ interactions. In addition there is a new ring formed by the interaction of four molecules, denoted $R_4^3(12)$. Two of the molecules involved in this new interaction form the $R_4^3(12)$ group (Figure 5.7).

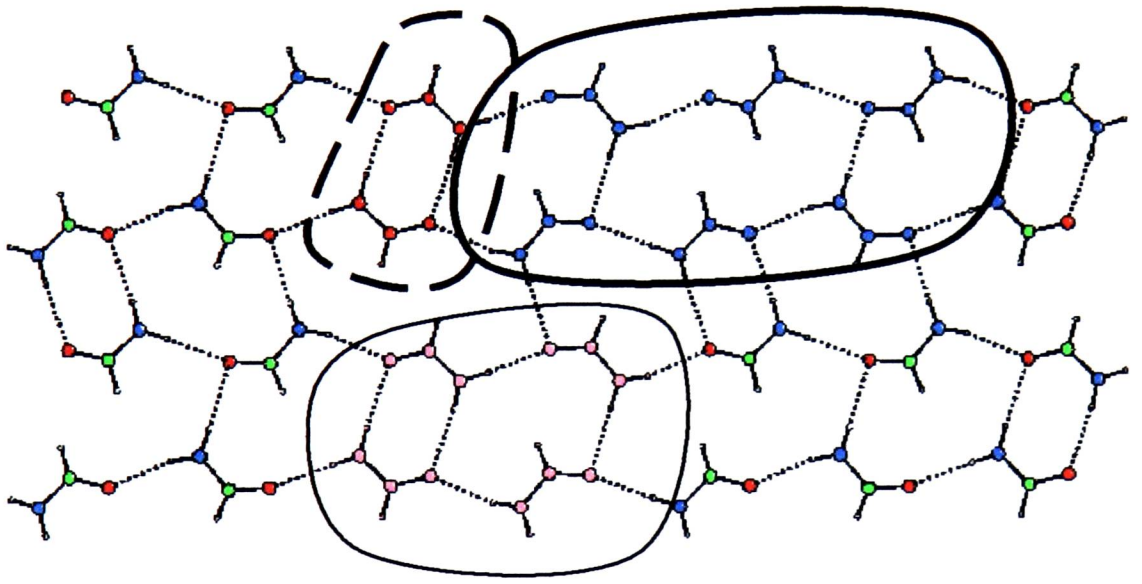

Figure 5.7. Hydrogen bonding motifs in phase II of formamide. Molecules in red form a $R_2^2(8)$ interaction, molecules in blue a $R_6^4(16)$ interaction and molecules in pink a $R_4^3(12)$ motif. The molecules involved are outlined.

There are four unique hydrogen bonds in this crystal structure. Two of the unique interactions are made between two chains and two made within one chain. One hydrogen bond is used in the $R_2^2(8)$ unit - this interaction involves only one of the independent molecules. The interactions made by the two independent molecules are shown in Figure 5.8.

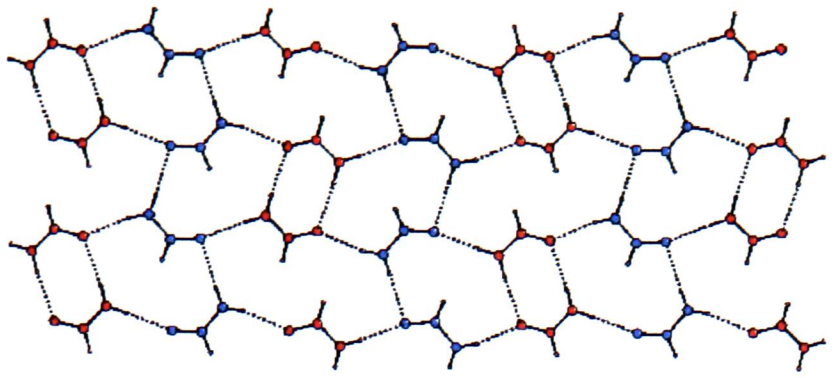

Figure 5.8. One layer of formamide showing the differing interactions of inequivalent molecules. Molecules are coloured red and blue according to symmetry equivalence

As in phase I the hydrogen bonds between the chains (1 and 2 in Figure 5.9) are longer than those within the chains, with the longest and shortest varying by 0.100(6) Å (Table 5.8). The difference is smaller at 90 K, where the two hydrogen bonds vary by 0.065 Å. The average hydrogen bond length in the 4.4 kbar structure (2.920(10) Å) is not significantly different to the 90 K structure, 2.916 Å.

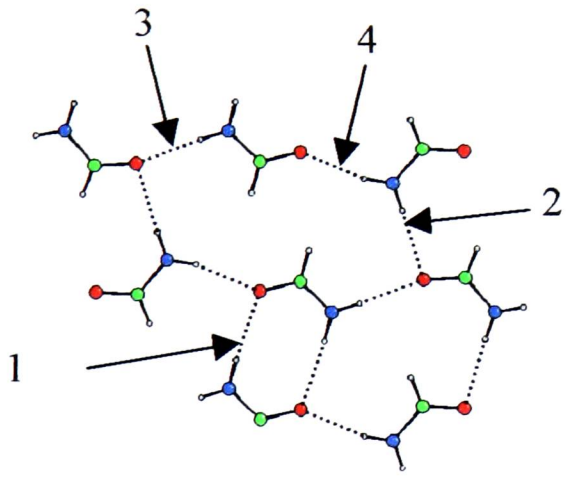

Figure 5.9. Hydrogen bonds in phase II

Interaction	N...O / Å	N...O / Å 90 K
1	2.959(3)	2.948
2	2.948(7)	
3	2.913(5)	2.883
4	2.859(5)	

Table 5.8 Hydrogen bond lengths in phase II

The $R_2^2(8)$ interactions in the two phases are very similar, not only in the lengths of the hydrogen bonds but also in the angles made by these interactions (Table 5.9). In both cases the molecules making up the $R_2^2(8)$ groups are related by inversion.

Conditions (Phase)	C-O...N / °	C-N...O / °
90 K (I)	117.92	116.91
2 kbar (II)	119.15	117.01
4.4 kbar (II)	119.0(3)	116.9(4)

Table 5.9. Internal angles in $R_2^2(8)$ groups

The $R_6^4(16)$ group geometry differs between phase I and phase II.. The angles made within the ring are significantly different in the two phases (Table 5.10). The angle at the "end" of the ring (angle 1, Figure 5.10) is 12 ° smaller in phase II while the other internal ring angles are larger.

	N...O...N (1) / °	C-O...N (2) / °	C-N...O (3) / °
90 K	102.3°	127.5	110.4
2kbar	98.84	134.37	109.74
4.4kbar	89.8°	148.2	118.42

Table 5.10. Internal angles in $R_6^4(16)$ groups. Numbers in brackets refer to Figure 5.10 (right)

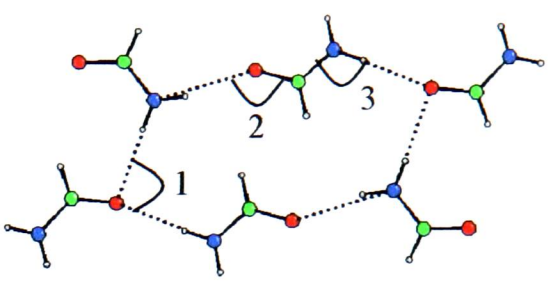

Figure 5.10. Internal angles in $R_6^4(16)$ groups

The $R_6^4(16)$ units in phase II are more planar than in phase I - the mean deviation from the plane defined by the ten heavy atoms in the ring is 0.0683 Å in phase II compared to 0.2513 Å in phase I. The difference in the two $R_6^4(16)$ units is shown in Figure 5.11.

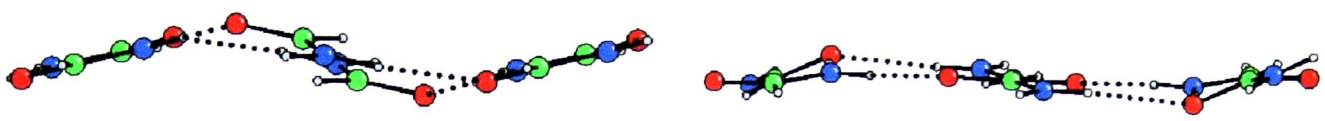

Figure 5.11. $R_6^4(16)$ units in phase I (left) and phase II (right) viewed from the side, showing the difference in planarity.

These changes in angle have affected the intermolecular separations. The molecules at either end of the ring are further apart in phase II but the molecules at the side of the ring are closer together (Table 5.11). The former observation can be explained by the flattening out of the ring, and the latter by the decreased angle at the oxygen atoms at the ends of the ring.

Conditions (Phase)	O...O / Å	C...C / Å
90 K (I)	8.556	4.620
2 kbar (I)	8.791	4.476
4.4 kbar (II)	9.212	3.652

Table 5.11 Intermolecular separations in $R_6^4(16)$ units

The topology of the layers in the two phases differs. In both cases the layers are sinusoidal in form rather than planar (Figure 5.12).

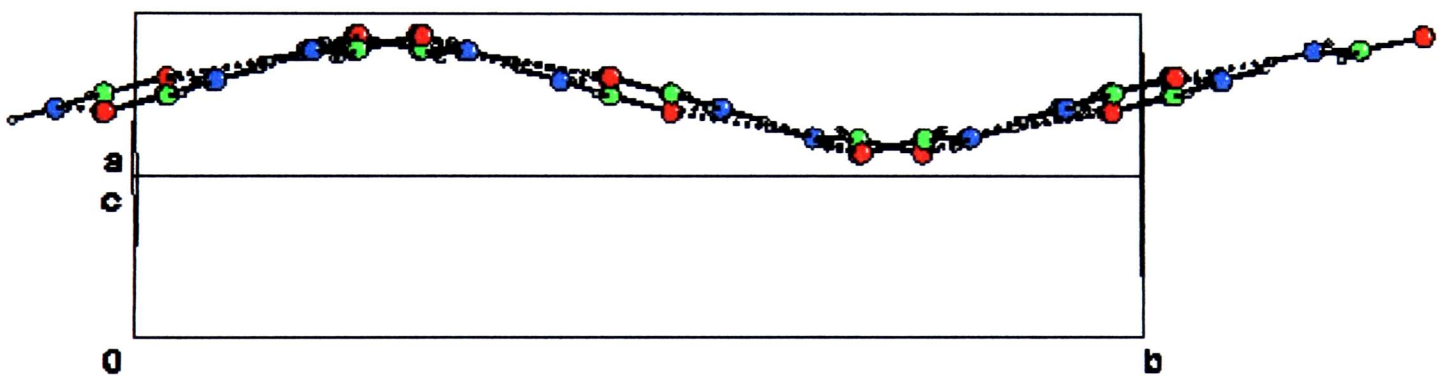

Figure 5.12. One layer in phase I (top) and phase II of formamide (bottom) viewed perpendicular to the (1 0 1) plane.

There are two differences obvious from Figure 5.12. Taking the sine wave analogy further, phase II has double the amplitude and double the wavelength of phase I (this is another way of describing the doubling of the *b* axis).

Although the sinusoidal shape is more pronounced in phase II, the layers are actually smoother than in phase I. Moving across one layer perpendicular to *b*, phase II is smoother than phase I. This is due to the "flattening out" of the $R_6^4(16)$ units in the structure.

The distance between the layers in the two phases are comparable. In each case the layers are parallel to the (1 0 1) plane. At 90 K the layers are 2.939 Å apart, at 2 kbar 2.994 Å and in phase II at 4.4 kbar 3.039 Å. This is an increase of 0.1 Å (3.4%) compared to the structure at 90 K.

Topological analysis

The new phase of formamide has a higher density than the low temperature form. The volume per molecule at 90 K is 56.17 $Å^3$, increasing slightly to 57.2 $Å^3$ at 2 kbar; in the new phase the volume per molecule is 53.35 $Å^3$, a reduction of 5% relative to the 90 K structure. This cannot be explained in terms of shorter hydrogen bonds in the higher pressure polymorph, as shown above. Neither can it be explained by the layers being closer together. Instead, the higher density of phase II can be rationalised on topological grounds. The structures of both phases are based on cubic close packed arrangements, with six contacts to molecules within one hydrogen bonded layer, three to the layer above and three to the layer below. The contacts to molecules in adjacent layers are staggered, giving the a b c a b c arrangement indicative of cubic close packing.

The six closest contacts of one molecule within one hydrogen bonded layer in phase I are shown in Figure 5.13, and the contacts at 90 K and 2 kbar are tabulated in Table 5.12.

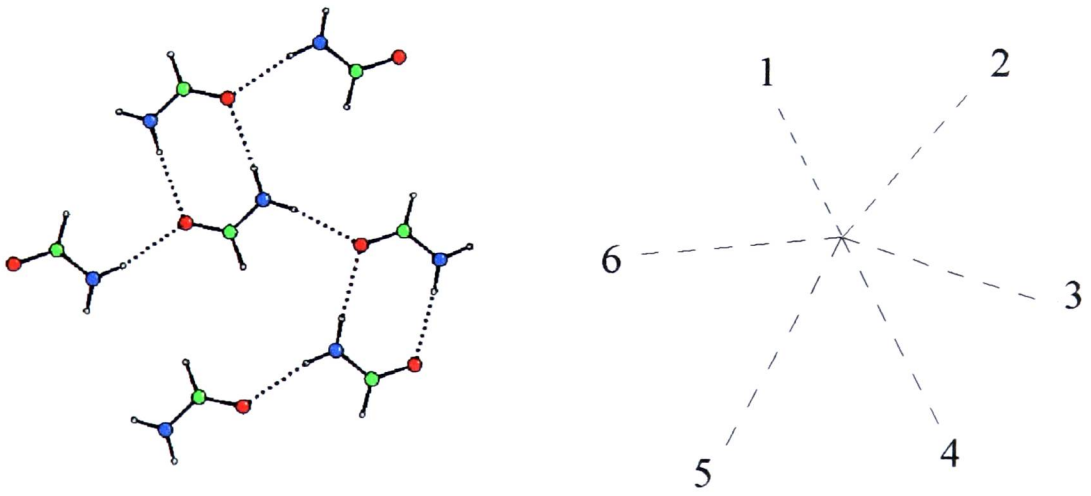

Figure 5.13. Left: a. The six nearest neighbours of one molecule within a layer in phase I. Right: b. As (a), showing only the molecular centroids. The numbers refer to the interactions listed in Table 5.12.

	Centroid Separation / Å	
	90 K	2 kbar
1	4.639	4.749
2	3.675	3.665
3	4.993	4.912
4	4.639	4.749
5	4.993	4.912
6	5.569	5.516

Table 5.12. Separations of molecular centroids in phase I of formamide. The numbers refer to the labels in Figure 5.13

At 90 K, of the six contacts within one layer there are four contacts in the range 4.64 Å to 4.99 Å. One contact is 1Å shorter at 3.68 Å and one in ~1 Å longer at 5.57 Å. The distribution is similar at 2 kbar, although the spread of values has reduced slightly to 3.67 Å to 5.52 Å.

Contacts to molecules above and below the plane are similar at 90 K and 2 kbar (Table 5.13). Each molecule makes three contacts to the layer above and the layer below (Figure 5.14). The centroids in the upper and lower layers are not eclipsed; an abcabc arrangement of layers is formed indicative of cubic close packing (Figure 5.14d).

	Separation / Å	
Contact	90 K	2 kbar
7	3.604	3.681
8	3.700	3.827
9	4.509	4.474
10	4.653	4.581
11	4.509	4.474
12	3.604	3.681

Table 5.13. Contacts above and below one hydrogen bonded layer in phase I of formamide. Numbering scheme is shown in Figure 5.14.

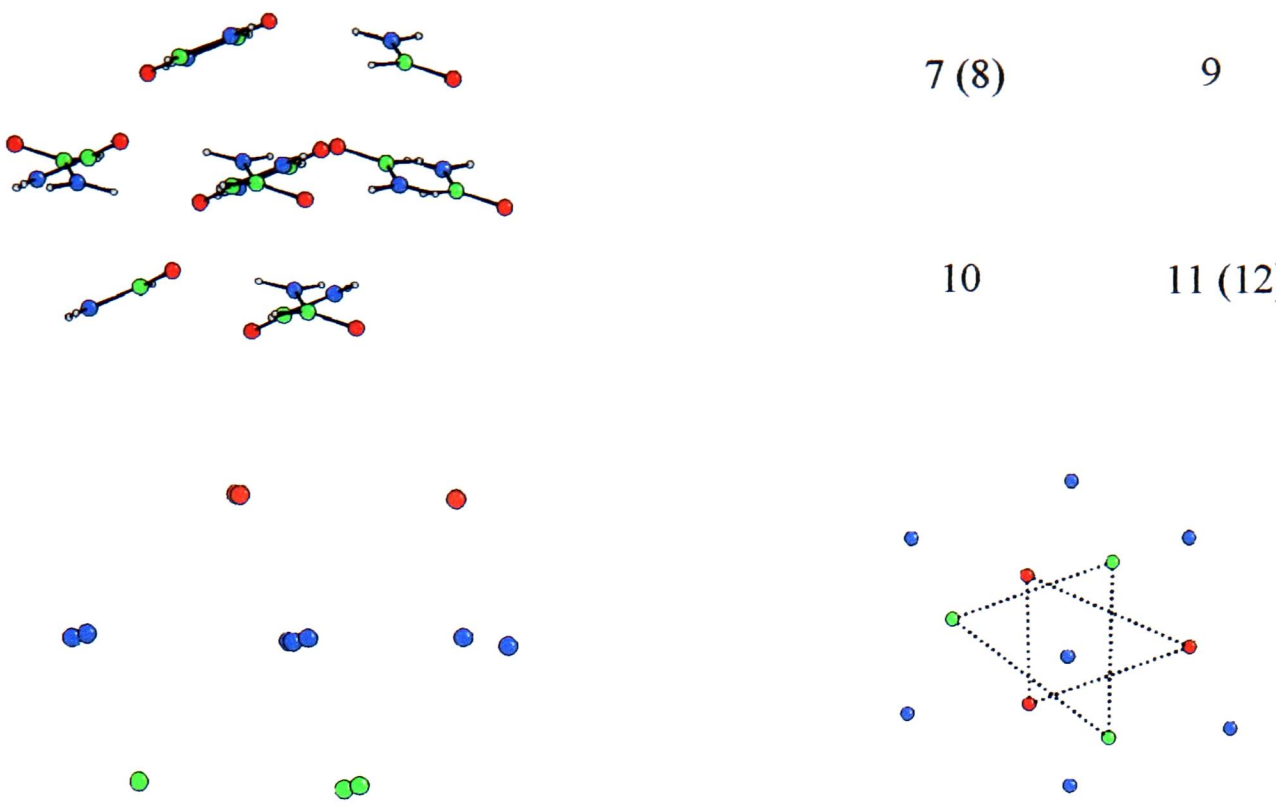

Figure 5.14. Contacts to molecules above and below one layer.
Top left. a. Twelve neighbours of a central molecule, viewed parallel to layers
Top right. b. Numbering scheme for centroids in adjacent layers (used in Table 5.13)
Bottom left. c. As (a), with molecular centroids only.
Bottom right. d. As (a), viewed from above. The lines indicate the contacts between the centroids in the upper and lower layers. The staggered arrangement of the centroids indicating ccp packing is clear.

The distortion from cubic close packing is shown by two further contacts to the lower layer (Figure 5.15). At 5.453 Å (90 K) these contacts are 0.1Å shorter than the long 5.57 Å contact within one layer (Table 5.13).

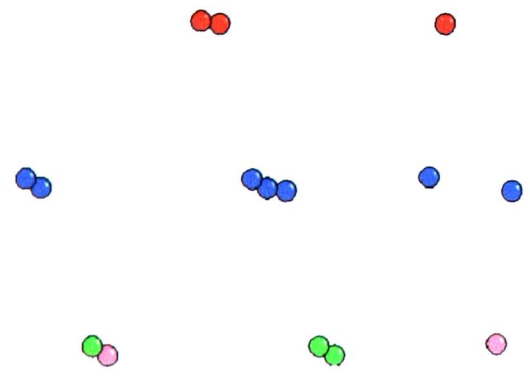

Figure 5.15. Two long contacts are formed between the central molecule and two molecules in the lower hydrogen-bonded layer. These are shorter than the long intralayer contact.

In phase II there are two molecules to consider. Each is surrounded within one layer by two symmetry equivalent molecules and four inequivalent molecules (Figure 5.16). Contacts to molecules within the same hydrogen-bonded layer are different for the two independent molecules. For molecule 1 the contacts within one layer are spread more evenly than in phase I, ranging from 4.22 Å to 4.82 Å (Table 5.14). This molecule does not participate in the $R_2^2(8)$ interaction (Figure 5.16). The second molecule makes one short contact of 3.67 Å with the rest in the range 4.66 to 4.82 Å. The shortest contact is to the second molecule of the $R_2^2(8)$ motif. Neither molecule makes a contact longer than 4.65 Å, in contrast to the 5.5 Å contact in phase I.

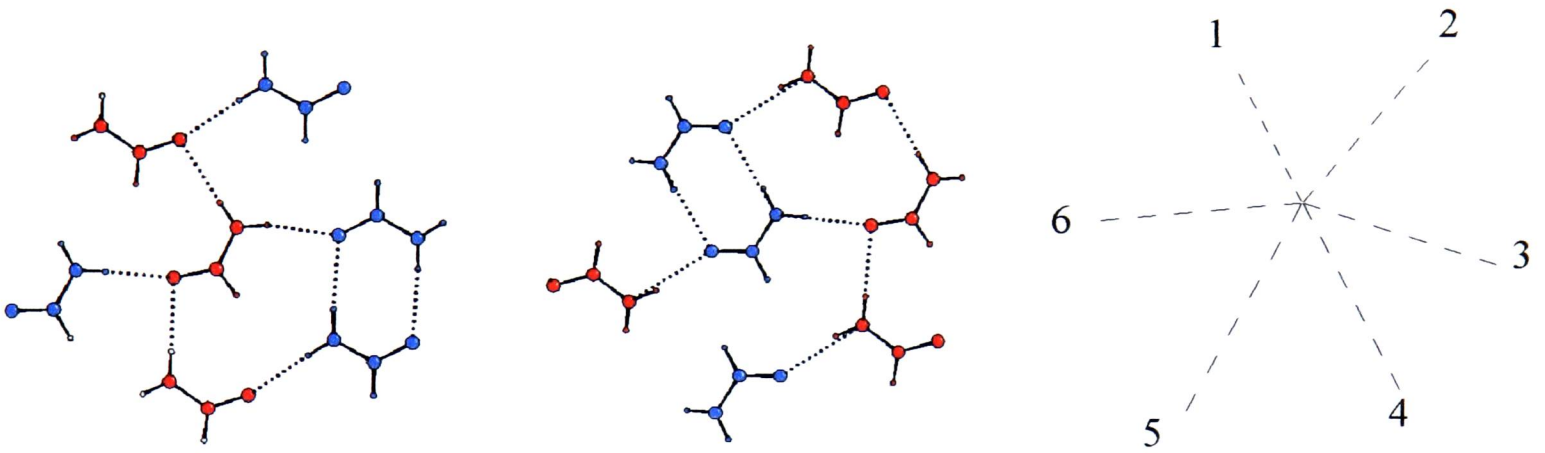

Figure 5.16. The six closest contacts to molecules within the same hydrogen-bonded layer for each of the independent molecules. Red (molecule 1) and blue (molecule 2) colours show the symmetry equivalent molecules. The numbering scheme for the contacts is shown to the right.

Molecule 1		Molecule 2	
Contact	Distance / Å	Contact	Distance / Å
1	4.22	1	3.67
2	4.71	2	4.66
3	4.82	3	4.78
4	4.66	4	4.71
5	4.22	5	4.78
6	4.78	6	4.82

Table 5.14. Separations of molecular centroids in formamide phase II within one layer

Molecule 2 has the more similar environment to the molecule in phase I (Figure 5.17). The largest reduction in intermolecular contact has occurred where one molecule has rotated (see Section 5.3.1 above). This rotation has shortened the very long contact by 0.74 Å. Changes in the other contacts are more modest. Overall the environment of the formamide molecule is more symmetrical in one layer in phase II, although in strict crystallographic terms the symmetry of the structure is lower.

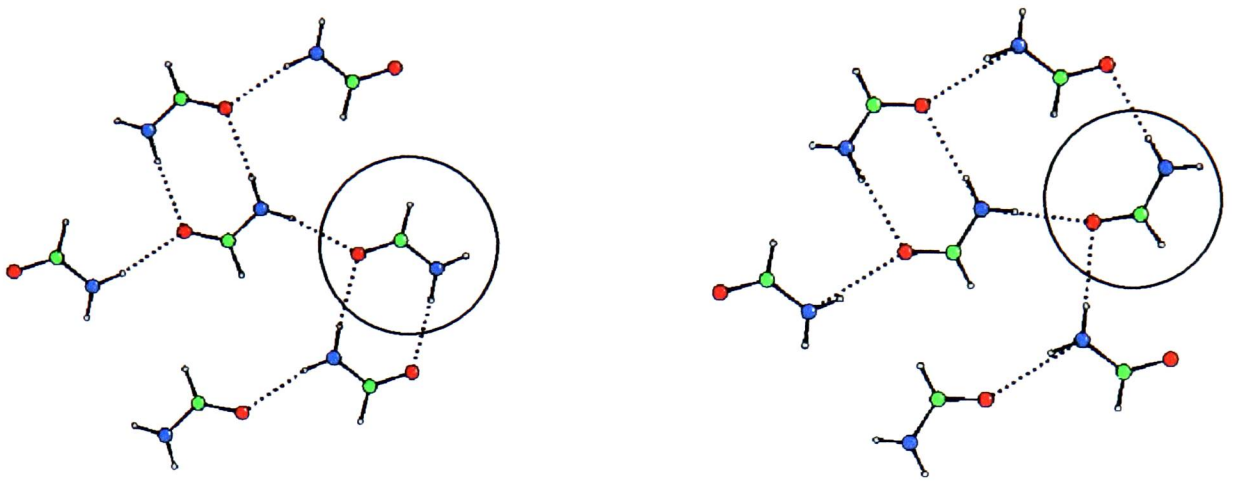

Figure 5.17. The largest change in the intralayer contacts for molecule **2**, phase II, relative to phase I. The centroid of the ringed molecule is 0.74Å closer to the central molecule in phase II (right) than in phase I (left).

Contacts to molecules in different layers follow a slightly different trend to phase I. These contacts span a broader range than in phase I, varying between 3.60 Å and 4.99 Å (Table 5.15) compared to 3.60 Å to 4.65 Å at 90 K. The centroids of these closest molecules have maintained the ccp arrangement observed in phase I (Figure 5.18). At the same time the two longer contacts made in phase I have expanded further, with the next closest contacts at 5.59 Å and 5.73 Å compared to 5.43 Å at 90 K.

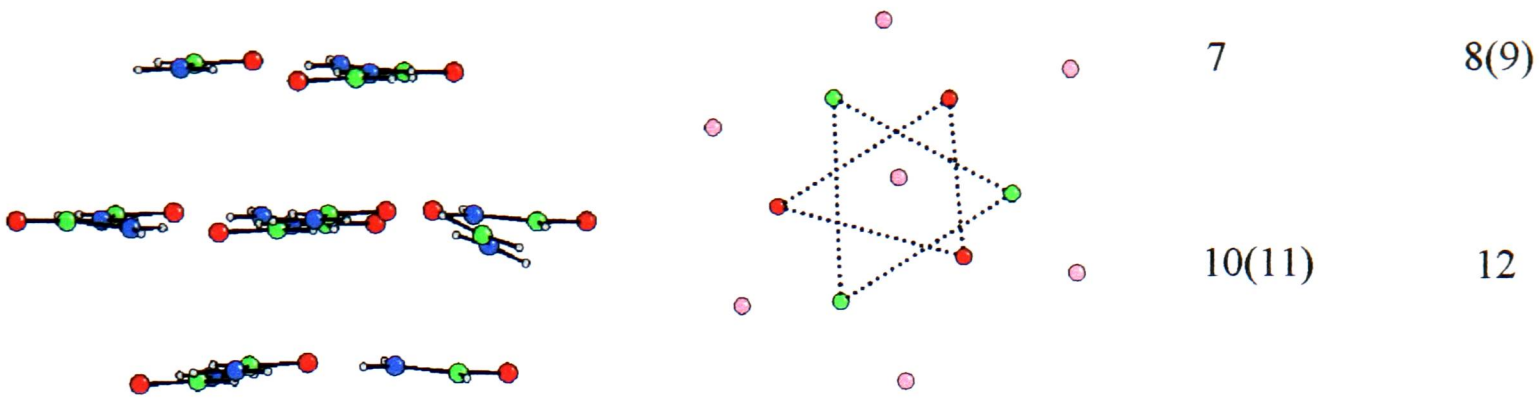

Figure 5.18. Cubic close packing in phase II of formamide. Left: the twelve nearest neighbours of molecule **2**. Centre: As left, viewed from above. The red circles represent the molecular centroids of the top layer of molecules, the pink circles the central layer and the green circle the lower layer. The staggered arrangement is clear. Right: numbering scheme for molecules in far left figure for Table 5.15.

	Separation / Å	
Contact	Molecule 1	Molecule 2
7	3.60	3.63
8	4.05	3.60
9	4.03	4.99
10	4.049	4.51
11	4.986	3.60
12	3.601	4.03

Table 5.15. Interlayer contacts in formamide phase II.

The symmetrisation of phase II of formamide can be seen in the lattice VDPs for the two phases (Figure 5.19). The VDP for molecule **2**, phase II, has more equally sized faces than the VDP for phase I. The size of the faces is proportional to the strength of the contact; phase II has a more symmetric distribution of intermolecular contacts. Both phases are significantly distorted from the ideal cubic close packed case; phase II is closer. The change towards cubic close packing can be quantified by the Continuous Symmetry Measure (Pinsky & Avnir, 1994) relative to ccp; for the molecular centroids in phase I the CSM is 3.11 relative to ccp. This reduces to 2.34 for molecule **1** and 2.65 for molecule **2**.

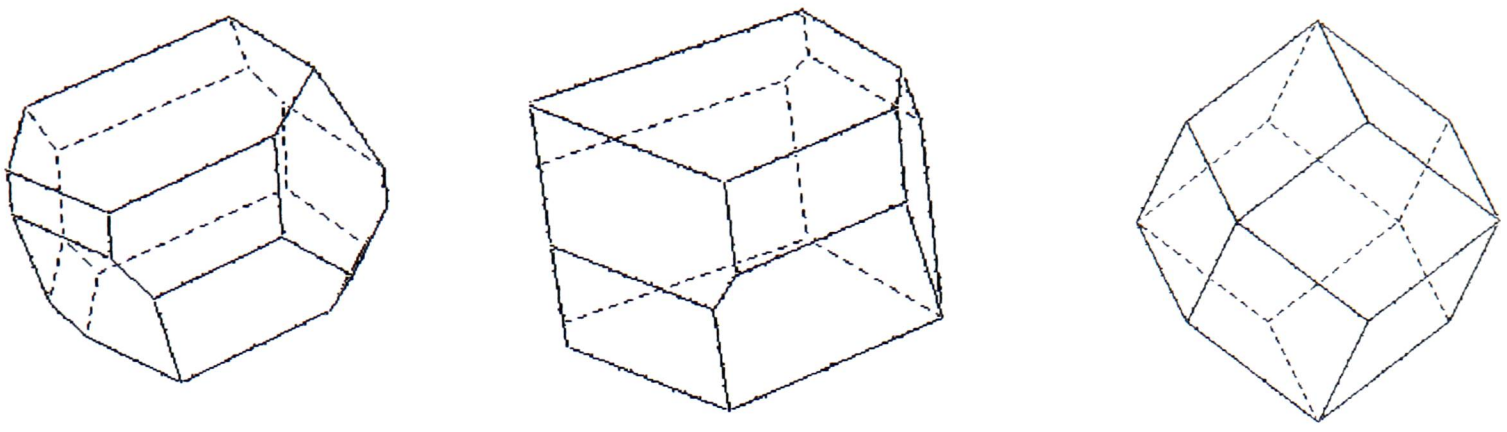

Figure 5.19. Left to right: Lattice VDPs for formamide phase I, phase II (molecule **2**) and ideal cubic close packing. The faces of the VDP for phase II are more equal in size than phase I.

Differential Scanning Calorimetry

The DSC trace for formamide is shown in Figure 5.20. On cooling, a sharp transition begins at 249K due to crystallisation of the sample. This is 26 K lower than the "normal" freezing point of formamide - supercooling is a common feature of DSC measurements. On the heating cycle, a broad transition starts at about 275 K due to melting of the sample.

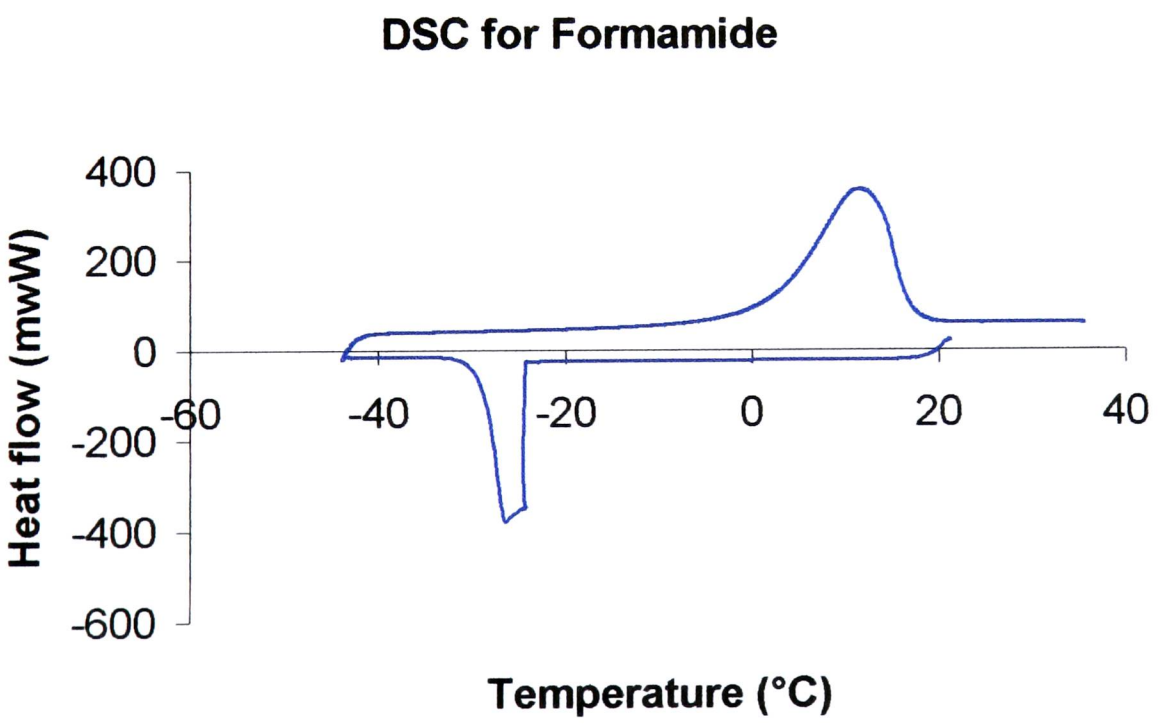

Figure 5.20. DSC trace for formamide.

There is no evidence in the DSC trace of any further temperature induced solid-solid phase transitions as there are no other peaks or troughs aside from the crystallisation and melting features. This indicates that phase II of formamide is not formed between 90 K and melting; phase transitions at very low temperatures may be possible.

5.3.2 N-methyl formamide

The structure at 250 K and 3 kbar consists of four fold helical chains parallel to the *b* axis (Figure 5.21). The molecules are in the same conformation as described by Neuefeind *et al.* (1996). Both of the crystallographically independent molecules make two hydrogen bonds; there are two unique hydrogen bonds in the structure as both types of molecule alternate within each chain. The lengths of the hydrogen bonds are shown in Table 5.16. There is very little difference in the hydrogen bonds under the various conditions of this study.

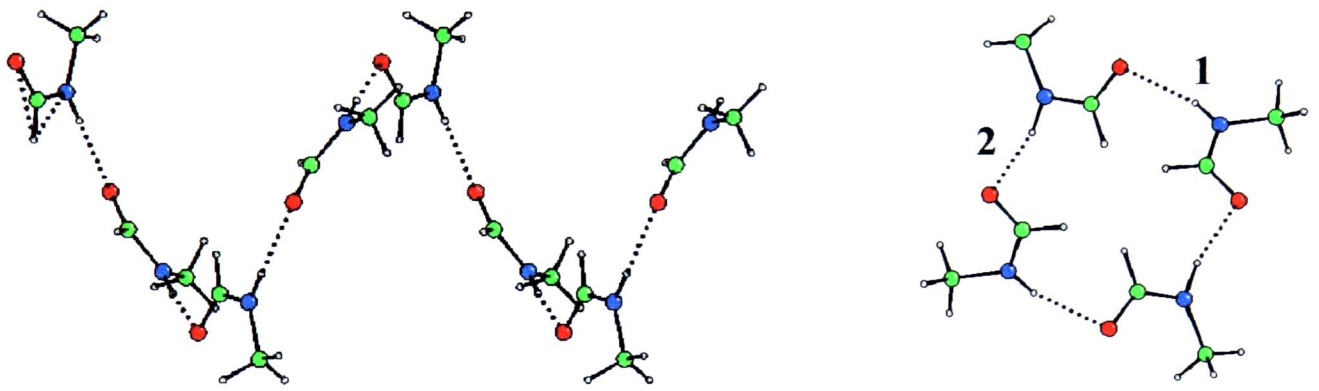

Figure 5.21. Structure of N-methyl formamide viewed perpendicular to the *a* (left) and *b* (right) unit cell axes.

Conditions	N...O (**1**) / Å	N...O (**2**) / Å	C-O...N (**1**) / Å	C-O...N (**2**) / Å
100 K	2.8630(14)	2.8728(14)	114.53(8)	101.99(8)
150 K	2.8670(17)	2.8812(17)	114.40(10)	102.50(9)
250 K	2.881(3)	2.895(3)	113.82(14)	104.04(13)
3 kbar	2.885(6)	2.905(12)	114.9(5)	104.4(5)
5 kbar	2.887(13)	2.856(15)	114.4(9)	104.0(6)

Table 5.16. Hydrogen bond parameters in the structure of N-methyl formamide. The interactions (**1** and **2**) are shown in Figure 5.15.

There are no hydrogen bonding interactions between helices. The helices are interleaved parallel to the *c* axis, building up layers within the structure with the methyl groups bounding the layers above and below (Figure 5.22). The closest contact between helices is between the oxygen atom of one molecule and the formyl carbon of the adjacent helix. The orientation of the C-H makes this contact unlikely to have any weak hydrogen bond character (contact 1 in Figure 5.22); the closest possible weak hydrogen bond is the next closest contact (contact 2 in Figure 5.22). This distance changes by only 0.02 Å with changing conditions (Table 5.17).

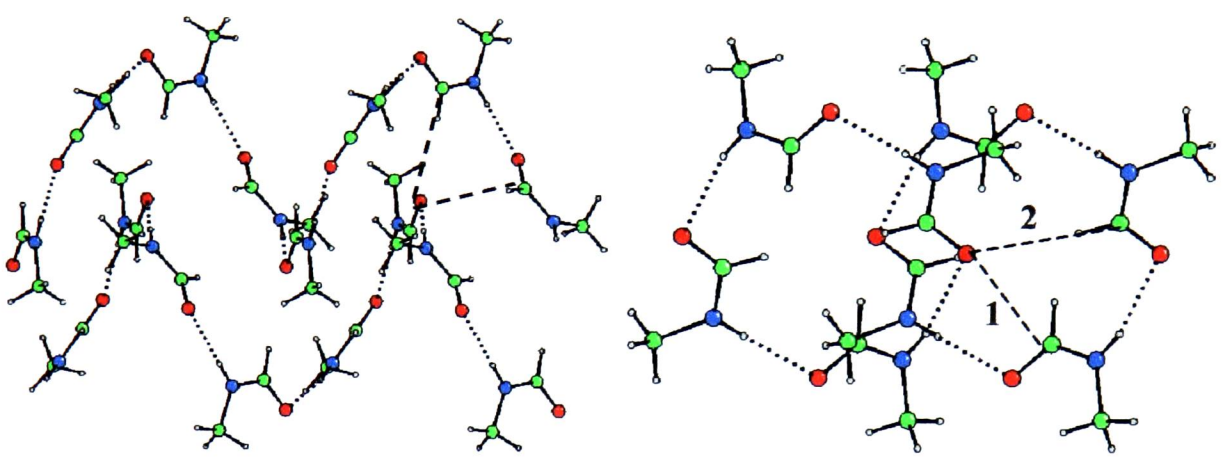

Figure 5.22. Interleaving of two helices viewed perpendicular to the *a* (left) and *b* (right) unit cell directions. Dashed lines indicate the closest contact between helices. The changes in length of these contacts are given in Table 5.17.

The closest contact between the layers of interleaved helices is the methyl - methyl contact (Figure 5.23). The changes in this contact with changing conditions are listed in Table 5.17; as with the other distances there is little change with altering conditions.

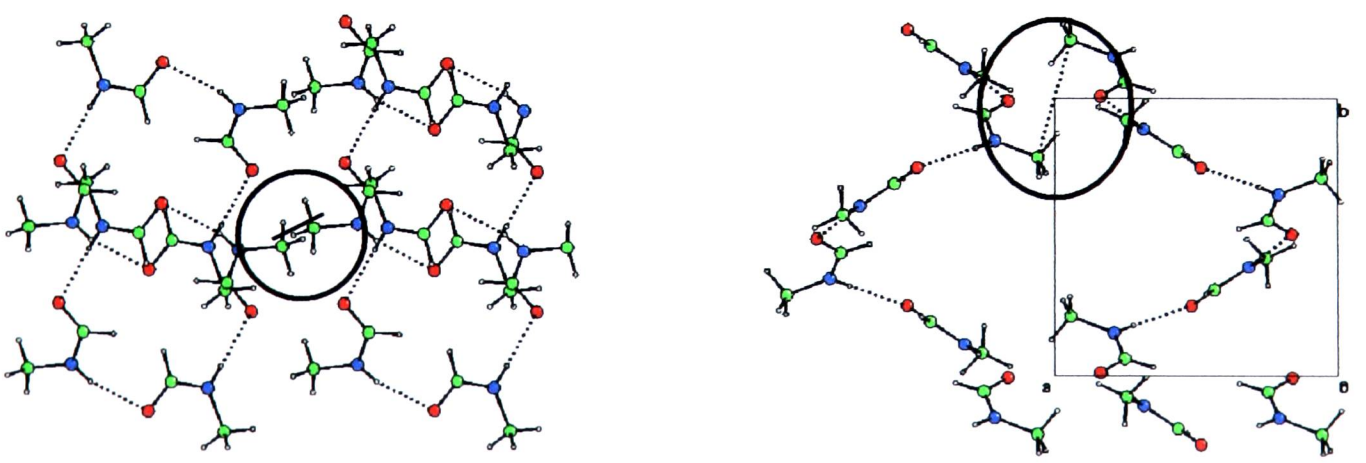

Figure 5.23. Packing of layers in N-methyl formamide, showing the methyl - methyl contact (contact **3** in Table 5.17). The ringed section shows the closest Me-Me contact (also shown with a dashed line)

	C...O between helices (**1**) / Å	C-H...O between helices (**2**) / Å	C...C between layers (**3**) / Å
100 K	3.189	3.505	3.779
150 K	3.211	3.513	3.811
250 K	3.269	3.518	3.861
3 kbar	3.250	3.528	3.845
5 kbar	3.210	3.523	3.843

Table 5.17 Close contacts in N-methyl formamide. The contacts are shown in Figure 5.22 and 5.23.

There are no large changes in the structure induced by the modest pressures described here; the effects of decreasing temperature are more pronounced than increasing pressure. The parameter most sensitive to both decreasing temperature and increasing pressure is the *b* unit cell length. This is linked to the tightness of the helix, which can be seen quantitatively in the angle made between three molecules (Figure 5.24 and Table 5.18).

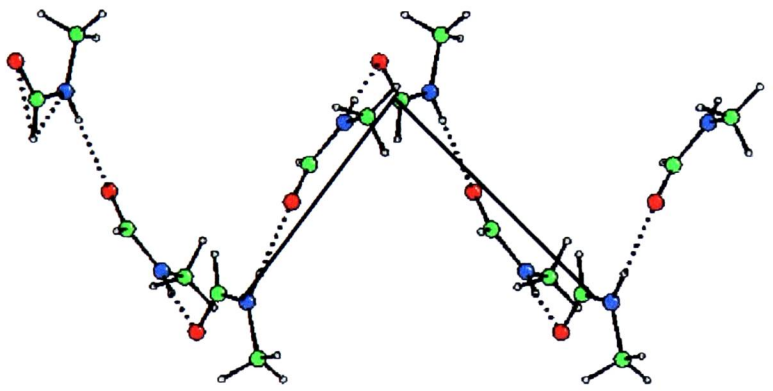

Figure 5.24. Side view of helix

	b / Å	Angle / °
100 K	8.4148(13)	75.54(2)
150 K	8.4720(11)	75.90(2)
250 K	8.661(9)	77.07(8)
3 kbar	8.5234(12)	75.95(11)
5 kbar	8.3748(14)	74.9(3)
20 kbar	7.653(5)	-

Table 5.18. Changes in helices

Differential Scanning Calorimetry

The DSC trace (Figure 5.25) for N-methyl formamide contains more features than that of formamide. On cooling, freezing occurs at 180 K with no other transitions appearing. On warming there are three transitions; at 168 K a small trough is clear which could be due to a solid-solid transition, at 223 K a small peak can be seen before the broad main melting peak which peaks at 271 K.

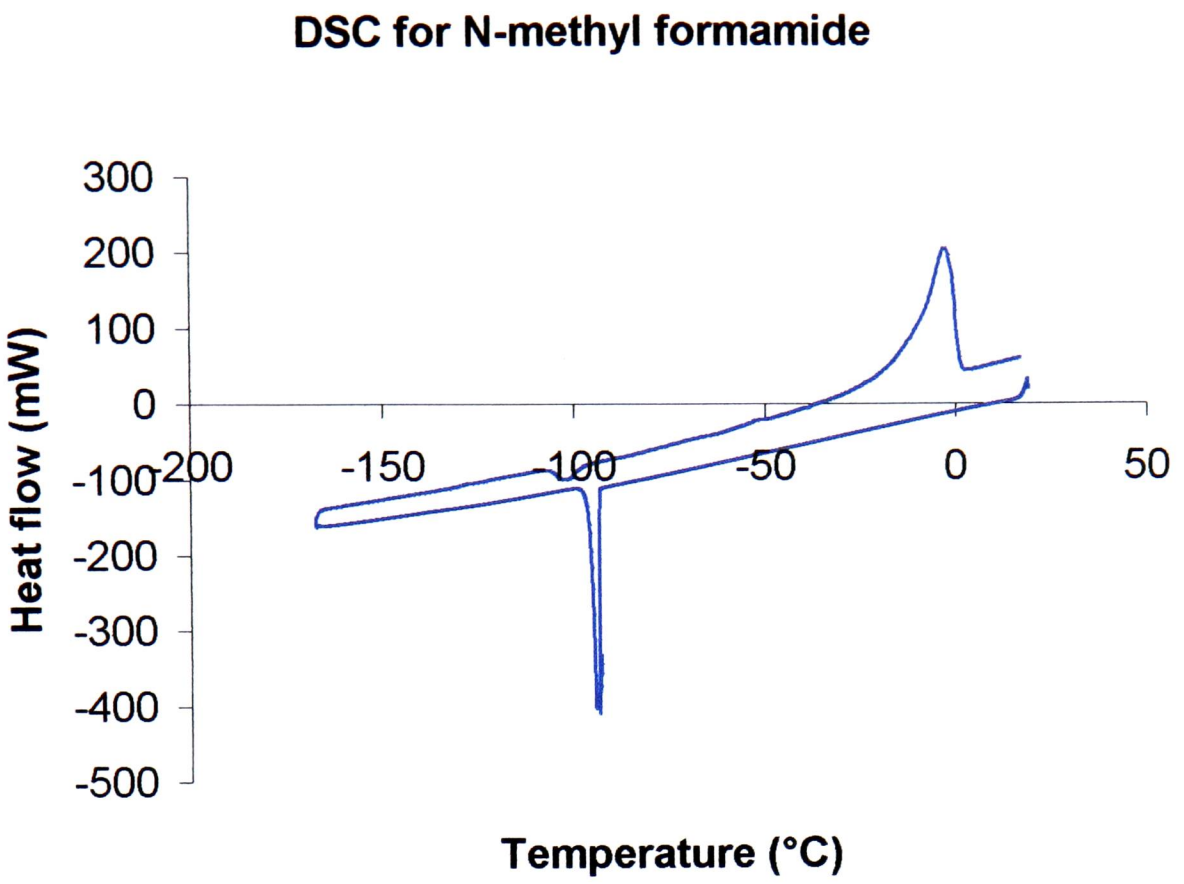

Figure 5.25. DSC trace for N-methyl formamide

The behaviour around the small trough was investigated by collecting data on a single crystal at 250 K, 150 K, 100 K and then warming to 200 K. No phase transitions were observed. The trough could be due to some small rearrangement of the structure, for example, a second order transition due to changes in the CH_3 torsional motion. The barrier to the transition for a single crystal is likely to be greater than for a polycrystalline material like that in the DSC. A variable temperature neutron powder study would be necessary to investigate the temperature behaviour of N-methyl formamide more fully.

5.3.2 N,N - dimethyl formamide

Under pressure DMF crystallises in the same crystal structure as observed at low temperature. Several crystal-growing experiments were performed and in each case the same structure was observed. As discussed in the introduction the only intermolecular interactions in the structure are weak C-H...O hydrogen bonds, so this system provides an opportunity to examine the effects of pressure on this type of interaction.

It is clear from a consideration of the unit cell dimensions alone that there has been substantial compression of the structure (Table 5.4). Since the structure has triclinic symmetry, the maximum values of strain in the structure cannot lie along each of the unit cell axes. The principal axes of the strain tensor were calculated for the DMF structures determined here relative to the low temperature structure using the method of Hazen and Finger (1982) and are shown in Table 5.19.

	Strain Tensor					
Pressure / kbar	1	2	3	Direction 1	direction 2	Direction 3
11	-0.01538	-0.02131	-0.0297	6 1 -3	3 -2 18	1 7 4
14	-0.02535	-0.02741	-0.04411	11 0 -6	3 0 20	2 7 2
26	-0.03148	-0.03692	-0.07129	10 0 3	-2 1 10	2 7 1
43	-0.04434	-0.0412	-0.07504	5 -1 3	-3 2 10	3 7 1

Table 5.19 Principal components of the strain tensor in DMF

Two C-H...O motifs can be distinguished in the structure of DMF. Four molecules are linked into a centrosymmetric ring by two unique interactions, and these rings are then linked by dimer units (Figure 5.26). These are linked by close contacts to molecules above and below the plane of these rings. This structure is related to the formamide structure - the dimers are similar, with C-H...O interactions replacing the N-H...O interactions of formamide. Whereas the rings in the formamide structures form infinite layers, in DMF the methyl groups bound interactions within the plane to form ribbons of molecules. The planes of molecules are parallel to the (1 2 1) plane.

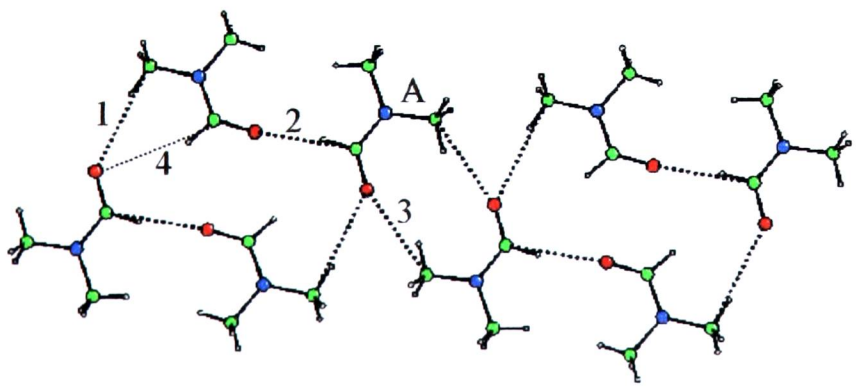

Figure 5.26 View of C-H...O interactions in one plane. The rings continue to the left and right of the diagram. The lengths of the interactions are given in Table 5.20.

	Interaction			
Conditions	1 / Å	2 / Å	3 / Å	4 / Å
90 K	3.414	3.294	3.471	3.713
11 kbar	3.374	3.204	3.403	3.490
14 kbar	3.342(9)	3.191(15)	3.368(19)	3.434(13)

Table 5.20 C-H...O interactions within one ribbon in DMF.

The three C-H...O interactions forming the ring structures decrease by about 0.1Å at 14 kbar compared to 90 K. The longer C-H..O interaction across the ring has decreased by almost three times as much.

The maximum value of the strain tensor is roughly parallel to the *b* axis (Table 5.19); this is approximately the separation of the layer regions in the crystal structure, which are parallel to the (1 2 1) plane. As pressure is increased the interlayer separation decreases (Table 5.21).

Condition	d_{121} / Å
90K	3.825
11kbar	3.194
14kbar	3.150
26kbar	3.067
43kbar	3.046

Table 5.21 Changes in separation between layers of ribbons with increasing pressure

Differential Scanning Calorimetry

The DSC trace for DMF is shown in Figure 5.27. The sample was initially quenched to low temperature, then warmed and cooled.

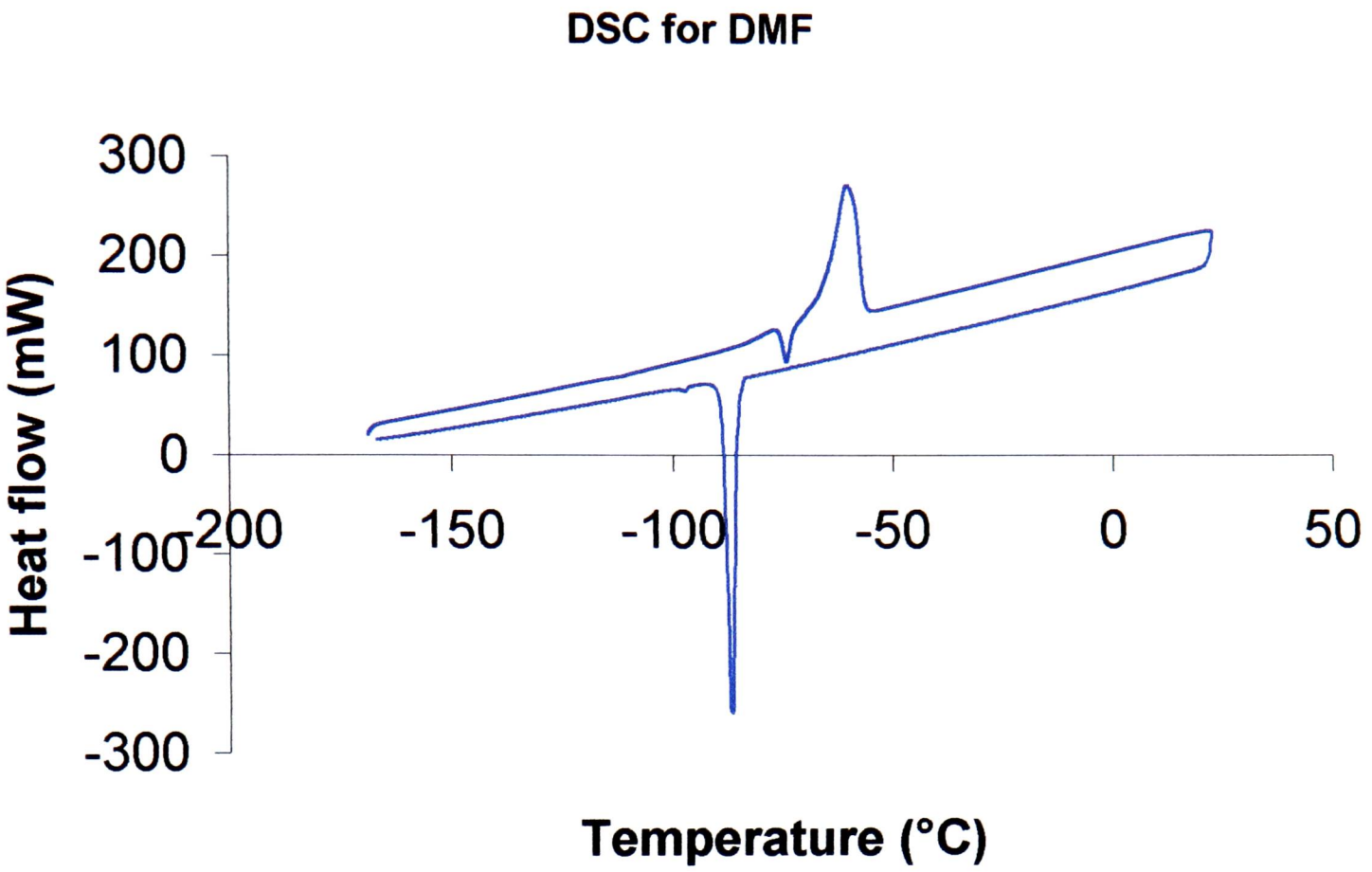

Figure 5.27. DSC trace for N,N-dimethyl formamide

On heating there is no evidence of the amorphous - crystalline phase transition at 148 K reported by Borrmann or the solid-solid transition at -95°C. This indicates that the crystalline phase was formed directly on rapid cooling. There is one exothermic event at 198 K just before the onset of melting at 205 K which could indicate a phase transition. On cooling there is a small peak at 175 K following the main freezing peak which could correspond to the phase transition reported by Borrmann *et al.*, although they did not observe the transition on cooling, only on initial heating. As with N-methyl formamide, a variable temperature study would be necessary to give further information on the changes in the structure with temperature.

5.4 Conclusions

A new crystalline phase of formamide is formed when crystallised by the application of pressure. The structures of the new phase is closely related to the previously determined structure, both structures consisting of hydrogen bonded layers with no interactions between the layers. The new structure supports the hypothesis that the molecules in the liquid are arranged in chains rather than rings, as the

difference between the two crystalline phases lies in the orientation of molecules within chains. The formation of phase II at high pressure can be rationalised on topological grounds; phase II has a packing arrangement closer to cubic close packing than phase I.

N-methyl formamide crystallises at high pressure in the same structure as at low temperature. The structure consists of hydrogen bonded helices parallel to the *b* axis, with the helices interleaved to form layers parallel to the *c* axis. There are no hydrogen bonding interactions between the layers of helices; methyl - methyl contacts are the closest contacts between the layers. The effects of pressure up to 5 kbar on the structure are less than the effects of reducing temperature to 100 K. The DSC trace implies there may be a phase transition.

N,N-dimethyl formamide crystallises in the same phase at high pressure as at low temperature. The structure is related to that of formamide with C-H...O contacts forming dimers similar to formamide.

5.5 References

Angel, R.J. (2003). ABSORB version 5.3. Crystallography Laboratory, Department of Geological Sciences, Virginia Tech., Blacksburg, VA, USA

Boese, R, Nussbaumer, M. (1994). *Correlations, Transformations, and Interactions in Organic Crystal Chemistry,* IUCr Crystallographic Symposia, Vol. 7, edited by D.W.Jones and A.Katrusiak, pp20-37, Oxford University Press.

Blessing, R.H. (1995). *Acta Cryst.*, **A51**, 33 - 38

Blessing, R.H. (1997). *J. Appl. Cryst.*, **30**, 421 - 426

Bormann, H., Persson, I., Sandstrom, M., Stalhandske, C.M.V. (2000). *J. Chem. Soc., Perkin Trans. 2*, 393-402

Bour, P., Tam, C.N., Sopkova, J., Trouw, F.R. (1998). *J. Chem. Phys.* **108**, 351 - 359

Bruker-AXS (2003). SAINT version 7.01A, Bruker-AXS, Madison, Wisconsin. USA.

Cabaleiro-Lago, E.M., Otero, J.R. (2002). *J. Chem. Phys.*, **117**, 1621 - 1632

Eberling, C.L. (1980). *Formic acid and derivatives,* Encyclopaedia of Chemical Technology, Vol. 11, edited by M. Grayson, Wiley (3rd edition)

Fantoni, A.C., Caminati, W. (1996). *J. Chem. Soc. Faraday Trans.*, **92**, 343 - 364

Hammai, F., Nasr, S., Oumezzine, M., Cortes, R. (2002). *Biomol. Eng.*, **19**, 201 - 205

Hazen, R.M, Finger, L.W. (1982). Comparative Crystal Chemistry, John Wiley & Sons, Chichester, p81

Ladell, J., Post, B. (1954). *Acta Cryst.*, **7**, 559 - 564

Miyake, M., Kaji, O., Nakagawa, N., Suzuki, T. (1985). *J. Chem. Soc. Faraday Trans. 2*, **81**, 277 - 281

Nasr, S., Bosio, L. (1997). *J. Chem. Phys.* **106**, 7913 - 7919

Nasr, S., Bosio, L. (1998). *J. Chem. Phys.* **108**, 2297-2301

Neuefeind, J., Zeidler, M.D., Poulsen, H.F. (1996). *Mol. Phys.*, **87**, 189-201

Ohtaki, H., Funari, A., Rode, B.M., Reibnegger, G.J. (1983). *Bull. Chem. Soc. Jpn.*, **56**, 2116 - 2121

Ohtaki, H., Katayama, N., Ozutsumi, K., Radnai, T. (2000). *J. Mol. Liquids,* **88**, 109 - 120

Parsons, S. (2003) , SHADE: Program for elimination of obscured reflections from high pressure data sets, The University of Edinburgh

Pinsky, M., Avnir, D. (1994). *Inorg. Chem.*, **37**, 5575 - 5582

Ramp, U., Gerharz, C.D., Doehmer, J., Oster, O., Gabbert, H.E. (1992). *Anticancer Res,* **12**, 537

Sheldrick, G. M. (1997). SHELX97. Programs for Crystal Structure Analysis (Release 97-2). University of Göttingen, Germany.

Sheldrick, G.M. (2002). SADABS. University of Göttingen, Germany.

Shimizu, H., Nagata, K, Sasaki, S. (1988). *J. Chem. Phys.*, **89**, 2743 - 2747

Spek, A.L. (1990). *Acta Cryst.* **A46**, C34. PLATON - A multipurpose crystallographic tool.

Stevens, E.D. (1977). *Acta Cryst.* **B34**, 544 - 551

Torrie, B.H., Brown, B.A. (1994). *J. Raman. Spec.* **25**, 183-187

Watkin, D. J., Prout, C. K., Carruthers, J. R., Betteridge, P. W. & Cooper R. I. (2003) CRYSTALS. Issue 12. Chemical Crystallography Laboratory, University of Oxford, England.

Chapter 6

Polymorphism in Pyridine

6.1 Introduction

6.1.1 Low temperature crystal structure

Under ambient conditions of pressure and temperature, pyridine is a colourless liquid with a freezing point of 231.4 K. The crystal structure at low temperature has been determined by Mootz and Wussow (1981). When crystallised at low temperature, pyridine forms an orthorhombic structure in space group $Pna2_1$ (Figure 6.1).

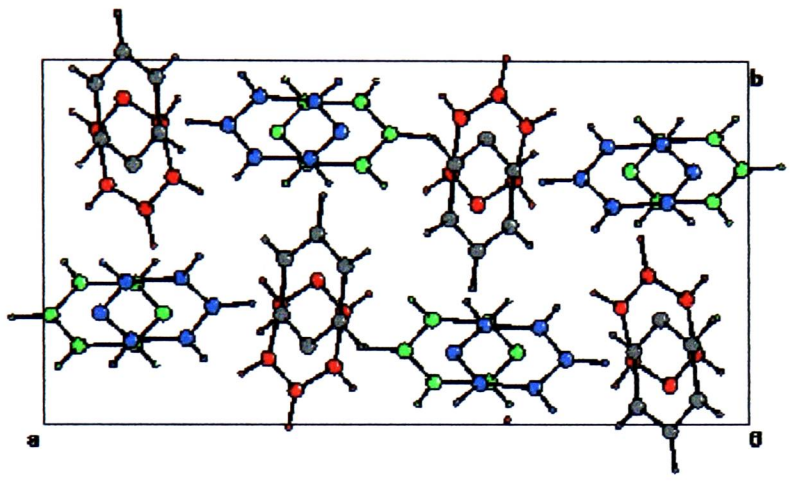

Figure 6.1. The crystal structure of pyridine at 153 K, viewed along the [0 0 1] direction. The molecules are coloured according to symmetry equivalence.

The crystal structure of pyridine is extremely unusual with four crystallographically independent molecules in the asymmetric unit. Of the ~300 000 entries in the Cambridge Structural Database (Allan & Kennard, 1993, CSD v5.42), 8.5% have $Z' > 1$ while only 1204 (0.41%) have more than three independent molecules. Whilst orthorhombic structures account for 19.6% of entries in the CSD, only 9.2% of structures with $Z' > 3$ are orthorhombic.

A smaller section of the low temperature structure of pyridine is shown in Figure 6.2. The only interactions in pyridine are weak C-H...N hydrogen bonds; there are no π - π interactions within 4.5 Å. The crystal structure is complex; only C-H...N contacts with a C...N separation less than 3.6 Å, with the angle at the hydrogen atom greater than 100°, are considered here. Determination of the exact distance criterion for a weak hydrogen bond is not straightforward (van der Berg & Seddon, 2003). Using this cut-off there are short chains in the structure where the four independent molecules are linked via C-H...N interactions (Figure 6.2). The angle

between the mean planes through molecules **2** and **4** is 1.9°, and between **1** and **3** is 9.2°.

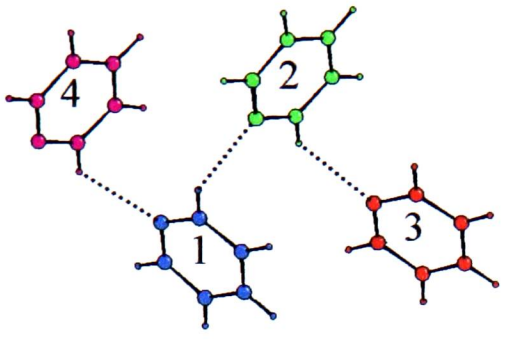

Figure 6.2. Chain of four molecules linked by C-H...N interactions in the structure of pyridine at 153 K. The lengths of the contacts are given in Table 6.1.

These short chain sections are linked by further C-H...N interactions to form the complex structure seen in Figure 6.1. The red molecule in Figure 6.2 makes no further C-H...N contacts to any molecule (within the limit described above). The magenta molecule forms a hydrogen bond to another four-molecule chain; in this way a three dimensional network is formed as this second four molecule chain is oriented at 90° to the first (Figure 6.3). The second chain then forms another weak hydrogen bond to a further chain, and so on.

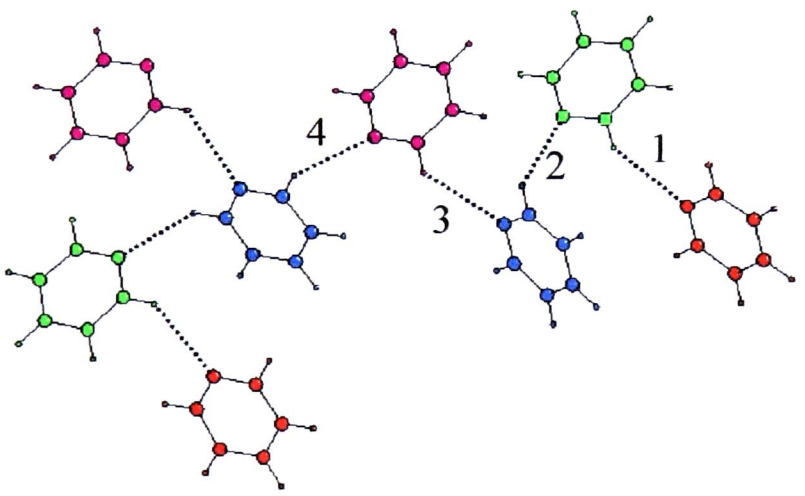

Figure 6.3. Interaction of two chains in pyridine

Interaction	C...N / Å
1	3.529
2	3.517
3	3.546
4	3.516

Table 6.1. C-H..N interactions in pyridine

There are four unique C-H...N interactions in the structure of pyridine, the lengths of which are listed in Table 6.1. The red molecule (molecule **3** in later description) is involved in one interaction, the green (molecule **2**) and magenta (molecule **4**) form two weak hydrogen bonds and the blue molecule (molecule **1**) participates in three weak hydrogen bonds.

Extensive studies by Boese *et al.* (2003, carried out concurrently with this work) have shown that there are no easily accessible polymorphs of pyridine at low temperature; neither does perdeuterated pyridine have any polymorphs when crystallised in the pure form. Differential scanning calorimetry to 123 K showed there were no phase transitions in either structure. However, crystallisation from a 1:1 solution of deuterated pyridine in pentane at 188 K yielded a new polymorph. Crystallisation from pentane allows access to polymorphs formed far below the melting point of a compound, as the temperature of crystallisation is reduced.

6.1.2 Theoretical studies

Recent crystal structure prediction calculations by Price *et al.* (2002) have shown there are a number of possible polymorphs of pyridine of similar energy (within 6 kJ mol^{-1}) to the observed structure. Over a dozen structures were identified that should crystallise competitively with the observed structure. None of these structures has been observed to date.

6.2 Experimental

6.2.1 Crystal growth and data collection

A sample of pyridine (Aldrich, used as received) was loaded into a diamond anvil cell equipped with 600 μm culet diamonds, a tungsten gasket with a 300 μm hole and a small chip of ruby. The sample was crystallised by the application of pressure and a crystal grown as described for formamide (Chapter 5). Crystals were grown at 8 kbar and 10.3 kbar. A new sample was loaded and a crystal was grown at 10.8 kbar.

Data were collected on the crystals prepared as described in Chapter 2. In each case data were collected with the cell in only one orientation - as each of the crystals was orthorhombic there is no increase in coverage by collecting data in more than one orientation.

6.2.2 Structure solution and refinement

The crystals grown at 8 kbar and 10.3 kbar indexed with similar cell dimensions to the low temperature structure using Gemini (Sparks, 2000). The data

were integrated using Saint (Bruker-AXS, 2003), using dynamic masks. An absorption correction for the effects of the diamond anvil cell was applied using Shade (Parsons, 2003) and for the crystal absorption using Sadabs (Sheldrick, 2002). The data were merged using Sortav (including Friedel equivalents) (Blessing, 1997). The previously determined co-ordinates (Mootz & Wussow, 1981, PYRDNA01) were used for structure refinement at 8 kbar, which was against $|F|^2$ using Shelxl (Sheldrick, 1997). Full refinement details for the 8 kbar sample are shown in Table 6.2; data for the crystal grown at 10.3 kbar were of too poor quality to allow full structure refinement but the cell dimensions are included in Table 6.2 for information.

The crystal grown at 10.8 kbar indexed with a new, orthorhombic unit cell. The space group was determined to be $P2_12_12_1$, with only one crystallographically independent molecule. The data were indexed, integrated and corrected for absorption as described for phase I. The structure was solved using direct methods (Sir92, Giacovazzo *et al.*, 1993) and refined against $|F|^2$ using Crystals (Watkin *et al.*, 2003). Due to the low number of data, thermal motion was treated isotropically. Full details of the refinement are shown in Table 6.2. Distance and angle restraints based on the geometry of the molecule at low temperature were applied.

Crystal Data			
Crystal system	Orthorhombic	Orthorhombic	Orthorhombic
Space group	$Pna2_1$	$Pna2_1$	$P2_12_12_1$
a / Å	17.416(3)	17.12(2)	5.4136(8)
b / Å	8.8803(10)	8.828(8)	6.8001(17)
c / Å	11.172(2)	11.042(140	11.245(3)
V / Å^3	1727.9(5)	1669(3)	413.95(16)
Z	16	16	4
ρ_{calc} / Mg m^{-3}	1.216	1.259	1.269
Number of reflections for cell (θ range, °)	477 (3.1 < θ < 23.1)	-	211 (3.5 < θ < 18.3)
Crystal description, size [mm]	colourless cylinder, 0.3 x 0.3 x 0.15	colourless cylinder, 0.3 x 0.3 x 0.15	colourless cylinder, 0.3 x 0.3 x 0.15
Pressure / kbar	8	10.3	10.8
Data Collection			
	8kbar	10.8kbar	
Reflections collected	1987	762	
Independent reflections	846	168	
R_{int}	0.0767	0.0892	
h	-12 to 11	-5 to 5	
k	-9 to 9	-6 to 6	
l	-10 to 11	-9 to 9	
Absorption correction (T_{min}, T_{max})	0.436, 1.0	0.492, 1.0	
Solution and Refinement			
Solution (Program)	Known (CSD refcode PYRDNA01)	Direct (Sir92)	
Refinement program	Shelxl	Crystals	
Hydrogen atom placement	Geometric	Geometric	
H refinement	Riding	no refinement	
R [F_o>4σ(F_o)]	0.0699 (395 data)	0.0678 (114 data)	
wR_2	0.1950	0.1635	
Goodness of fit on F^2	0.912	1.0330	
Restraints	81	6	
Parameters	98	25	
Maximum Δ/σ	0.006	0.000	
Weighting scheme x, y	0.0974, 0	0.0813, 0.356	
Largest difference map residuals [e Å^{-3}]	+0.153, -0.152	+0.39, -0.42	

* where $w = 1/ [\sigma^2(F_o^2) + xP^2 + yP$, $P=(F_o^2 + 2F_c^2)/3$

Table 6.2. Crystal data and refinement details for pyridine

6.3 Discussion

6.3.1 Phase I at 8 kbar

At 8 kbar there is a 3.16% reduction in the unit cell volume of phase I compared to 153 K. The largest contraction is in the *c* unit cell length (Table 6.3). As the structure is orthorhombic the principal axes of the strain tensor must lie along the unit cell axes. At 8 kbar the linear strain along *a* is -0.0056(3) $kbar^{-1}$, along *b* -0.0099(3) $kbar^{-1}$ and along *c* -0.0159(3) $kbar^{-1}$. The greatest strain is along the direction of the strongest interactions.

Conditions	*a* / Å	*b* /Å	*c* / Å	Volume / $Å^3$
153 K	17.524(3)	8.969(2)	11.352(2)	1784.225
8 kbar	17.416(3) (0.6%)	8.8803(10) (0.99%)	11.172(2) (1.59%)	1727.9(5) (3.16%)
10.3 kbar	17.12(2) ((2.3%)	8.828(8) (1.6%)	11.042(14) (2.7%)	1669(3) (6.4%)

Table 6.3. Changes in unit cell parameters of phase I of pyridine with changing conditions. Numbers in brackets are the percentage change relative to 153 K

There have been small changes in the lengths of the C...N weak hydrogen bonds, listed in Table 6.4. The average length of the four unique interactions has reduced from 3.527 Å to 3.49(3) Å. The changes in all of these interactions are small (less than 0.1 Å). The precision of the measurements at 8 kbar is low - it is not possible to assign any of the changes in the C...N interactions as statistically significant.

Interaction	C...N at 153 K / Å	C...N at 8 kbar / Å
1	3.529	3.481(18)
2	3.517	3.50(2)
3	3.546	3.527(17)
4	3.516	3.43(2)

Table 6.4. Changes in C-H...N interactions in phase I of pyridine at 8 kbar

There have been changes in other separations in the structure. One of the molecules takes part in only one weak hydrogen bond (molecule 3 in Figure 6.3 above). The hydrogen bonded chain of molecules terminates on this molecule; there are two C-H...C contacts made to an adjacent chain (Figure 6.3). These separations have reduced in length asymmetrically, with one decreasing very slightly from 3.772Å to 3.744(18) Å while the second has decreased by 0.3Å from 4.039 Å to 3.71(2) Å.

6.3.2 Analysis of the structure of phase II

At 10.8 kbar pyridine crystallises in the orthorhombic space group $P2_12_12_1$. This structure is the same as that observed by Boese for perdeuterated pyridine crystallised from pentane. The structure is much simpler than phase I, with one independent molecule in the asymmetric unit. The pyridine molecules form chains parallel to the *a* axis. The molecules within the chains are linked via weak C-H...N hydrogen bonds (Figure 6.4). These chains extend infinitely along the *a* axis.

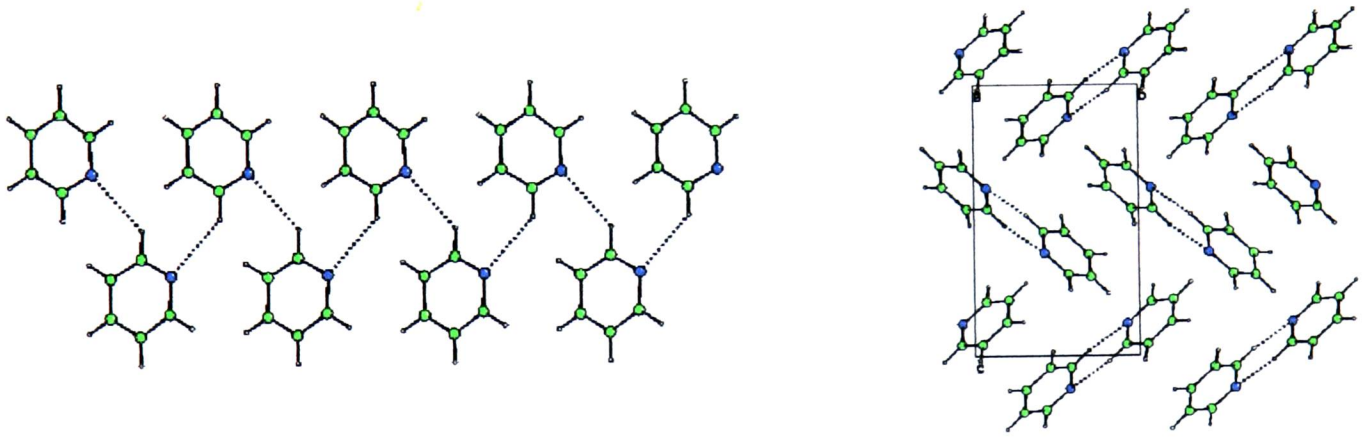

Figure 6.4. Chains formed by C-H...N interactions in phase II of pyridine (left). Right: Packing of chains (viewed along [1 0 0]

The C...N interaction in this structure is 3.411(13) Å, compared to the average C...N separation at 153 K of 3.527 Å. The chains are packed in a herring-bone pattern (Figure 6.4). As in phase I there are no π - π interactions in the structure within 4.5 Å.

There are similarities between the two polymorphs of pyridine. The weakly hydrogen bonded tetramers in phase I have a comparable geometry to the hydrogen bonded chains of phase II (Figure 6.5). There are small differences in the orientations of the molecules within each chain section in phase I; from the symmetry of phase II

this cannot be the case. Similarly the lengths of the hydrogen bonds vary in phase I but they are all equal in phase II.

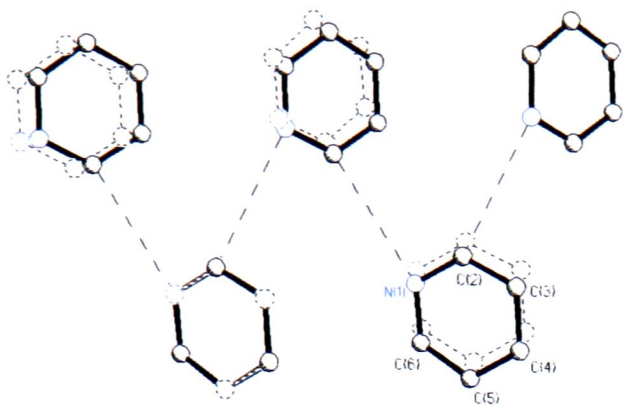

Figure 6.5. Overlay of phase I (dashed) and phase II (solid) of pyridine, showing the short range similarity of the two phases.

6.3.3 Topological analysis

Centroid separation

Mootz & Wussow (1981) describes the packing in the low temperature structure as similar to body centred cubic. Considering only the molecular centroid separations, it is possible to describe the packing in both phases as based on body centred cubic. The environment of one molecule (**2**) is shown in detail in Figure 6.6 with the separations of the molecular centroids listed in Table 6.5 at both 153 K and 8 kbar.

Contact (molecule)	Separation / Å		Contact (molecule)	Separation / Å	
	153 K	8 kbar		153 K	8 kbar
1 (3)	4.54	4.48	8 (3)	4.70	4.64
2 (1)	4.85	4.79	9 (4)	6.38	6.28
3 (3)	5.99	5.96	10 (4)	5.55	5.61
4 (1)	5.96	5.95	11 (4)	7.02	6.96
5 (1)	4.70	4.58	12 (4)	6.20	6.10
6 (3)	6.09	6.06	13 (4)	5.86	5.80
7 (1)	6.08	6.08	14 (4)	5.95	5.87

Table 6.5 Closest contacts of one molecule (molecule 2) in phase I of pyridine. The numbers in brackets refer to the other symmetry independent molecules (Figure 6.2)

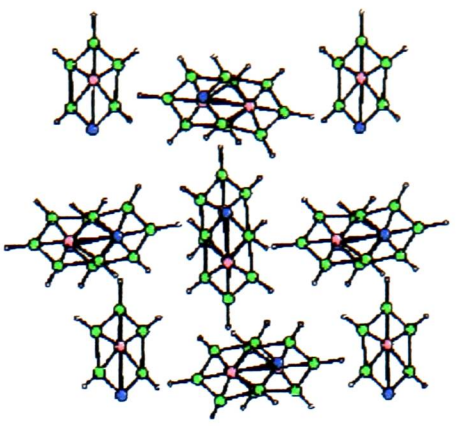

Figure 6.6 Schematic showing numbering scheme for separations of molecular centroids in phase I and phase II of pyridine. C marks the central molecule in the bcc array

The six "longer" contacts to the body centres of adjacent cubes are formed to molecule **4** (N4), while the eight contacts forming the cube corners are to molecules **1** and **3**. There are no significant changes in these contacts when the conditions are altered between 153 K and 8 kbar, with similar small changes in the separations of the other molecules. The Continuous Symmetry Measure (Pinsky & Avnir, 1994) for the molecular centroids with respect to bcc is 2.54 for molecule **2** at 153 K and 2.61 at 8 kbar.

The packing in phase II is also based on a distorted body centred cubic arrangement. Figure 6.8 below shows in detail how the environment of one molecule differs from phase I, and the separation of the molecular centroids are listed in table 6.6. The continuous symmetry measure relative to body centred cubic for this phase is 2.82; phase II is more distorted from ideal bcc than phase I. This is due to the six contacts to the body centres of adjacent cubes; the variance of these values is higher in phase II.

Contact	Separation	Contact	Separation
1	4.50	8	4.70
2	4.50	9	6.80
3	5.94	10	6.80
4	5.94	11	5.41
5	4.70	12	5.41
6	5.88	13	5.85
7	5.88	14	5.85

Table 6.6 Separation of molecular centroids in phase II of pyridine. The numbering is the same as in table 6.2 and Figure 6.6 above. The similarities in the environments in the two phases are shown in Figure 6.7.

Voronoi-Dirichlet Polyhedra

The above analysis is based solely on the separations of the centroids of the molecules. The centroids provide a convenient measure of the topology, but are not as rigorous as the Voronoi-Dirichlet Polyhedra (VDPs). In both polymorphs of pyridine the VDPs indicate a different topology to that derived from the centroid separations.

The lattice VDP for phase I for each molecule shows a coordination sequence of 13-47-110. This does not correspond to any of the sphere packing topologies, although it is close to the body centred cubic case of 14-50-110. Although the centroid analysis showed fourteen neighbours, the shape of the lattice VDP shows that the contact to one of these molecules is blocked by surrounding molecules. This blocked molecule is molecule 9 in Figure 6.6 above; this is not the furthest from the central molecule.

For phase II, the centroid analysis showed that the structure was more distorted from bcc than phase I (the CSM was 2.82 compared to 2.54 for phase I). The lattice VDP shows that the true coordination is based on cubic close packing; the coordination sequence is 12-42-92. Molecules 9 and 10 (Figure 6.6) do not correspond to a face of the VDP; these are the longest contacts in the bcc analysis. The CSM with respect to ccp for phase II is 2.45; the high pressure phase is thus more closely packed than phase I.

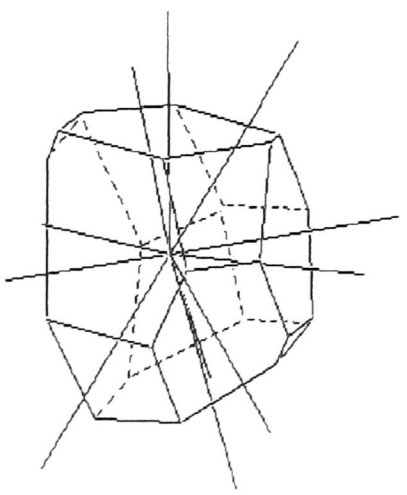

Figure 6.7 Lattice VDP for phase II of pyridine.

6.3.4 Comparison of the structures of phase I and phase II

The difference in the environments of the central molecule can be seen in Figure 6.8. The structures are very similar when viewed along [0 0 1]; however there are slight differences in the relative orientations of the molecules, illustrated for the ringed groups in phase I. These two groups have opposite tilt in phase I - the two groups are vertically related by the *n* glide plane, while in phase II molecules in similar positions are related by purely translational symmetry. Further differences in these groups of molecules are shown in Figure 6.8.iii - the two molecules within the pair have parallel orientations in phase II, but are perpendicular in phase I. Again the molecules are related by pure translational symmetry in phase II but by a glide plane (the *a* glide) in phase I.

6.4 Conclusions

The low temperature structure of pyridine is stable at 8 kbar and 10.3 kbar. Crystal growth at 10.8 kbar results in the formation of a new polymorph of pyridine, which is also observed for the perdeuterated molecule when crystallised from pentane at low temperature. The structures of the two phases are closely related at short range. Phase II can be viewed as a symmetrisation of the low temperature structure towards a more closely packed structure.

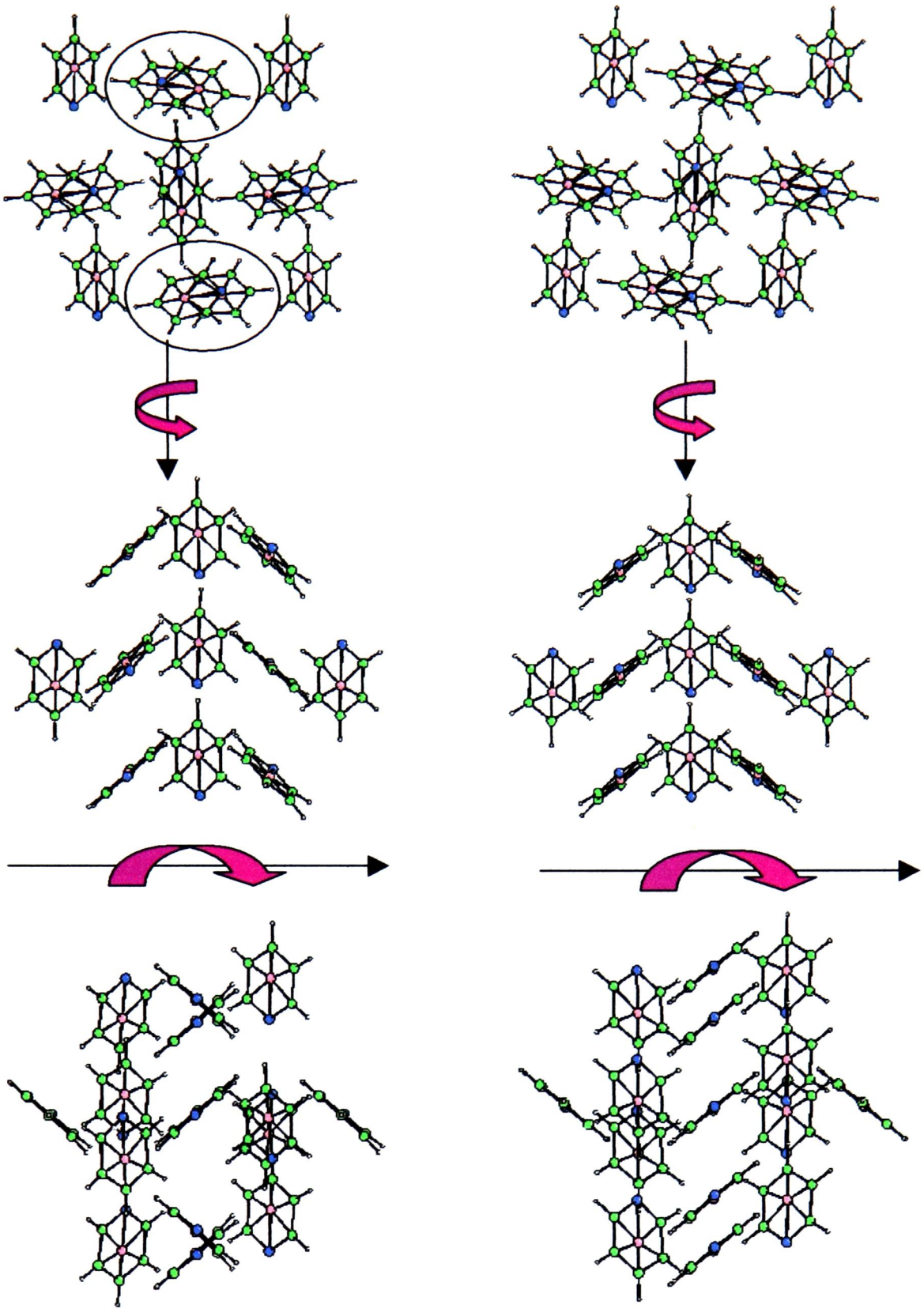

Figure 6.8. Comparison of body centred packing in pyridine. Left column - phase I. Right column - phase II.

From the top:

i. Viewed along [0 0 1]

ii. Phase I viewed along [[0 1 0], phase II viewed along [2 3 0]

iii. Phase I viewed along [1 0 0], phase II viewed along [-1 1 0]

6.5 References

Allen, F.H. & Kennard, O. (1993). *Chem Design Autom. News*, **8**, 31-37

Blessing, R.H. (1997). *J. Appl. Cryst.* **30**, 421-426

Bruker-AXS (2003). SAINT version 7.01A, Bruker-AXS, Madison, Wisconsin. USA

Boese, R., Kirchner, M.T., Gehrke, A., Blaser, D. (2003). private communication

Mootz, D., Wussow, H-G. (1981). *J. Chem. Phys.*, **75**, 1517 - 1522

Giacovazzo, C., Altomare, A., Cascarano, G., Guagliardi, A. (1993) *J. Appl. Cryst.* **26**, 343-350 SIR92 - A program for crystal structure solution.

Price, S.L., Anghel, A.T., Day, G.M. (2002). *CrystEngComm.*, 348-355

Parsons, S. (2003) SHADE: Program for elimination of obscured reflections from high pressure data sets, The University of Edinburgh

Pinsky, M., Avnir, D. (1994). *Inorg. Chem.*, **37**, 5575 - 5582

Sheldrick, G.M. (1997) SHELXL97, University of Göttingen, Germany.

Sheldrick, G.M. (2002) SADABS, version 2.04, University of Göttingen, Germany

Sparks, R.A. (2000). GEMINI version 1.05, Bruker-AXS, Madison, Wisconsin. USA

Van der Berg, J.-A., Seddon, K.R. (2003). *Cryst. Growth. Des.*, **3**, 643 - 661

Watkin, D. J., Prout, C. K., Carruthers, J. R., Betteridge, P. W. & Cooper R. I. (2003) CRYSTALS. Issue 12. Chemical Crystallography Laboratory, University of Oxford, England.

Chapter 7

Formation of piperidine hemi-hydrate

7.1 Introduction

7.1 Low temperature crystal structure

The structure of piperidine (C_5NH_{11}) at low temperature has recently been determined by Parkin *et al.* (2003). At 260 K piperidine crystallises as a monoclinic structure in $P2_1/c$ with one crystallographically independent molecule in the asymmetric unit. The piperidine molecules form chains linked by N-H...N hydrogen bonds parallel to the *b* axis of the unit cell. The N-H group acts as both a donor and acceptor in the hydrogen bonds (Figure 7.1).

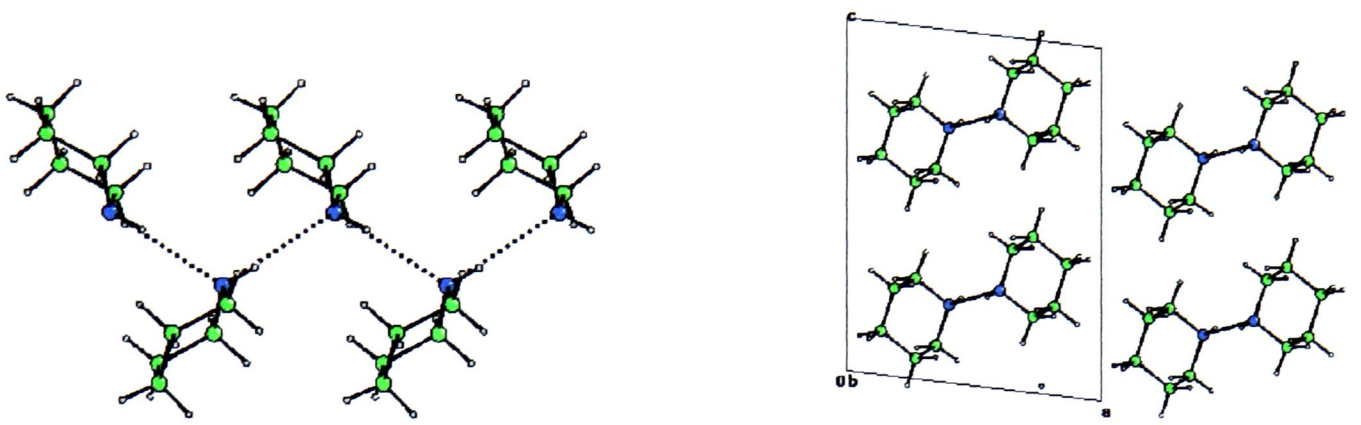

Figure 7.1. The crystal structure of piperidine consists of hydrogen-bonded chains of molecules (left) which pack to form the three dimensional structure (right)

7.2 Experimental

A sample of piperidine (Aldrich, used as received) was loaded into a diamond anvil cell equipped with 600 μm culet diamonds, a chip of ruby for pressure measurement and a tungsten gasket with a 300 μm diameter hole. A crystal was grown at 3.1 kbar in a similar manner to the formamide crystal (Chapter 5). The crystals grew as needles in the sample space, making it difficult to obtain a single crystal of suitable size.

Data were collected using a Bruker Smart diffractometer equipped with Mo-K_α radiation using the procedures described in Chapter 2. Several crystals were grown before data of sufficient quality for structure solution was obtained. For each sample the same unit cell was obtained, which was different to the unit cell obtained when a crystal was grown at low temperature. Two datasets were collected for the

final sample with the cell fixed to the goniometer head in two orientations. Structure solution and refinement (Section 7.3.1) showed this crystal to be piperidine hemi-hydrate.

Dry piperidine (>99.5%, Aldrich) was loaded into a diamond anvil cell under nitrogen to exclude water. The sample crystallised at 4 kbar, into a polycrystalline mass containing many small crystallites. Attempted growth of a single crystal of sufficient quality for structure solution and refinement was unsuccessful. The crystals grew with needle habits and nucleated from the gasket edge in large numbers. Reducing the pressure to reduce the number of crystallites resulted in fewer but much smaller crystals.

7.3 Results

7.3.1 Structure solution and refinement

The structure at 3.1 kbar indexed with a primitive monoclinic unit cell of approximately double the volume of the low temperature unit cell. This cell was repeatedly observed for a number of growth experiments; for the majority of these samples structure solution was hampered by poor quality data due to difficulties in crystal growth. The following description applies to the final sample.

The sample was initially indexed using Gemini (Sparks, 2000). Due to the large number of unindexed reflections the sample was re-indexed using a larger reflection array using the indexing program Cell_Now (Sheldrick, 2002). This program allows indexing of a sample using a previously determined unit cell (or indexing using an exhaustive vector search routine). From this indexing routine the sample was found to consist of one large crystal and several smaller crystals; from the 158 reflections manually harvested, 74 were indexed by the orientation index corresponding to the first domain. 69 of the remaining reflections were indexed by six further orientation matrices. The rotation matrices linking these orientation matrices to the first component were not symmetry elements of the crystal system or of a supercell - there were no pseudosymmetry relationships between the crystals in the sample.

The frames were integrated using the orientation matrix corresponding to the major component of the crystal using Saint (Bruker-AXS 2003), with dynamic masks.

The data were corrected for absorption by the diamond anvil cell using Shade (Parsons, 2003) and for absorption by the crystal using Sadabs (Sheldrick, 2002). The data were merged using Sortav (Blessing, 1997). Data from the two collections were treated for absorption separately and then merged.

Crystal Data	
Formula	$(C_5H_{11}N_1).0.5(H_2O)$
Crystal system	Monoclinic
Space group	$P2_1/c$
a / Å	5.1918(8)
b / Å	21.3565(19)
c / Å	10.3889(16)
V / Å^3	1133.7(3)
Z	8
ρ_{calc} / Mg m^{-3}	1.103
Number of reflections for cell (θ range, °)	442 (4 < θ < 23)
Crystal description, size / mm	0.20 x 0.15 x 0.10
Pressure / kbar	3.1
Data Collection	
Reflections collected	5264
Independent reflections	554
R_{int}	0.1505
h	-5 to 5
k	-23 to 23
l	-9 to 9
Absorption correction (T_{min}, T_{max})	0.814, 1.227
Solution and Refinement	
Solution (Program)	Direct (Shelxs)
Refinement program	Crystals
Hydrogen atom placement	Geometric (see text)
H refinement	No refinement
R [F_o>4σ(F_o)]	0.1083
wR_2	0.2690
Goodness of fit on F^2	0.987
Restraints	51
Parameters	53
Maximum Δ/σ	0.0025
Weighting scheme* x,y	0.094, 5.885
Largest difference map residuals [e Å^{-3}]	+0.34, -0.31

* where $w = 1/ [\sigma^2(F_o^2) + xP^2 + yP,\ P=(F_o^2 + 2F_c^2)/3$

Table 7.1. Crystal data and refinement details for piperidine hemi-hydrate.

The space group was determined to be $P2_1/c$. From the volume of the unit cell it appeared there were two crystallographically independent piperidine molecules in the structure. The structure was solved using direct methods (Shelxs, Sheldrick, 1997) and two piperidine molecules were identified. Difference Fourier refinement showed one large peak in the difference map indicating that the structure was of the hemi-hydrate rather than pure piperidine. The structure was refined against $|F|^2$ (Crystals, Watkin *et al.*, 2003) on all data. Distance restraints based on the geometry of the molecule at low temperature were applied. Similarity restraints were used to apply C_{2v} symmetry to the molecules and to link the geometry of the two molecules.

The CH_2 hydrogen atoms were placed geometrically. At low temperature the imino hydrogen is in the equatorial position and was assumed to be in the same orientation in the hemi-hydrate. Gas-phase electron-diffraction studies (Gundersen & Rankin, 1983) have shown the major component in the vapour phase has the imino hydrogen atom in the equatorial position. The hydrogen atoms on the water molecule were placed along the direction of possible hydrogen bonding. Full details of the refinement are shown in Table 7.1.

7.4 Discussion

Analysis of the crystal structure of the hemi-hydrate

Part of the structure of piperidine hemi-hydrate is shown in Figure 7.2. As in the low temperature structure the nitrogen atom acts as both a hydrogen bond donor and as an acceptor, participating in two hydrogen bonds. The water molecule has inserted in between the piperidine molecules to form O-H...N hydrogen bonds in place of the N-H...N interactions observed at low temperature.

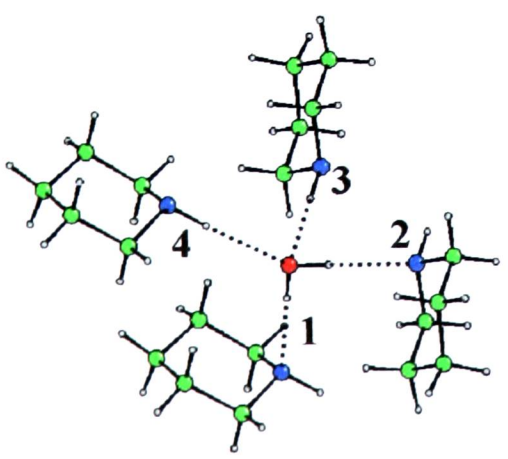

Figure 7.2. Hydrogen bonding environment of the water molecule.

Interaction	N...O / Å
1 O-H...N(11)	2.940(14)
2 O-H...N(22)	2.929(9)
3 N(21)-H...O	3.105(9)
4 N(11)-H...O	3.175(10)

Table 7.2. Hydrogen bond lengths in piperidine hemi-hydrate. The numbers in bold refer to Figure 7.2.

The water molecule participates in four hydrogen bonds (Figure 7.2). One of the piperidine molecules interacts with the water molecule to form hydrogen bonded chains parallel to the *a* axis (Figure 7.3). These chains are related to those observed in the low temperature structure of pure piperidine (Figure 7.1). The piperidine molecules linked in this way are equivalent by the space group symmetry (although linked by the intervening water molecules).

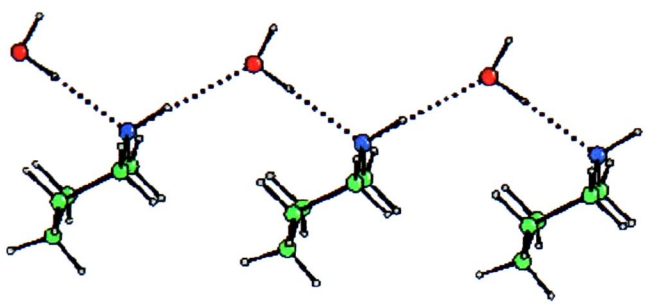

Figure 7.3. Insertion of a water molecule into the hydrogen bonded chain of piperidine to form chains related to those observed in the pure piperidine structure

Two of these chains are linked via the second independent piperidine molecule. This molecule forms hydrogen bonds to two water molecules in adjacent chains, forming a short chain perpendicular to the chains formed by molecule 1. The fourth interaction of the water molecule is to a second chain linking molecule (Figure 7.4).

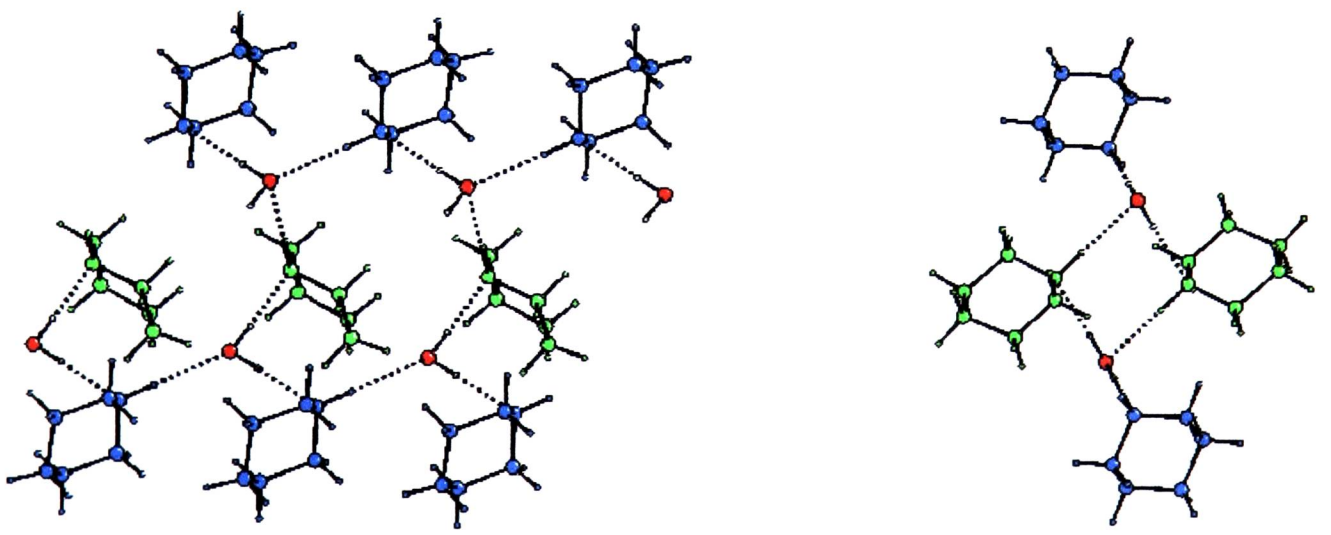

Figure 7.4. Interlinking of chains in piperidine hemi-hydrate. The piperidine molecules are coloured according to symmetry equivalence. The blue molecules are those which form the chains shown in Figure 7.3 above. Left - viewed along the (0 0 1) direction (second row of green molecules removed for clarity). Right - viewed along the (1 0 0) direction

The hydrogen bonds in which O-H is the donor are shorter than those where N-H is the donor (Table 7.2). These two hydrogen bonds are not significantly different. The chain forming N-H...O interaction is longer (0.070(13) Å) than the chain bridging N-H...O hydrogen bond. The N-H...N distance in the pure piperidine structure at low temperature is 3.184(1) Å, compared to the 3.175(1) Å N-H...O chain forming interaction in the hemi-hydrate.

To compare these hydrogen bond lengths with similar systems, searches were performed using the Cambridge Structural Database on secondary amines and water as hydrogen bond acceptors and donors, with a X...H separation of between 1.5 and 3.0 Å. The results are shown in Figure 7.5.

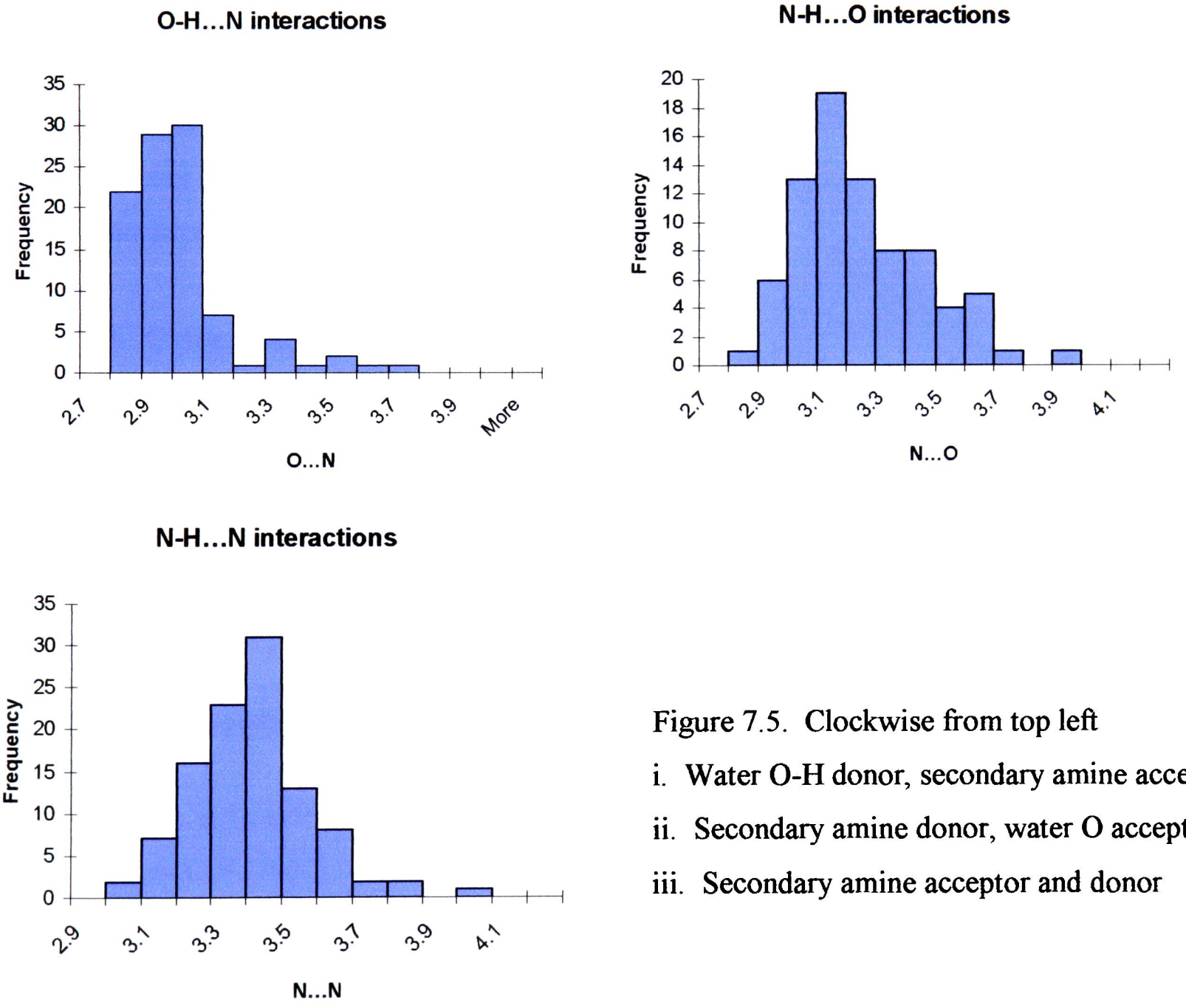

Figure 7.5. Clockwise from top left

i. Water O-H donor, secondary amine acceptor

ii. Secondary amine donor, water O acceptor

iii. Secondary amine acceptor and donor

N-H...N interactions of structures in the database cover a wide range of values, peaking between 3.4 and 3.5 Å. The hydrogen bond in pure piperidine (3.185 Å) is short for this type of interaction. The hydrogen bonds in the hemi-hydrate follow the trend seen for other structures for O-H...N interactions to be shorter than N-H...O; O-H is a better donor than N-H to N.

Formation of the hemi-hydrate

The sample of piperidine used in this work was taken from the same source as the sample originally used for the low temperature structure determination. However the hemi-hydrate was not observed at low temperature. This may be due to the difference in freezing points of the two compounds, which results in separation at low temperature. The slow heating and cooling cycles used in low temperature crystal growth could result in zone refinement of the sample. Similar results have been found for paracetamol, which forms a methanol solvate when crystallised from a saturated methanol solution at high pressure (Fabbiani *et al.*, 2003); a methanol solvate has never been observed at low temperature.

7.5 Conclusion

A novel hemi-hydrate of piperidine was formed at 3.1 kbar. The crystal structure consists of hydrogen bonded chains of molecules, with piperidine molecules are linked by water molecules. The chains are linked by short chains perpendicular to the main chains in the structure.

7.6 References

Blessing, R.H. (1997). *J. Appl. Cryst.* **30**, 421-426

Bruker-AXS (2003). SAINT version 7.01A, Bruker-AXS, Madison, Wisconsin. USA

Fabbiani, F., David, W.I.F., Parsons, S., Pulham, C.R., Allan, D.R., Dawson, A., McGregor, P.A., Oswald, I.D.H. (2003). *Chem. Commun.* in press

Gundersen, G., Rankin, D.W.H. (1983). *Acta Chem. Scand.*, **A37**, 865 - 874

Parkin, A., Parsons, S., Oswald, I.D.H. (2003). in preparation

Parsons, S. (2003) SHADE: Program for elimination of obscured reflections from high pressure data sets, The University of Edinburgh

Sheldrick, G.M. (1997) SHELXS97, University of Göttingen, Germany.

Sheldrick, G.M. (2002) SADABS, version 2.04, University of Göttingen, Germany.

Sheldrick, G.M. (2002). Cell_Now: a program for indexing diffraction patterns from multiple or twinned crystals. University of Gottingen, Germany

Sparks, R.A. (2000). GEMINI version 1.05, Bruker-AXS, Madison, Wisconsin. USA

Watkin, D. J., Prout, C. K., Carruthers, J. R., Betteridge, P. W. & Cooper R. I. (2003) CRYSTALS. Issue 12. Chemical Crystallography Laboratory, University of Oxford, England.

Chapter 8
Conclusions

8.1 Conclusions

The use of the CCD area detector in data collection for samples at high pressure has been demonstrated to be practicable. The problems associated with the background and restricted reciprocal space access caused by the diamond anvil cell can be overcome by the use of the correct integration and refinement strategies.

The general trend shown by the molecules studied in this thesis is towards the formation of more symmetric structures at high pressure. The packing of formamide, l-alanine and pyridine all become more symmetric with increasing pressure, although a counter example is the transition of the symmetric γ-glycine to the less symmetric δ-glycine structure. The new polymorphs formed at high pressure contained hydrogen bonds of comparable geometries to those seen in the ambient pressure phases; the increased density of the high pressure polymorphs could be related to overall increases in packing efficiency rather than radical compression of hydrogen bonds. The hydrogen bond network in l-alanine was found to influence the anisotropic compression of the crystal structure; of equal importance was the topology of the molecular packing. The high pressure studies detailed in this thesis represent a significant addition to the area of high pressure molecular science. However, drawing over-reaching conclusions from the relatively small number of systems described is dangerous, and a much larger body of knowledge will be required before any overall conclusions can be made regarding the effect of pressure on molecular crystal structures.

The polymorphs observed in the experiments performed in this thesis are formed under only modest pressures; the highest pressure at which a new polymorph was observed is 10.8 kbar for phase II of pyridine. The exploration of the phase diagrams over a larger pressure regime for even the small number of compounds described here represents a large amount of further experimentation. At much higher pressures the formation of metallic phases has been observed for elemental systems; the effects of multimegabar pressures on molecular systems represents a significant theoretical and experimental challenge.

Appendix

Lecture courses and meeting attended

Courses

November 2000:	Unix 1 and 2
November 2000:	Fortran90 Programming
April 2001:	BCA Intensive Crystallography course
June 2001:	Introduction to HTML
June 2001:	Exotic Instruments in Chemistry
December 2001:	Unix 3 (Shell programming)
April 2002:	BCA Rietveld refinement workshop
December 2002:	Graphing packages

Conferences attended

April 2001:	BCA Spring Meeting, Reading	Poster
September 2001:	USIC 2001, St Andrews	Poster
December 2001:	BCA PCG Winter meeting, Daresbury	
April 2002:	BCA Spring Meeting, Nottingham	Poster
August 2002:	IUCr XIX, Geneva	Poster
September 2002:	40th European High Pressure Meeting, Edinburgh	Poster
September 2002:	USIC 2002, Edinburgh	Co-organiser
November 2002:	BCA CCG Autumn meeting, London	Talk
December 2002:	BCA PCG Winter meeting, Edinburgh	
April 2003:	BCA Spring Meeting, York	Poster
September 2003:	USIC 2003, Strathclyde	Poster

Publications

Pressure-induced polymorphism in phenol. Allan, David R.; Clark, Stewart J.; Dawson, Alice; McGregor, Pamela A.; Parsons, Simon. *Acta Crystallographica, Section B: Structural Science* (2002), **B58**(6), 1018-1024.

Synthesis, X-ray Crystal Structure Determination, and Low-Temperature n-Hexane Glass Luminescence Studies of [$Cu_{26}(hfac)_{12}(C{\equiv}CR)_{14}$] (R = n-$C_4H_9$, n-$C_5H_{11}$, n-$C_6H_{13}$). Higgs, Timothy C.; Parsons, Simon; Bailey, Philip J.; Jones, Anita C.; McLachlan, Fiona; Parkin, Andrew; Dawson, Alice; Tasker, Peter A. *Organometallics* (2002), **21**(26), 5692-5702

Titanium(IV) chloride at 150 K. Dawson, Alice; Parkin, Andrew; Parsons, Simon; Pulham, Colin R.; Young, Amy L. C. *Acta Crystallographica, Section E: Structure Reports Online* (2002), **E58**(10), i95-i97.

Comparison of the high-pressure and low-temperature structures of sulfuric acid. Allan, David R.; Clark, Stewart J.; Dawson, Alice; McGregor, Pamela A.; Parsons, Simon. *Journal of the Chemical Society, Dalton Transactions* (2002), (8), 1867-1871.

Synthesis, structure and properties of [Pt(2,2'-bipyridyl-5,5'-dicarboxylic acid)(3,4-toluenedithiolate)]: tuning molecular properties for application in dye-sensitised solar cells. Geary, Elaine A. M.; Hirata, Narukuni; Clifford, John; Durrant, James R.; Parsons, Simon; Dawson, Alice; Yellowlees, Lesley J.; Robertson, Neil. *Dalton Transactions* (2003), (19), 3757-3762.

Pressure induced formation of a solvate of paracetamol. Fabbiani, F.P.A., Allan, D.R., Dawson, A., David, W.I.F., McGregor, P.A., Oswald, I.D.H., Parsons, S., Pulham, C.R.P. *Chemical Communications*, (2003). published on the web.

Abbreviations used

bcc	body centred cubic
ccp	cubic close packing
CSD	Cambridge Structural Database
CSM	Continuous Symmetry Measure
DMF	N,N-dimethyl formamide
DSC	Differential Scanning Calorimetry
hcp	hexagonal close packing
NMF	N-methyl formamide
VDP	Voronoi-Dirichlet Polyhedron

Crystallographic Information Files for the structures described in Chapters 3, 4, 5, 6 and 7 are on the attached CD.